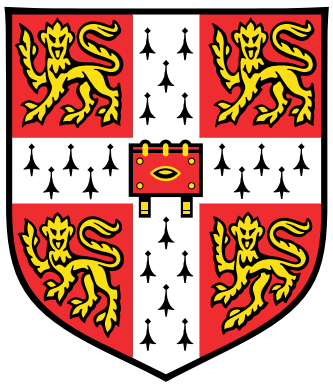

University of Cambridge

WEAR OF FINE PEARLITE, NANOSTRUCTURED BAINITE AND MARTENSITE

Subhankar Das Bakshi
Darwin College

This dissertation is submitted for the degree of Doctor of Philosophy
December, 2016.

ABSTRACT

Abrasion is a form of wear prominent particularly in the agricultural, mining, mineral and transportation industries. The cost of abrasive wear to the national economy is estimated to be about 1% of the gross national product, and it can compromise the safety and reliability of engineering components. The mechanism of wear is complex and dependent on all the materials involved in the process, environmental conditions and many subtle factors such as the shape of the abrading particles. Many abrasion-resistant steels are based on a quenched and tempered martensitic microstructure, because the hardness of the steel should intuitively matter in determining the wear rate. Nevertheless, the relationship between the rate of material loss and steel hardness is unlikely to be monotonic.

The purpose of the work presented in this thesis was primarily to study the abrasive wear behavior of a nanostructured bainitic steel that has been successful in structural applications, is capable of mass production, and can achieve hardness levels comparable to martensitic steels without compromising ductility, toughness and fatigue resistance. A variety of wear mechanisms have been studied, in each case with a detailed characterisation of the damage, the structural evolution and a panoply of theoretical approaches.

In the case of three-body abrasion, it is found that huge variations in hardness, achieved by changing the structure from pearlite, nanostructured bainite to martensite by heat treatment, do not lead to significant differences in the wear rate. This is because the wear mechanisms change, for example from severe sub-surface deformation leading to sticking in the case of pearlite, to brittle detachment of material in the martensitic state. The nanostructured bainite, on the other hand, undergoes reaustenitisation at the surface that leads to the formation of a fine martensitic layer with consequent surface hardening, in contrast to the pearlite and martensite, both of which soften at the contact surfaces. It is the presence of stable austenite in the nanostructured bainite that causes this difference, because austenitisation becomes easier to achieve.

This hypothesis has been further tested by eliminating the austenite from the nanostructured bainite. The experiments confirm that a reaustenitised layer no longer forms during three-body abrasion. The softening observed on martensitic samples also disappears when similar tests are done on tempered martensite, indicating the effect of the localised heat generated during dry abrasion on untempered martensite.

In contrast to three-body abrasion using silica where the weight loss is insensitive to hardness, the nanostructured bainite outperforms most commercial alloys of equivalent hardness, and sometime even harder materials, during dry rolling/sliding wear. The mechanisms involved have been rationalised in terms of structural damage mechanisms, the development of beneficial residual stresses, and detailed changes in crystallite size and dislocation character as a function of rolling.

It has, in general, been possible to rationalise the observed variations in different types of wear tests and micro- or nanostructures, and it is believed that the work will be of use in designing commercially important products.

DECLARATION

This dissertation is submitted for the degree of Doctor of Philosophy at the University of Cambridge. The research reported was conducted under the supervision of Professor Sir H. K. D. H. Bhadeshia in the Department of Materials Science and Metallurgy, University of Cambridge, between October 2011 and September, 2014.

This is my own work and contains nothing that is the outcome of work done in collaboration with others, except where specifically indicated in the text. Neither this, nor any substantially similar work has been or is being submitted for any degree or diploma or other qualification at any other university or institution. The dissertation does not exceed the prescribed limit of 60,000 words without appendices.

Some part of the work has been published in the literature as follows:

- Three-body abrasive wear of fine pearlite, nanostructured bainite and martensite, **S. Das Bakshi**, P. H. Shipway and H. K. D. H. Bhadeshia, Wear, vol. 308, page 46-53, 2013.
- Dry rolling/sliding wear of nanostructured bainite, **S. Das Bakshi**, A. Leiro, B. Prakash and H. K. D. H. Bhadeshia, Wear, vol. 316, page 70-78, 2014.
- Dry rolling/sliding wear of nanostructured pearlite, **S. Das Bakshi**, A. Leiro, B. Prakash and H. K. D. H. Bhadeshia, Materials Science and Technology,vol.31, no 14, page 1735-1744, 2016.

Subhankar Das Bakshi
Cambridge, 2016.

Acknowledgements

It is a delight to look over the life that I experienced during the course of my Ph.D project over the last three years; to remember and appreciate all my friends and family, who have motivated, helped and supported me to make this journey, one of the most fulfilling experiences of my life.

My words are falling short to express my gratitude to my supervisor Professor Harshad Kumar Dharamshi Hansraj Bhadeshia for his guidance, advice and enthusiasm. Besides his academic brilliance and infectious passion on science which has helped me to formulate, design and execute the work, my biggest takeaway is to be associated with him which has benefited me immensely in many aspects of life.

I gratefully acknowledge the generous financial support and study leave provided by my employer Tata Steel Limited to pursue my doctoral work at the University of Cambridge. I must thank my industrial supervisor Dr. Debashish Bhattacharjee, (Director, Global RD&T-Tata Steel) for his guidance and support. I earnestly acknowledge Dr. T. Venugopalan and Mr. Vinay Mahashabde of Tata Steel Limited, India, for their support to pursue my higher studies at Cambridge. I am thankful to Dr. Saurabh Kundu for helping me at many occasions on several issues related to my work and office during my stay abroad.

It gives me pleasure to thank Mary Vickers for her teaching and guidance on the analysing of X-ray diffraction profiles. I also thank Kevin Roberts, Andrew Moss, Andrew Rayment, David Nicol and Simon Griggs for assisting me in carrying out experiments in the heat treatment laboratory, X-ray, Nanoindentation, FIB-TEM and SEM respectively. Ken Thorn and Paul Stokes need a special appreciation for machining out all of my experimental samples with fine precision. I would like to thank Professor A. L. Greer and Professor M. G. Blamire for providing state-of-the art laboratory facilities at the Department. I earnestly acknowledge the help provided by Satya Kondapalli and Saman Saedi from Welding Alloys, Royston, UK for conducting the three-body abrasion tests. I would also like to thank Professor Braham Prakash and Alejandro Leiro of the Luleå University of Technology, Sweden for conducting the rolling/sliding tests.

The insightful suggestions and perceptive comments by Professors David Rigney (The Ohio State University,USA), Phil Shipway (University of Nottingham, UK),

Tamas Ungar and Gábor Ribárik (Eötvös Loránd University, Budapest, Hungary) over the difficult aspects of work has immensely helped me.
I would like to thank all who have developed and contributed to the open software I used to prepare my thesis. I am indebted to the selfless acts of the developers of Linux Ubuntu, gcc, Gnome, GNUPlot, Gimp, ImajeJ, inkscape and especially LaTeX.
I am thankful to the past and present members of the Phase Transformation Group for their friendship. It is a joy to work in this group. Special thanks to Mathew, Hala, Aseel, David, Yan Pei, Chris, Tim, Steve, Ed, James, Guo Lei, Wilberth, Mandla, Neel and Arunim. Anita and Anne needs a special mention on helping me over official matters. Suman, Ayan, Surajit, Sneha and Mudrika, my dear comrades in Cambridge; thank you very much for making life so wonderful during my stay at Cambridge.
My work is a tribute to all my teachers, who have instilled a love of creative pursuits within me. I am indebted to late Professor Pratul Chandra Rakshit, late Mr. Biresh Ghosh, Mr. Dibakar Chakrabarty, Professor Partha Pratim Chattopadhyay and to all my teachers and professors of Hare School, St. Xavier's College, Kolkata and IIEST-Shibpur, India who have inspired and helped me to indulge my passion for science.
Finally, I warmly acknowledge the encouragement, support and unconditional love from my family. My wife, Antara, put up a with a lot in past three years and my work would not have been complete in time without her unwavering love and sacrifice on her personal front. My parents have been a constant source of inspiration and encouragement for me. Nothing would have been more delightful than Aneesh, the light of my life, who has given me so much of strength and motivation in last two years.

Contents

List of Figures

List of Tables

Chapter 1

Introduction

The primary aim of the work detailed in the thesis was to investigate the abrasive wear behavior of nanostructured steel, comprising of an incredibly fine mixture of bainitic ferrite and thin film retained austenite under three-body and two-body conditions. Along with nanostructured bainite, a fine scaled pearlite and untempered martensite produced from the same alloy has also been tested under similar conditions. Their wear rates and mechanisms of wear have been discussed. Using contact stress modelling and detailed characterisation of the worn surfaces, it has been possible to explain the tribological behaviors of a variety of structures under conditions of abrasion.

The work begins with a critical assessment of the literature available on abrasive wear of steels, presented in Chapter 2. This summarises general understanding about the abrasive wear of steel microstructures and the properties of abrasives and environment that influence wear. However, the wear rate and mechanisms of wear are unique to particular tribological systems reported and are difficult to generalise. A relevant summary of the literature pertinent to particular wear experiments is therefore presented at the beginning of each chapter.

The abrasive wear experiments and detailed characterisations carried out there after to understand the mechanism of abrasion in various structures are described in Chapter 3, which describes the procedures of the wear tests conducted and the theories that help understand the damaged structures.

The three-body abrasive wear of fine pearlite, nanostructured bainite and martensite is discussed in Chapter 4 and the effect of tempering on abrasive wear of

nanostructured bainite is briefly discussed in Chapter 5 in order to reveal the role of retained austenite.

The investigations on dry rolling/sliding wear of the same set of structures are detailed in Chapters 6, 7 and 8 respectively.

The general concluding remarks are presented in Chapter 9 which also includes some comments on the scope of future work.

The commercial abrasion resistant steels, their chemical compositions and mechanical properties are listed in Appendix A to have a comparative view on existing practice and the novel structures being studied. The theory behind the contact stress modelling of rolling /sliding based on rigid, parallel and axial cylinders experiencing Hertzian contact stress is detailed in Appendix B and the code written to solve these set of equations is listed in Appendix C.

Chapter 2

Literature Review

2.1 Introduction

The topic of wear is a huge subject, so the aim of the review presented here is to deal with the specific subject of abrasion and rolling/sliding mechanisms. This is because it is these mechanisms that have been investigated in detail for a number of novel micro and nanostructures in the chapters that follow. The chapter begins with a review of abrasion in context and finishes with rolling/sliding.
Wear, a physical and chemical process of material damage and removal, broadly includes four distinct processes, all of which involve the removal of material from the surface [7],
(a) abrasive or cutting wear;
(b) adhesive or galling wear;
(c) corrosive wear, and
(d) surface fatigue.
Apart from these major mechanisms of wear, which cover more than 95% scenarios, there exist some specialised cases, such as, erosion, commonly observed in propeller blades of ships, and impact chipping witnessed in excavation equipment. A typical wear-system involves (a) contact between at least two materials; (b) force; (c) relative movement between the two materials and finally, (d) the environment. Amongst all these types of wear, abrasive wear generally causes the maximum material loss.

2.2 Abrasion

A typical abrasive wear system consists of the *body*, which forms the engineering component; the *more robust body*, commonly known as *abrasive*; the *environment* and the *contact force* [8]. The mechanism can either be plastic flow and subsequent detachment of ductile material or brittle detachment.

2.2.1 Two-body abrasion

This is a relatively simple form of abrasion, with two solid rubbing surfaces having dissimilar hardness and a degree of surface roughness [Fig. 2.1]. This type of wear is common in machines and sometimes in bearings. It can be minimised by lowering surface roughness and elastohydrodynamic lubrication. Hard abrasive particles may form through fracture and exacerbate abrasion [9–11].

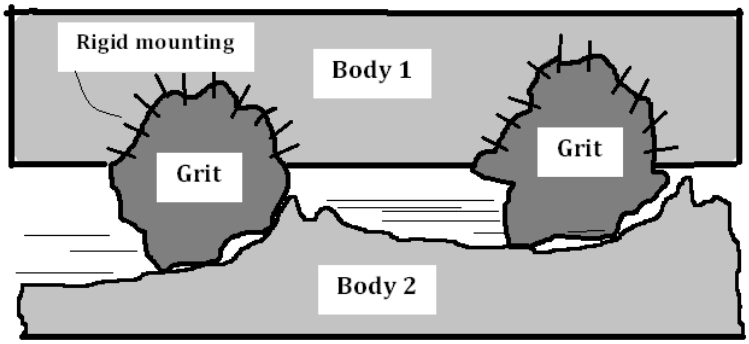

Figure 2.1: Schematic of two-body abrasion.

2.2.2 Three-body abrasion

In this, abrasive particles not only slide on the surface but also can roll as illustrated in Fig. 2.2. It has been demonstrated that the sliding action leads to cutting wear [12], whereas rolling particles cause localised plastic deformation of the contact surface [13]. The detailed mechanism depends also on the gap between the two main bodies relative to the particle size [14–16].

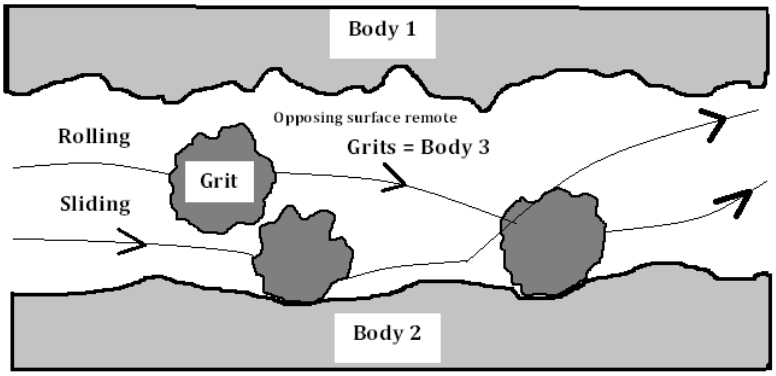

Figure 2.2: Schematic of three-body abrasion.

2.2.3 Abrasive wear and its economic importance

Abrasive wear is relatively rapid [17], and accounts for 35-50% of material loss over all possible wear scenarios [Table 2.1] [18]. Mining and comminution equip-

Table 2.1: Relative importance of the forms of wear.

Type of Wear	Eyre(1976) [17]	Rabinowicz(1983) [18]
Adhesive Wear	23%	45%
Abrasive Wear	58%	36%
Corrosive Wear	5%	4%
Surface Fatigue Wear	14%	15%

ment are particularly prone to abrasion; Fig. 2.3 shows the extent of damage in a crusher tooth. A deposit of hardfacing alloy on the tooth could not resist the wear [Fig. 2.4].

Figure 2.3: The tooth on the left is at the beginning and the one at the right after it has been worn down by abrasive oil sands. Courtesy H. K. D. H. Bhadeshia.

Figure 2.4: Wear of the hardfacing layer on the tooth. Courtesy H. K. D. H. Bhadeshia.

2.3 Abrasive wear of steels

2.3.1 Introduction

The wear behavior of alloyed steels may sometimes depend on its microstructure, wear conditions and environment, although there exist no exact relationships between these variables [19]. Moore attempted to correlate the microstructure of steel against wear resistance as shown in Fig. 2.5.

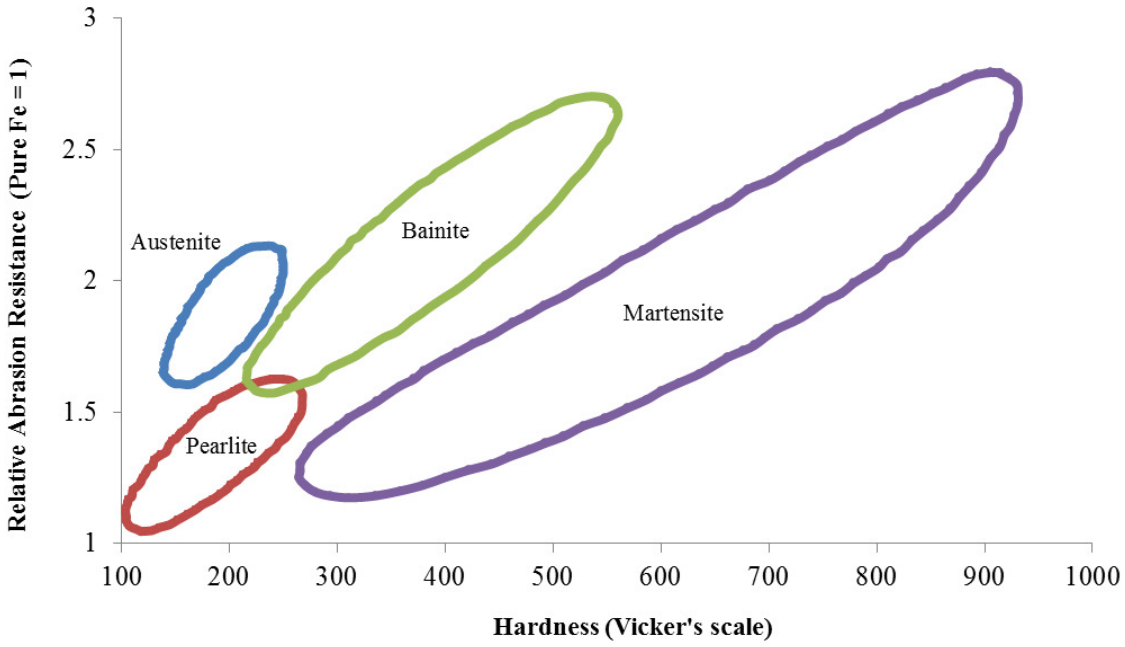

Figure 2.5: Effect of microstructure and bulk hardness on relative abrasion resistance of steel against 20 μm alumina particles [20].

It is interesting that steels with similar hardness but different microstructures vary in their abrasion resistance. Austenitic steels show a higher abrasion resistance compared to bainitic and pearlitic alloys of equivalent hardness. This phenomenon is attributed to the strain hardening ability and ductility of austenite compared to bainite and pearlite. Bainitic steels are superior to those which are martensitic as the latter can be less ductile, leading to greater material removal during abrasion. Austenite and bainite, for the same reason exhibit higher

abrasion resistance than martensite [21]. Moreover, austenitic steels produce a tough work-hardened layer on the abraded surface during abrasion which helps resist further damage [22].

2.3.2 Abrasive wear behavior of various microstructures

Hardness helps in reducing the extent of penetration of abrasive particles, whereas, toughness limits crack formation and material detachment. The deformation of the surface regions and extent of work hardening also play a role in material removal. According to Vingsbo and Hogmark, once steady-state abrasive wear is reached, the structure and properties of the abrading surface and underlying material change considerably relative to the bulk. It is the properties of this layer which control the abrasion resistance rather than those of the unaffected material [23].

2.3.2.1 Ferritic steels

In a ferrite-pearlite mixture, the pearlite wears less than the ferrite [24], with a steady increase in two-body abrasive wear resistance with the pearlite fraction [Fig. 2.6] [25, 26]. The pearlite colonies are dispersed as hard phases in the softer ferritic matrix, thereby hindering the penetration and subsequent material removal by abrasives. The pearlite also constrains the deformation in ferrite thereby reducing the rate of material removal.

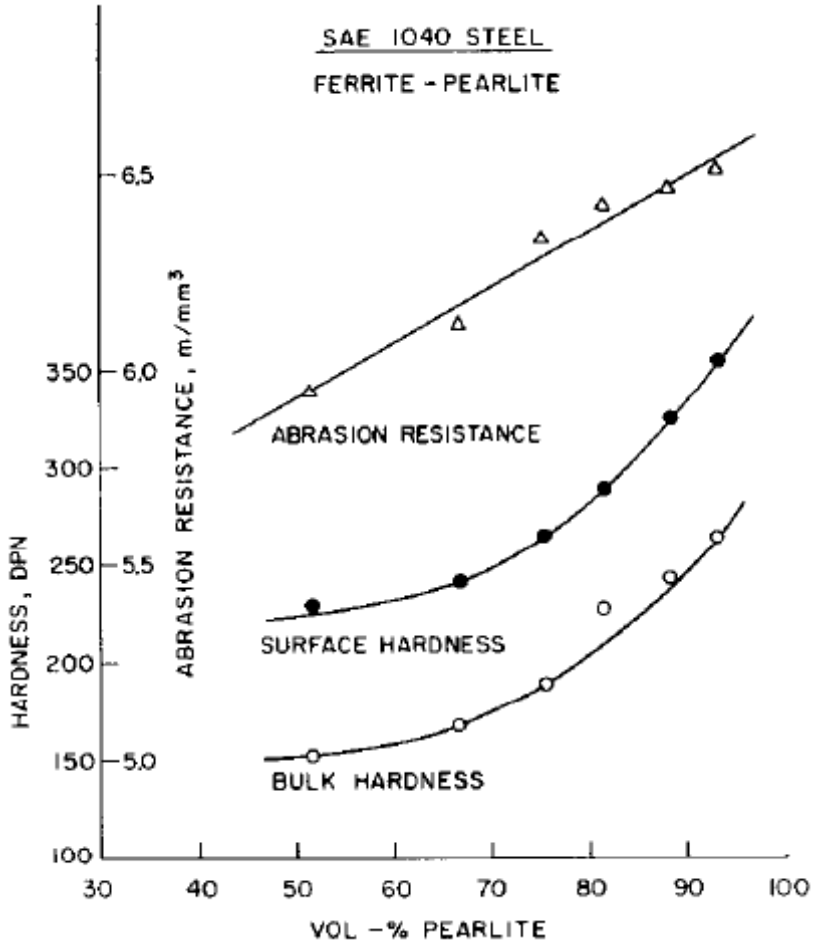

Figure 2.6: Abrasion resistance and bulk hardness of ferrite-pearlite steel against volume percent of pearlite. After Larsen-Badse [26].

2.3.2.2 Pearlitic steels

It is the morphology of the iron carbide in steel which plays an important role in abrasion resistance. Previous studies have indicated that lamellar pearlite performs better than spheroidal carbides at similar hardness [27, 28]. A greater energy is needed to deform and fracture lamellar carbide [29]. In hypo-eutectoid pearlitic steels, the abrasion resistance scales with the carbon content and inversely with the interlamellar spacing. In hyper-eutectoid steels, the continuous network of cementite at the prior austenite grain boundaries can not plastically deform during abrasion, resulting in brittle fracture and cracking along the those

boundaries. This could be responsible for the saturation of wear resistance in hyper-eutectoid steels.

The lamellae in pearlite act as barriers to the moving abrasive particles, resulting in shallow abrasion. Wang *et al.* found the least abrasion with a completely pearlitic structure, with bainite, tempered martenstite and spheroidised carbide in decreasing order of abrasion resistance [30]. Lamellar pearlite is also better than tempered martensite containing fine carbides [31]. However, the performance of pearlite varies with the size of the abrasive particles. Coarse abrasive particles cause more damage than fine ones [Fig. 2.7], with some 50 times greater wear rate as the abrasive size increase from 15 μm to 115 μm [32].

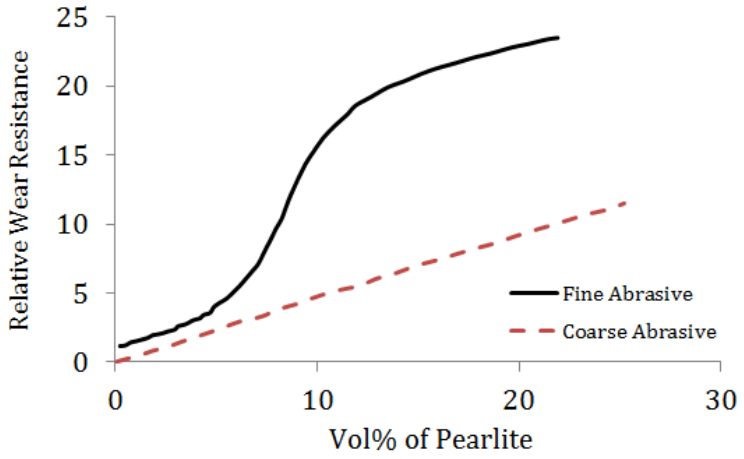

Figure 2.7: Effect of abrasive size and volume % of pearlite on relative wear resistance of completely pearlitic steel. After Stachowiak [33].

In spheroidised steels, the size and distribution of carbides are important factors in governing the abrasion resistance. Small and uniformly distributed spherical carbides cannot act as rigid barriers and are unable to resist the cutting or ploughing action by the hard abrasives. Spheroidised carbides having size and shape comparable to that of hard abrasives can protrude from the surface and thereby reduce abrasion by small particles [Fig. 2.8].

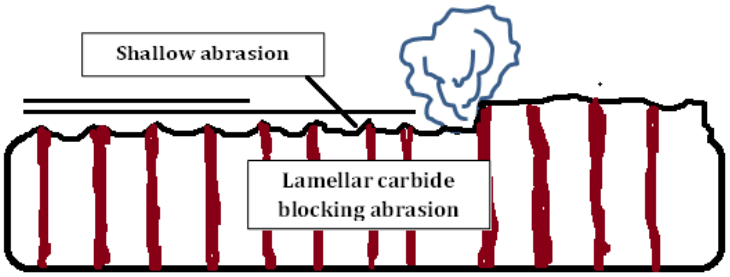

(a)

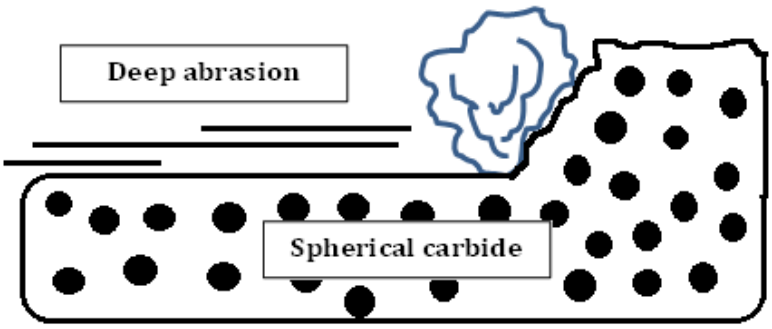

(b)

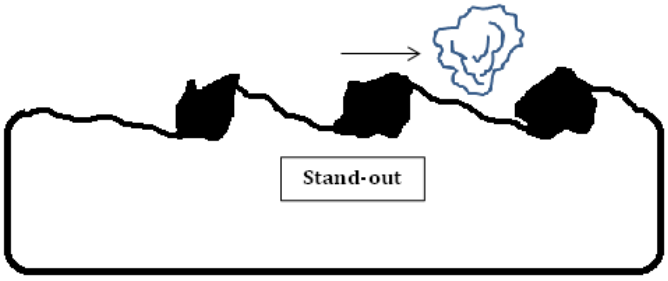

(c)

Figure 2.8: Effect of carbide morphology on abrasive wear resistance; (a) lamellae of cementite in pearlite (b) small and uniformly dispersed carbides in softer ferritic matrix and (c) carbides comparable to the size of abrasive grit. After Stachowiak [34].

2.3.2.3 Bainitic steels

Richardson first demonstrated that bainitic steels better resist abrasion than those which are martensitic, when the comparison is at similar hardness and composition [35]. Hurricks found good abrasion resistance in lower bainite due to its ductility and hardness [31]. Xu and Kennon carried out two-body abrasion tests on plain carbon steels over a wide range of compositions (0.10 - 1.4 wt% C) and microstructures and found that for C <1.0 wt%, bainite has the highest wear resistance followed by tempered martensite and rest of the annealed structures. Spheroidised structures are found to have lowest wear resistance [36]. Field abrasion tests on South African soil demonstrated a higher abrasion resistance of lower bainite when compared against other microstructures [37]. The observation of high abrasion resistance in bainitic steel is believed to be due to lower plastic deformation wear due to high toughness under three-body abrasion [38].
However, contradictory observations exist. The wear rate of bainitic steel has been found to be three times higher than pearlitic steel under two body abrasion, possibly due to the low strain hardening rate of lower bainite [39, 40].

2.3.2.4 Martensitic steels

According to a number of studies [41–43], martensite has better abrasion resistance compared to ferrite, pearlite and bainite owing to its high hardness, although contradictory results are also available [31, 35]. During dry sand rubber wheel testing, a greater wear resistance has been reported for a ferrite and martensite structure compared to ferrite and pearlite mixture, attributed to the higher volume fraction of martensite [44]. High carbon martensitic steel (C $\sim$ 0.65 -1.2 wt%) has been found to exhibit higher wear rates compared to low carbon (C $\sim$ 0.16 - 0.37 wt%) martensites owing to relatively low toughness [24].

2.3.2.5 Tempered martensitic steels

It has been reported that the tempered martensite exhibits better wear resistance compared to quenched martensite owing to its increased ductility regained due to tempering [24]. Prasad and Kulkarni found a point of inflection when plotting wear resistance against tempering time for tempered martensitic steels. The

wear resistance initially increases as the hardness is reduced due to an increase in toughness with tempering. As the ferrite becomes progressively softer, carbides coarsen and fail to resist intrusion by hard abrasives, resulting in enhanced abrasion [24]. Under the dry sliding wear conditions in pin-and-disc abrasive tests, tempered martensite performs better compared to pearlite and ferrite, as lower load restricts the abrasion to mild wear. However, at excessive loads, the wear rate of tempered martensite exceeds that of pearlite and ferrite due to an inferior work hardening of the martensite [45].

2.3.2.6 Austenitic steels

Austentic steels exhibit high gouging and impact abrasion resistance because of their exceptional work-hardening capacity, attributed to a low stacking fault energy and deformation-induced martensitic transformation [46]. Fine-scaled retained austenite, uniformly dispersed in a matrix of high yield strength and toughness seems to contribute more towards abrasion resistance than blocky austenite [47]. Blocky retained austenite in the form of a continuous structure with poor mechanical stability spalls off easily during abrasion and reduces the overall abrasion resistance of the steel.

2.3.2.7 Tool steels

The major contribution of wear resistance in tool steel comes from high volume fraction of hard (1500 - 2800 HV) M_6C type primary carbides (1-10 μm diameter) dispersed in a martensitic matrix [48, 49]. The wear resistance of tool steel increases marginally with the coarsening of primary carbides [Fig 2.9] [50, 51]. These phases in tool steel have a very large range of hardness, so the abrader hardness becomes particularly important in any test. Very hard abrasive is able to cut all phases whereas an intermediate hardness abrader will plough the softer matrix but is eventually blunted by the harder carbides.

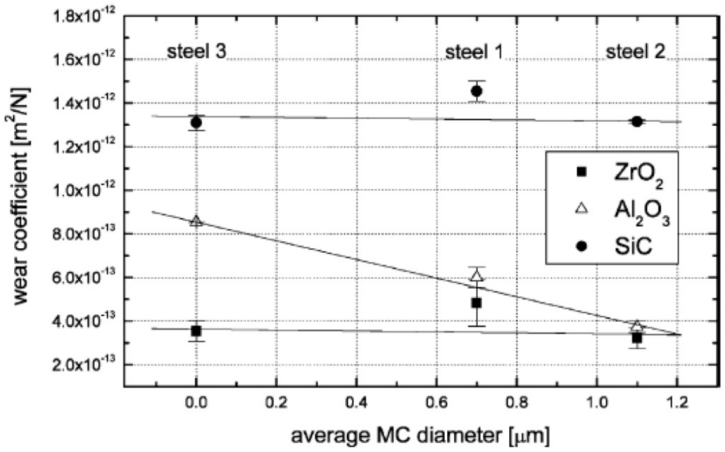

Figure 2.9: Comparison of wear coefficient against size of metallic carbide (MC) in tool steel. Steel-1 has a fine and uniformly dispersed MC (65 HRC), steel-2 annealed to obtain coarse carbides (65 HRC), steel-3 has a completely martensitic structure (60 HRC) with no primary carbides; ZnO_2 having very low hardness (1000 - 1100 HV) and SiC having very high hardness (3000 HV) and alloy carbides make no difference to the wear coefficient. With Al_2O_3, which has an intermediate hardness of 2100 HV, steel 2 shows higher resistance to abrasion than steel 1. Steel-3 exhibits maximum wear. After Badisch *et al.* [50].

Despite extensive research over the past six decades on abrasive wear of steels and efforts made in correlating wear resistance with various mechanical properties, a thorough and clear understanding on the subject remains elusive. The reasons could be that wear is more of a system property than a material property, hence explaining wear only in terms of material properties, therefore neglecting the influence of environment may lead to erroneous inferences. The environment could be dynamic and complicated (like, change in temperature, contact stress, lubrication), which changes the wear mechanism and finally the material could undergo various stages of deformation during wear, namely elastic, plastic, fatigue and fracture depending on the contact stress condition, which further induces complications in correlation studies between wear resistance and material properties. Every wear system, comprising of the material and environment,

seems to be unique in nature and therefore needs critical assessment pertaining to that system only.

2.4 Some parameters influencing abrasive wear of steel

2.4.1 Bulk hardness

Khruschov and Babichev found a linear relationship between wear resistance and bulk hardness in two-body abrasion tests with annealed metals and hardened steels [35, 52–54], as shown in Fig. 2.10,

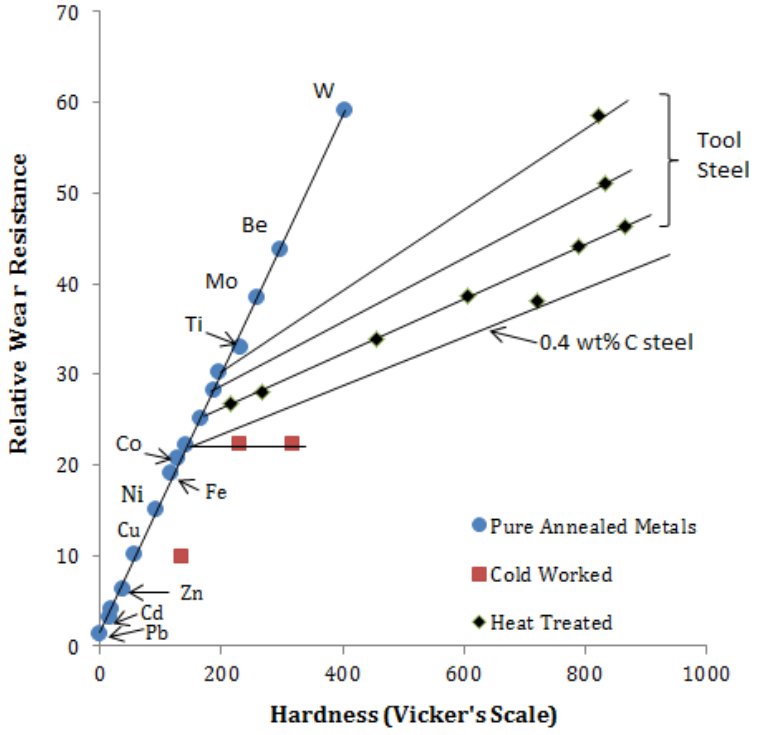

Figure 2.10: Relative wear resistance as a function of initial bulk hardness. (a) pure metals and annealed steels follow a linear relationship. After Khruschov and Babichev [55].

where,

$$\varepsilon = bH, \tag{2.1}$$

ε is the relative wear resistance, H is the Vickers hardness and b is a constant of proportionality. Moreover, they proposed that the wear-resistance depends

strongly on the physical and mechanical properties of the abrasive, consistent with other work [12,56]. This relationship does not hold good for work-hardenend metals and alloys [31].

In general, the abrasion resistance of steel does depend on its hardness [57], but also on the microstructure [Fig. 2.11] [31, 58]. It is found that the surface hardness after abrasion has a better correlation with the wear resistance [59, 60] but their observations were inconsistent with [61], who proposed that the extent of wear depends rather on the plastic flow, plastic strain and fracture properties of the worn surfaces, others [24] emphasise the toughness and microstructural features. In a tumbler-based impact-abrasion test, a non-linear relation between bulk hardness and wear resistance was found because the microstructure and hardness of the worn surface controls the wear resistance [62]. All these studies indicate that a higher hardness does not necessarily guarantee a better resistance to abrasion.

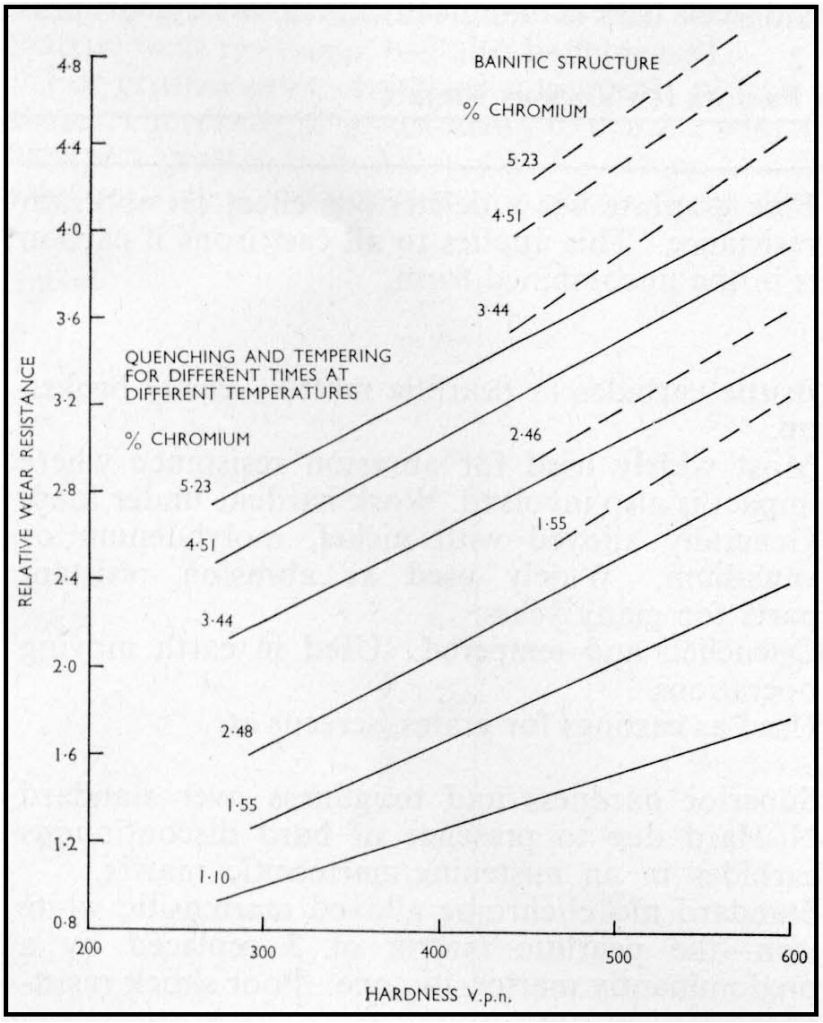

Figure 2.11: Effect of chromium addition and heat treatment on abrasive wear resistance of 0.73 wt% carbon steel. An increase in wear resistance observed with increased chromium content. Also bainitic structure offers higher abrasion resistance compared to tempered martensite. After Hurricks [31].

2.4.2 Temperature

There are two aspects regarding the effect of temperature on abrasive wear rate, (a) the influence of the ambient temperature during abrasion, and (b) increase in temperature due to plastic deformation of abrading surface by abrasive grit. Abrasives which retain hardness at high temperatures cause greater wear, Fig. 2.12(a). The second situation is often associated with the high strain rate during abra-

sion. A localised increase in temperature $\sim$ 1000 °C has been reported with abrasion [63]. With the small time of contact between an individual grit and the substrate, most of the heat generated at high strain rate remains within the deformed metal. As a result, transient thermal softening of the deformed abrading steel surface occurs whereas the grit retains its hardness [Fig. 2.12(b)]. In such a case, steel can be abraded by a softer material such as coal [64]. However, such an abrasion often transforms to a corrosive and oxidative wear for steel. As an example, work rolls in the finishing strands of any hot mill need to resist hot abrasion. There is an increase in wear resistance with hardness in high speed steel rolls (62 HRC) from chilled cast iron rolls (55 HRC) [65]. However the conditions do not simulate the complex abrasion environment at the roll bite. It has been observed that the mean roughness (R_a) after abrasion correlates with the difference in hardness between the martensite matrix and carbides. High speed steel rolls exhibit lower R_a, hence smoother surface and higher abrasion resistance compared to chilled cast iron rolls after hot abrasion.

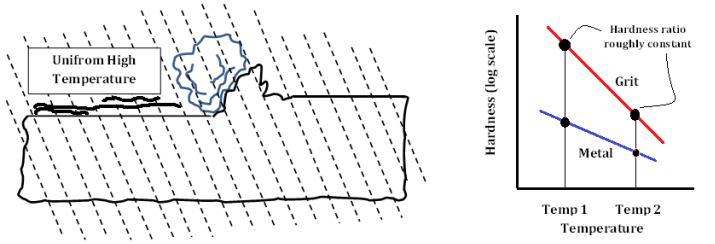

(a)

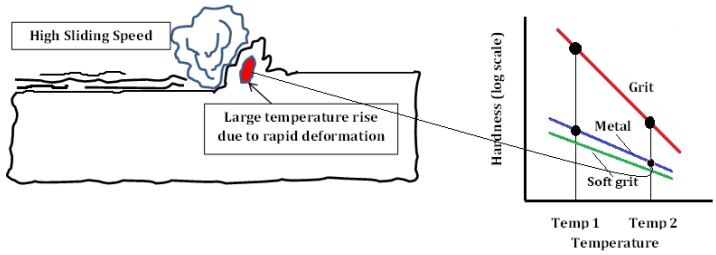

(b)

Figure 2.12: Effect of temperature on abrasion resistance. After Stachowiak [33].

2.4.3 Particle size

Three categories of abrasion were observed with changes in particle size, as shown in Fig. 2.13 [12,55,59,66,67]. At first, the wear rate increases slowly with increase in particle diameter followed by a rapid increase and finally the wear rate becomes independent of grit diameter.

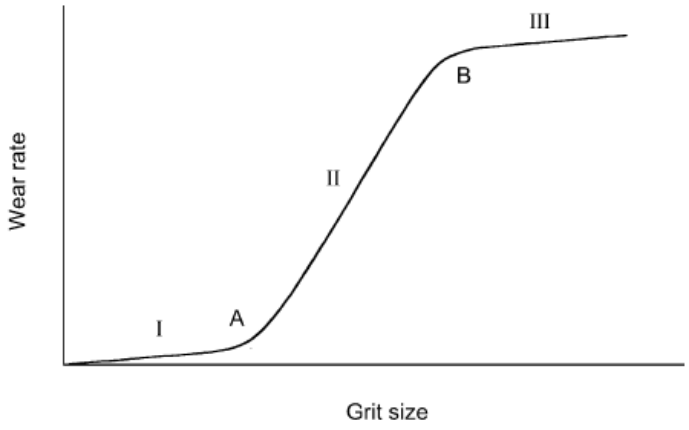

Figure 2.13: Abrasive particle size and stages of wear. After Garbar [67].

The lower wear rate observed with smaller grit size is because of different indenter geometries and clogging of troughs between surface asperities by abrasion debris. Such particles are large enough to clog the asperities and thereby reduce the interaction area and wear rate [Fig. 2.14] [68]. With very large abrasive particles, the shape of the indentation becomes independent of abrasive particle size and hence, so does the wear rate [68].

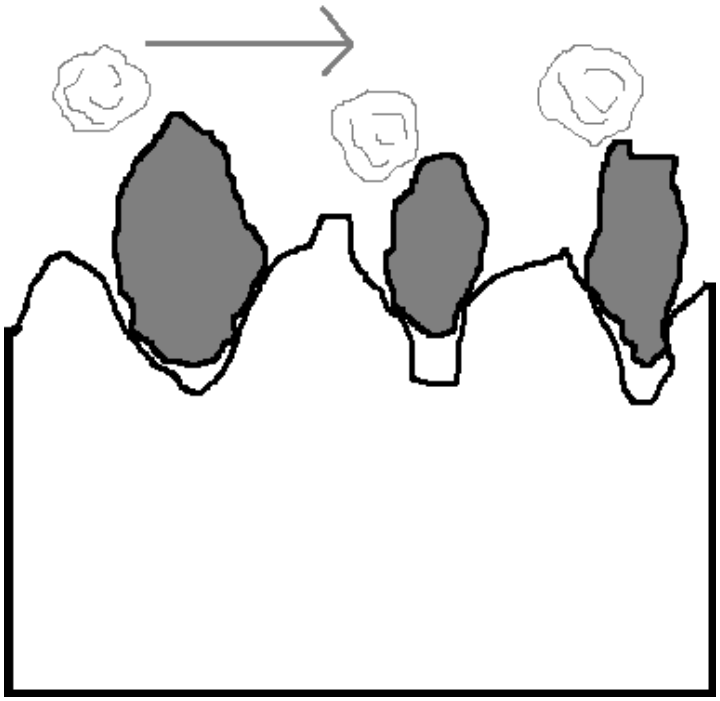

Figure 2.14: Large adhesive wear debris lowering abrasion by blocking troughs. After Rabinowicz [68].

Such clogging is indeed found in the case of soft aluminium (114 HV) and mild steel (233 HV) [59, 69].

2.4.4 Lubricant

Lubricants can effectively flush away the wear debris from the abrasion system and thereby increase the efficiency of the abrading particles. In a series of two-body abrasion tests, Moore observed a mixed result with the application of lubricant, in some cases the wear is more severe, in others it is more benign compared to dry abrasion [70]. In a dry-sand rubber-wheel test, an increased wear rate observed with lubrication was attributed to the cooling effect of the lubricant on the rubber wheel, thereby retaining its hardness [71, 72]. On the other hand, with round and small abrasive particles, the presence of water reduces the abrasive wear rate of mild steel by reducing friction [73, 74].

2.4.5 Humidity

The abrasive wear rate varies with moisture content of the environment. Tests conducted in summer gave 10 - 20% greater wear than those done in winter. Two-body abrasion tests revealed an increased wear rate as the relative humidity changed from 0% to 65%. The effect is more pronounced for harder materials and can be attributed to the lubricating effect of the moisture [75]. However, Mercer and Hutchings observed the opposite trend [76] and attributed it to the lubricating effect of water molecules.

2.4.6 Alloy carbides

There exist contradictory results on the effect of alloy carbides on abrasion resistance of steels. According to Hurricks, only carbide forming elements (like Cr, Mo, V, Ti and Nb) increase the abrasive wear resistance of steels, whereas elements which go in solid solution (like Ni, Si and low Mn) have limited or no effect on abrasion resistance [31]. Katsuki *et al.* observed an opposite phenomenon of decreased two-body abrasion wear resistance in case of V-added 0.4 wt%-C pearlitic steel compared to a V-free pearlitic steel having similar composition and attribute this observed phenomenon to lower dissipation of the energy of abrasion towards plastic deformation of pearlite [77].

2.5 Abrasion mechanisms

Material removal by hard abrasive particles involves microcutting, microfracture, pull-out of individual grains and accelerated fatigue by repeated deformation as shown schematically in Fig. 2.15 [78]. For a ductile material, the movement of hard abrasive particles may plastically deform the mating surface in the direction of motion resulting in the cutting mode abrasive wear. The wear debris is heavily deformed in such cases. For brittle materials, cracks are generated upon indentation and they may converge at sub-surface level to remove material by fracture

mode. When the abrasive is relatively blunt and the material is subjected to a large number of passes, as in case of Fig. 2.15(c), the worn surface becomes fatigued by repeated deformation and material removal is caused by fatigue. For a material with weak grain boundaries, as in ceramics, the removal occurs via weakening and subsequent detachment of grains by hard abrasives as shown in Fig. 2.15(d) [33].

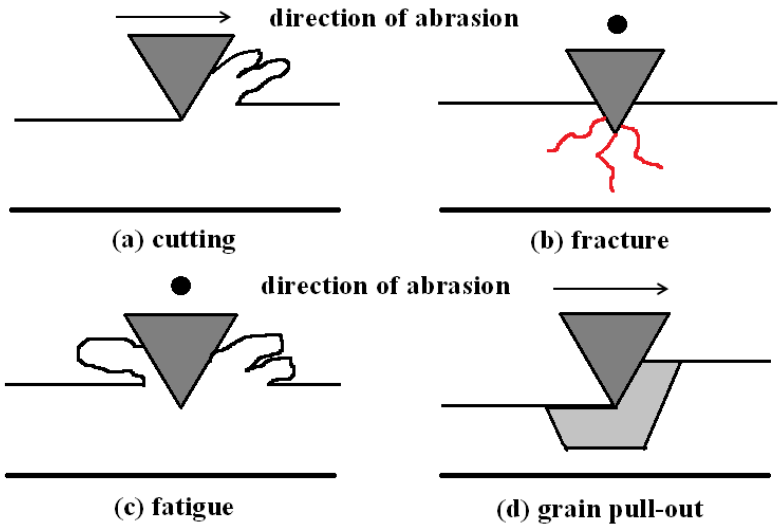

Figure 2.15: Abrasive wear mechanisms; material removal by (a) cutting, (b) fracture, (c) fatigue by repeated ploughing and (d) pull-out of grains. After Stachowiak [33].

Cutting :

The understanding of this mode of abrasive wear became clear when researchers carried out abrasion test inside an SEM and observed the abraded tracks with repeated abrasion at high magnification. A series of studies was carried out with a round indenter [79] and pin-on-disk technique [80] inside a scanning electron microscope. Pure cutting and wedge-formation (ploughing) were revealed as the dominating mechanisms. The cutting mode was found to be more efficient in material removal than the wedge-formation. Considerable plastic deformation is normally observed beneath the abraded surface created under ploughing mode and subsequent work-hardening reduces the abrasive wear loss.

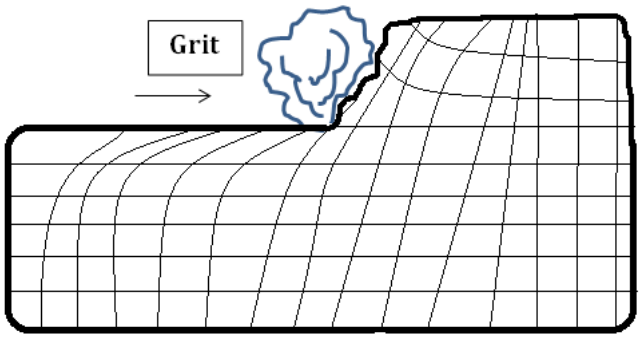

Figure 2.16: A schematic illustration of the subsurface deformation under cutting mode during abrasion. After Stachowiak [33].

Fracture:

Brittle materials cannot accommodate strain during deformation by hard abrasives and results in cracking of the abrading surface. Philips studied the abrasive grinding of glass and fused silica and found three different types of cracks, namely the vent cracks at an angle of 30° to the surface, localised fragmentation and deep median cracks responsible for material removal from the surface. With repeated abrasion, these cracks increase in length, coalesce beneath the surface, resulting in removal of a large quantity of material in a catastrophic manner [81]. The extent of abrasive wear by fracture increases with increased brittleness of the material, applied load and number of sharp corners in individual abrasives [Fig. 2.17].

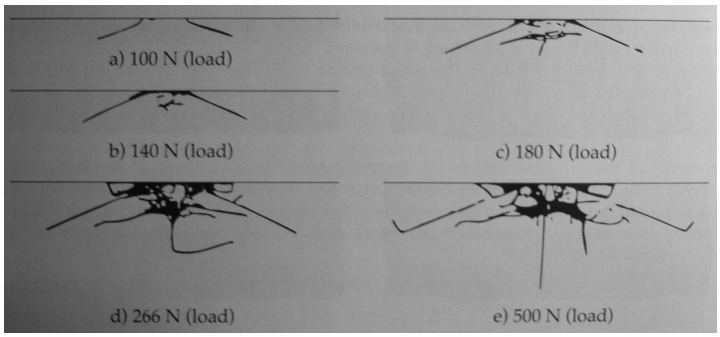

Figure 2.17: Propagation of cracks under load in transparent brittle material. After Philips [81].

Fatigue :
The actual amount of material removal during typical abrasion of a ductile material is much higher than expected from a "cutting-only" mode and because of the simultaneous operation of cutting and fatigue. Cross sectional observation of abrasion tracks in ductile metals reveals the presence of extrusions at the edges of the tracks. An SEM investigation of wear debris found in mild steel by repeated abrasion revealed fragmented extrusions caused by metal fatigue [Fig. 2.18] [82].

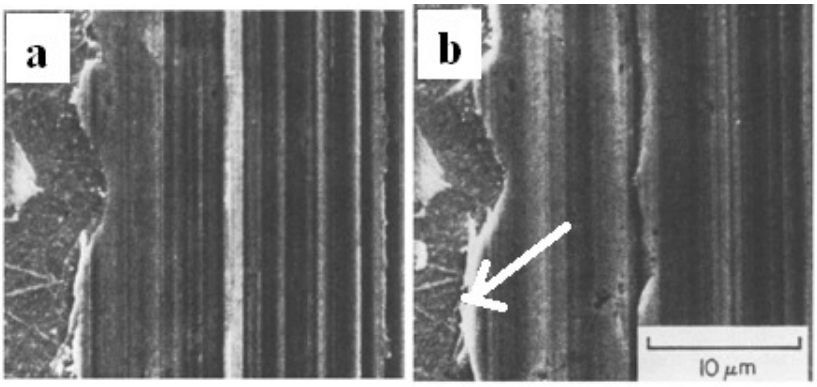

Figure 2.18: Formation of extrusions at the edges of abrasion track due to metal fatigue in mild steel (a) after 4 passes , (b) after 6 passes of abrasion After Glaeser [82].

Grain pull-out: Ceramics with grain boundaries and large grain size exhibit this kind of abrasive wear, a mechanism almost non-existent in steels.

2.5.1 Theory of abrasion

Abrasion involves systems of at least two bodies with dissimilar properties, relative motion, force and often the presence of a lubricating fluid and constant change in the physical and chemical properties of the elements involved.

2.5.1.1 Theory of micro-cutting

In the analytical model for abrasive wear, a single particle of abrasive rigidly held after indention is modelled by a cone indenting the surface of the abrading

material and traversed on the surface under the application of a tractional force [Fig. 2.19]. The model assumes that the entire amount of material displaced by the movement of the abrasive is lost in the form of wear debris. The load on the grit is expressed as:

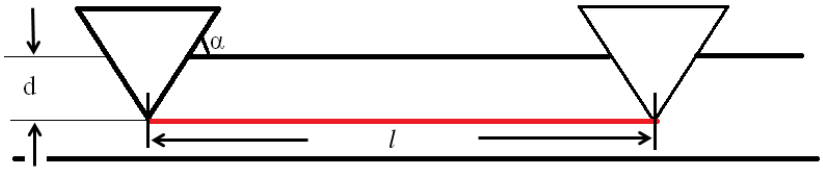

Figure 2.19: Abrasion by a simple grit. After Stachowiak [33].

$$W_g = 0.5\pi(d\cot\alpha)^2 H \tag{2.2}$$

where,
W_g is the load on an individual grit, [N],
d = depth of the indentation, [m],
α = angle of the cone, [°], and,
H = hardness of the material, [Pa].
If l is the total distance traversed by the conical particle, then the volume loss is estimated as:

$$V_g = ld^2\cot\alpha \tag{2.3}$$

where,
V_g = volume of the material removed by the cone, [m^3].
Substituting d in eqn.2.2 gives the expression of volume loss made by a single conical abrasive in terms of load, shape of the abrasive and the distance traversed:

$$V_g = \frac{2l\tan\alpha}{\pi H} \times W_g. \tag{2.4}$$

Now summing over all abrasives:

$$V_{total} = \sum V_g = \frac{2l\tan\alpha}{\pi H} \times \sum W_g \tag{2.5}$$

or,

$$V_{total} = \sum V_g = \frac{2l \tan \alpha}{\pi H} \times W_{total} \tag{2.6}$$

where,
V_{total} = total wear volume, [mm^3],
W_{total} = total applied load, [N].

2.5.1.2 Theory of micro-ploughing

The assumption that the total volume traversed by the conical abrasive is lost as abrasive wear is dubious as not all the material displaced gets removed during abrasion. Some accumulates around the edges of the abrasive groove marks, especially for ductile metals [Fig. 2.20]. A new factor, f_{ab} is introduced to define the ratio of the volume of material removed from the surface to the volume of the wear groove formed due to the movement of the abrasive and is expressed as:

$$f_{ab} = 1 - (A_1 + A_2)/A_v \tag{2.7}$$

where,
$f_{ab} = 1$, for ideal micro-cutting, meaning all material is lost after grooving, $f_{ab} = 0$, for ideal micro-ploughing and $f_{ab} > 0$, for micro-fracture, where more material is removed than the volume traversed, A_v is the cross ectional area of the wear groove, [m^2], and $(A_1 + A_2)$ is the cross sectional area of the build-up around the edges of the groove in the case of ductile metals, [m^2].

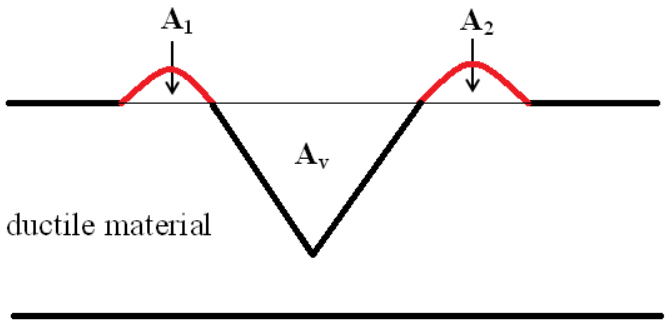

Figure 2.20: Abrasion and build-up on ductile material. After Stachowiak [33].

The volumetric wear loss ΔV_l is expressed as:

$$\Delta V_l = \Delta V/l = f_{ab} A_v \tag{2.8}$$

where, ΔV_l is the volumetric wear loss in terms of sliding distance, and ΔV is the total loss of volume. The linear wear rate per sliding distance is expressed as:

$$\Delta V_{d,ductile} = \Delta V/lA = f_{ab} A_v/A \tag{2.9}$$

where,
A is the apparent contact area of the grit, [m^2], and ΔV_d is the linear depth of wear per sliding distance.
The ratios A_v/A is expressed as:

$$A_v/A = \phi_1 p/H_{def} \tag{2.10}$$

where,
ϕ_1 is a factor which depends on the shape of the abrasive particle, normally 0.1 for pyramidal particles, p is the externally applied pressure and assumed to have uniform value, and, H_{def} is the hardness of the deformed material.

2.5.1.3 Theory of micro-fracture

In abrasive wear of brittle materials [Fig. 2.21], the factor f_{ab} is modified to consider cracking and spalling of material around the grooves. Since there is a loss of material around the edges of the crack, the A_1 and A_2 are negative in case of brittle material so that,

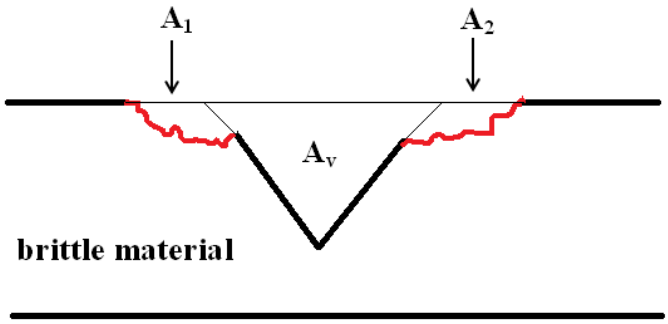

Figure 2.21: Abrasion on brittle surface. After Stachowiak [33].

$$f_{ab} = 1 + |A_1 + A_2|/A_v. \tag{2.11}$$

The expression for the linear wear rate in a brittle material is given by,

$$\Delta V_{d,brittle} = \phi_1 p/H_{def} + \phi_3 A_f D_{ab} p^{1.5} H^{0.5} \mu^2 \Omega / K_{1C}^2 \tag{2.12}$$

where, ϕ_3 is a factor that depends on the shape of cracking during abrasive wear, normally is equal to 0.12 for pyramidal abrasives, A_f is the area fraction of the flaw in material, D_{ab} is the effective size of the abrasive particle, [µm], μ is the coefficient of friction of the leading face of the abrasive, K_{1C} is the fracture toughness of the material under tension, [$m^{1/2}$Pa], and Ω is a parameter expressed as,

$$\Omega = 1 - e^{-\left(\frac{p}{p_{crit}}\right)^{0.5}} \tag{2.13}$$

where, p_{crit} is the critical surface pressure for any material containing cracks or lamella of very brittle material. From the above expression, it is evident that, toughness of material is also a very important parameter in abrasion resistance,

especially structures containing brittle features as a material having low K_{1C} material is bound to have higher abrasive wear loss.

2.6 Effect of abrasive properties

An abrasive can be a third body freely moving between the meeting surfaces or an integrated part of the bodies in contact, having similar or completely different physical and mechanical properties. Certain properties of the abrasive, like hardness, shape, size and its ability to fracture or retain shape during abrasion control the efficiency of abrasion.

2.6.1 Hardness of the abrasives

Early research indicates that the abrasive wear increases with the decrease in the H_m/H_a ratio, where, H_m is the hardness of the worn material and H_a is the hardness of the abrasive. There exists a critical value (~ 0.8) of H_m/H_a beyond which the abrasive wear rate decreases rapidly [33].

2.6.2 Shape of the abrasives

It has been observed that abrasive particles with shaper edges create more damage than their spherical counterparts. Moore observed a 2 - 5.5 times increase in abrasive wear volume with crashed angular silica abrasives compared to spherical silica [83]. A numerical parameter has been introduced to define the shape of an abrasive and its connection with the abrasively of the particle. The particle boundary is traversed at unit steps and the start and the end points are connected to construct a triangle [Fig. 2.22]. As the sharpness of the triangle increases, *i.e.* smaller the apex angle and larger the perpendicular height, greater is the abrasion efficiency of the particle. This is often described as a spike parameter [33].

2.6.3 Size of the abrasives

It has been reported widely that abrasive wear loss tends to increase with the increase in abrasive particle size [84]. The effect is more pronounced at low sliding speeds [85]. In a three-body abrasive wear test conducted with silicon carbide abrasive, Sasada *et al.* found a sharp drop in specific wear when the abrasive size dropped below the critical size. On further reduction in the abrasive size, the

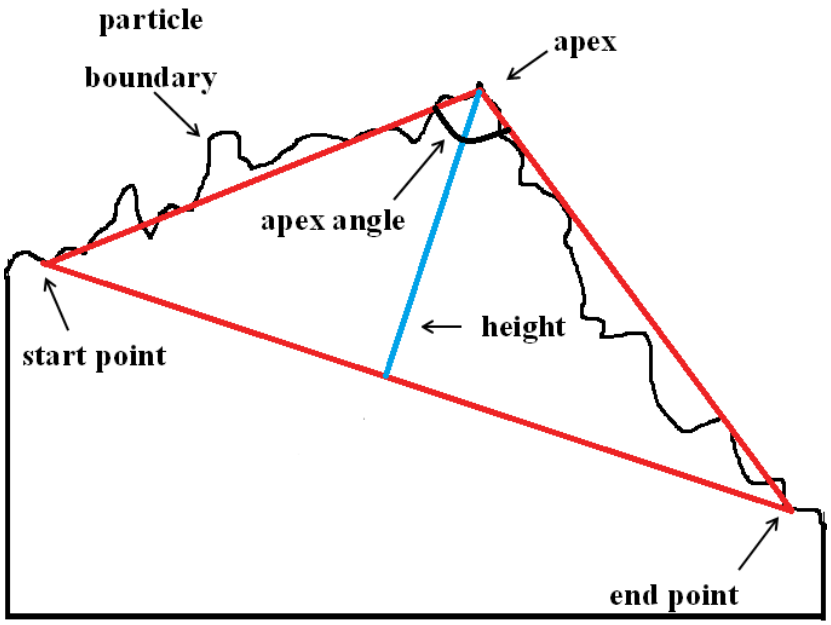

Figure 2.22: Schematic of the particle angularity measurement. After Stachowiak [33].

mechanism of wear loss shifts from abrasion to adhesion and the wear loss again increases rapidly. A smaller abrasive carries a correspondingly smaller fraction of the total load applied and, as a result, damage made by individual particle is less. Also large wear debris can clog the troughs of the surface and prevent smaller abrasives from making contact with the surface.

2.6.4 Wear of abrasive particles

The abrasive particles may also suffer wear from the very beginning of the abrasion and their degradation, in terms of shape and size, have considerable effect on the wear of abrading material. Hosseini and Radziszewski [86] studied the fragmentation of abrasive particles in a steel wheel abrasion test under high stress. They observed that an increase in the applied load has a pronounced effect on both wear rate and abrasive fragmentation, where as, the rotational speed of the wheel has limited or no effect on fragmentation. A very brittle abrasive may fracture easily during abrasion and make several small particles and thus minimises wear. Very tough abrasives do not fracture easily and may not offer new cutting-faces to augment abrasion. Only a moderately tough grit may self-sharpen during

abrasion and offer new cutting faces to accelerate abrasion [Fig. 2.23] [33].

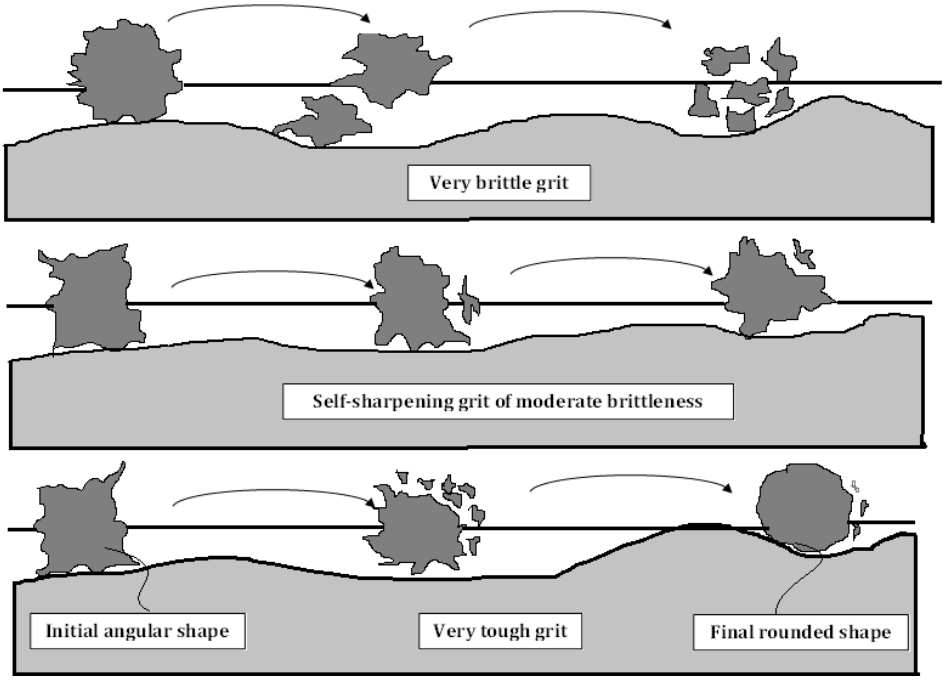

Figure 2.23: Effect of grit brittleness on abrasive wear [33].

2.7 Commercial abrasion resistant steels

The commercial abrasion resistant steels, available either in a quenched or quenched and tempered martensitic condition, are also sometimes supplied in a stress-relieved condition. Table A.1 in Appendix A lists most wear resistant steels containing Mn, Cr and B, sometimes Ni, in addition to carbon. Most of the steels yield at 1000 - 1500 MPa, with an ultimate tensile strength in the range of 1100 - 1700 MPa and hardness ranging between 400 - 550 HV. A comprehensive list of common wear resistant steel plates with their chemical composition and mechanical properties is listed in Appendix A.

The "Fora" is a series of water-quenched martensitic steels and "Creusabro" is either TRIP assisted, microalloyed or austenitic grades. "Creusabro-Superten" having relatively low hardness is a high-resilience steel suitable for the use in massive structures. "Creusabro-Dual", alloyed with Ti (0.6 wt%), has a fine dispersion

of primary TiC precipitates in the matrix leading to superior high-stress abrasive wear resistance. "Cruesabro -M", containing 13 wt% Mn is a completely austenitic steel developed for shock and high impact resistance. "Creusabro-4800"and "Creusabro-8000" [87, 88] are TRIP assisted steels having fine and homogeneous dispersion of Cr, Mo and Ti carbides. The "Abrazo"series are cold-formable grades available in either quenched or quenched and tempered condition [89]. The "Hardox"series falls under the same category of "Abrazo", though the former having much leaner chemistry compared to the later [90–92].

The microstructure of majority of these steels are martensitic. The Cruesabro series are having microstructure comprising of martensite, bainite and retained austentite with fine and homogeneous dispersion of alloy (Ti, Cr, Mo) carbides in the matrix. Manufacturers claim that steels containing bainite and retained austenite exhibit 50% more abrasion resistance life compared to any conventional martensitic steels having Vickers hardness equivalent to 500 HV. However, none of these steels contain incredibly fine microstructural features like in nanostructured-bainite developed by Bhadeshia [93]. Therefore, such a steel, with a combination of high toughness (40 - 50 MPa $m^{1/2}$) and hardness (610 - 630 HV), is worth comparing against commercially available grades.

2.8 Literature Review on Rolling/Sliding Wear

A part of the work presented in this thesis will deal with the so-called carbide-free bainitic steels that have impressive levels of hardness (640 HV_{10}), with potential applications in wear-resistant plates for the mining industries. However, the literature covers only lower strength variants of this microstructure, which is reviewed here to set the scene. Furthermore, the same steels used to generate the new carbide-free bainite can be used in a "nano-pearlitic"state, so rolling/sliding wear is relevant also in that state and will be reviewed here.

2.8.1 General mechanisms of rolling/sliding wear

Wear during rolling/sliding is a function of the state of the stresses generated by contact between two rolling and sliding elements and the microstructure may have a role. For an elastic-plastic material, the consequences of cyclic loading depends on the contact stress (p_0) and the shear yield strength (k) of the material. The ratio p_0/k, can be used to characterise the material response into three distinct regions, namely (a) the elastic, (b) shakedown and (c) ratcheting.

2.8.2 Elastic region

When two regular geometric bodies are brought into contact, the application of a force causes them to deform elastically and the contact area increases. The consequential stress field generated at and below the contact surface, as given by Hertz [94], is detailed in Appendix B for contact between rigid, parallel cylinders for the case of pure rolling.

In case of rolling/sliding, besides the normal forces, a tangential force also acts near the surface. This is often referred to as a tractional force, which substantially changes the magnitude and distribution of sub-surface stresses [95, 96]. As the applied load increases, the material yields plastically beneath the surface near the zone of maximum shear stress, assuming that the contact surfaces are initially smooth. With increased coefficient of friction, the maximum shear stress is at the surface and the material begins to deform plastically in that region. For ductile material, the von Mises yielding criterion is widely used to define the onset of plastic deformation,

$$J = \sqrt{\frac{1}{6}[(\sigma_1 - \sigma_2)^2 + (\sigma_2 - \sigma_3)^2 + (\sigma_3 - \sigma_1)^2]}, \tag{2.14}$$

where, σ_1, σ_2 and σ_3 are the principal stresses. The von Misses stress (J), normalised against the contact stress (J/p_0) for different coefficients of friction (μ), are listed in Table 2.2. With 5% slip and $\mu = 0.55$, the calculated values for the distribution of von Mises stress in the $x - z$ plane shows an asymmetric distribution with respect to the axis of symmetry ($x = 0$) with the maxima at the surface [Fig. 2.24]. The example presented is to illustrate the problem, but the detailed calculations and method used to generate Fig 2.24 are given in Appendix B.

Table 2.2: von Mises stresses for various coefficient of frictions.

	J/p_0	x/a	z/a
μ=0	0.358	0	0.481
μ=0.1	0.361	-0.112	0.475
μ=0.3	0.381	-0.319	0.428
μ=0.5	0.552	-0.550	0

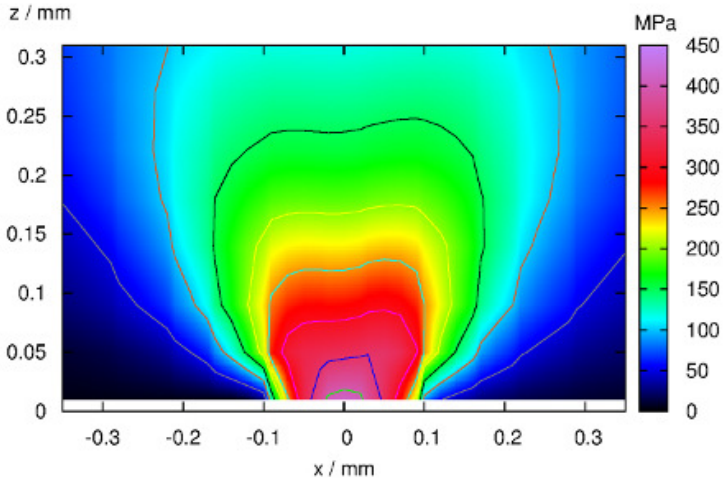

Figure 2.24: Distribution of von Mises stress for 5% slip, μ=0.55 and overlapping width of 5 mm between discs of diameter 45.0 ± 0.1 mm.

2.8.3 Elastic shakedown

The rolling/sliding tests described later in this thesis have the two discs in contact experiencing cyclic loading. Under such conditions, plastic deformation initiates when the contact stresses near the asperities exceed the yield condition. "Asperities "represent protuberances associated with microscopically rough surfaces. This leads to a development of a compressive residual stress along with the strain hardening of the deformed layer [1]. With the progress of rolling/sliding, the contact area also increases, so the contact stress actually decreases. If the load remains same, a situation may arise, in which conditions reach a steady state, where plastic deformation ceases and the material is said to have entered into the elastic shakedown regime. For a pair of rigid axial cylinders, the shakedown limit

is defined as,

$$3.1 \leqslant \frac{p_0}{k} \leqslant 4.0, \tag{2.15}$$

where p_0 is the contact stress and k is the shear yield strength of the material [1].

2.8.4 Ratcheting

If either p_0 or μ increases, there will be a corresponding increase in the shakedown limit. If this happens, then plastic deformation reoccurs until a new shakedown limit is reached. This process can repeat, leading to ratcheting, a phenomenon that is a manifestation of cyclic plasticity. Fig. 2.25 shows the shakedown region, that lies between the elastic shakedown limit and line representing elastic region. The region above shakedown limit represents cyclic plasticity. The plastic strain accumulation with repeated shear deformation, is an important mechanism of metallic wear [97]. The cycle of plastic strain may include reversing components, believed to be the cause ratcheting.

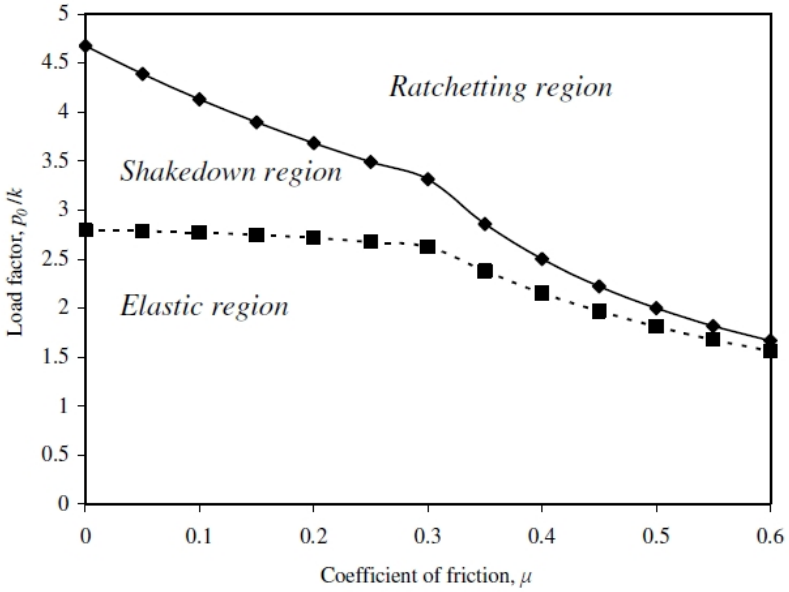

Figure 2.25: Shakedown map for point contact plotted against increasing coefficient of friction. Increasing the coefficient of friction beyond 0.3 reduces the elastic regime. Both the elastic limit and the ratcheting zones are shown [1].

2.8.5 Contact between rough surfaces

The contacting surfaces are never geometrically smooth; machining, for example, always leaves a degree of roughness at the surfaces. This leads to an error in calculating contact stresses using available models [95, 96]. The contact between two rough surfaces is made by initially the asperities so the real area of contact is significantly smaller (1/100) than the nominal area of contact calculated on the basis of the geometry of smooth objects. There is, therefore, a concentration of stress will be much greater than that associated with smooth surfaces. It has been observed that a roughness of 0.5 μm can result in a contact stress of as high as 20 GPa compared to its equivalent Hertzian stress of 0.6 GPa [1].
In a summary, the mechanism of metallic wear and the formation of laminar wear debris can be explained by the process of plastic ratcheting. The geometry, applied load, coefficient of friction, work-hardening and residual stress controls the shakedown limit and ratcheting behavior of elastic-plastic material.

2.8.6 Rolling/sliding wear related to microstructures

Early research work on the rolling/sliding wear of bainitic steels began with comparisons of wear rates between conventional pearlitic rail steels against much stronger bainitic steels with the aim of assessing possible replacement of pearlitic rails [61, 98–105]. Observations were contradictory, as in certain studies [61, 98–101], bainitic steels exhibited inferior wear resistance compared to pearlitic varieties, until Clayton and co-workers challenged previous findings with systematic studies on rolling/sliding wear of a series of bainitic alloys [106–112]. Though a direct comparison is difficult, Table 2.3 lists the wear rates of a few alloys with various microstructures and hardnesses. Pearlite of hardness upto 39 HRC was found to outperform all other structures in terms of wear resistance, whereas, carbide-free bainite beyond 39 HRC hardness showed significantly better wear resistance compared to much harder martensite and tempered martensite varieties. Shipway contradicted the observation by Mutton *et al* as well, proving superior wear resistance of hard bainite compared to martensite or pearlite [113]. Jin & Clayton made an effort to compare the rolling/sliding wear resistance of various pearlitic and bainitic steels. Their findings carried out with a contact stress of 1200 MPa with 35% slip are summarised in Fig. 2.26 and Table 2.3. It is

interesting to note that the wear resistance of pearlite depends strongly on bulk hardness, whereas the hardness has a smaller influence in the case of bainite [112]. The wear resistance in pearlitic steels is found to increase with increasing hard-

Table 2.3: Comparison of rolling/sliding wear of various structures and hardnesses

Alloy	Microstructure	Properties	Wear rate	[Ref]
0.45C-2.08Si-2.69Mn	Bainite(422°C)	HV590±6	0.25×10^{-12} m^3 m^{-1}	[113]
	Bainite(382°C)	HV423±7	1.1×10^{-13} m^3m^{-1}	[113]
	Bainite(329°C)	HV484±14	1.0×10^{-13} m^3m^{-1}	[113]
	Martensite	HV760±9	0.50×10^{-12} m^3m^{-1}	[113]
	Tempered martensite	HV531±4	0.24×10^{-12} m^3m^{-1}	[113]
	Normalised	HV320±8	0.2×10^{-12} m^3m^{-1}	[113]
(0.32-0.79C)-(0.54-1.52)Mn-(0.28-1.86Si)	Pearlite	interlamellar spacing 0.23-0.30µm	2.5×10^{-2}-$1.0\times10^{-1}$$mm^3$ cm^{-1}	[106]
0.71C-0.88Mn-0.57Cr-0.1Ni-0.2Mo	Pearlite	39 HRC	22.80 mg m^{-1}	[110]
	Bainite	39 HRC	77.56 mg m^{-1}	[110]
	Bainite	49 HRC	No Type III wear	[110]
	Bainite	54 HRC	No Type III wear	[110]
0.18C-2.01Mn-1.94Cr-0.48Mo-0.0027B	carbide-free bainite	40 HRC	13.5×10^{-6} g $m^{-1}mm^{-1}$	[105]
0.11C-3.97Mn-0.017Cr-0.47Mo-0.0027B	lower bainite	35 HRC	17.0×10^{-6} g $m^{-1}mm^{-1}$	[105]
0.08C-2.03Mn-1.97Cr-1.93Ni-0.47Mo-0.0031B	granular bainite	35 HRC	16.0×10^{-6} g $m^{-1}mm^{-1}$	[105]
0.023C-2.02Mn-1.96Cr-1.93Ni-0.47Mo-0.0030B	granular bainite	27 HRC	12.0×10^{-6} g $m^{-1}mm^{-1}$	[105]
0.026C-4.04Mn-0.018Cr-0.019Ni-0.47Mo-0.0030B	carbide-free lath ferrite + massive ferrite	26 HRC	17.0×10^{-6} g $m^{-1}mm^{-1}$	[105]
0.04C-0.08Mn-0.19Si-2.76Cr-1.93Ni-0.25Mo-0.0023B	bainite	223 HRB	8.0×10^{-3} g m^{-1} mm^{-1}	[114]
0.11C-0.57Mn-0.19Si-1.68Cr-4.09Ni-0.58Mo-0.0023B	bainite	293 HRB	8.4×10^{-3} g m^{-1} mm^{-1}	[114]

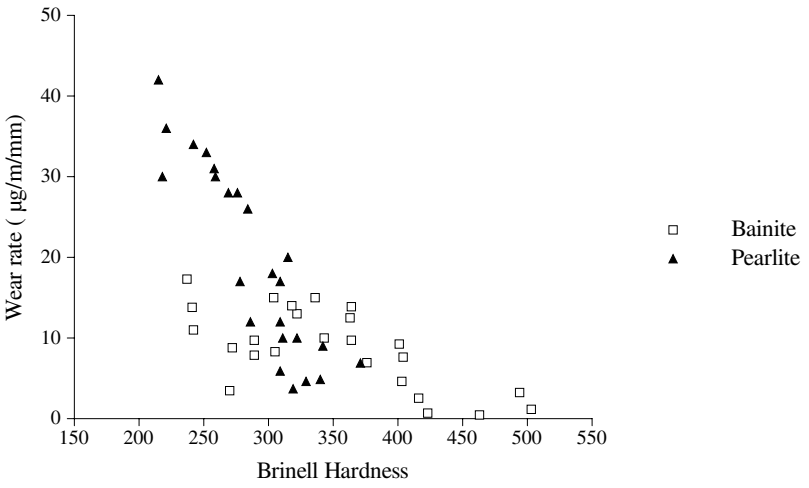

Figure 2.26: Rolling/sliding wear rate of a few pearlitic and bainitic steels with varying hardnesses [114].

ness achieved via decreasing interlamellar spacing [106, 114] and bainitic steels with superior impact toughness can match conventional pearlitic steels under similar test conditions [108]. Another variant of low-C, Mo-B containing carbide-free bainitic steel [Table 2.3] outperformed pearlitic steels of equivalent or much higher hardness, especially at contact pressures of > 1000 MPa [109]. With increasing carbon content and refining of the bainitic structure by holding at lower

transformation temperatures (200-250°C), a much improved wear resistance was obtained from the same alloy compared with pearlitic counter-parts; where severe wear could not be induced in bainite under similar test conditions [110]. In a separate work by Jin & Clayton with carbide-free bainite with/without retained austenite, as proposed by Bhadeshia & Edmonds [115], claimed to have achieved a dry rolling/sliding wear resistance comparable to that of Hadfield's Mn steels under severe conditions [112].

Carbide-free bainitic steel with fine bainitic ferrite laths separated by films of high-C austenite show impressive wear resistance, both in bulk [116] and case-hardened forms [117, 118], compared to structures of equivalent/more hardness [4–6, 116–121]. The refined mixed structure imparts a high hardness and toughness with the austenite retarding crack propagation, thus reducing wear. In all these cases, a hard thin friction layer of extremely fine ferrite grains is found at the wear surface forming due to martensitic transformation of the retained austenite caused by surface shear strains due to sliding. The wear resistance was found to increase as the the initial structure was refined by lowering the transformation temperature [118].

There exists a difference between the mechanisms of deformation during the wear of pearlite and bainite. Alignment of cementite lamellae occurs along the rolling/sliding direction with both ferrite and cementite undergoing significant plastic strains. In contrast, the high dislocation density (10^{14} m mm^{-3}) in bainitic ferrite resists similar deformation [120]. At lower loads of rolling/sliding, pearlite performs exceptionally well, as the significant plastic deformation and subsequent alignment of the pearlite lamellae in the direction of wear offers greater surface area of hard carbide plates on the friction surface. The wear resistance further improves with improving cleanliness of steel and reductions in the interlamellar spacing of pearlite, which leads to greater work-hardening. Higher plastic flow and fracture strain of fine pearlite are believed to be the key factors in achieving high wear resistance [101].

In bainitic steels, depending on the severity of the applied load, the rolling/sliding wear resistance depends significantly on the hardness and the scale of the structure. Low-C (0.04 wt%-C) bainitic steels fail miserably compared to conventional pearlitic steels under similar conditions, owing to their low hardness, coarse structure and presence of martensite-austenite islands [101]. At low stresses, typically 100-800 MPa, the wear resistance increases with increasing hardness of bainite,

which can be achieved by utilising greater carbon and manganese concentrations in the steel. Under severe wear conditions, the hardness of bainite does not correlate well with the wear resistance, rather it is the extent of refinement of the structure that plays a major role. Fine bainitic structures, transformed at low temperatures devoid of embrittling martensite or carbide, have been found to resist wear than other structures of even higher hardnesses [112,114], presumably because of their combination of hardness and toughness. A high hardness naturally resists deformation whereas the generation of wear debris is reduced if the toughness is optimised [113, 114].

Apart from the absence of carbides in carbide-free bainite, the thin-films of austenite are claimed reduce wear [5, 6, 120–122]. In contrast, blocky austenite readily transforms into untempered martensite which can cause embrittlement. However, these conclusions are not rigorous because the formation of martensite at the wear surface may lead to hardening and therefore can reduce wear.

2.8.7 Summary

Qualitative observations indicate that wear resistance improves with the refinement of structure and if retained austenite is present. However, unambiguous conclusions are difficult to draw because there are multiple consequences of the presence of retained austenite. The stability and TRIP effect of high-C thin film retained austenite at various stages of wear also needs deeper investigation. In work presented later in the thesis, an effort has been made to characterise the worn surface of three different structures after rolling/sliding experiments, namely fine pearlite, carbide-free bainite and martensite, for comparison purposes and theoretical analysis.

Chapter 3

Experimental Procedures

This chapter gives an overview of the general experimental techniques adopted for the research. Experiments specific to a type of microstructure and/or wear test are discussed separately in respective chapters.

3.1 Alloy, sample preparation and heat treatment

3.1.1 Chemical composition

The steel was produced as a part of a larger programme of work on the development of nanostructured bainite for commercial engineering-applications. Nine tonnes of material were continuously cast in round sections of 150 mm diameter [Fig.3.1]. The chemical composition is listed in Table 3.1. Silicon is added to prevent the precipitation of cementite during the bainite transformation. Molybdenum helps to prevent embrittlement due to phosphorus. Manganese and chromium enhance hardenability. Cobalt and aluminium help in accelerating the transformation. Elements like tin and copper are not intentionally added, but can be treated as common impurities present in most industrial melts [123]. Prior to any heat treatment, this shaft was slowly cooled through the temperature range of 700 - 550 °C to ensure that the initial microstructure is pearlitic in order to avoid possible cracking associated with martensitic transformation.

Table 3.1: Chemical composition of the experimental alloy (wt %).

C	Mn	P	S	Si	Al	Cu	Cr	Mo	V	Co	Sn	Nb
0.83	2.28	0.011	0.008	1.9	0.044	0.12	1.44	0.24	0.11	1.55	0.019	0.023

Figure 3.1: A section of the shaft material in as-received condition.

3.1.2 Sample preparation

The samples for wear tests were machined out from the normalised shaft, as machining after heat treatment is difficult and induces additional residual stress due to cold work.

3.1.2.1 Sample for dry-sand rubber wheel test

Samples for abrasion tests were machined as rectangular blocks of size 25 × 60 × 14 mm from the centre of the shaft using electro-discharge machining. A thickness of about 1 mm was removed from each side of the broad faces with 240 grit wet SiC abrasive paper to avoid any damage from the discharge machining [Fig. 3.2].

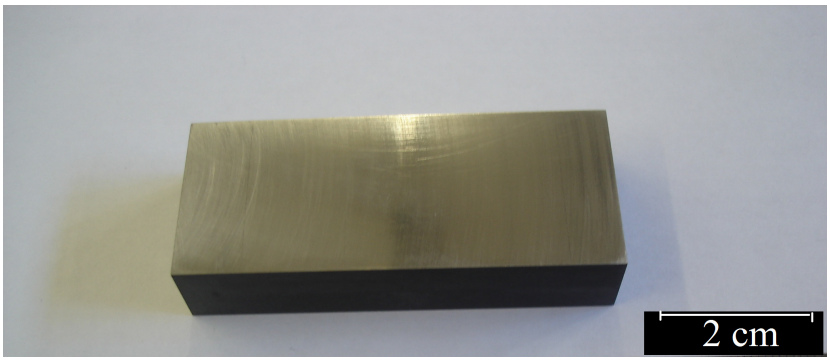

Figure 3.2: The test specimen for dry-sand rubber-wheel abrasion test before heat treatment.

3.1.2.2 Sample for dry rolling/sliding test

Cylindrical disc specimens [Fig. 3.3] for dry rolling/sliding wear were also machined out of the shaft using electro-discharge machining. The curved surfaces were smoothed to the required surface roughness by gently grinding over 1200 and 2500 grits of SiC followed by polishing using 6 μm and 1 μm diamond abrasives respectively. The samples were dried in acetone and dessicated to prevent any oxidation of polished surfaces before wear.

3.1.3 Making of fine pearlite

Earlier research showed the potential of the experimental alloy to transform into very fine pearlite with interlamellar spacing $< 50\,\text{nm}$ during continuous cooling from austenitisation temperature followed by isothermal heat treatment [3]. A fine pearlitic structure was therefore obtained by austenitising the sample at 930°C for 60 min in an argon atmosphere, followed by cooling at a rate of $1^\circ\text{C}\,\text{s}^{-1}$ to 550°C and holding there for 4 h followed by air cooling to room temperature. Water quenching after isothermal holding was avoided to eliminate the possibility of developing fine quench cracks and thermal stresses, which could adversely affect the wear resistance of the microstructure. A thin layer of oxide film, developed during air cooling, was subsequently removed via gentle grinding and polishing. Details of the heat treatment and the mean with standard error of Vickers hardness (30 kg load) measured at ten different locations are listed in Table 3.2.

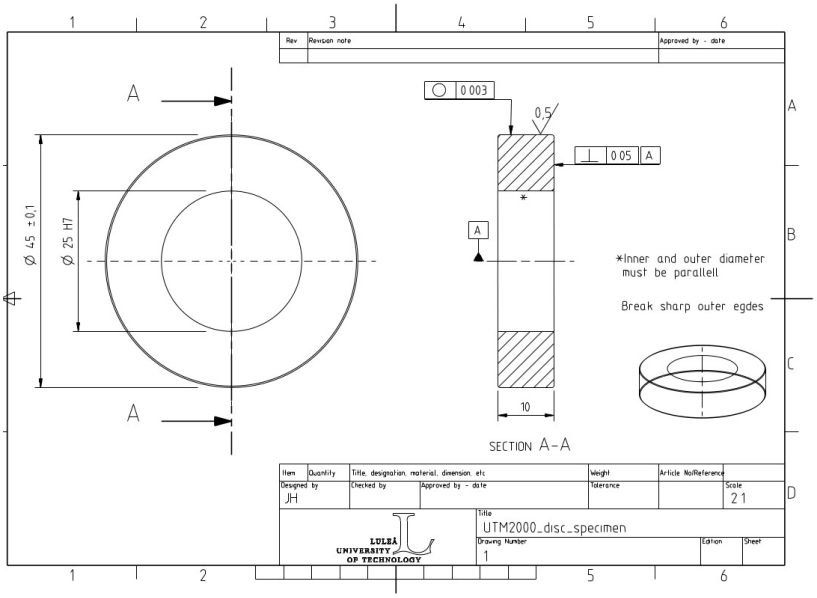

Figure 3.3: Engineering drawing of the sample for twin disc rolling/sliding wear test. All units are in mm. Courtesy : Lulea Institute of Technology, Lulea, Sweden.

Table 3.2: Heat treatment and resultant hardness measured in Vickers scale.

Sample	Heat Treatment	Vickers hardness/kgf-mm^2
Fine pearlite	930 °C 60 mins, air cooled to 550 °C, held for 4 h, air cooled	378 ± 9

3.1.4 Transformation to nanostructured bainite

The sample was austenitised at 930°C for 1h followed by forced cooling at $5°C\,s^{-1}$ to 200°C and then transferred into a carbolite box oven maintained at the same temperature and held there for 10 days in order to complete the transformation. The forced cooling was assisted by holding the austenitised sample fitted with a K-type thermocouple in front of an electric fan and continue the cooling till the temperature drops to the required level. Hardness values measured at ten different locations were averaged and reported in Table 3.3.
To remove the oxide layer, the sample surfaces were ground using wet SiC abrasive paper to a 400 grit final finish. Approximately 1 mm was removed in this way, resulting in a final thickness of 10 mm [Fig. 3.2]. The samples were then kept in a desiccator. Two other sets of equivalent samples were prepared for hardness testing and microstructural characterisation.

Table 3.3: Heat treatment and resultant hardness measured in Vickers scale.

Sample	Heat Treatment	Vickers hardness/kgf-mm^2
Bainite	930 °C 60 mins, air cooled at $2°C\,s^{-1}$ to 200 °C, held for 10 days, air cooled	640 ± 13

3.1.5 Air cooled martensite

The continuous cooling transformation diagram provided by Tata Steel for the experimental steel is shown in Fig. 3.4. For cooling rates $> 2\,°C\,s^{-1}$ from the austenitising temperature of 930 °C to below 200°C should produce martensite. Temperatures were monitored using a 90 Ni-10 Cr wt% K-type thermocouple attached to the sample surface. The specimen was placed on an alumina crucible and inserted into a tube furnace maintained at 930 °C for 1h with a steady flow of argon maintained through the tube. The sample was then taken out of the furnace and cooled in forced-air, to cool below 200 °C with a cooling rate of $5\,°C\,s^{-1}$ and then left to cool further to room temperature (23 °C). Table 3.4 lists the average hardness of the resultant structure.

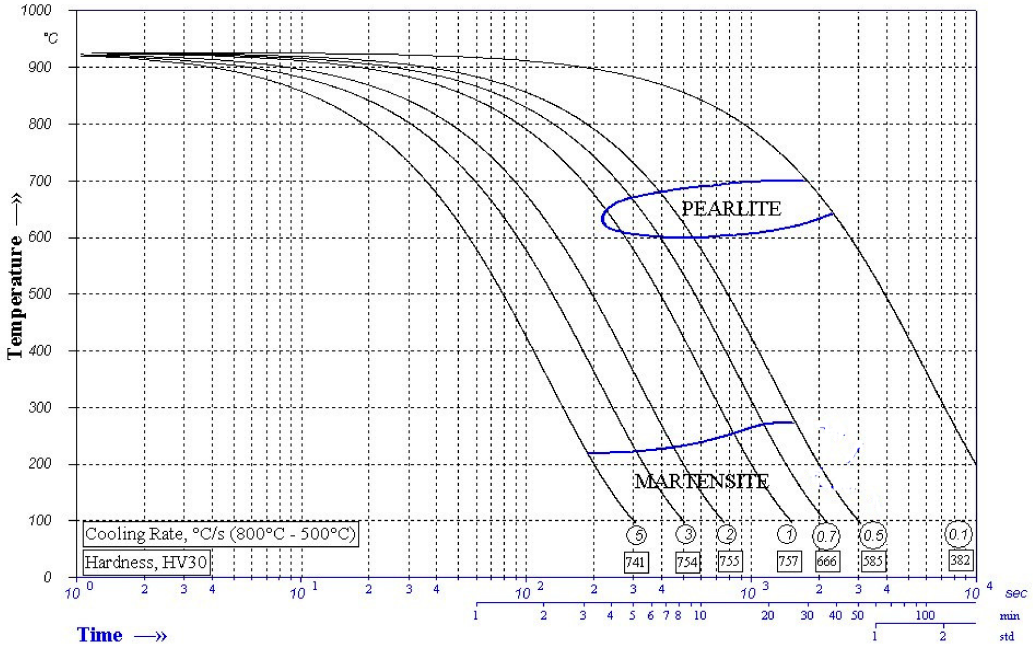

Figure 3.4: The continuous cooling transformation diagram of the steel with the chemical composition listed in Table 1 [Courtesy : Tata Steel Europe].

Table 3.4: Heat treatment and resultant hardness measured in Vickers scale.

Sample	Heat Treatment	Vickers hardness/kgf-mm^2
Martensite	930 °C 60 mins, air cooled at 5°C s^{-1} to 23 °C	780 ± 7

3.1.6 Tempering of bainite

Tempering of nanostructured bainite was carried out in the same Ar-purged tube furnace at 500°C for one hour [Table 3.5]. The samples were wrapped with stainless steel foil filled with crushed titanium to consume any traces of oxygen present inside the furnace. After the tempering is over, the samples were immediately quenched in water and approximately 0.5 mm was ground off from the surfaces via metallographic grinding and polishing. Thus a smooth surface with an average roughness, $R_a \sim 1\mu m$, was prepared for abrasion test.

Table 3.5: Vickers hardness values (30 kg load) following specified heat treatments

Sample	Heat Treatment	HV30 / $kgf\,mm^{-2}$
Tempered bainite	Nanostructured bainite tempered at 500 °C 1 h, water quenched	570 ± 12

3.2 Wear tests

Both three-body abrasive wear and rolling/sliding wear were performed on fine pearlite, nanostructured bainite and martensite. The following sections briefly describes the test procedure and parameters of each set of experiments.

3.2.1 Dry sand-rubber wheel abrasion

Three-body abrasion tests were conducted broadly in accord with standard practice [124], using the parameters listed in Table 3.6. Before each test the sample was weighed with a precision of 0.0001 g. The surface subjected to abrasion, was cleaned and dried with ethanol so as to remove any dirt. The non-standard values of the rotational speed and total number of wheel revolution were chosen to ensure appreciable wear of the samples. Samples were ground using 400 grit SiC papers prior to the experiments, which utilised silica sand with an average

particle size of 300 μm as the abrasive medium. The equipment and the abrasive sand used are illustrated schematically in Fig. 3.5(a) and (b) respectively. The sand flow rate and rotation speed of the wheel were kept constant throughout each experiment. The test was stopped after every 2700 rotations for 10 min in order to prevent excessive heating of the sample and the rubber wheel. The worn samples were then cleaned in acetone and the specific wear rate and wear coefficient were determined from weight loss data.

Table 3.6: Three-body abrasion test parameters

Wheel	Rubber-clad steel wheel
Rubber	Chlorobutyl
Hardness of rubber	Durometer A-60
Abrasive used	Silica sand, grade HR 30 (Prince Minerals, UK)
Mean particle size of silica sand	300 μm
Hardness of silica sand	956 ± 22 kgf mm^{-2} (200 g load)
Rotational speed	250 revolutions min^{-1}
Load	130 N
Sand flow rate	300 g min^{-1}
wheel diameter	22.86 cm
Total number of wheel revolution	16200
Total sliding distance	11.62 km

3.2.2 Twin disc rolling/sliding

Rolling/sliding tests were performed in a UTM 2000 twin-disc machine [Fig. 3.6], using self-mated pairs of 10 mm thick cylindrical discs of 45±0.1 mm external and 25 mm of internal diameter. The two discs, when made to contact at their edges during rotation, develop a rectangular area of contact. Because of the surface roughness and geometrical/dimensional tolerance, full contact over the entire length of overlap was never made possible. Theoretically, the contact should first be made between the highest asperities and should gradually increase as the wear progresses. A roll-slide parameter, equal to $\xi = 0.95$, was introduced by administering differential velocities between the discs.[1] This would influence the two

[1]The parameter is calculated from the difference of circumferential velocities of the two discs. Mathematically, it is 1-(% slip/100).

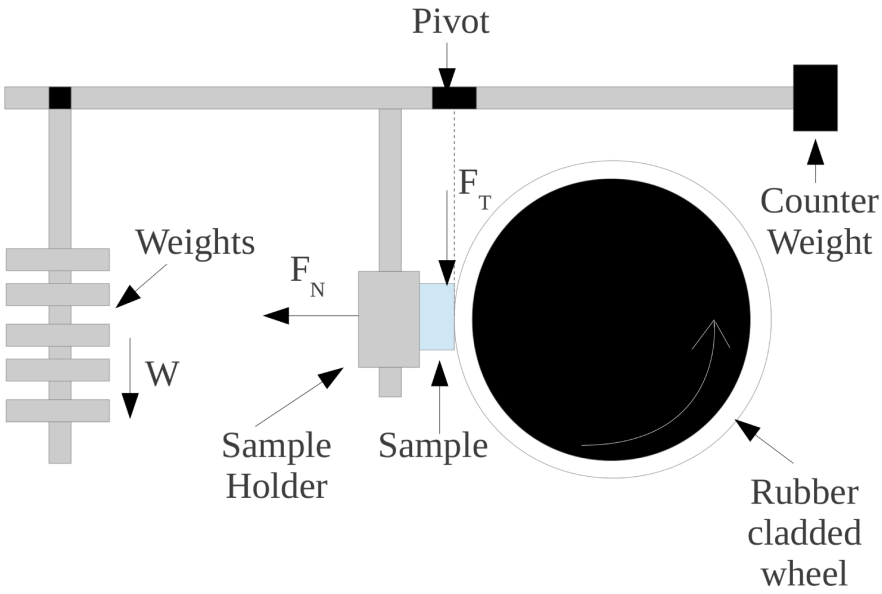

(a)

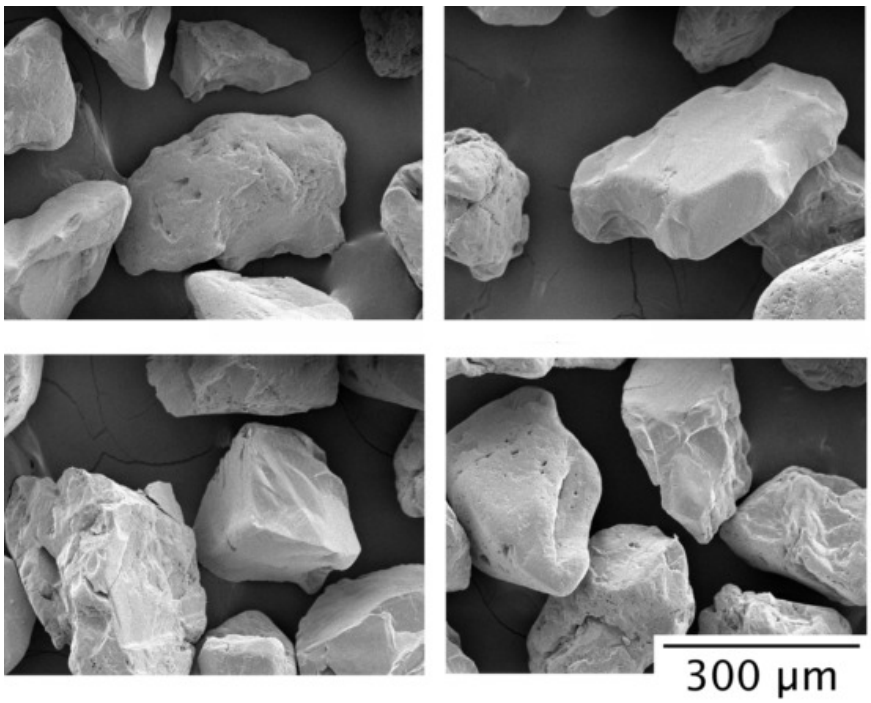

(b)

Figure 3.5: (a) Schematic illustration of the abrasion-test equipment, (b) SEM images of the abrasive sands.

normal stress and the shear stress component in plane stress condition. The tests were conducted in a controlled environment (∼25 °C, 23% humidity) without any lubrication. The tribometer offers a range of rotational speed from 60 up to 2000 rpm with application of load through a dead weight and lever mechanism, which enables an applied load up to 1000 N. There is a provision for application of lubricating oil at the contact zone for wet rolling/sliding experiments in which the oil can be heated up further to carry out tests at higher temperatures. Experiments were conducted for three pairs of discs for 30,000 cycles at a rotational speed of 100 rpm and 95 rpm respectively with an externally applied load equal to 300 N.

The samples were used in as machined condition with an average surface roughness (R_a) ranging between 0.3 to 0.55 μm. The samples were cleaned and weighed before and after wear with a precision level up to five places after the decimal. Weight losses were measured for three pairs of discs and normalised against load and the distance traveled by a point on the perimeter over the duration of test as shown in eqn.3.1. The average value of specific wear rates for three discs along with respective statistical standard errors are reported as the wear loss for each microstructure studied.

$$SWR = \frac{volume\ loss\ (\mathrm{mm}^3)}{load\ (\mathrm{N}) \times sliding\ distance\ (\mathrm{m})} \tag{3.1}$$

3.2.3 Limitations of Experiments

Three-body and two-body abrasion was simulated in the laboratory using dry-sand rubber wheel and twin disc rolling/sliding tests respectively. Three-body abrasion is a common wear phenomenon in mineral handling and transportation, whereas, rolling/sliding wear is encountered when rolling elements traverse a surface. It is difficult to physically simulate the exact condition that prevails in real life, without monitoringperformance in service, but a number of laboratory tests are available that enable ranking and give some idea of wear mechanisms. These include the tests described below.

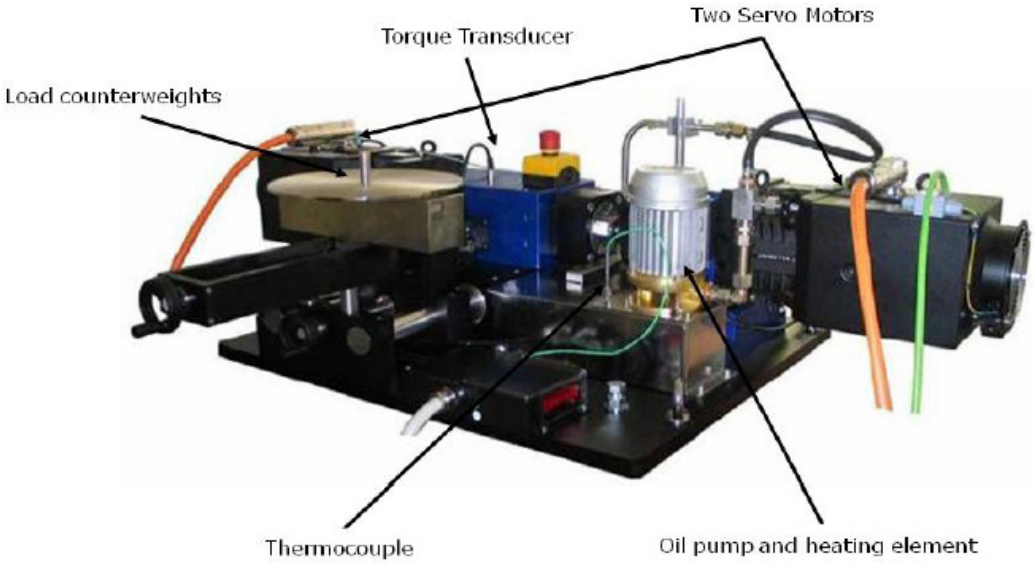

(a)

Figure 3.6: (a) Configuration of the UTM-2000 twin disc machine.

Three-body abrasion

- The dry-sand rubber wheel test used to simulate three-body abrasion is a typical low-stress abrasion experiment, where the load applied (130 N) is much less than encountered during abrasion in mining equipment. This is because in mining operations, some particles will be large enough to gauge the steel by impact deformation. However, the intention here is to use more controlled experiments for detailed characterisation of the worn surface.

- The tests were carried out with only one set of parameters with respect to abrasive size (300 μm), feed rate (300 g m^{-1}), speed (250 rpm), load (130 N) and humidity (30% humidity at 23°C) to compare wear rates of various microstructures of comparable hardnesses [125]. It is possible to extend the test with higher loads, or smaller and angular abrasives like alumina, both of which would aggravate wear [126]. Abrasion in wet media would reveal the effect of lubrication by moisture on wear rate, which might decrease with increasing moisture content [73]. The detailed effect of abrasive properties on three-body abrasion has been described in Chapter 2.

Dry rolling/sliding wear

- Rolling/sliding tests were also performed using a fixed set of parameters, such as sample geometry, applied load, % slip and duration of test. The major advantage of adopting this regime is to enable comparisons against a significant quantity of published work on other steels and microstructures [5, 6, 127], where the same conditions were used. A change in sample geometry or %slip could lead to dramatic change in the contact stress condition, as detailed in Appendix B.

- The rolling/sliding tests were interrupted after 30,000 cycles, at which point, a measurable wear loss was obtained. The tests, however, could have been extended to the point of catastrophic failure due to sub-surface damage, but the purpose here was to examine damage mechanisms on a microscopic scale.

- The tests were conducted in dry condition.In principle, future work could include wet conditions but this would dramatically increase the number

of variables due to the account for fluid compositions and chemical reactions [128, 129].

- The contact stresses in rolling/sliding were calculated using Hertzian contact with traction (Appendix B). In the absence of the strain hardening parameters of the structures studied, the effect of kinematic hardening on the rolling/sliding stress and subsequent ratcheting was not considered. As a result, the mathematics discussed is limited in explaining the variations in the strain observed for the variety of microstructures studied.

3.3 Metallography

3.3.1 Sample preparation

Metallographic sample preparation of worn structure needs special care, as conventional grinding and polishing techniques could induce unprecedented artifacts, such as sub-surface cracks in the polished sample, which could be confused with a fatigue crack generated during wear. There exists a possibility of partial or complete loss of worn structure during conventional grinding, polishing and etching [130]. The edge of the specimen, which is actually the worn structure, often gets rounded-off due to plastic smearing. Moreover, the compressive stress ahead of the abrasive grit of the grinding paper could get relaxed by plastic deformation of ductile material and the tensile zone behind can often develop cracks [131].

3.3.2 Optical metallography

All of the optical microscopy work, with magnification in the range 50-500×, was performed using both a Zeiss Axiotech optical microscope fitted with a QImaging MicroPublisher 3.3 RTV camera and a Leica Microsystems DM2500M upright light microscope with an attached DFC295 camera. Leica Application Suite software, ImageJ [132] and GIMP were used for minor digital modifications of the micrographs taken (e.g. cropping, addition of scale bars, brightness and contrast adjustments).

3.3.3 Scanning electron microscopy

The secondary electron images were taken in a Jeol 5800LV scanning electron microscope, operated under 15 kV gun potential, with 67 μA filament current. The working distance was maintained within 8-12 mm for high resolution (× 10,000) images.

3.3.4 Focused ion beam milling of samples

The sample for TEM was prepared using a dual-beam FEI Helios Nanolab equipped with a FEG-SEM and an advanced FIB. The area of interest, about 20 μm long and 520 μm wide, was selected from the featureless WEL (White Etching Layer). An approximately 2 μm thick protective layer of Pt was deposited over the selected area so as to prevent further damage of the material underneath during thinning using Ga^+. The next step was making of the trench from both sides of the selected area using the Ga^+ source operated at 30 kV and 2800 nA current. A micro-manipulator was used to lift out the sample and fix on the Cu-grid using Pt deposition. The thinning of the sample was conducted from both the sides by tilting around its major axis in three steps using 1000 pA, 500 pA and 150 pA current respectively so as to attain a final thickness less than 100 nm [Fig. 3.7(a-e)]. The sample was later observed under bright-field imaging mode in a Jeol JEM-200CX transmission electron microscope with selected area diffraction pattern.

3.3.5 Transmission electron microscopy

For transmission electron microscopy of bulk specimens, thin foils approximately 200 μm thick were slit, from which discs of 3 mm diameter were machined using spark-erosion. The discs were ground down to 50 μm thickness using 2500 and 4000 grit SiC abrasive papers successively and foils were prepared by electropolishing at -4°C in an electrolyte comprising of 5% perchloric acid, 15% glycerol and 80% methanol by volume. The electropolishing voltage was kept between 21-24 V with a current ranging between 16 -19 mA for various structures.
Electron images and diffraction patterns were taken on a JEOL 200CX transmis-

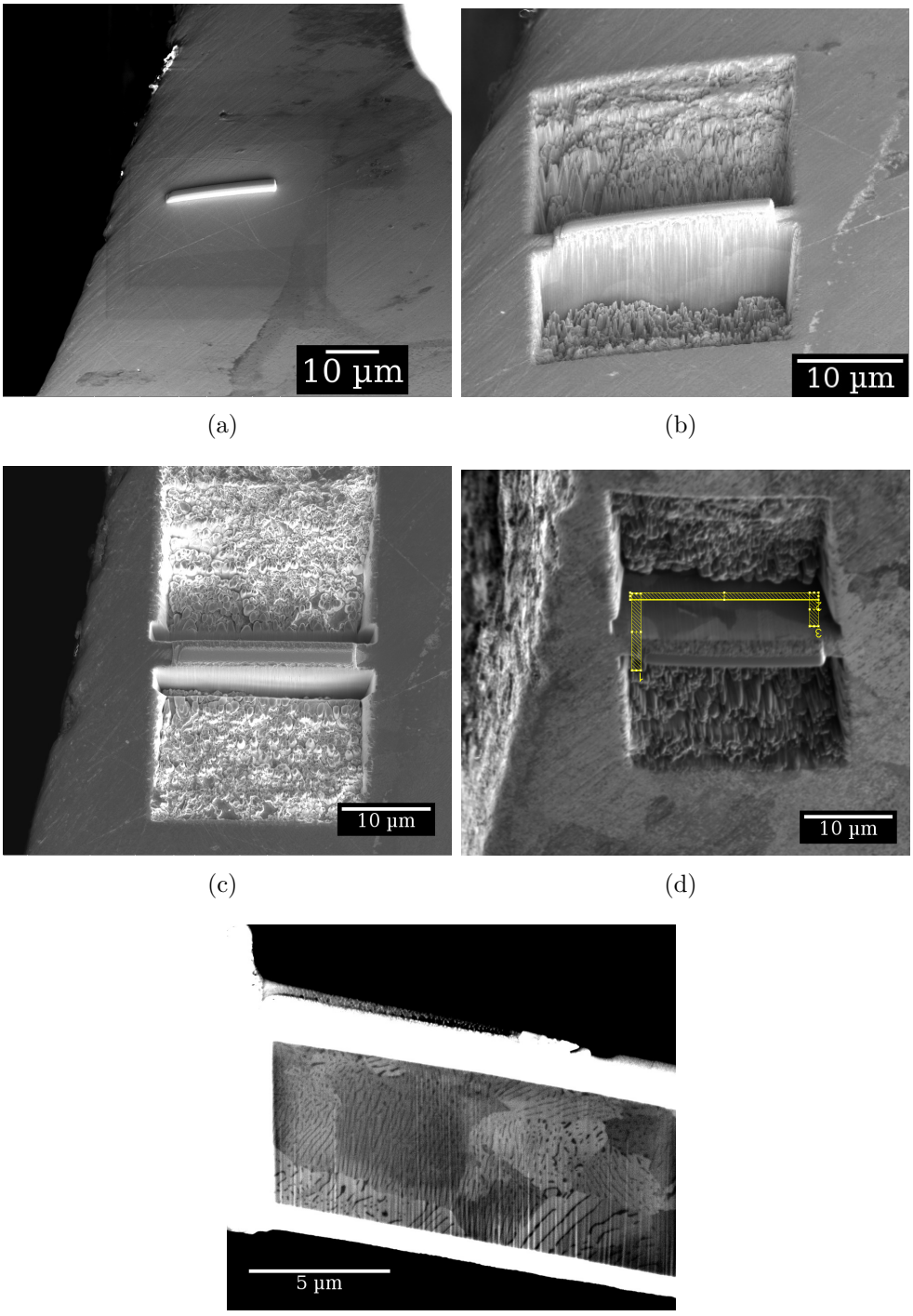

(a) (b) (c) (d) (e)

Figure 3.7: Secondary electron and ion channel contrast images of the TEM sample milled inside FIB, (a) deposition of Pt layer on the deformed sub-surface, (b-c) milling out the specimen, (d) undercut and thinning of the specimen and (e) ion channel contrast image of the electron transparent specimen.

sion electron microscope operated at 200 kV. The spot size was varied between 1 to 3 for bright field images with proper adjustments of condenser lenses for magnifications ranging between 15,000 to 100,000×.

Measuring true interlamellar spacing of pearlite: The mean true-spacing, $\overline{L}_0$, of pearlite is measured using the Underwood's intersection method [133]. A circular test grid of diameter d_c is drawn on the micrographs. The perimeter of the test grid intersects the lamellae of carbides at n points, which is counted as number of intersections. The process was repeated randomly on a number of fields on the micrograph so that $\overline{L}_r$, is given by apparent spacing,

$$\overline{L}_r = \frac{\pi d_c}{nM} \tag{3.2}$$

where, M is the magnification of the image. According to Saltykov [134], $\overline{L}_0$ can be calculated as,

$$\overline{L}_0 = 0.5\overline{L}_r \tag{3.3}$$

Measuring bainitic ferrite plate thickness : The mean lineal intercept ($\overline{L}$) was measured in the direction perpendicular to the trace of the habit plane of the bainitic and tempered bainitic ferrite plates from randomly selected locations of transmission micrographs, in order to estimate the true thickness (t) using the relation [135]:

$$t = 2\overline{L}/\pi \tag{3.4}$$

3.4 Surface roughness

The surface roughness was measured using light optical interferometry profilometer, the details of which are explained in following section.

3.4.1 Optical interferometry

The WYCO profilometer measures the profile of a solid surface using the principle of optical interferometry [Fig. 3.8]. The intensity of the light will be at a

maximum for a given interference pattern when the optical path difference between the reference and the sample beam is zero, and reduces sharply as the optical path difference becomes half the wavelength. There exist two methods for the measurement. Phase-shift interferometry (PSI) uses a single wavelength of light whereas, vertical-shift interferometry (VSI) uses the multiple wavelengths. The former mode is generally used for continuous surfaces having step-heights less than quarter of the wavelength of light or approximately 150 nm, with an accuracy of ∼1 nm. The vertical mode is used for more irregular surfaces having step-heights of the order of mm with an accuracy of 10 - 30 nm. In the present work the roughness of the abraded surface was measured using the VSI method at five different places and averaged out.

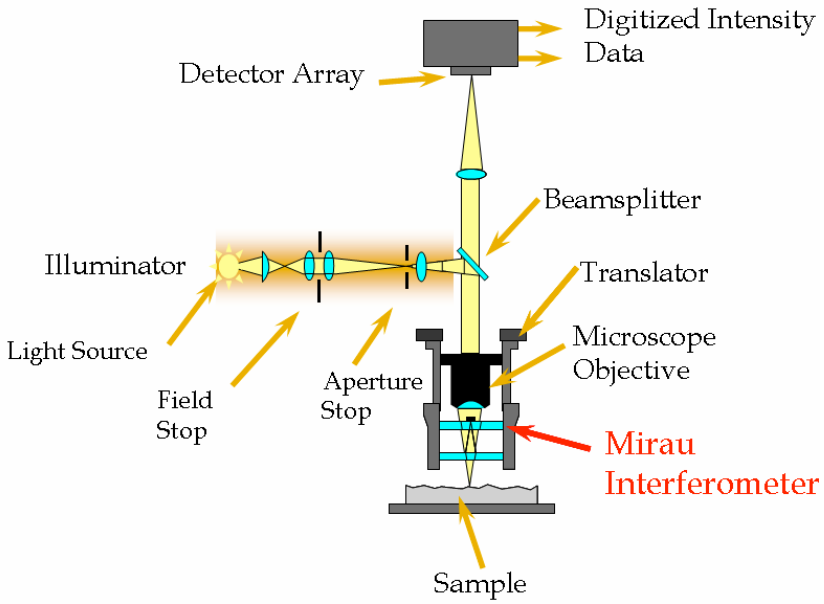

Figure 3.8: Schematic illustration of the light interferometer microscope. Adapted from [136].

3.5 Mechanical testing

3.5.1 Hardness measurement

Bulk hardness was measured using a Vickers hardness tester applying 30 kg dead load. The average of the two diagonal lengths of the projected square indentation

made by the pyramidal indenter was measured optically and the hardness was determined under constant load using eqn.3.5;

$$HV \sim \frac{0.1891F}{d^2} \tag{3.5}$$

where, F is the applied load in Newtons and d is the measured diagonal length of the indentation in mm. A gap equal to at least $2.5d$ between two nearest indentations were maintained in order to avoid the increase in hardness due to the work-hardening of the deformed structure due to indentation. At least five indentations were taken for each structure, readings of which were averaged out during reporting. The standard deviation of the measurement, σ, was taken to calculate the statistical standard error ($\sigma/\sqrt{N}$), where, N is the number of indentations made.

3.5.2 Nanoindentation testing

A series of constant depth nanoindentations using a sharp Berkovich nanoindenter were made on the deformed sub-surface layer after abrasion. The indenter was calibrated against fused silica before making indentations on the experimental sample. The surface on which indentation was made was polished with a 0.4 μm colloidal silica for 5 min and the average surface roughness was measured before indentation using a Vecco stylus. A 5 × 4 rectangular array of indents were made below the abraded surface and nanoindentations were carried out under constant depth of 400 nm. The load-displacement data were used for subsequent analysis and the sample after indentation was ultrasonically cleaned in acetone before doing optical microscopy of the nanoindentations.

3.5.2.1 Measurement of nanoindentation hardness

For a frictionless, quasi-static indentation made on a elastic-plastic material, the load-displacement curve will have an elastic-plastic loading and elastic unloading profile as shown in Fig. 3.9. We made an assumption that the residual stress is equi-biaxial, in-plane and remains uniform over the indentation depth equal to 400 nm. Based on the half-space elastic deformation theory, the contact hardness, H and the elastic modulus E^* can be calculated from the load-displacement data

using Oliver and Pharr's method [137],

$$H = \frac{P_{max}}{A} \tag{3.6}$$

$$A = 3\sqrt{3}h_c^2 \tan^2\theta = 24.5h_c^2 \tag{3.7}$$

where, P_{max} is the maximum load, A is the contact area and .

$$h_{max} = h_c + \left[\frac{2(\pi - 2)}{\pi}\right]\frac{P}{dP/dh} \tag{3.8}$$

$$E^* = \frac{dP}{dh}\frac{1}{2}\frac{\sqrt{\pi}}{\sqrt{A}}. \tag{3.9}$$

where, P and h are the instanteneous load and displacement respectively, A is the projected area of contact, θ is the cone semi-angle [138]. Once h_{max}, P_{max} and dP/dh are obtained from the load-displacement data, h_c can be calculated using the above set of equations. The unloading curves are often approximated as;

$$P = \alpha(h - h_f)^m \tag{3.10}$$

where, α and m are power law fitting constants. h_c is expressed as,

$$h_c = h_{max} - \epsilon\frac{P_{max}}{dP/dh} \tag{3.11}$$

where, ϵ, is a constant expressed as the Γ-function of the power law fitting constant of the unloading curve, m [139][2].

$$\epsilon = \left[1 - \frac{2\Gamma(\frac{m}{2(m-1)})}{\sqrt{\pi}\Gamma(\frac{1}{2(m-1)})}(m-1)\right]. \tag{3.12}$$

[2]Γ function is a factorial function with is argument reduced by 1, i.e. Γ(n) = (n-1)!

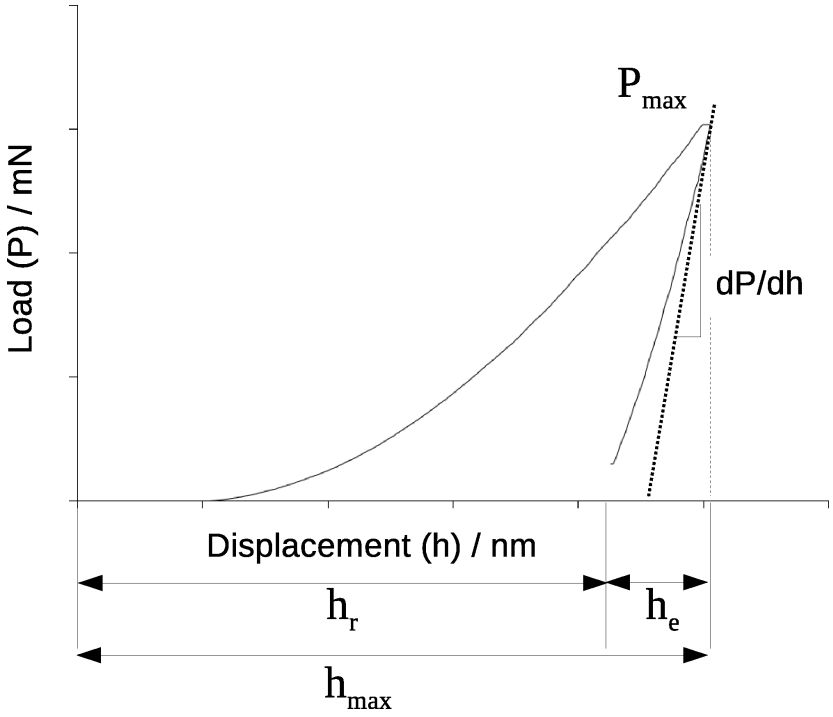

Figure 3.9: Schematic of the load-displacement curve during nanoindentation made on elastic-plastic material, showing maximum load, P_{max}, maximum indentation depth beneath surface, h_{max}, slope of at the onset of elastic unloading, dP/dh, depth of the residual impression, h_r and displacement due to elastic recovery of test material during unloading, h_e. Adapted from [2].

3.5.2.2 Measurement of residual stress

The volume indented by the indenter represents the total work done by the applied load during indentation. Therefore, the volume integral of the load-displacement curve during loading represents the energy spent during indentation. During unloading, elastic recovery of the deformed material occurs. The volume integral under the unloading curve-displacement denotes the energy recovered due to elastic recovery. Hence the area enclosed by the loading and the unloading curves represents the energy lost during indentation, which is stored in the form of residual plastic deformation of the indented volume of material and elastic energy contribution due to residual stress of the indented volume.
The model for the measurement of residual stress by Wang *et al.* is based on the difference in the maximum load, P_{max}, of nanoindentation load-displacement curve obtained from the stressed and unstressed part of the structure and is expressed as [140];

$$\sigma_{residual} = \frac{P_{max}^{stressed} - P_{max}^{stress-free}}{2\pi h_r^2 \tan^2 \theta}, \tag{3.13}$$

where, $\sigma_{residual}$ is the residual stress to be measured on the stressed area, $P_{max}^{stressed}$ and $P_{max}^{stress-free}$ are the maximum loads obtained on the stressed and the stress-free area [138]. The value of θ is the cone semi-angle of the impression of the residual indentation and can be considered as a geometric correction factor used for other sharp indenters and is normally estimated from the best fit between finite element modeling simulation and nanoindentation tests [140]. h_r is the residual depth of the impression made by nanoindentation, after removal of the indentation load [137]. Wang's model assumes that there is no variation in the half-angle of the indentation and assumes it equals that of the indenter half-angle. Fig. 3.10 shows the schematic of the geometry of the impression made during loading and after unloading of the indenter. It is most likely that the elastic recovery over the indentation depth is not uniform as the tip of the indentation is expected to recover more compared to base of indentation assuming a non-linear plastic regime of the stress-strain curve. Once the indentation load is withdrawn, a material with compressive residual stress will have a tendency to contract, which reflects in an increase in the residual half-angle. As the residual compressive stress increases, the difference in residual half-angle before and after withdrawal also

increases. Following eqn.3.13, the absolute value of the residual stress is inversely proportional to the $\tan^2\theta$, which is more pronounced at higher angles.
Bao *et al.* proposed a method for calculating the residual half-angle of the indent, based on the elastic parameters and energy-dissipation capacity of the indented material by analysing the residual indent trail [141]. They have introduced a parameter, λ, which is related to the indenter angle as expressed by;

$$\lambda = \frac{2}{\pi\varepsilon}\frac{\eta}{1-\eta}[\cot(\theta_0) - \cot(\theta)] \tag{3.14}$$

This parameter, λ, is also calculated from the ratio of nanoindentation hardness, H to the modulus, as expressed in previous section. The geometrically correct indent angle, θ_0, of the Berkovich indenter is taken as 70.3° in the present work. The other two parameters, ε and η are material constants and related to the slope m exponent of the unloading curve via,

$$\varepsilon = m\eta \tag{3.15}$$

Thus, the value of ε and η can be calculated from m, which is obtained by taking natural logarithm of the Kick's law of unloading curve [142];

$$\ln P = \ln\alpha + m\ln(h - h_f) \tag{3.16}$$

η is also a function of the exponent m and Woirgard and Dargenton proposed the expression as [143];

$$\eta = 1 - \frac{1}{\sqrt{\pi}}\frac{\Gamma[0.5(m-1)^{-1} + 0.5]}{\Gamma[0.5(m-1)^{-1} + 1]} \tag{3.17}$$

From eqn.3.17 and eqn.3.15, the value of η and ε and m can be obtained. These values are then used to calculate the value of α, which are shown in Tables 3.7 - 3.9 for pearlite, bainite and martensite abraded under rolling/sliding conditions. The difference between the geometrical indenter angle, which is taken as 70.3°, and the residual indent angle is also shown in the tables which denotes the extent

of change in residual stress. The calculation of residual stress and their variation with distances from the wear surfaces are discussed in the relevant chapters.

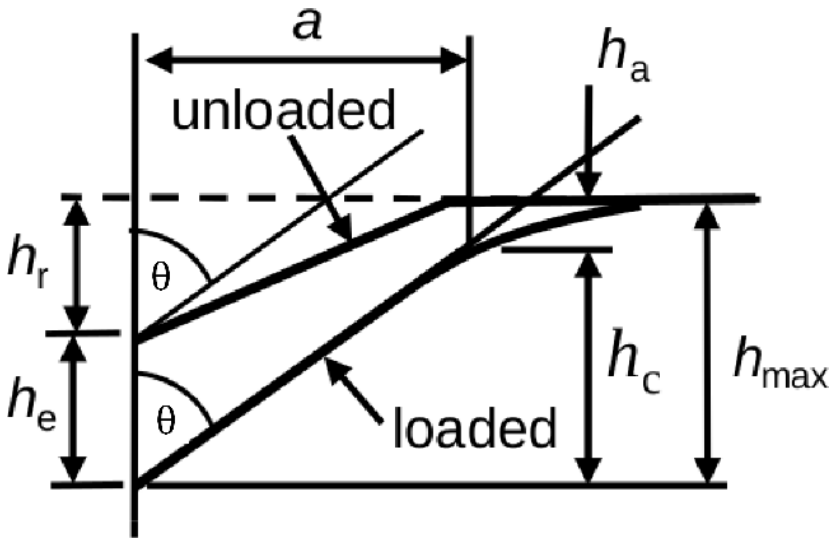

Figure 3.10: Schematic illustration of indentation during and after withdrawal of the load. Adapted from [2].

Table 3.7: Parameters used to determine the indent angle after removal of the load on pearlite.

Depth / µm	λ	m	η	ε	θ / °
98.83	0.053	1.210	0.653	0.790	71.06
82.32	0.054	1.214	0.649	0.789	71.08
66.25	0.051	1.428	0.529	0.756	71.07
49.49	0.056	1.214	0.649	0.788	71.11
38.51	0.051	1.238	0.632	0.783	71.05
24.72	0.036	1.386	0.548	0.760	70.85
14.84	0.042	1.278	0.610	0.776	70.93
8.83	0.046	1.291	0.599	0.773	70.99
4.90	0.044	1.233	0.636	0.784	70.95
3.66	0.035	1.546	0.483	0.746	70.73
2.40	0.028	1.427	0.530	0.756	70.83

Table 3.8: Parameters used to determine the indent angle after removal of the load on bainite.

Depth / µm	λ	m	η	ε	θ / °
51.62	0.046	1.513	0.699	0.806	70.93
45.21	0.053	1.098	0.755	0.829	70.95
40.35	0.049	1.075	0.784	0.844	70.86
35.30	0.050	1.071	0.791	0.847	70.86
30.91	0.052	1.080	0.779	0.841	70.90
25.08	0.040	1.084	0.773	0.838	70.77
21.64	0.042	1.141	0.710	0.811	70.87
14.79	0.051	1.071	0.792	0.848	70.87
12.07	0.047	1.056	0.812	0.858	70.79
6.65	0.037	1.123	0.737	0.822	70.77
4.60	0.040	1.011	0.921	0.930	70.52
1.88	0.056	1.055	0.815	0.860	70.88

Table 3.9: Parameters used to determine the indent angle after removal of the load on martensite.

Depth / µm	λ	m	η	ε	θ / °
107.41	0.041	1.080	0.778	0.841	70.77
91.37	0.054	1.055	0.814	0.859	70.97
77.41	0.048	1.071	0.790	0.847	70.83
62.61	0.047	1.069	0.794	0.849	70.82
50.91	0.049	1.086	0.771	0.837	70.88
37.84	0.057	1.098	0.756	0.830	71.00
27.34	0.056	1.089	0.767	0.836	70.97
19.36	0.064	1.090	0.765	0.834	71.07
9.54	0.067	1.045	0.833	0.870	70.95
4.71	0.053	1.773	0.413	0.734	71.06
2.25	0.047	1.063	0.802	0.853	70.80

3.6 X-ray diffraction

A Philip's PW1730 vertical X-ray diffractometer was used with the Bragg-Brentano geometry under step scanning mode over a range of 2θ = 38°-150° with a scan step of 0.03° and dwell time of 14 s per step. The radiation used was Cu K_α so much of the diffracted information comes from a depth of about 1 µm. The diffracted beam out of the surface was focused on a curved graphite monochromator through an anti-scatter slit of 0.2° and a receiving slit of 0.5°. Together with the quantitative phase analysis, crystallite sizes and lattice microstrains were also estimated.

3.6.1 Correction for instrumental broadening

Standard strain-free crystals of LaB_6 were diffracted in the same instrument over a 2θ range of 20-150° in order to measure the instrumental broadening using the Caglioti equation [144],

$$\beta_{\text{standard}} = \sqrt{u \tan^2 \theta + v \tan \theta + w} \tag{3.18}$$

The Caglioti parameters for LaB_6 spectra obtained after full-pattern refinement in XPert HighScore+ are $u = 0.004531$, $v = 0.000513$ and $w = 0.007907$ respectively, parameters used subsequently to calculate instrumental broadening [Fig 3.11]. The broadening ranged between 0.1°-0.2° over the 2θ range studied. Appropriate values of instrumental broadening ($\beta_{\text{broadening}}$) have been deduced and subsequently stripped off from the total broadening (β_{measured}). However, the individual peak widths were actually a complex addition of both Lorentzian and Gaussian components and therefore, peak widths were calculated twice assuming once a pure Lorentzian and then again assuming a pure Gaussian shape. This resulted in two values each for crystallite size and lattice microstrain, the actual value being somewhere in between these two.

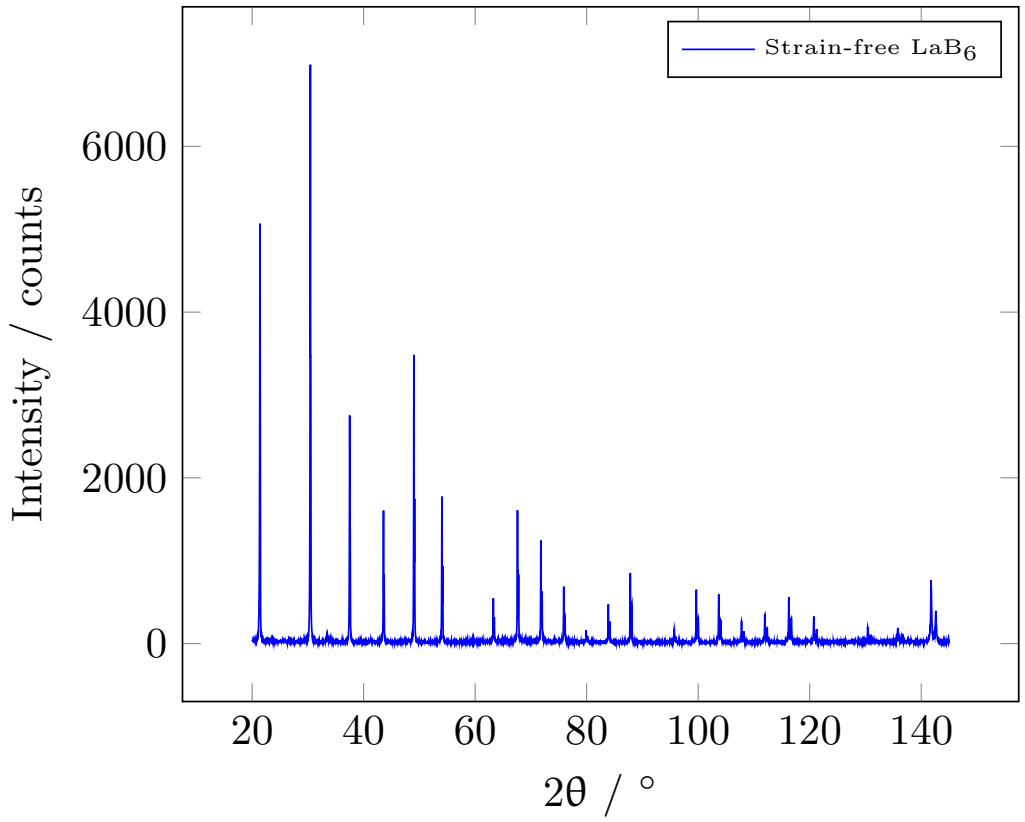

Figure 3.11: X-ray diffraction profile of strain free pure LaB_6 crystals used for the calculation of instrumental broadening of the diffractometer.

3.6.2 Quantitative phase analysis : full pattern Rietveld analysis

The objective of the Rietveld analysis is to minimise the residual function (WSS = weighted sum of squares) between the experimental (I_i^{exp}) and calculated (I_i^{calc}) values of X-ray intensity and is given by the equation;

$$WSS = \sum_i w_i (I_i^{exp} - I_i^{calc})^2, w_i = \frac{1}{I_i^{exp}} \tag{3.19}$$

where,

$$I_i^{calc} = S_F \sum_{j=1}^{Nphases} \frac{f_j}{V_j^2} \sum_{k=1}^{Npeaks} L_k |F_{k,j}|^2 S_j (2\theta_i - 2\theta_{k,j}) P_{k,j} A_j + bkg_i \tag{3.20}$$

Where, S_F is the beam intensity, f_j is the phase volume fraction, V_j is the phase cell volume, θ_i is the Bragg angle at which the intensity is calculated and $\theta_{k,j}$ is the number and position of the peak for a particular phase. The phase scale factor, S_j, is defined as,

$$S_j = S_F \frac{f_j}{V_j^2} \tag{3.21}$$

L_k is the Lorentz-polarisation factor, which depends onn geometry, monoschromator angle, detector, beam size/sample volume and angular sample positioning.

The scale factor S_j for individual phases is defined as;

$$S_j = S_F \frac{f_j}{V_j^2} \tag{3.22}$$

S_j is integrated over all the phases present in the material, and thus defined as the overall Rietveld generic scale factor.
The Lorentz polarisation factor, L_k depends upon the instrument geometry, detector, beam size/sample volume, angular positioning of the sample with respect to the beam and the detector.
The structure factor, $|F_{k,j}|^2$ depends upon the multiplicity (m_k) of the k_{th} reflection (with h, k, l Miller indices), the temperature factor B_n and is given by;

$$|F_{k,j}|^2 = m_k \left| \sum_{n=1}^{N} f_n e^{-B_n \frac{\sin^2 \theta}{\lambda^2}} \left(e^{2\pi i (hx_n + ky_n + lz_n)} \right) \right|^2 \tag{3.23}$$

where, N is the number of atoms, x_n, y_n, z_n are the coordinates of the nth atom, f_n is the atomic scattering factor and θ is the Bragg reflection angle.
The texture or the preferred orientation, $P_{k,j}$, is expressed as the Marsch-Dollase formula;

$$P_{k,j} = \frac{1}{m_k} \sum_{n=1}^{m_k} \left(P_{MD}^2 \cos^2 \alpha_n + \frac{\sin^2 \alpha_n}{P_{MD}} \right)^{-\frac{3}{2}} \tag{3.24}$$

where P_{MD} is the March-Dollase parameter, α_n is the angle between the preferred orientation vector and the crystallographic plane hkl and m_k is the equivalent hkl reflection.
The term $S_j(2\theta_i - 2\theta_{k,j})$ is the profile shape function and there exists quite a few models like, Gaussian, Cauchy, Voigt and Pseudo-Voigt(PV) and Pearson VII.
The absorption factor, A_j, for thicker samples is defined as:

$$A_j = \frac{1}{2\mu} \tag{3.25}$$

where, μ is the linear absorption coefficient of the sample.
The term bkg stands for background and is a function of θ given by ;

$$bkg_i = \sum_{n=0}^{N_b} a_n (2\theta_i)^n \tag{3.26}$$

where, N_b is the polynomial degree, a_n is the polynomial coefficient, and θ_i is the Bragg angle for which the intensity is calculated.

A good matching between I_i^{exp} and I_i^{calc} is obtained by a low goodness of fit (GOF) which is expressed as;

$$GOF = \frac{R_{wp}}{R_{exp}} \tag{3.27}$$

where,

$$R_{wp} = \sqrt{\frac{\sum_{i=1}^{N}\left[w_i\left(I_i^{exp} - I_i^{calc}\right)\right]^2}{\sum_{i=1}^{N}\left[w_i I_i^{exp}\right]^2}} \tag{3.28}$$

and,

$$R_{exp} = \sqrt{\frac{(N-P)}{\sum_{i=1}^{N}\left[w_i I_i^{exp}\right]^2}}. \tag{3.29}$$

Where, N is the number of points and P is the number of parameters. After the acquisition of the spectra, the Rietveld analysis was carried out in both X-Pert High Score+ and MAUD software. A series of iterations with refining several global parameters and lattice parameters were carried out to obtain a reasonably good match between ${I_i}^{exp}$ and ${I_i}^{calc}$ with a low GOF and R_{exp}.

3.6.3 Analysis of X-ray line broadening

X-ray diffraction profile, which is eventually a one-dimensional plot of the intensity, I, for a range of reflection angle, 2θ, provides quantitative information about the crystallographic features, like size, microscopic strain and plannar defects. In practice, the reflection angle, 2θ is converted to a variable K in reciprocal space, which is commonly known as the absolute diffraction vector, is expressed as [145]:

$$K = \frac{2\sin\theta}{\lambda}. \tag{3.30}$$

When the Bragg's diffraction condition is satisfied, K is denoted by K_B and is expressed as:

$$K_B = \frac{2\sin\theta_B}{\lambda}. \tag{3.31}$$

The difference between K and K_B, is an indicator of the change in the intensity profile and is expressed as

$$s = K - K_B \tag{3.32}$$
$$= \frac{2}{\lambda}[\sin\theta - \sin\theta_B] \tag{3.33}$$
$$= \frac{2}{\lambda}[2\sin\frac{1}{2}(\theta - \theta_B)\cos\frac{1}{2}(\theta + \theta_B)] \tag{3.34}$$

Therefore, the characteristic of the intensity function, $I(s)$, corresponding to the Bragg reflection, $2\theta_B$, is expressed as,

$$I_0 = \max\{I(s)\}|\forall s \in \mathbb{R} \tag{3.35}$$

Similarly, the full width at half maximum (FWHM) is mathematically expressed as,

$$FWHM\{I(s)\} = s_2 - s_1 \tag{3.36}$$

and,

$$I(s_1) = I(s_2) = \frac{I_0}{2} \tag{3.37}$$

Where, s_1 and s_2 are the Bragg angles at $I(s_2)$ and $I(s_1)$ respectively. Integrating the intensity function with change in diffraction vector and normalising against maximum intensity gives the value of integral breadth, β, which is mathematically expressed as,

$$\beta = \frac{\int_{-\infty}^{\infty} I(s)ds}{I_0} \tag{3.38}$$

The diffraction vector (K) and integral breadth (β) are subsequently used for analysis of size and strain broadening of X-ray peaks, as discussed in following section.

3.6.3.1 Williamson-Hall plot

After the necessary correction is made in the measured broadening of peaks, the average size of the crystallites or the coherent domains of diffraction (D) can be

calculated using the Debye-Scherrer's formula,

$$D = \frac{k\lambda}{\beta_{hkl}^{crystallite\ size}\cos\theta} \tag{3.39}$$

Where, k is the shape coefficient for the reciprocal lattice point, normally taken as 1.05 for iron and λ is the unfiltered wavelength of the Cu_{k_α} radiation assumed equal to 0.158054 nm.
If the microstrain induced in the crystallites due to imperfections like dislocations, voids, stacking faults are assumed to be uniform in all crystallographic directions, then the microstrain (ε) is expressed as,

$$\varepsilon = \frac{\beta_{hkl}^{crystallite\ strain}}{4\tan\theta} \tag{3.40}$$

Though the Scherrer equation is accurate enough to calculate the crystallite size, in case of abrasive wear, where high strain accumulates near surface, striping off peak broadening due to lattice microstrain, ε, along with instrumental broadening should result in more accurate calculation. If the measured peak broadening is expressed as, $\beta_{hkl}^{measured}$, then, for purely Lorentzian profile of the X-ray peak, it can be expressed as,

$$\beta_{hkl}^{measured} = \beta_{hkl}^{crystallite\ size} + \beta_{hkl}^{crystallite\ strain} \tag{3.41}$$

and, for purely Gaussian peaks,

$$(\beta_{hkl}^{measured})^2 = (\beta_{hkl}^{crystallite\ size})^2 + (\beta_{hkl}^{crystallite\ strain})^2 \tag{3.42}$$

After necessary correction of the instrumental broadening and substituting from eqn.3.39 and eqn.3.40 to eqn.3.41, the measured broadening can be re-written as,

$$\beta_{hkl}^{measured} = \frac{k\lambda}{D\cos\theta} + 4\varepsilon\tan\theta \tag{3.43}$$

Rearranging eqn.3.43 yields,

$$\beta_{hkl}\cos\theta = \frac{k\lambda}{D} + 4\varepsilon\sin\theta \tag{3.44}$$

These set of equations are commonly known as the Williamson-Hall equations, shortly W-H equations. For isotropic nature of the size of the coherent domain of diffraction and crystallite microstrain, a $\beta_{hkl}\cos\theta/\lambda$ against $4\sin\theta/\lambda$ plot should yield a straight line. The slope of the line gives an estimation of crystallite microstrain and the inverse of the y-intercept yields the coherent domain size [146].

3.6.3.2 Modified Williamson-Hall plot

Plotting of $\beta_{hkl}\cos\theta/\lambda$ against $4\sin\theta/\lambda$ for bcc-ferrite, fcc-austenite and bct-martensite after abrasion often showed non-monotonic change in FWHM or integral breadth against diffraction vector. As a result, the linear regression line bears a poor correlation with the experimental data, which would lead to an erroneous calculation of the coherent domain of diffraction (D) and lattice microstrain (ε). Such perturbation from the monotonic change in the FWHM or integral breadth of $\{hkl\}$ peaks with diffraction vector, K, indicates anisotropic behavior of specific $\{hkl\}$ towards strain which is detailed by Ungar and co-workers [145, 147–149]. This observation triggers examining the anisotropic nature of the elastic and plastic properties of the microstructure under study as the strain of deformation would induce more changes in some preferred crystallographic planes than others. The strain anisotropy observed with increasing diffraction vector could possibly be due to changes in the dislocation densities in the bcc-α phase. To test this hypothesis, a modified Williamson-Hall plot has been used. It has been derived after introducing changes in the classical Williamson-Hall plot, where the diffraction vector K ($=2\sin\theta/\lambda$) has been replaced by $K\sqrt{\bar{C}}$, where $\bar{C}$ is the average dislocation contrast factor for a specific hkl plane. The modified Williamson-Hall model used for calculation is expressed as [147–149],

$$\Delta K \cong \frac{k}{D} + \left(\frac{\pi M^2 b^2}{2}\right)^{\frac{1}{2}} \rho^{\frac{1}{2}} K \bar{C}_{hkl}^{\frac{1}{2}} + O(K^2 \bar{C}_{hkl}) \tag{3.45}$$

where, D is the size parameter, k equals to 0.9, ρ and b are the average dislocation density and the length of the Burgers vector of dislocations. M is a constant defined as the outer cut-off radius of dislocations and O stands for the higher order terms in $K^4\bar{C}^2$ [149]. The quadratic form of the above expression is given

by,

$$(\Delta K)^2 \cong \left(\frac{k}{D}\right)^2 + \left(\frac{\pi M^2 b^2}{2}\right)\rho K^2 \bar{C}_{hkl} + O(K^4 \bar{C}_{hkl}^2) \tag{3.46}$$

where,

$$\Delta K = \frac{2\beta \cos\theta}{\lambda} \tag{3.47}$$

$$K = \frac{2\sin\theta}{\lambda}. \tag{3.48}$$

In the quadratic form (eqn.3.46), the higher order terms of $K\bar{C}^{\frac{1}{2}}$ become negligible and eqn.3.46 can be modified as,

$$(\Delta K)^2 \cong \left(\frac{k}{D}\right)^2 + \left(\frac{\pi M^2 b^2}{2}\right)\rho K^2 \bar{C}_{hkl}. \tag{3.49}$$

Introducing $\alpha = (k/D)^2$ and $\beta = \pi M^2 b^2 \rho/2$, eqn.3.49 can be rewritten as,

$$[(\Delta K)^2 - \alpha]/K^2 \cong \beta \bar{C} \tag{3.50}$$

where,

$$\bar{C} = A + BH^2 \tag{3.51}$$

where, A and B are the constants depending on the elastic constants of the crystal [149]. Substituting eqn. 3.51 in eqn.3.50,

$$[(\Delta K)^2 - \alpha]/K^2 \cong \beta A + \beta B H^2. \tag{3.52}$$

The inverse of the intercept made by the linear regression line of the $[(\Delta K)^2 - \alpha]/K^2$ vs. H^2 plot, q, is an important parameter to assess the nature of change in dislocation type for a particular hkl plane [149–151].

In this dislocation model of strain anisotropy, the dislocation contrast factor for a specific set of $\{hkl\}$ planes for a crystal are calculated numerically from the elastic constants of elements for specific crystallographic axes as detailed in elasticity theory of solids [152].

3.6.3.3 Modified Warren-Averbach analysis

The dislocation density is calculated from the real part of the Fourier coefficients obtained from the modified Warren-Averbach expression [153],

$$\ln\ A(L) \cong \ln\ A^s(L) - \rho\frac{\pi b^2}{2}L^2\ \ln\Big(\frac{R_e}{L}\Big)(K^2\bar{C}) + O(K^4\bar{C}^2). \tag{3.53}$$

A(L) and $A^s(L)$ are the real part and the size of Fourier coefficients respectively, the exponent term, s, denotes the coherent domains of diffraction and L is the Fourier length. L is often expressed as,

$$L = na_3 \tag{3.54}$$

where, $a_3 = \lambda/[2(\sin\theta_2 - \sin\theta_1)]$, n assumes integral values starting from zero, $(\theta_2 - \theta_1)$ is the angular spread of the measured diffraction profile and R_e is the effective outer cut off radius of the dislocations [154]. Ungar and Tichy showed that for cubic crystals the average dislocation contrast factor, $\bar{C}$, linearly varies with the invariant of the fourth order polynomial of the Miller's indices [155]. For fcc and bcc lattices, the average contrast factor for a particular Bragg reflection *hkl*, $\bar{C}$ can be calculated from the contrast factor of $\{h00\}$, C_{h00} as explained in [148];

$$\bar{C} = C_{h00}(1 - qH^2) \tag{3.55}$$

Where, C_{h00} is constant corresponding to the elastic properties of the microstructure [148]. For fcc and bcc lattice, H can be expressed as,

$$H^2 = \frac{(h^2k^2 + k^2l^2 + l^2k^2)}{(h^2 + k^2 + l^2)^2} \tag{3.56}$$

and q, is the parameter corresponding to the type of dislocations and its numerical value changes with the change in fraction of edge and screw dislocations in the microstructure [148, 156]. The higher order quadratic term of eqn.3.53, $Q(K^4\bar{C}^2)$ can be neglected, and eqn.3.53 can be re-arranged as;

$$\frac{\ln A^s(L) - \ln A(L)}{L^2(K^2\bar{C})} = \rho\frac{\pi b^2}{2}\ln(R_e) - \rho\frac{\pi b^2}{2}\ln(L) \tag{3.57}$$

or,

$$\frac{Y}{L^2} = \rho\frac{\pi b^2}{2}\ln(R_e) - \rho\frac{\pi b^2}{2}\ln(L) \tag{3.58}$$

where, $Y = [\ln A^s(L) - \ln A(L)]/K^2\bar{C}$. The dislocation density, ρ, is calculated from the slope of the linear plot of Y/L^2 against $\ln(L)$.

Chapter 4

Three-body abrasive wear of pearlite, nanostructured bainite and martensite

4.1 Introduction

There have been a number of previous studies on the wear of carbide-free bainitic steels, some of which were reviewed by Bhadeshia [157], but the interest here is on the nanostructured form[1]. The dry sliding wear resistance of nanostructured bainite has been studied by Wang *et al.* [159]; who found that the austenite in the vicinity of the sliding surface decomposes under the influence of high shear strains developed, resulting in the formation of an even finer structure with grains of ferrite only a few nanometers in size. They concluded that the formation of this fine microstructure resulted in a slight increase in wear resistance. In another study, nanostructured carbide-free bainite was produced in a case-carburised layer, and it was demonstrated that the structure outperformed somewhat harder martensite [160]. The differences in behavior were small under low applied loads (where

[1]The term 'nanostructure' has unfortunately become a generic reference to a wide range of grain and precipitate structures, to the extent that it is often misleading and taken to represent structures far coarser than the adjective would imply [158]. We define it to represent cases where the interfacial area per unit volume, S_V, is large enough to make the governing length scale $\overline{L} = 2/S_V$ comparable to the narrower dimensions of carbon nanotubes, i.e., of the order 20-50 nm.

mild wear dominated with debris being predominantly in the form of oxide). However, under higher loads, the wear debris was shown to be primarily metallic in nature (with delamination flakes being $> 10\,\mu m$ in size); under these conditions, the bainitic structure (with its higher strain to fracture) was able to resist delamination more effectively than the martensitic structure, resulting in a higher wear resistance being exhibited. A similar conclusion was reached when comparing the bulk form of the nanostructured bainite, which again had a lower sliding wear-rate than harder martensite [161]. The dry rolling-sliding wear of series of steels said to contain carbide-free bainite has been reported recently [6] (a high slip of $\sim 5\%$ was used in the test programme); here, the carbide-free bainitic steels were shown to exhibit significantly lower rates of wear ($\sim 50\%$) than a steel with a lower bainitic microstructure, even at similar hardness levels and this was attributed to the desirable combination of hardness and toughness of the carbide-free bainitic microstructure. However, the metallography reported is not of sufficient resolution to establish the presence of a nanostructure, and the higher transformation temperatures used are consistent with coarser forms of bainite. In contrast, the alloy studied here has had many levels of detailed characterisation, as reviewed elsewhere [162].

The present work was motivated from observations of the severe wear of steel at the oil sands mines in Alberta, Canada, particularly in earth moving operations involving large transporters. In light of the benefits that have been observed in sliding wear performance of carbide-free bainitic steels, a study was initiated to examine first the capability of the new steel to resist dry abrasion. The nanostructured bainite contains only two phases, bainitic ferrite and retained austenite, generated by isothermal transformation at 200°C; it achieves the vast majority of its strength because of the closely packed interfaces between these phases [163, 164]. The structure is therefore unusual and it was felt that it would be useful to study also the pearlitic and untempered martensitic states in the same steel. For example, untempered high–carbon martensitic steels can achieve a maximum hardness of about 800 $\mathrm{kgf\,mm^{-2}}$ [165] but the dissolved carbon tends to make the martensite extremely brittle and the pearlitic state is interesting because the interlamellar spacing in this kind of steel can be made to be extremely fine at ordinary cooling rates [166, 167].

4.2 Experimental Procedures

14 × 25 × 60 mm samples were machined out of the steel shaft of chemical composition as listed in Table 4.1. The machined samples were then austenitised in an argon atmosphere tube furnace and subsequently heat treated to transform into fine pearlite, nanostructured bainite, air-cooled martensite, as listed in Table 4.2 and detailed in Chapter 3. The samples were then weighed to a precision of 0.0001 g and preserved in a desiccator. Small samples for metallography were cut from the heat treated samples and observed under optical and scanning electron microscopy. X-ray diffraction profiles were taken from the broad faces (25 × 60 mm) of the heat treated samples. The same surfaces were subjected to dry sand rubber wheel test as detailed earlier. The wear losses were compared and the same characterisation techniques were repeated on the worn surfaces to understand the mechanism of wear for different structures.

Table 4.1: Chemical composition of the experimental alloy (wt %).

C	Mn	P	S	Si	Al	Cu	Cr	Mo	V	Co	Sn	Nb
0.83	2.28	0.011	0.008	1.9	0.044	0.12	1.44	0.24	0.11	1.55	0.019	0.023

Table 4.2: Heat treatment and resultant hardness measured in Vickers scale.

Sample	Heat Treatment	Vickers hardness
Fine pearlite	930 °C 60 mins, air cooled to 550 °C, held for 4 h, air cooled	378 ± 9
Bainite	930 °C 60 mins, air cooled at 2°C s^{-1} to 200 °C, held for 10 days, air cooled	640 ± 13
Martensite	930 °C 60 mins, air cooled at 5°C s^{-1} to 27 °C	780 ± 7
Tempered bainite	Bainite tempered at 500 °C 1 h, water quenched	570 ± 12

4.3 Results

4.3.1 Metallography prior to abrasion

Fig. 4.1a shows the typical microstructure of pearlite. The mean true-spacing between the lamellae, $\overline{L}_0$, was measured by subjecting scanning electron micrographs to quantitative analysis [168] and was found to be 85 ± 7 nm. Recent work has shown that the presence of cobalt in the steel helps achieve such a fine inter-lamellar spacing by increasing the driving force for transformation from austenite to pearlite [167]. Nanostructured bainite of the type studied here has been char-

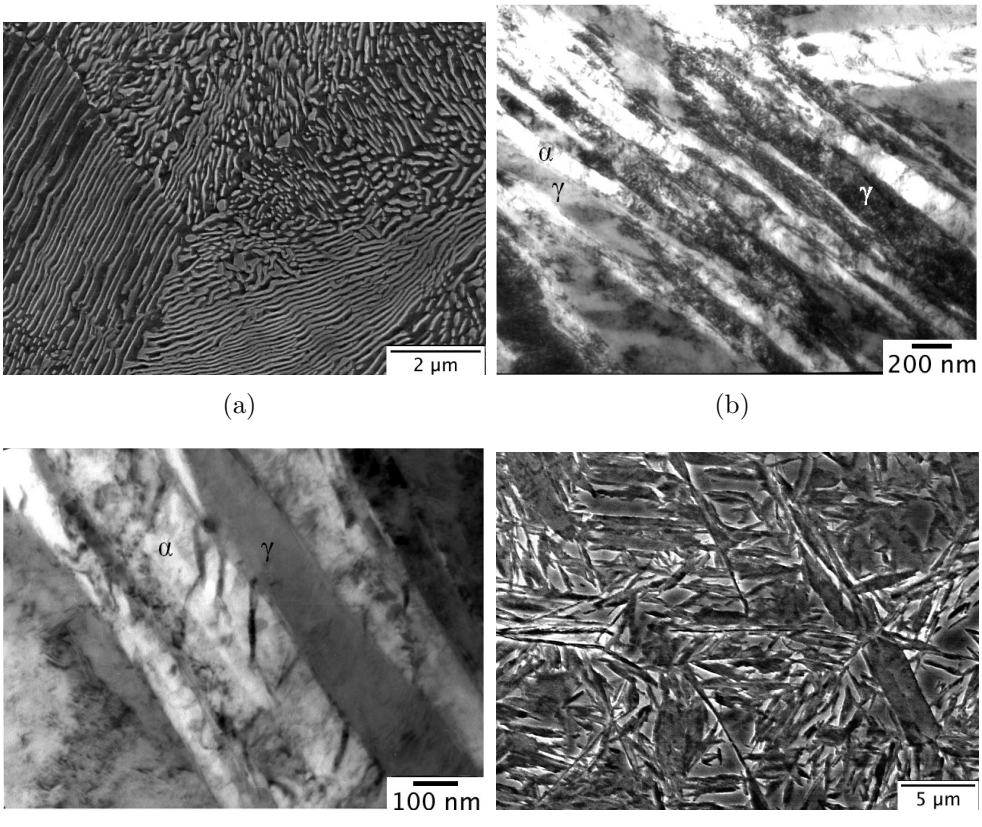

(a) (b)

(c) (d)

Figure 4.1: (a) Scanning electron micrograph of fine pearlite. (b) Mixture of bainitic ferrite and carbon-enriched retained austenite, (c) higher magnification image of bainite, and (d) martensite.

acterised thoroughly in previous work [162, 169], and many hundreds of images are available on archives [170]. Nevertheless, confirmatory transmission electron

microscopy gives confidence that the right structure has been obtained, as shown in Fig. 4.1b,c where there are just two phases, the fine bainitic ferrite plates and the intervening films of austenite. The mean lineal intercept ($\overline{L}$) measured in the direction normal to the trace of the habit plane of the ferrite plates was measured at fifty randomly selected locations from transmission micrographs, in order to estimate the true thickness (t) using the relation [171]:

$$t = 2\overline{L}/\pi \tag{4.1}$$

to be 54 ± 4 nm. In contrast, the martensite plates illustrated in Fig. 4.1d are rather coarse, with islands of untransformed austenite in between.

4.3.2 Abrasion test results and effect of hardness

The volume loss measurements following 16200 cycles of abrasion, corresponding to ≈ 11.62 km of sliding distance, are listed in Table 5.3, along with published data for comparison purposes. Although there are differences, the data show that the wear rate is not very sensitive to the structure of the steel studied, in spite of the substantial differences in hardness (Table 4.4). In fact the martensite, which is the hardest at $\approx 780\,\mathrm{kgf\,mm^{-2}}$, shows the largest wear rate whereas the soft pearlite ($\approx 380\,\mathrm{kgf\,mm^{-2}}$) fares better. In all cases, the specific wear rate observed in the present steel are significantly smaller than other published data listed in Table 5.3; the notable exception is the richly-alloyed tool steel which can resist abrasion through the presence of large alloy carbides in the microstructure [172].

The results are at first sight surprising given that hardness is the most discussed parameter when it comes to abrasive wear resistance. This outcome cannot be attributed to correlations between hardness and wear failing because the microstructure is coarser than the grit size [25], since the latter is much coarser at 300 μm than the length scales of any of the structures studied. However, it is necessary to distinguish between cases where the resistance is measured as a function of microstructure in the same steel, or for materials with similar microstructures but different compositions. In the latter case, a strong correlation is found between hardness and abrasive wear resistance as long as the size of the abrasive is much larger than the controlling scale of the microstructure [25]. For

example, the wear resistance and hardness increase as the fraction of pearlite in a mixture with ferrite, becomes larger [25]. It is difficult to make comparisons because experimental data are differently derived, but the variation in abrasive-wear rate seems greater when the pearlite fraction is changed by altering the carbon concentration of the steel [25,35,173], as opposed to when it is altered by changing the heat treatment for the same steel [174]. Nevertheless, the fact that in the present work, large variations in hardness do not lead to corresponding differences in wear rate is inconsistent with published three-body tests reported on 4340 steel where about a 40% improvement was achieved in three-body abrasive wear resistance for a hardness increase of 325 $\mathrm{kgf\,mm^{-2}}$ [175].

A further possibility is that it is the mechanical properties of the work-hardened layer after the initial shakedown stage of abrasion that matter [174, 176,177]. Nanoindentation hardness tests were then carried out in MTS nanoindenter using a Berkovich indenter and the results are shown in Fig. 4.2. The nanostructured bainite exhibits the greatest amount of surface hardening, to a maximum hardness of about 850 $\mathrm{kgf\,mm^{-2}}$ and a depth which is greater than the size of the SiC particles. The martensite, on the other hand, shows considerable surface softening with the hardness unchanged after about 20 μm of depth, a value much smaller than the size of the 300 μm grit. The pearlite similarly shows a surface softened layer. The results are consistent with the bainite showing marginally better wear resistance than the martensite which has a greater bulk hardness, but the performance of pearlite still cannot be explained. These results, in combination with metallography, will be discussed later.

4.3.3 Surface roughness

The topographic contrast of the abraded surfaces of the pearlite, bainite and martensite are shown in Fig. 4.3. The blue represents troughs and the red portions are crests. The martensitic sample has the smoothest topography, followed by

Table 4.3: Abrasive wear loss data of fine pearlite, nanostructured bainite and martensite.

Steel	Hardness ($kgf\ mm^{-2}$)	Specific wear rate ($mm^3\,N^{-1}\,m^{-1}/10^{-5}$)	Reference
Pearlite	378	8.7	
Bainite	622	8.1	
Martensite	739	9.4	
Hardox500	530	12.7	[178]
Stainless steel, type 304	164	91.1	[179]
Low-alloy steel, ASTM A514	286	71.8	[179]
Low-alloy steel, AISI 4340	560	39.6	[179]
Tool steel, type D2	640	7.8	[179]
Carbon steel, AISI 1060	795	17.2	[179]
Armco Iron	80	67.3	[180]
AISI 1006	117	82.7	[180]
AISI 1013	242	55.7	[180]
Hardox400	473	31.53	[180]
Ground flat stock, tool steel	830	36.5	[180]

Table 4.4: Hardness values (HV30) following specified heat treatments

Sample	Heat Treatment	HV30 / $kgf\ mm^{-2}$
Pearlite	930 °C 1h, cooled 0.1 °C s^{-1} to 550 °C, held for 4 h, air-cooled	378 ± 9
Bainite	930 °C 1h, air cooled to 200 °C, held for 10 days, air cooled	622 ± 13
Martensite	930 °C 1h, air cooled	780 ± 7

the pearlitic and bainitic samples. These results are consistent with the nanoindentation data [Fig. 4.2], where the bainite is seen to experience the deepest deformation. The data presented in Fig. 4.4 also show that the martensitic steel tends to develop wider and flatter grooves whereas those in the pearlitic and bainitic states tend to be narrow and deep.

4.3.4 Scanning electron microscopy

Scanning electron microscopy of the abraded surfaces qualitatively confirms the interferometry observations [Fig. 4.5]. The abraded pearlite exhibits both groove marks and a large number density of pits, similar to what has been reported else-

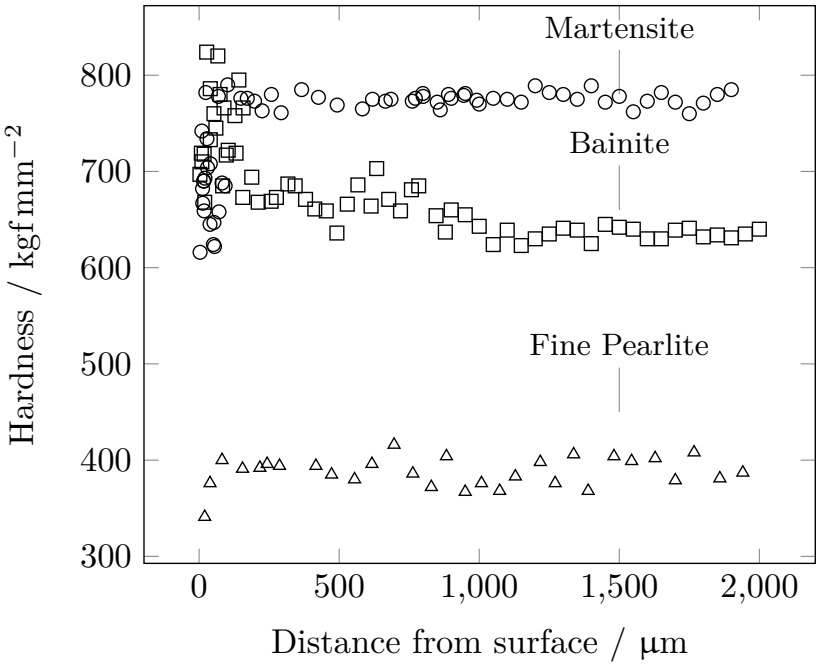

Figure 4.2: Nanoindentation hardnesses of microstructures along the depth away from the abraded surface after dry sand rubber wheel test.

where [177]. The grooves are of two kinds, wide ones delineated by ridges generated by plastic deformation, and much narrower grooves. The pits are indicative of the obstacles to the motion of abrasive particles, causing the termination of some grooves at the pits. In contrast, the nanostructured bainite and martensite samples show much smaller and fewer pits.

4.3.5 Sub-surface characterisation

White-etching layers were found on the surfaces of all three microstructures studied, in contradiction of work presented in [181] where dry sand abrasion tests at 130 N load failed to produce such layers. Fig. 4.6(a) shows a thick and adherent featureless, white-etching layer. The featureless character is believed to be due to its extremely fine and probably severely deformed structure; there have been many mechanisms proposed for such layers, for example localised austenitisation followed by martensitic transformation and deformation [37,63,177,182,183], but it is not the intention here to resolve these issues, but rather to highlight differ-

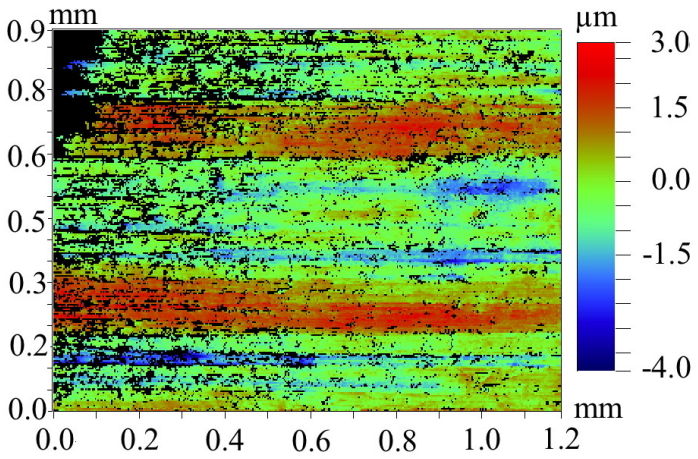

(a)

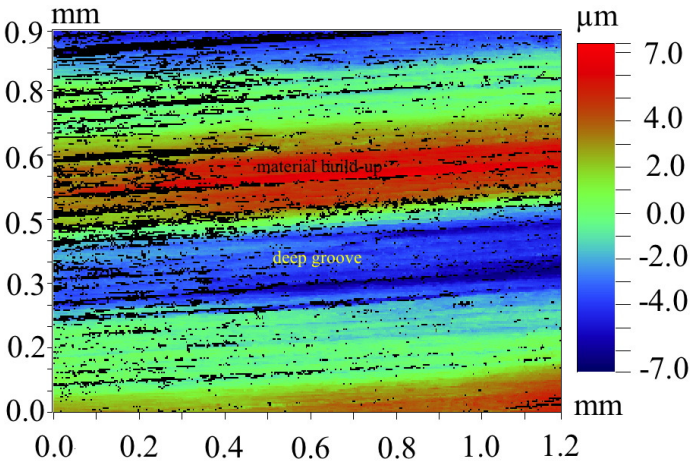

(b)

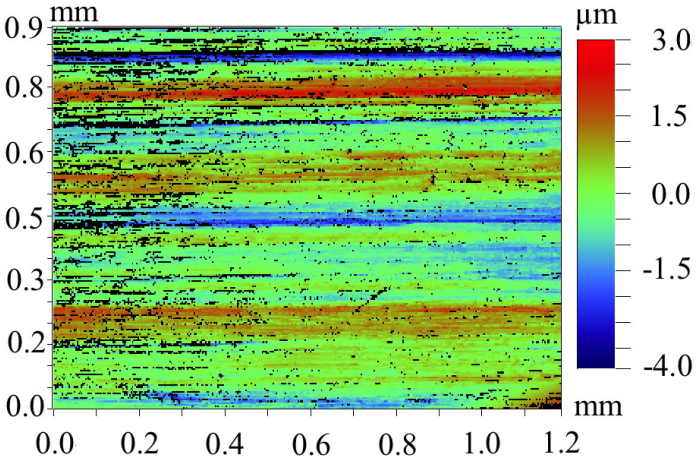

(c)

Figure 4.3: Interference micrographs of the abraded surfaces of (a) pearlite, (b) bainite and (c) martensite. Note that the colour scales are not all identical.

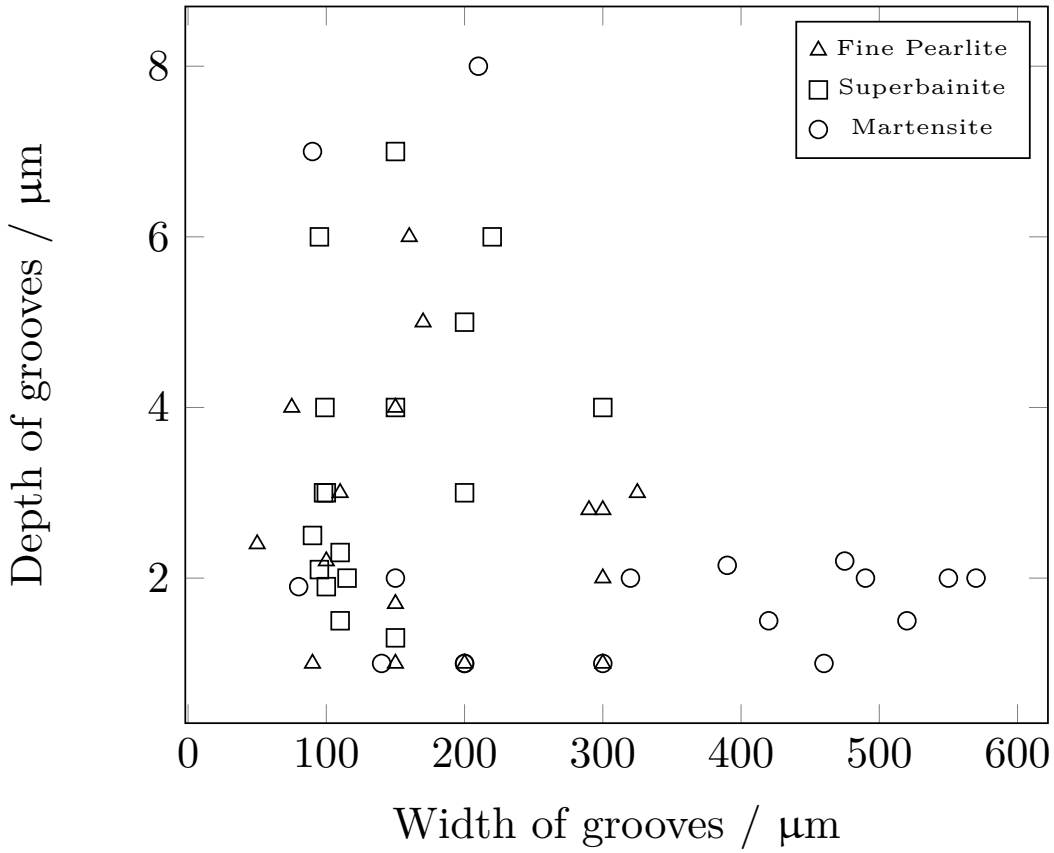

Figure 4.4: Groove characteristics for the three kinds of abraded samples.

ences between the three kinds of sample. But it is notable that the nanoindentation tests presented earlier show a degree of softening rather than hardening. Indeed, the cementite lamellae are clearly plastically deformed in the abrasion direction [Fig. 4.6(b)], as is commonly observed in the severe deformation of pearlitic wires. It is possible that the layer reaches temperatures high enough to cause softening but not sufficient to cause austenitisation. The relatively soft initial hardness of the pearlite, and the softening of the abraded region implies that the white layer is relatively ductile and hence the displaced material remains attached to the surface, accounting for the low wear loss in the pearlitic sample.

The white-etching layer on the nanostructured bainite is thinner than that in the pearlitic sample, Fig. 4.6(c), and much harder than the underlying unaffected structure [Fig. 4.2]. This could be attributed to the transformation of retained austenite into particularly hard martensite, since the former contains

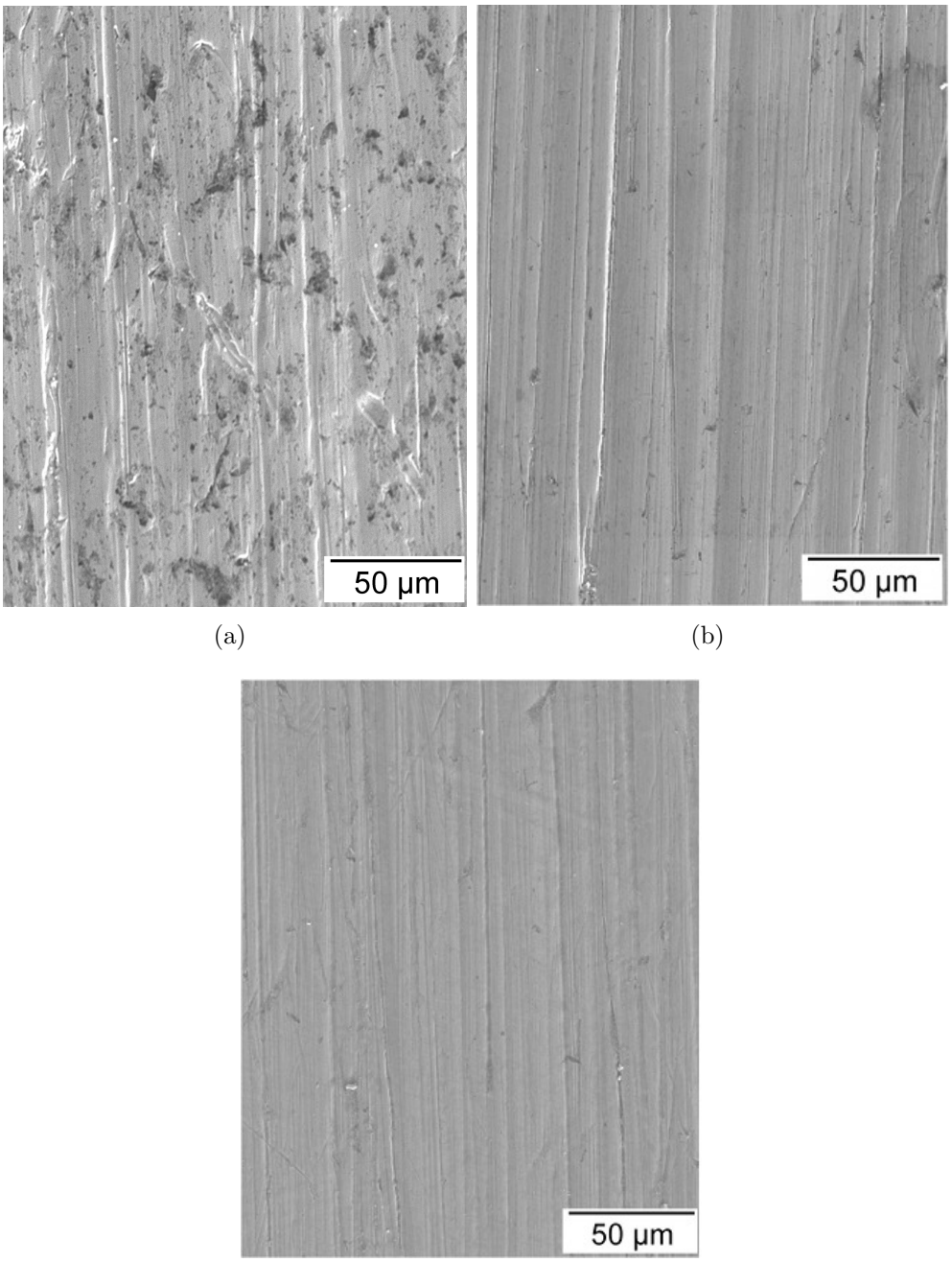

(a) (b)

(c)

Figure 4.5: Secondary electron micrographs of the abraded surface of (a) pearlitic, (b) bainitic and (c) martensitic samples.

carbon concentrations in excess of 1.2 wt%. However, a close examination of the white layer in Fig. 4.6(c) shows that it has undeformed plates indicating phase transformation after layer formation into martensite. This would imply that the region was reaustenitised by the intense deformation. The rapid austenitisation of the heavily deformed structure could be due to a high level of carbon in the ferrite which has a reduced austenitisation temperature and the presence of intervening thin films of austenite which act as potential nucleation sites [184]. Indeed, the hardness of the surface layer is consistent with that of the unaffected martensitic specimen [Fig. 4.2]. Note that the plates cannot be bainite since that transformation is very slow. As with pearlite, substantial regions of the layer remain adherent to the surface.

In contrast, Fig. 4.6(d) of the martensite shows extensive fragmentation and, hence, the remaining white etching layer is considerably thinner than in the other samples. The fragments are not adherent to each other or to the surface and can be easily removed by the impact of sand particles, which may account for the relatively higher specific wear rate for martensite. The nanoindentation data show a softening at the surface, presumably the martensite tempering under the influence of deformation heat. Samples with tempered martensitic structure that were abraded under similar conditions and sub-surface hardness measured after did not show any sign of softening.

4.3.6 FIB-TEM study of the worn surface

An effort has been made to characterise the white-etching layer (WEL) in detail by FIB-TEM. Adherent layers of pearlite and bainite make it possible to machine out the TEM sample from FIB, but martensite presents difficulties owing to the non-adherent and fragmented nature of the WEL.
An early observation of WEL made by Stead [185] and Trent [186] inferred extremely fine grained martensite produced by flash heating and cooling, though Bowden *et al.* [187] showed that the time duration of flash heating is of the order of milliseconds and thus kinetically insufficient for re-austenitisation and subsequent martensitic transformation. It has also been postulated with limited microstructural evidence that, heat of abrasion could be as high as 600-1000 °C [188] and the volume strain associated with martensitic transformation lead to subsurface

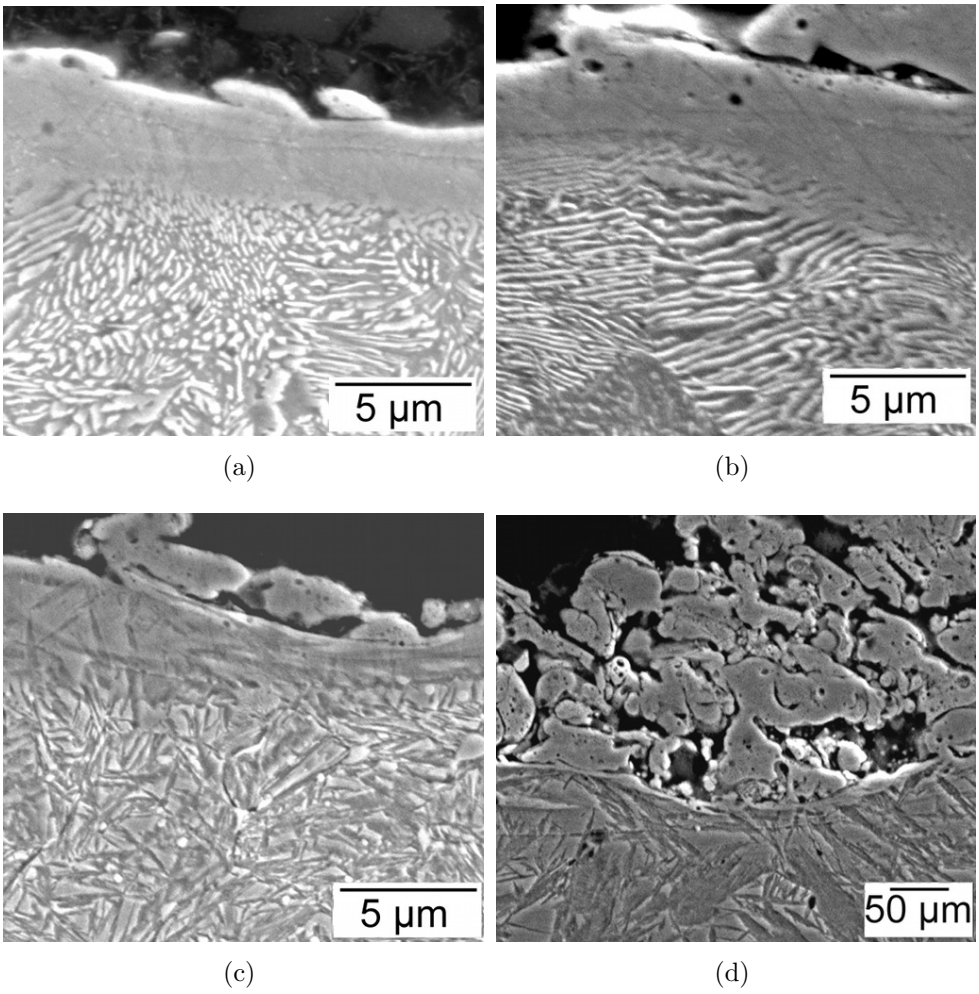

(a) (b)

(c) (d)

Figure 4.6: Sub-surface observations. (a) Pearlite: thick, continuous white etching layer. (b) Pearlite: severe deformation of the pearlite lamellae near white etching layer. (c) Bainite, showing a thin, continuous white-etching layer. (d) Martensite, showing a discontinuous layer with evidence of chip formation.

cracks which augment catastrophic removal of material from the surface [177]. In a different sliding and impact wear test, refinement of the microstructure near the deformation zone was reported by Rice *et al.* with no evidence of re-austenitisation [189], whereas, in a dry sliding wear test, Yang *et al.* reported severe plastic deformation of grains near the surface with no particular emphasis on the structure of WEL [161]. As the importance of the WEL in wear is widely accepted, it is necessary to understand the microstructure of WEL in detail to explain the observed changes of the surface and sub-surface layer during abrasive wear.

4.3.7 FIB-TEM of WEL in fine pearlite

Bright field TEM images of the grains near the abraded surface and selected area diffraction (SAD) patterns from various depths from the surface are shown in Fig. 4.8. A gradual change in the thickness of the deformed grains have been observed across the abrasion layer where the grains within 100 nm from the surface are highly elongated towards the direction of abrasion with an average thickness of 12 nm. The SAD pattern, Fig. 4.8(a), taken at 850 nm from the abrading surface shows a faint ring inside of {110} α-Fe, which indicates the presence of a second phase inside ferritic matrix. The lattice spacing of this ring, was measured to be 2.54 Å, which closely matches with the d_{hkl} of the {020} reflection of cementite. However, except this no reflections from any other diffracting planes were observed in the SAD pattern. Such weak and diffuse rings indicate an extremely fine sized, randomly oriented and low volume fraction of the second phase. A similar diffraction pattern, Fig. 4.8(b), was observed in the the medium sized grains at a depth of 500 nm from the surface indicating the presence of cementite along with nano-scaled ferrite. However the {020} ring of cementite was missing in the electron diffraction pattern observed within 100 nm from the surface, Fig. 4.8(c), indicating possible dissolution of carbide into the ferritic matrix. Hence, under the prevailing experimental conditions, even within the featureless WEL, carbides can still remain in the fragmented and dispersed condition though possible dissolution cannot be neglected. The ferrite grains are also heavily fragmented with extensive dislocation cell structures and numerous interfaces, which can augment faster diffusion of carbon atoms at an elevated temperature during abrasion.

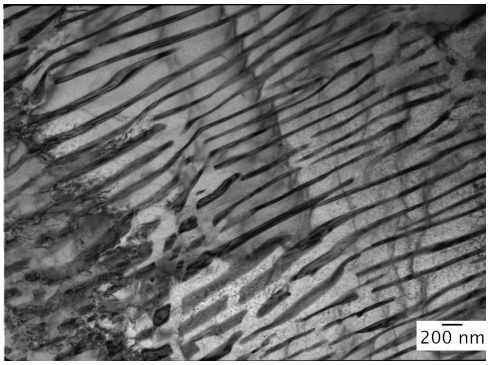

(a)

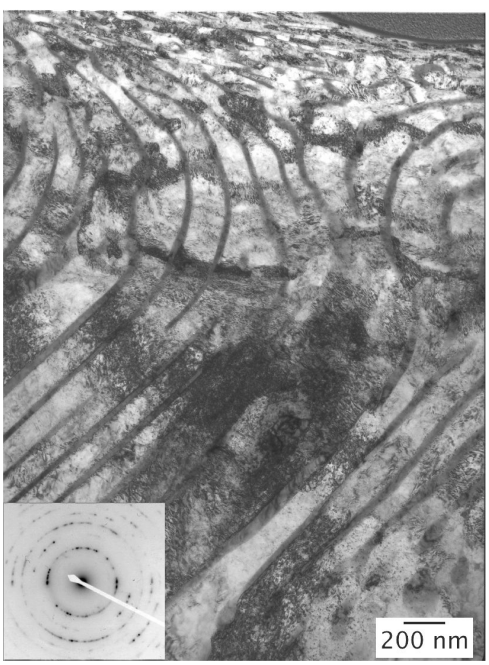

(b)

(c)

Figure 4.7: (a) Bright field TEM image of pearlite before abrasion,(b) pearlite after abrasion showing bending of cementite lamellae in the direction of abrasion, (c) formation of extremely fine grains of ferrite near the surface.

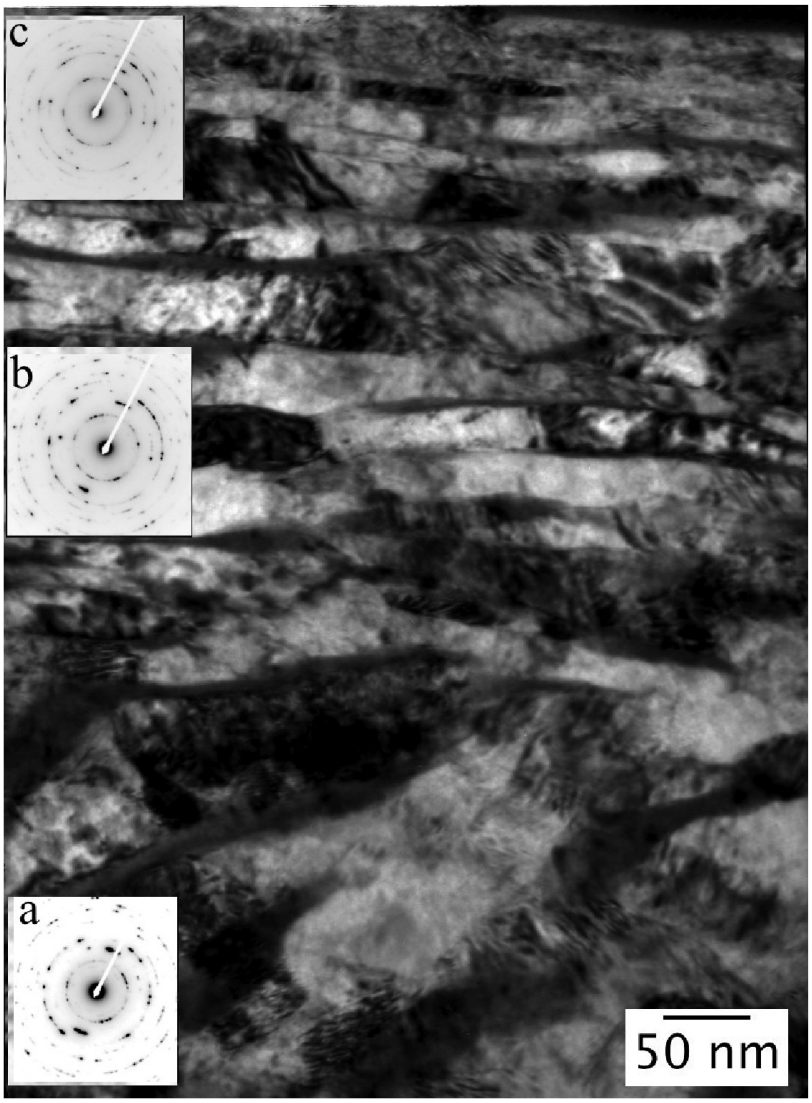

Figure 4.8: Bright field TEM image of deformed grains near surface along with SAD patterns taken from large (a), medium (b) and extremely fine sized (c) grains near the surface.

The aim of this work is to explore the deformation of pearlite near the surface and sub-surface region after three-body abrasion, cementite dissolution and phase transformation associated with the heat of abrasion, if any. No evidence of re-austenitisation followed by martensitic transformation in and around the abraded surface was observed. The deformed grains are strained orthogonally to the direction of abrasion comprising of numerous sub grains and dislocation cells. A significant amount of energy of abrasion is consumed in both creating heavily fragmented, strained grains with dislocation cells due to strain hardening of the pearlite and fracture of cementite lamellae near the surface.

4.3.8 FIB-TEM of WEL in nanostructured bainite

Fig. 4.9(a) shows the montage of TEM images taken across the WEL and material beneath and Fig. 4.9(b) is the electron diffraction pattern taken near the surface. The microstructure near the surface is coarser than the parent nanostructure and aligned in the direction of abrasion. There are plates of martensite observed upto 1-2 μm from the surface. Below this, there exists a mixed microstructure comprising of martensite and parent nanostructured bainite which is also strained in the direction of abrasion. A gradual transition from this plastically deformed structure to the undeformed parent microstructure is observed at a depth > 5 μm from the surface. No surface or subsurface cracks were detected in any of TEM images taken from the small volume of material examined [Fig. 4.9(a)]. During the first stage of abrasion, the bainite first deforms and gets strained in the direction of the movement of abrasive sand particles. As the abrasion progresses, the temperature of the surface layer increases due to frictional heating. It has been experimentally verified that during abrasion, the temperature of the contacting asperities could be raised to the austenitisation temperature very quickly ($\sim 10^{-3}$ - 10^{-4} s) and subsequently quenched very rapidly by the colder subsurface with the collapse of the asperity contact [190]. In the present scenario, a thin layer of the abrading surface could possibly reach the α/γ transition temperature locally and may initiate reaustenitisation, particularly because the nucleation of γ is unnecessary. Martensitic plates were only visible within the narrow region of WEL [Fig. 4.9(c)] and no more obtained in the material beneath [Fig. 4.9(d)]. The surface hardening [Fig. 4.2] of the sample observed after abrasion can be

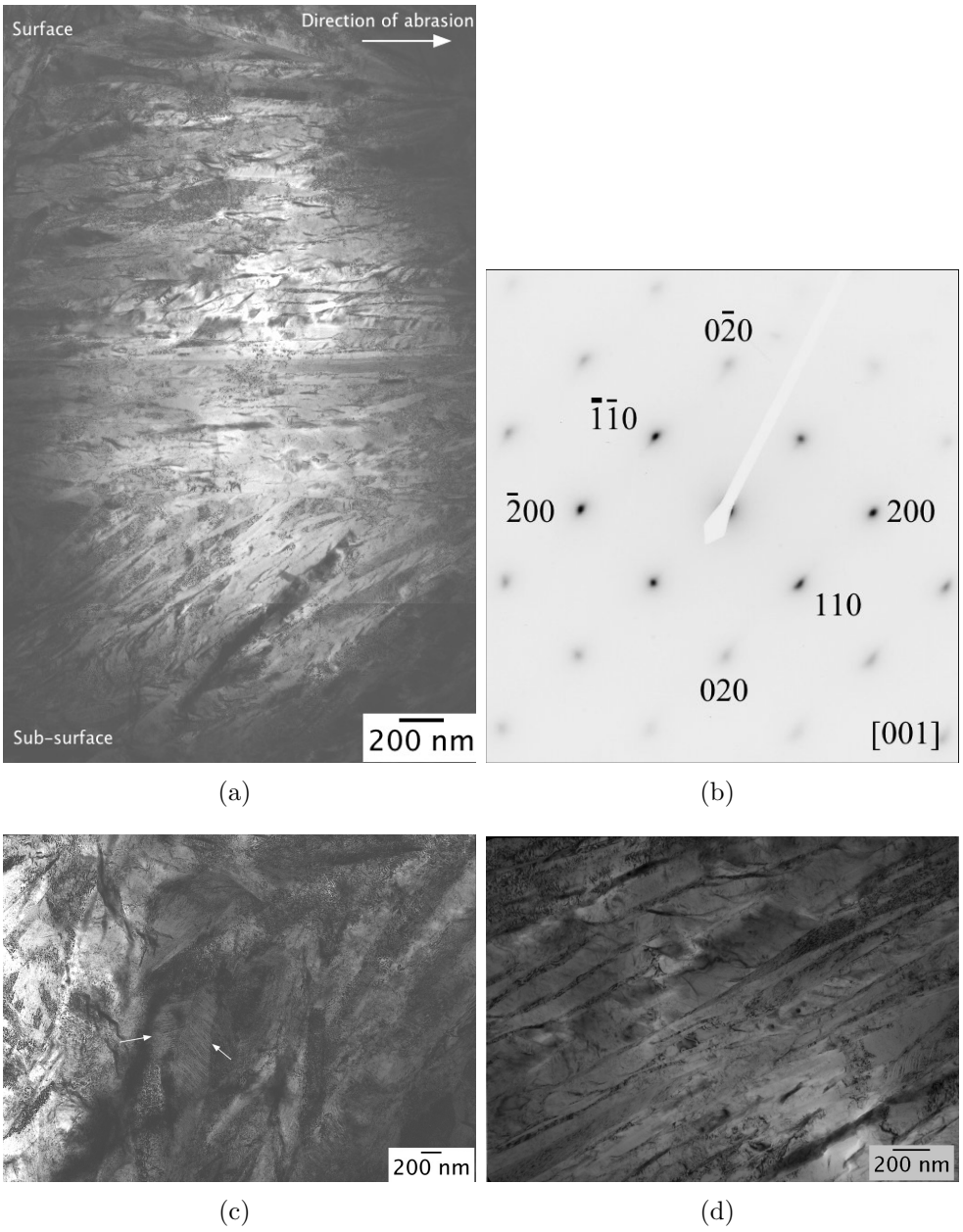

(a) (b)

(c) (d)

Figure 4.9: (a) Montage of TEM images showing deformation of bainitic ferrite near surface and sub-surface, (b) electron diffraction pattern taken near the surface reflecting $[001]_\alpha$ pattern, (c) coarse martensitic plates formed near surface bearing signature of reaustenitisation and (d) relatively undeformed structure at a depth of 300 μm from the surface.

attributed to martensite formation and its subsequent work hardening by friction.

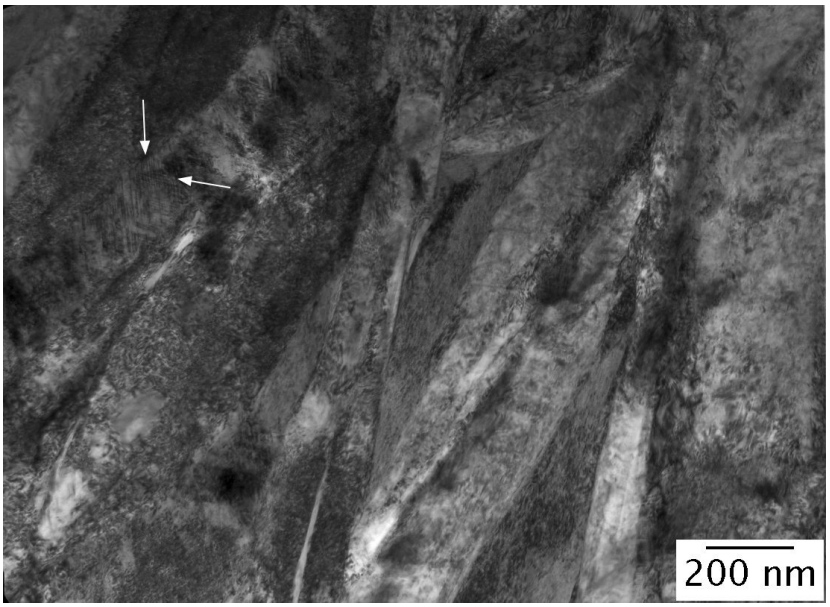

Figure 4.10: Bright field TEM image of martensite observed near abraded surface containing features that could be attributed to be deformation twins.

Analysis of the XRD data of the abraded sample using MAUD is shown in Table 4.5.The crystallite size of martensite is much greater than that of the remaining austenite. The microstrain associated with the martensite plates are also much higher than in austenite and ferrite, as expected from the nature of martensitic transformation.

4.3.9 FIB-TEM of WEL in martensite

Machining of TEM samples using FIB from the WEL of martensite is difficult as the layer is non-adherent, rough and discontinuous. Nevertheless, an attempt was made to prepare a sample from a smooth adherent area close to the wear surface, which could possibly bear some signature of wear. Fig. 4.11(a) shows the

Table 4.5: Crystallite size and microstrain measurement of the surface of nanostructured bainite after abrasion.

Phase	hkl	Crystallite size / nm)	Microstrain
Martensite	{110}	124	.008
	{200}	108	.005
	{002}	131	.016
Austenite	{111}	15	.001
	{200}	12	.002
	{220}	14	.001
Banitic Ferrite	{110}	37	.002
	{200}	24	.003
	{220}	37	.002

bright-field image of the undeformed martensite at a depth of 300 μm from the surface. The martensite near the wear surface contains a high density of defects and voids, as shown in Fig. 4.11(b). Numerous parallel shear marks inside the coarse plates of martensite are also visible at certain places [Fig. 4.11(c)].

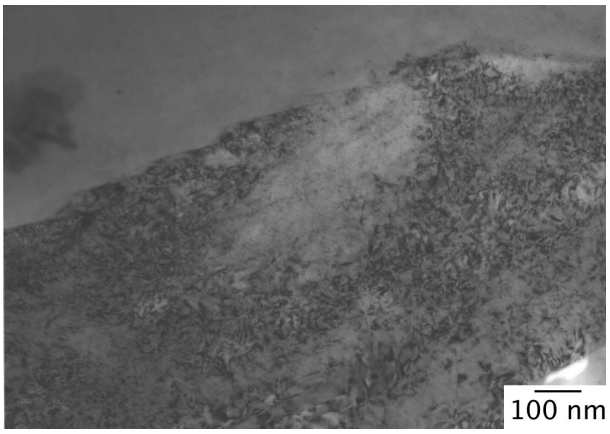

(a)

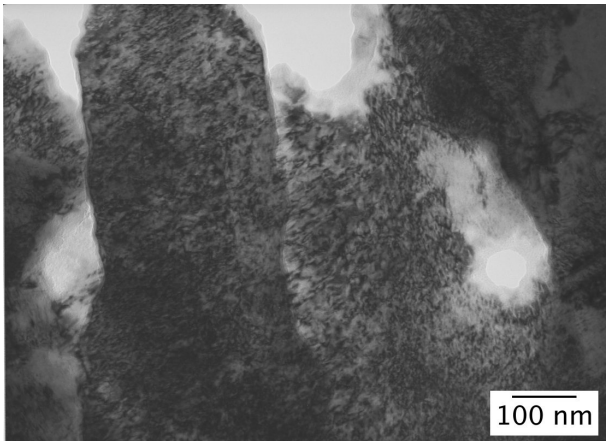

(b)

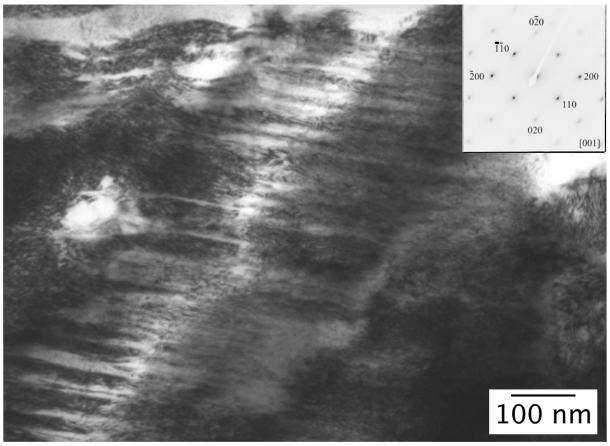

(c)

Figure 4.11: Bright filed TEM image of martensite taken at (a) 300 μm below the wear surface showing unabraded martensite, (b) near the wear surface and (c) marks indicating deformation twinning of martensite after abrasion.

4.3.10 X-ray diffraction

X-ray diffraction was carried out before and after abrasion to identify any transformation of austenite at the abraded surface; the data are illustrated in Fig. 4.12 and the results of quantitative full profile Rietveld analysis are listed in Table 4.6. There is no significant change in the austenite content of the martensitic specimen, presumably because the abrasion leads to a cutting action on the surface, leaving only a very thin layer of white-etching material on the surface. In contrast, there is a large decrease in the case of the bainite, which could be interpreted as follows. The bainite clearly undergoes severe deformation and if the interpretation of Fig. 4.6(c) is correct, then this deformation causes austenitisation followed by martensitic transformation. This would leave a smaller amount of retained austenite, and as Table 4.6 shows, the quantity left [12 ± 3 %] is not dissimilar to that expected from a directly quenched martensitic sample [17 ± 4 %].

Table 4.6: X-ray diffraction analysis by full pattern Rietveld refinement.

Microstructure	Austenite volume %
Martensite, before abrasion	17 ± 4
Martensite, after abrasion	16 ± 4
nanostructured bainite, before abrasion	27 ± 3
nanostructured bainite, after abrasion	12 ± 3

4.4 Conclusions

The somewhat unexpected outcome for the steel studied, is that there is not much of a variation in the abrasion data in spite of the large differences in hardness between the three structures (fine pearlite, nanostructured bainite, and untempered martensite) that have been studied. Within the small differences in the measured wear rate, the hardest phase martensite has the greater wear rate, whereas pearlite better resists abrasion. A clear transition is observed from the

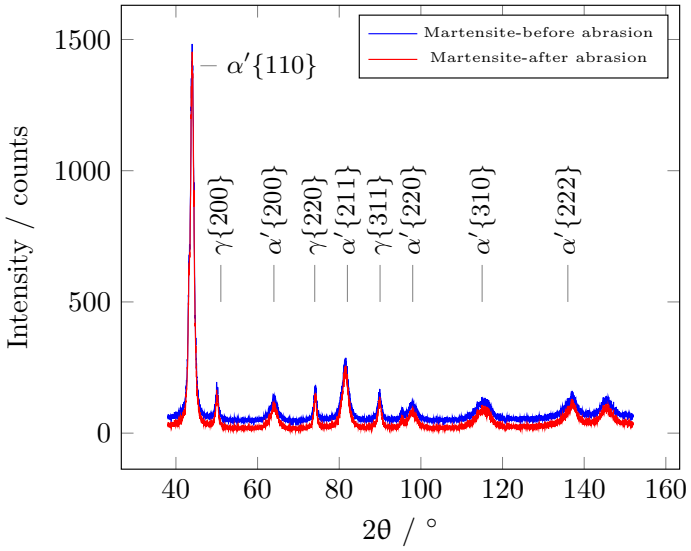

(a)

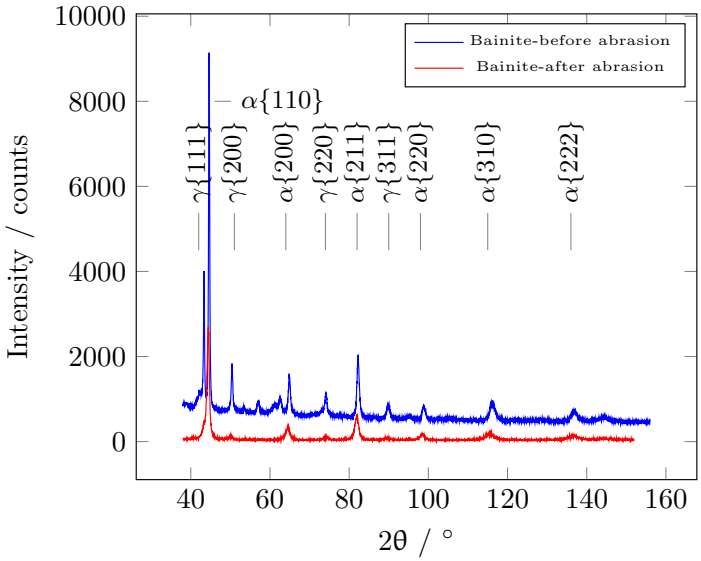

(b)

Figure 4.12: X-ray diffraction spectra before and after abrasion. (a) Martensite. (b) Bainite.

sliding of particles in the harder samples, to stopping and pitting in the case of the pearlite, as has been observed in previous studies [175, 180, 191–193]. Nanostructured bainite has the largest resistance to abrasion and is the only structure found to harden at the surface, possibly because of austenitisation of the surface layer during the course of abrasion. The bainite wears by a combination of grooving and relatively minor pitting, whereas in the case of the hard martensite it is the cutting that dominates. Furthermore, martensite suffers from greater fragmentation at the surface, and hence exhibits the largest weight loss. This presumably is a reflection of the brittle nature of high-carbon martensite, and the clean removal of material from the surface is consistent with the fact that the austenite content at that location does not change. The bainite shows the most interesting behavior, with minimal pitting, a large change in retained austenite content and the minimum wear rate under the experimental conditions reported here.

The following conclusions may be reached from these studies:

1. Experiments have been conducted in which a novel steel designed for the large scale production of nanostructure, has been transformed instead into fine pearlite, nanostructured bainite, and coarse untempered martensite. These three conditions differ greatly in hardness, but lead only to small changes in the three-body abrasive wear tests conducted using silica. In all cases, the abrasive wear resistance is superior to many steels available commercially or reported in research publications.

2. The insensitivity of the wear resistance to structure is because different mechanisms of surface damage operate in each case. In the case of pearlite, the abrasive particles slide and are sometimes halted in their progress, leading to extensive pitting. Fragmentation of the surface is the mechanism for the untempered martensite, with very little affected material adhering to the steel surface. Like pearlite, there is significant plastic deformation at the active surface of bainite, with good adhesion of the damaged material.

3. Nanoindentation tests show that only the bainitic structure is hardened at the surface, and there are indications that reaustenitisation occurs, with subsequent martensitic transformation which causes hardness levels to in-

crease. Both the pearlitic and martensitic samples show significant softening in the abraded surface regions.

Chapter 5

Three-body abrasive wear of tempered bainite

5.1 Introduction

The nanostructured bainite described in Chapter 4 showed interesting characteristics during three body abrasive wear tests. Some of these characteristics were attributed to the presence of mechanically stable thin-films of retained austenite. The bainite was the only structure to exhibit surface hardening, as a consequence of austenitisation of the wear surface. The austenitisation was assumed to be helped by the presence of high carbon retained austenite in the initial structure. Experiments were therefore initiated on samples tempered to eliminate the austenite, without causing a significant change in hardness [from 640 to 570 $\mathrm{kgf\,mm^{-2}}$] [194]. The resultant structure would therefore be comprised of bainitic ferrite and carbides.

Earlier studies indicate an uncertain role of retained austenite in reducing abrasive wear [195]. The austenite is beneficial if the transformation-induced plasticity occurs at an appropriate stage during abrasion. However, at high strain rates, the resulting martensite could crack and thereby enhance wear [196].

5.2 Experimental Procedures

The tempering heat treatment was carried out to decompose the thin film austenite into ferrite and carbide with out compromising much with the bulk hardness. The purposes for this heat treatment was primarily to examine the effect of the absence of retained austenite in wear resistance and whether the precipitated carbide offers any additional resistance to the motion of hard abrasives. Same alloy, as listed in Table 5.1, was taken for heat treatment and the resultant hardness after heat treatment is listed in Table 5.2. Similar set of experiments and characterisation, as discussed in Chapter 3 and Chapter 4, were conducted and the findings are discussed in the following sections.

Table 5.1: Chemical composition of the experimental alloy (wt %).

C	Mn	P	S	Si	Al	Cu	Cr	Mo	V	Co	Sn	Nb
0.83	2.28	0.011	0.008	1.9	0.044	0.12	1.44	0.24	0.11	1.55	0.019	0.023

Table 5.2: Heat treatment and resultant hardness measured in Vickers scale.

Microstructure	Heat Treatment	Hardness / kgf-mm^{-2}
Tempered bainite	Bainite tempered at 500 °C 1 h, water quenched	570 ± 12

5.3 Results

5.3.1 Metallography

The parent structure before tempering consists of fine and homogeneous dispersion of plates of bainitic ferrite of average thickness $\sim$ 45-54 nm along with thin films of austenite with both phases rich in dislocations [Fig. 5.1(a)]. Earlier studies [194] showed that tempering upto 400°C for one hour, does not lead to

significant changes in structure or properties. An increase in the tempering temperature to 450°C induces the decomposition of austenite and subsequent precipitation of alloy carbides, though the plate morphology of bainitic ferrite remains more or less unaltered. The interphase precipitation of carbides causes the hardness to increase marginally [194]. Further increase in the tempering temperature to 500°C and holding for one hour leads to the complete decomposition of austenite [Fig. 5.1(b)], also confirmed by using X-ray diffraction [Fig. 5.5]. However, a small increase occurs in the thickness of the plates of bainitic ferrite [Fig. 5.1(c)]. Further increase in tempering temperature to 600°C and holding there for one hour, leads to the ripening of precipitates along with coarsening of bainitic ferrite plates, which leads to the drop in hardness below $500\,\mathrm{kgf\,mm^{-2}}$ [194].

The surface after abrasion consist of numerous grooves with very few pits, as observed in case of martensites, indicative of cutting by the abrasives rather than pitting or ploughing [Fig. 5.2(a)]. There exists a featureless white-etching layer on the surface [Fig. 5.2(b)], with a deformed sub-surface structure. The white-etching layer is discontinuous and non-adherent at places indicating a loss of deformed materials from the surface [Fig. 5.2(c)] and is thicker than similar layers on nanostructured bainite, Fig. 5.2(d). The bending of bainitic ferrite plates below the surface in the direction of abrasion indicates greater damage of the structure compared to that of untempered sample.
The cross-sectional micrographs [Fig. 5.2(b,c)] when studied in conjunction with the surface roughness profile [Fig. 5.3] after abrasion indicates wide and deep grooves signifying a large amount of material loss from the surface. The fine precipitates of carbides generated by tempering are probably too small compared to the abrasives and get easily gouged by the impact of abrasion [197].

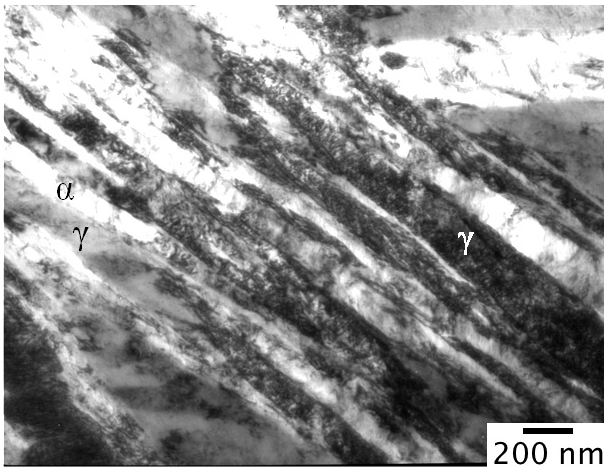

(a)

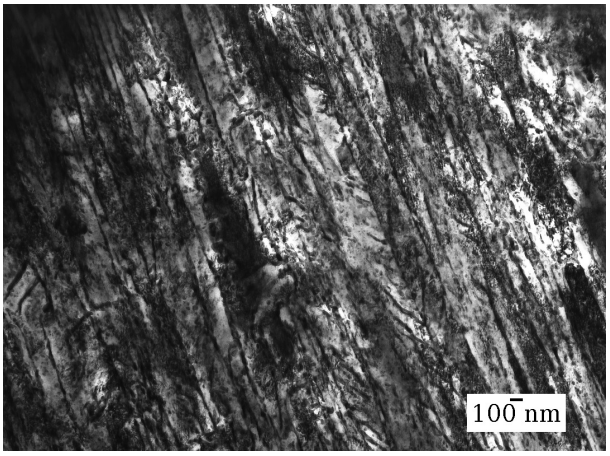

(b)

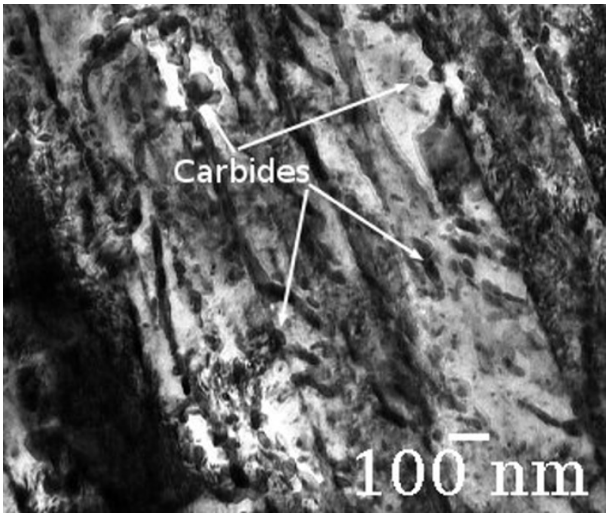

(c)

Figure 5.1: Bright field TEM image of (a) untempered nanostructured bainite, (b) after tempering at 500°C for 1 h, (c) distribution of fine carbides.

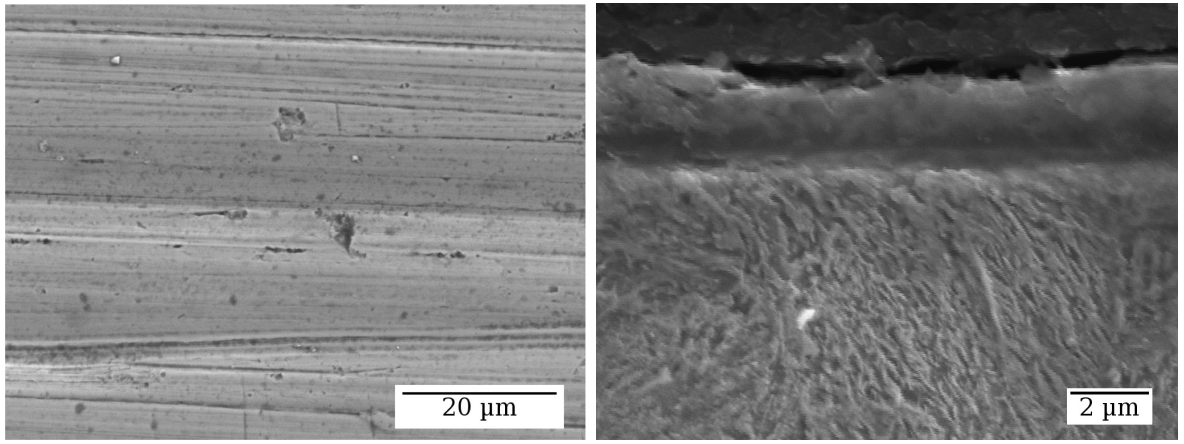

(a) (b)

(c) (d)

Figure 5.2: Secondary electron image of (a) the surface of tempered bainite after abrasion, (b) cross section of the abraded surface in the direction of sand particle flow with adherent white-etching layer, (c) with discontinuous white-etching layer at places, (d) cross section of abraded nanostructured bainite showing adherent white-etching layer.

5.3.2 Wear test data

The wear rate, normalised against the load and linear distance covered by the abrasive wheel, is presented in Table 5.3, together with other experimental microstructures of comparable hardnesses [Chapter 4]. A 50% increase in the specific wear rate was recorded compared to that of the nanostructured bainite. The observed wear rate was comparable to Hardox-500, a tempered martensitic structure, tested under similar condition. The high wear rate could be attributed to the loss of austenite as the structure significantly looses its ability to work-harden and therefore could not resist indentation by abrasives.

Table 5.3: Abrasive wear loss data of tempered bainite compared against other structures and Hardox 500.

Steel	Hardness ($kgf\,mm^{-2}$)	Specific wear rate ($mm^3\,N^{-1}\,m^{-1}/10^{-5}$)	Reference
Tempered Bainite	575±7	12.3	
Pearlite	378±13	8.7	
Bainite	622±9	8.1	
Martensite	780±11	9.4	
Hardox500	530±8	12.7	[178]

5.3.3 Surface roughness

The line profile of roughness of the surface before and after abrasion is shown in Fig. 5.3(a-b). The surface of tempered bainite is much rougher compared to that of untempered nanostructured bainite abraded under similar conditions [Chapter 4]. The troughs made by the moving abrasives are much wider and deeper compared that of the untempered structure. The greater penetration by abrasive particles is probably due to the loss in ductility or toughness of the tempered nanostructure.

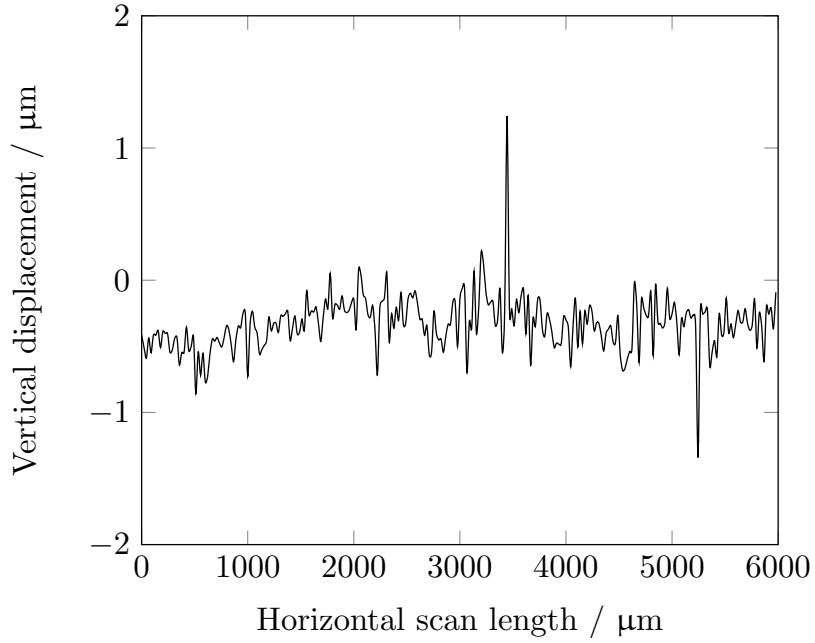

(a)

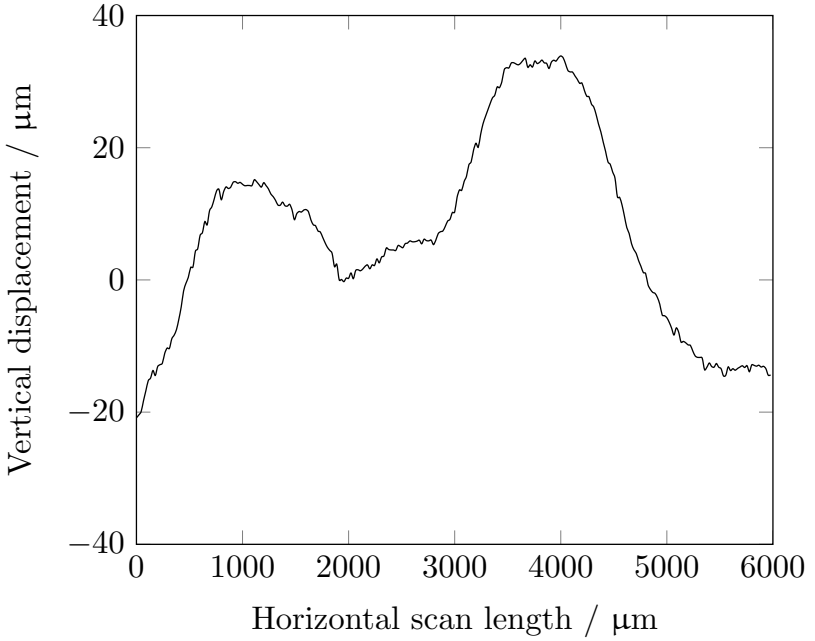

(b)

Figure 5.3: Line scan profile of the surface of the sample (a) before abrasion, (b) after abrasion.

5.3.4 Nanoindentation results

The hardness of the deformed sub-surface and the residual stress developed are shown in Fig 5.4(a) and (b) respectively. Though an increase in the hardening of $\approx$ 1.0 GPa has been measured near the surface compared to the bulk, the hardness falls off rapidly within 20 μm from the surface [Fig. 5.4(a)]. The maximum hardness at the surface is about 1 GPa less than that observed with untempered structure, which had a reaustenitised surface that transforms into untempered martensite. Moreover, the thickness of the work-hardened layer is smaller than that observed in case of nanostructured bainite.

Residual stress [Fig. 5.4(b)] is also significantly lower than the untempered bainite tested under rolling/sliding condition [Chapter 7]. Though the condition of stresses can not be compared, but the order of magnitude indicates the role of retained austenite in abrasive wear. The large fraction of residual stress arises from the compressive stress generated from transformation induced martensite during abrasion.

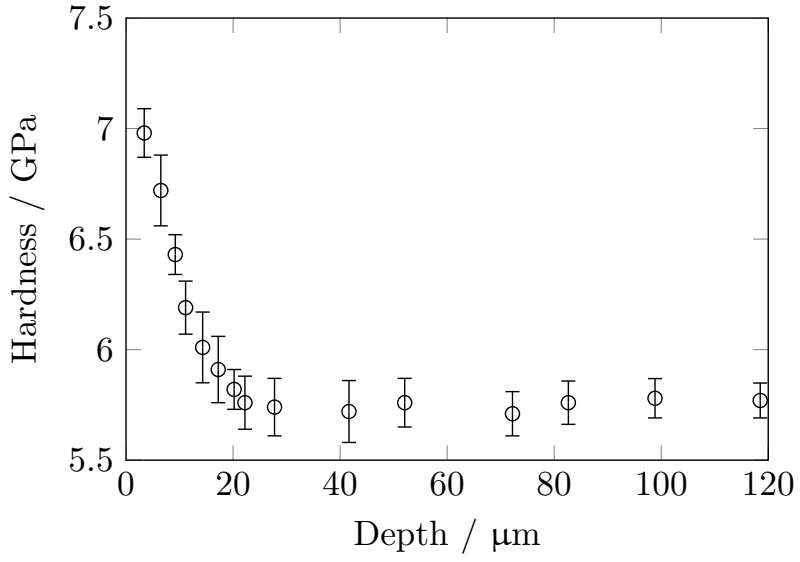

(a)

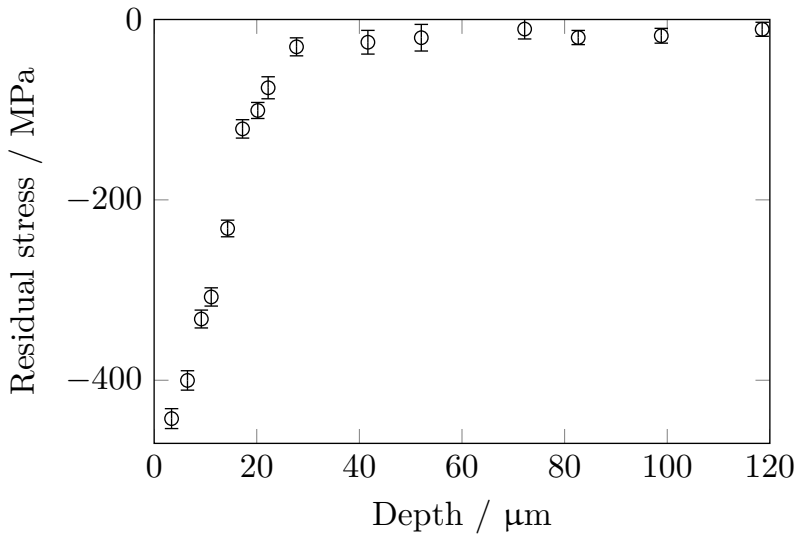

(b)

Figure 5.4: Nanoindentation results showing (a) marginal increase in nanoindentation hardness and (b) residual stress developed near surface and subsurface region of tempered bainite after abrasion.

5.3.5 X-ray diffraction

The comparison of the X-ray diffraction profiles taken before and after abrasion is shown in Fig. 5.5. Tempering at 500°C for one hour was sufficient to eliminate the austenite. Therefore any plastic deformation caused by abrasion and subsequent change in the crystallographic features of the structure, like size of the coherent domains of diffraction, type and density of dislocations, can be estimated from the change in the characteristics of the bcc-ferrite peaks after abrasion. Plotting of ΔK against diffraction vector (K) for bcc-ferrite according to the conventional W-H plot reveals an increased degree of strain anisotropy after abrasion [Fig. 5.6(a-d)], which necessitates further modification according to the modified W-H analysis by invoking average dislocation contrast factor, $\bar{C}$ for specific hkl planes [148, 156]. The details of the calculation can be found in the literature [148, 151, 156]. The diffraction vector K is therefore replaced by $K\sqrt{\bar{C}}$ and the anisotropic broadening were analysed for {110}, {002}, {112}, {013} and {222} peaks of bainitic ferrite according to the modified Williamson-Hall approach.

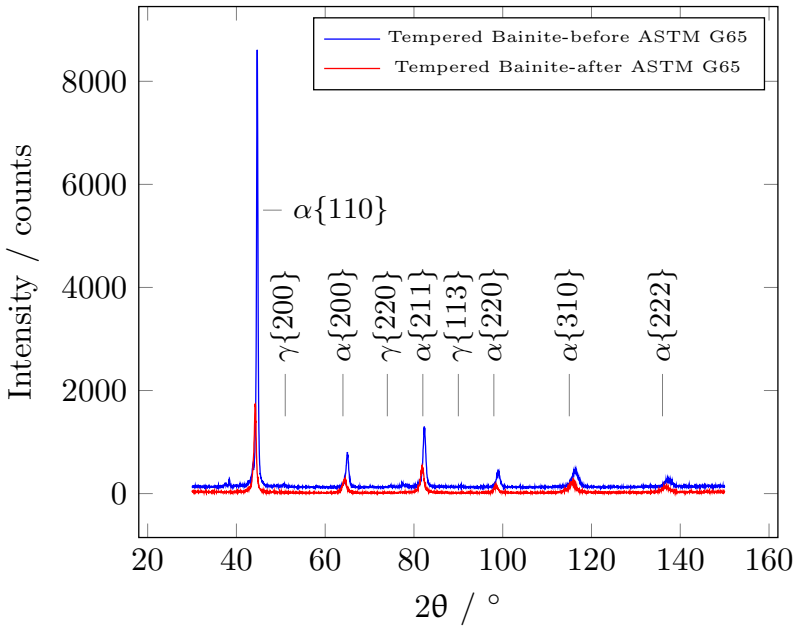

Figure 5.5: X-ray diffraction line profiles of tempered bainite (500°C-60m) before abrasion and after abrasion.

The value of q, which is calculated from the inverse of the x-intercept of the

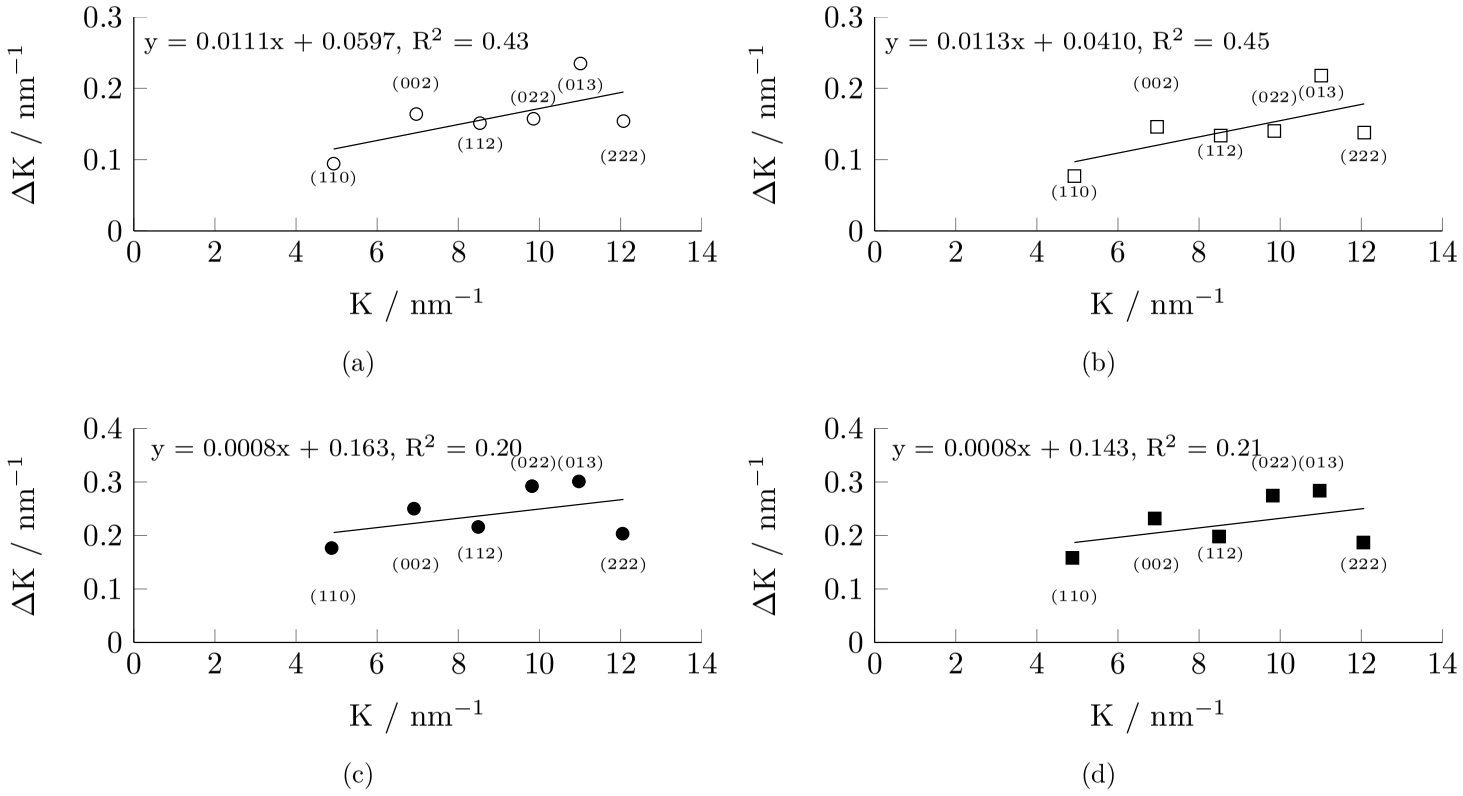

Figure 5.6: Conventional Williamson-Hall plot of 500°C-60m tempered bcc-α ferrite (a) before abrasion assuming Gaussian peak broadening, (b) before abrasion assuming Lorentzian peak broadening, (c) after abrasion assuming Gaussian peak broadening and (d) after abrasion assuming Lorentzian peak broadening.

$[(\Delta K)^2 - \alpha]/H^2$ vs. H^2 plot, was found to change marginally from 1.78 to 1.93. In the absence of the elastic constants for bainitic ferrite, the same for bcc-α iron has been considered for calculation which is equal to, c_{11} = 230.1 GPa, c_{12} = 134.6 GPa and c_{44} = 116.6 GPa. Assuming these, the $\bar{C}_{200}^{edge}$ for ferrite calculates out to be equal to 0.2648 and that of $\bar{C}_{200}^{screw}$ is found to be equal to 0.3055. Subsequently, the other values of $\bar{C}_{hkl}$ for pure edge and pure screw dislocations have been calculated and listed in Table 5.4 for $q = 1.78$ and 1.93 respectively.

Table 5.4: Average dislocation contrast factor of pure edge and pure screw dislocations for *hkl* planes in bcc-α Fe before rolling/sliding.

	$q = 1.78$		$q = 1.93$	
{hkl}	$\bar{C}_{hkl}^{edge}$	$\bar{C}_{hkl}^{screw}$	$\bar{C}_{hkl}^{edge}$	$\bar{C}_{hkl}^{screw}$
{110}	0.1476	0.1703	0.1370	0.1580
{002}	0.2648	0.3055	0.2648	0.3055
{112}	0.1476	0.1703	0.1370	0.1580
{022}	0.1476	0.1703	0.1370	0.1580
{013}	0.1476	0.1703	0.1370	0.1580
{222}	0.1085	0.1252	0.0944	0.1089

The modified W-H plot has been made by introducing the average dislocation contrast factor, $\bar{C}_{hkl}$ for pure Gaussian and pure Lorentzian distribution and is shown in Fig. 5.7(a-d). A much better correlation between the ΔK and modified dislocation contrast factor, $K\sqrt{\bar{C}}$ has been found.

The variation in the q parameter with distance from the worn surface indicates very little change in the type of dislocation, as shown in Fig. 5.8(a). The average size of the coherent domains of diffraction can be found from the y-intercept of the modified W-H plot and is presented in Table 5.5 for all possible combinations of dislocation types and peak shapes. A marginal decrease in the domain size after abrasion indicates limited plastic strain of the surface during abrasion [Fig. 5.8(b)], which otherwise, would have been much less as observed during rolling/sliding wear of soft and ductile ferrite of pearlite [Chapter 6]. Loss of austenite due to tempering not only lowers the work-hardenability of the structure, but limits its ability to absorb the energy of abrasion via structural change like reduction in domain size via increasing dislocation cell formation.

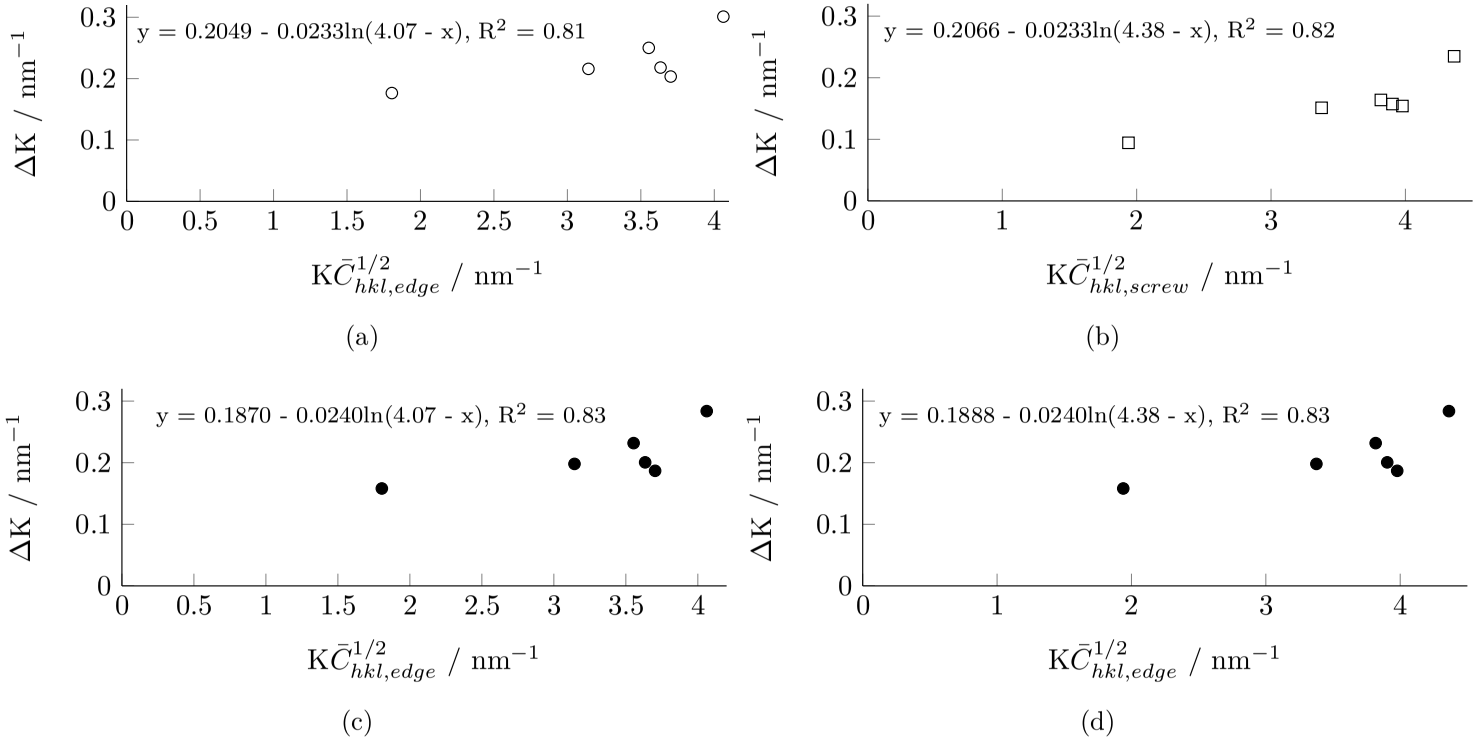

Figure 5.7: Modified Williamson-Hall plot for bcc- of tempered bainite (a) for pure edge dislocation and Gaussian peak broadening, (b) for pure screw dislocations and Gaussian peak broadening, (c) for pure edge dislocation and Lorentzian peak broadening and (d) for pure screw dislocations and Lorentzian peak broadening.

Table 5.5: Average size of the coherent domains of diffraction in bcc-α_b of tempered bainite after abrasion, as a function of the diffraction peak shape.

Dislocation type	Coherent domain size / nm	
	Gaussian	Lorentzian
edge	42	56
screw	42	56

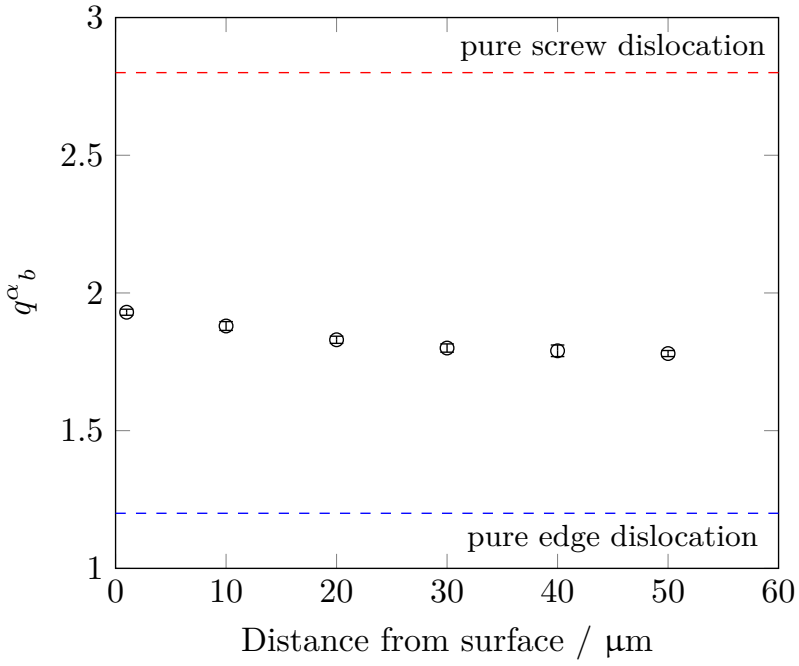

(a)

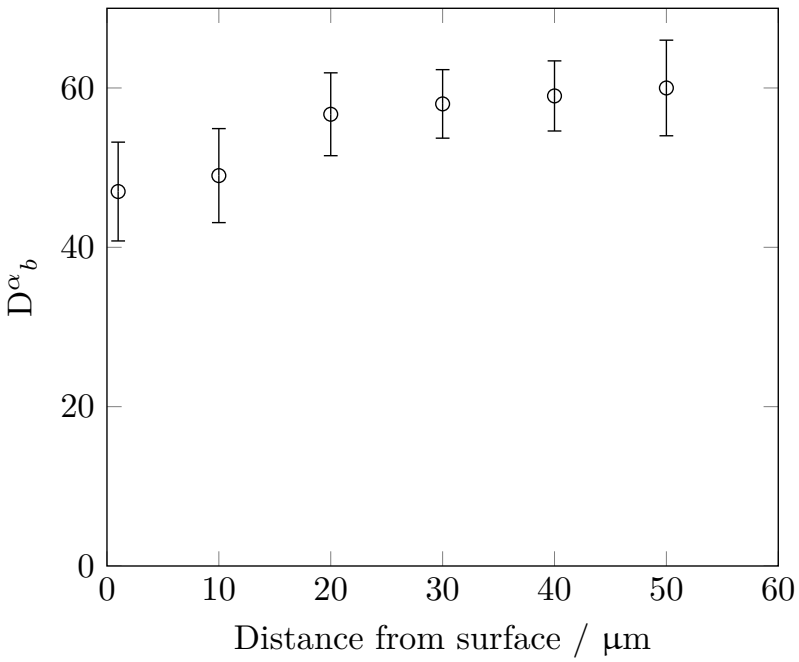

(b)

Figure 5.8: (a) variation in the q parameter and (b) change in the size of the coherent domain of diffraction from worn surface to the core of the structure.

5.4 Conclusions

Three-body abrasive wear of tempered nanostructured bainite has been studied and, based on experimental evidence, the following general conclusions can be made,

1. Tempering of nanostructured bainite at 500°C for one hour leads to the complete decomposition of austenite to ferrite and carbide. The precipitated carbides were fine, typically < 20 nm, and uniformly distributed all over the structure. The tempering did not induce coarsening of bainitic ferrite as the carbides from the decomposition of austenite deposit at the interfaces and pin them.

2. A transition in the mechanism of abrasion from limited grooving and ploughing, observed in the case of nanostructured bainite, to significant removal of material via cutting that occurs with the tempered state.

3. In the absence of retained austenite, the fine scale of bainitic ferrite alone does to contribute much towards the abrasive wear resistance. The structure looses its work-hardenability causing abrasives to penetrate deeper into the substrate causing more damage.

4. Fine scale carbides, compared to the size of abrasives, do not contribute much towards the wear resistance, either by acting as physical barriers or by hindering the motion of dislocations in bainitic ferrite.

Chapter 6

Rolling/sliding wear of pearlite

6.1 Introduction

The dry wear behavior of pearlite has been, in the past, characterised as a function of contact load [104, 198–201], relative slip [103, 104, 198, 200–203], chemical composition [104, 106, 110, 204], mechanical properties [106, 203, 205] and microstructure [104,110,203,205–208]. Studies indicate that the rolling/sliding wear resistance of pearlite is enhanced by reducing the distance between ferrite (α) and cementite (θ) lamellae [106, 203, 205].

Refined pearlite has a greater flow stress and work-hardening rate, both of which lead to a reduction in the wear rate [205, 208, 209], although the fatigue strength is insensitive to the interlamellar spacing [210, 211]. Finer cementite is able to accommodate more deformation prior to fracture so the pearlite is able to flow in a narrow zone at the wear surface [212, 213].

Similar work has recently been reported on pearlite produced by isothermal transformation, but under conditions of severe slip (20%) in order to simulate extreme wear at railheads on curved tracks, whereas the present work is limited to 5% slip in order to permit comparisons against other microstructures tested under the same conditions [214].

6.2 Experimental Procedures

Rolling/sliding tests were conducted on a pair of flat, cylindrical discs machined out from the same alloy [Table 6.1] and heat treated [Table 6.2] to make fine pearlite. The tests were conducted with 300 N load and 5% slip for period of 30,000 cycles. Weight loss was measured after wear test, normalised against load and sliding distance, and the worn surface was characterised using optical and scanning electron microscopy. As the worn surface is curved, X-ray diffraction experiments were carried out with a parallel-beam monochromator. The surface was characterised both before and after rolling/sliding and compared to understand the wear mechanism, as detailed in following sections.

Table 6.1: Chemical composition of the experimental alloy (wt %).

C	Mn	P	S	Si	Al	Cu	Cr	Mo	V	Co	Sn	Nb
0.83	2.28	0.011	0.008	1.9	0.044	0.12	1.44	0.24	0.11	1.55	0.019	0.023

Table 6.2: Heat treatment and resultant hardness measured in Vickers scale.

Structure	Heat Treatment	Vickers hardness/kgf-mm^{-2}
Fine pearlite	930 °C 60 mins, air cooled to 550 °C, held for 4 h, air cooled	378 ± 9

6.3 Results

6.3.1 Microstructure

Fig. 6.1(a) shows the completely pearlitic structure obtained, without any proeutectoid phases, which are known to be detrimental to mechanical properties [215]. The true interlamellar-spacing, $\overline{L}_0$, was measured to be 85 ± 7 nm on transmission electron micrographs [Fig. 6.1(b)] using Underwood's intersection method [133]. This can also be taken as the mean free path within ferrite, a parameter that

influences the strength and work-hardening rate of pearlite [209]. The hardness achieved is compared against published data in Fig. 6.1(c), a plot that indicates an approximately linear relationship between hardness and the reciprocal of the interlamellar spacing [216], although it is noted that a Hall-Petch type relationship can be used with similar fit within the limits of experimental data [217,218].

6.3.2 Wear observations

As expected, surface roughness increased following rolling/sliding, but a comparison with much harder nanostructured bainite (Table 8.1) tested under the same circumstances shows that the extent of roughening is greater by a factor of about 3 in the average roughness following testing. It is known that contact pressures become greater with rough surfaces when compared against those that remain smooth, resulting in sub-surface plastic deformation extending to tens of micrometers, even though the nominal loading should leave the material in an elastic state [219].

Table 6.3: Surface roughness parameters of discs before and after rolling/sliding. Data for nanostructured bainite Chapter 7 are presented for comparison.

	Disc 1		Disc 2	
	before test	after test	before test	after test
Nanostructured pearlite, 378 kgf mm^{-2}				
Average roughness R_a/ µm	1.2	3.0	1.2	2.6
Distance between highest crest and lowest trough R_z/ µm	1.5	3.8	1.4	3.4
Maximum height of ridges R_t/ µm	8.1	29.2	8.2	25.2
Nanostructured bainite, 640 kgf mm^{-2},[Chapter 7]				
R_a/ µm	1.3	1.1	1.1	1.1
R_z/ µm	7.0	13.9	7.0	11.4
R_t/ µm	7.5	15.2	7.2	11.8

In spite of the development of roughness, Fig. 6.2 shows good specific-wear resistance for the nanostructured pearlite, both when compared against somewhat softer pearlitic steels, and against a variety of bainitic steels, some of which are much harder (even harder bainitic steels do, of course, show a smaller wear rate). These comparisons are made for steels studied under identical conditions to the present work [4]. The work emphasises the fact that techniques of estimating wear simply on the basis of phase fractions [220] or hardness are unlikely to correctly predict wear resistance, when mechanisms of wear are dependent on the details

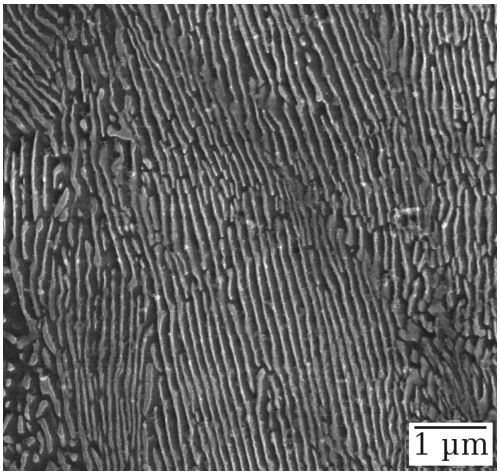

(a)

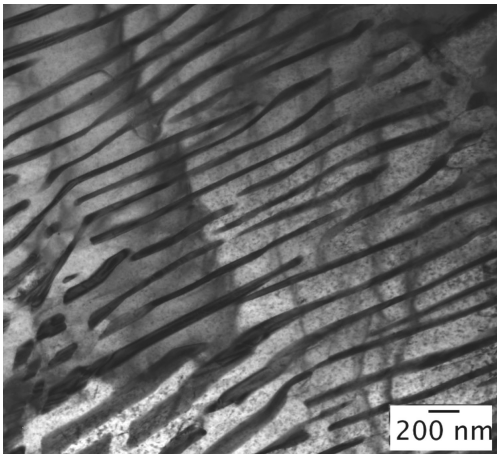

(b)

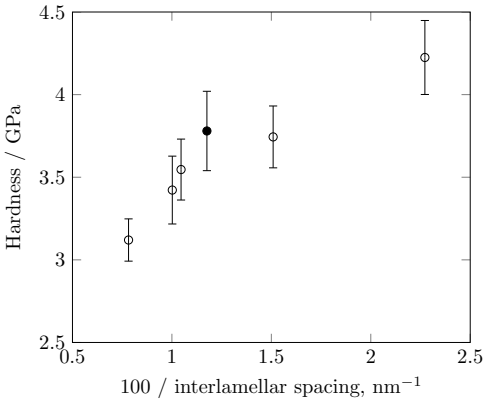

(c)

Figure 6.1: (a) Secondary electron image of the fine pearlite, (b) TEM image showing fine alternate arrangement of ferrite and cementite and (c) comparison of bulk hardness against interlamellar spacing of experimental alloy (closed circle) and other nanostructured pearlite (open circles) [3].

of the structure.

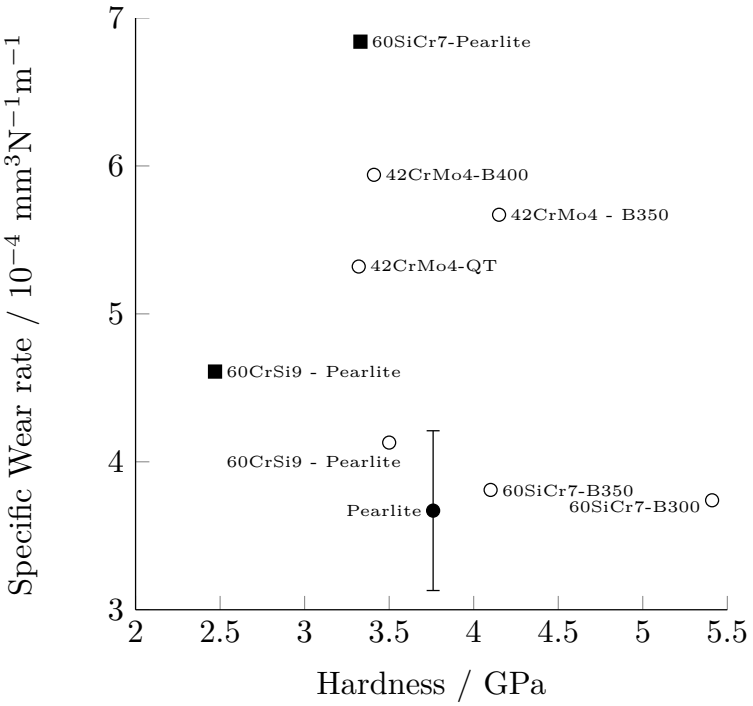

Figure 6.2: Specific wear rates measured in rolling/sliding tests. The open circles represent bainitic steels [4], and the filled points pearlite (square from [4] and circle: present work).

6.3.3 Dynamic coefficient of friction

The stresses experienced by the steel have been calculated based on Hertzian contact theory [95, 221]. The computer program for doing such calculations are detailed in appendix B which is also made available freely on:

http://www.msm.cam.ac.uk/map/steel/programs/contact.html

Based on the observed range of dynamic friction coefficients [Fig. 6.3] calculations indicate that the corresponding variations in the stresses experienced are negligible, fluctuation is most prominent in tractional stress, $\sigma_x = 379$ - 385 MPa, $-\sigma_z = 441.7 \pm 0.2$ MPa and maximum shear stress, $-\tau_{xz} = 115$ - 113 MPa.

Fig. 6.4 shows how the stresses are distributed on the xz plane. Given that

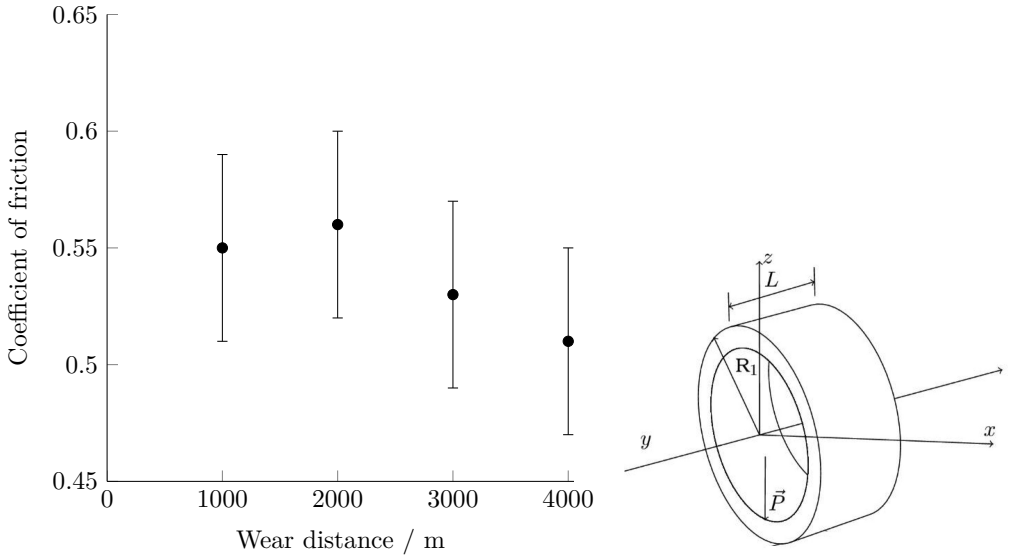

(a) (b)

Figure 6.3: (a) Measured dynamic coefficient of friction as a function of the wear distance, (b) Coordinate system.

the simulation is for a small amount of slip (5%), it is expected that the maximum shear stress occurs below the contact surface, at a depth of about 50 µm. However, the analysis is not properly representative, for example, the shear stress calculated at the surface is quite small < 100 MPa), which is surprising because there is clear evidence of plastic deformation to a depth of at least 40 µm. This can be seen in the scanning electron micrographs presented in Fig. 6.5. The explanation must lie in the fact that the calculations assume a smooth surface, whereas it is far from smooth once the wear process begins [Table 8.1]. As already noted in section 6.3.2, the consequence of roughness is to exaggerate stresses and induce plastic deformation. Therefore, the calculated shear stress is the minimum stress that could be experienced with a geometrically smooth surface, whereas the actual stress are undoubtedly greater. Similar experience has been found in rails, where the operating contact pressure is kept below the shakedown limit of pearlitic rail steel [222], but there is nevertheless severe plastic deformation observed to a depth of tens of micrometers because of the higher stresses experienced at asperities associated with surface roughness [219]. Surface roughness that persists during the wear test causes the contact pressures to far exceed those associated with the smooth surface theory.

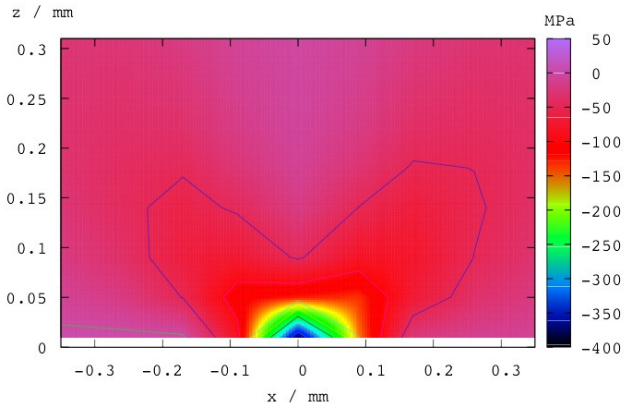

(a) σ_x

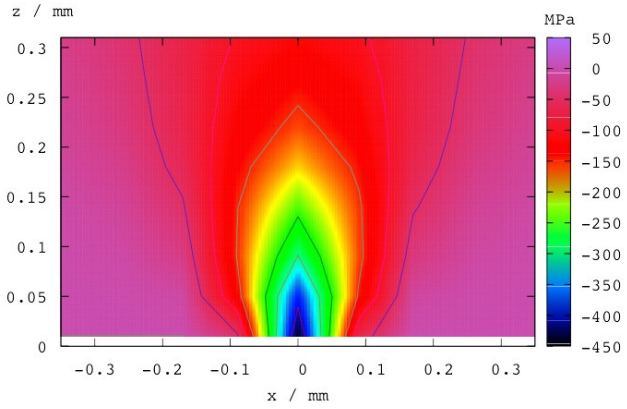

(b) σ_z

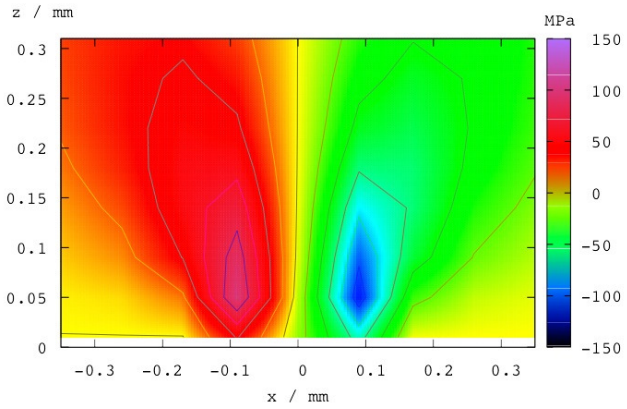

(c) τ_{xz}

Figure 6.4: Stress distributions calculated assuming $\mu = 0.57$ and $d = 4000\,\mathrm{m}$.

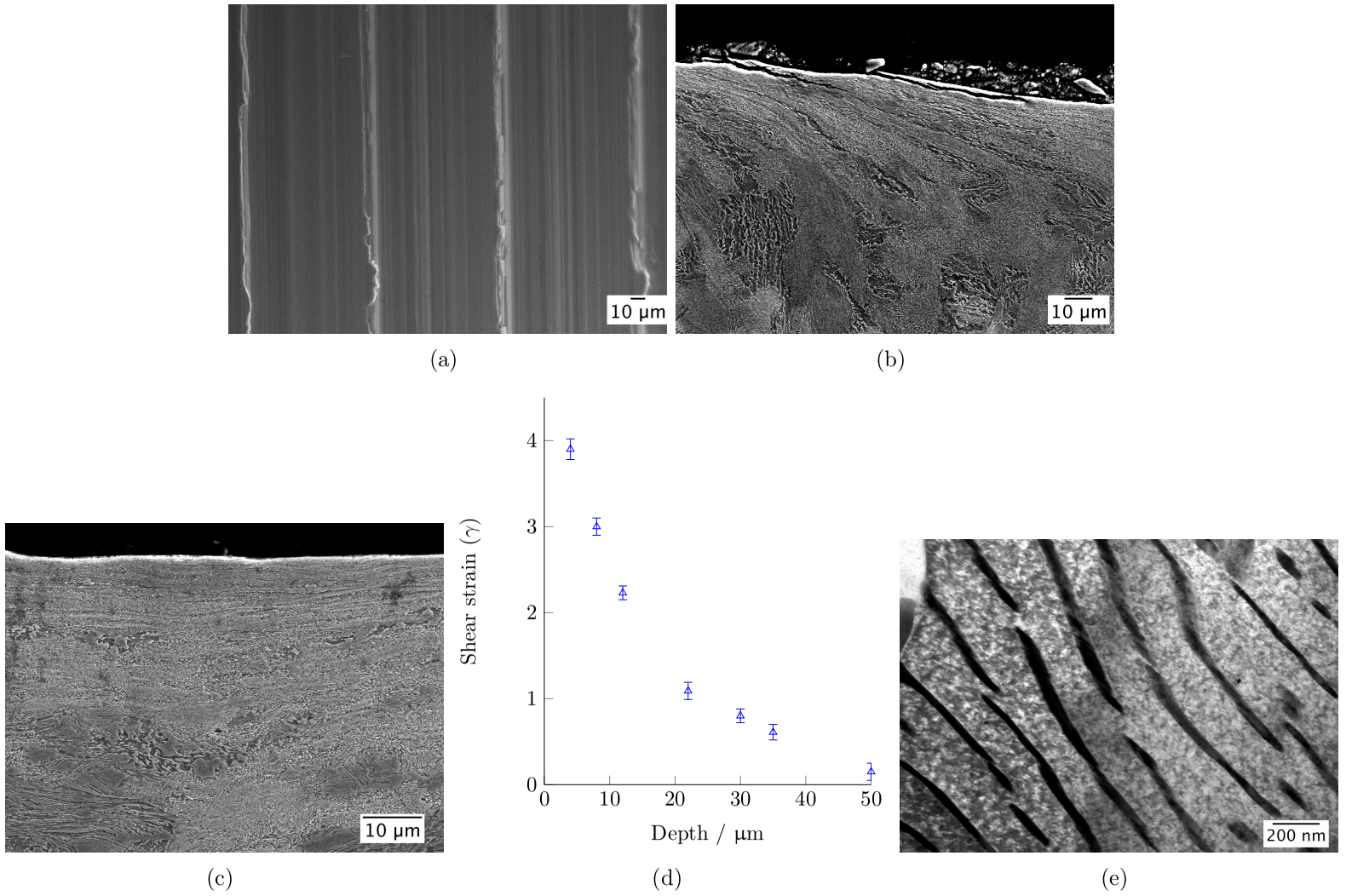

Figure 6.5: Secondary electron image of the surface and subsurface structure after rolling/sliding (a) Wear tracks on the surface, cross section image (b) along the rolling/sliding direction, (c) along transverse direction and (d) measured shear strain as a function of depth, (e) bright-filed TEM image of pearlite after rolling/sliding showing plastic necking of thin cementite lamellae.

Fig. 6.5 also shows that there is significant plasticity even in the cementite that is deformed in the vicinity of the contact surface. Although frequently regarded as a brittle phase, it is well-known to behave in a ductile manner when the cementite lamellae are fine [223, 224] and such plasticity is a common feature of the surfaces of worn rail steels [214, 219]. The shear strain of the deformed pearlite, as shown in Fig. 6.5(d), is measured from the tangent, that the cementite lamellae makes with the rolling/sliding surface at increasing depths.

6.3.4 Nanoindentation results

The hardness derived from the nano indentation load-displacement curves [137] is shown in Fig. 6.6(a) as a function of the depth below the contact surface. An increase of about 1 GPa occurs relative to the bulk, which is consistent with the X-ray derived structural information reported below, and recent observations on pearlite wear in a Fe-1C-0.7Mn-0.4Si-0.25Cr steel [214]. The observed surface hardening below the surface is considered beneficial towards reducing wear in pearlite as long as it does not lead to excessive detachment of wear particles [200, 225–227].

Fig. 6.6(b) shows the elastic recovery following removal of the indentation load, a phenomenon indicative of the presence of residual stresses, which can be estimated by studying the indent residual-depth and residual cone-angle after removal of the applied load [140, 141, 143, 228]. Fig. 6.6(c) shows that the stress in the plane parallel to the wear surface is compressive in the direction of rolling sliding; it is this which is known to control wear [229, 230]. It should be emphasised that the stresses measured cover approximately five grains and hence refer to type II residual stress [231], but the compressive nature should nevertheless help in resisting the applied traction stress σ_x.

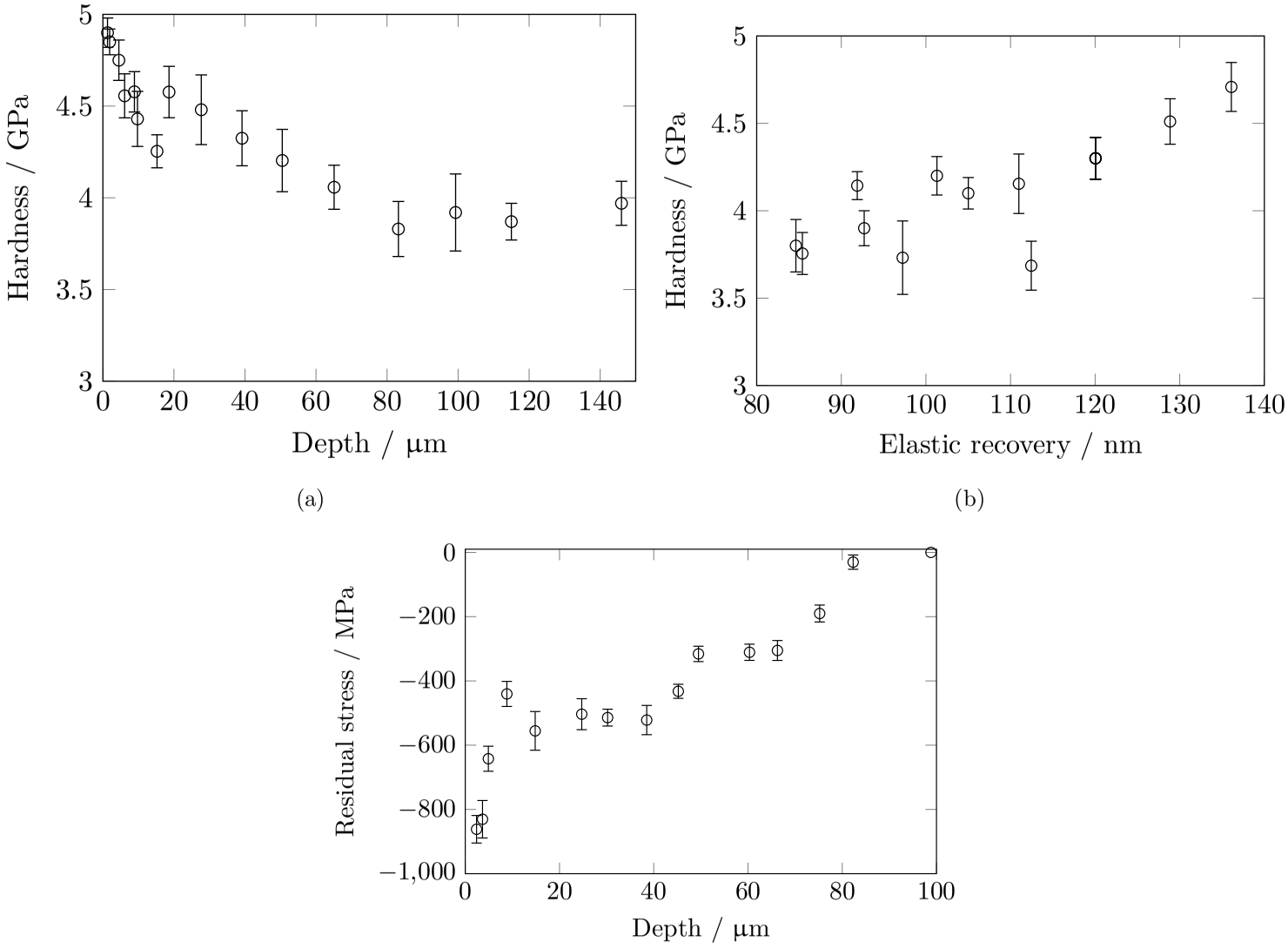

Figure 6.6: Nanoindentation test results (a) distribution of nanoindentation hardness of the surface and subsurface layers after rolling/sliding, (b) elastic recovery of pearlite after withdrawal of the nanoindentation load and (c) distribution of compressive residual stress with depth after rolling/sliding.

6.3.5 X-ray diffraction

The observed X-ray peak broadening is indicative of the state of the microstructure following abrasion [Fig. 6.7], and can be used to estimate the size of the coherent domains along with the residual microstrain within the crystallites. These two parameters can be deconvoluted by plotting the peak width at half the maximum height (FWHM in radians) $K = 2\sin\theta/\lambda$ where θ is the Bragg angle and λ is the X-ray wavelength. This is known as the Williamson-Hall plot, but as seen in Fig. 6.8(c-d), revealed rather poor correlation to the plotting function.

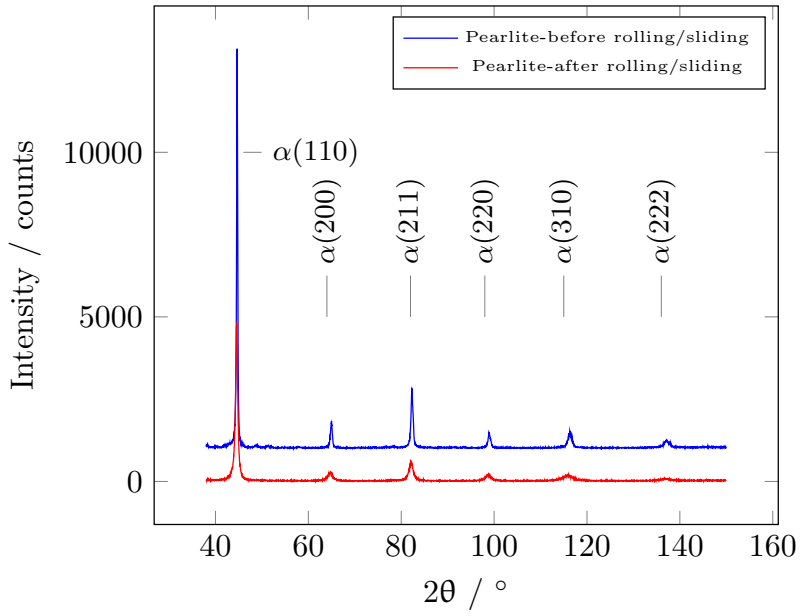

Figure 6.7: X-ray diffraction profiles from the surface of pearlitic discs before and after rolling/sliding.

As a consequence, elastic anisotropy was taken into account in the analysis [147–149], replacing the function $K = 2\sin\theta/\lambda$ by $K\sqrt{\bar{C}}$, where $\bar{C}$ is the average dislocation contrast factor for a specific *hkl* plane. The diffraction profiles of {110},{002}, {112}, {022}, {013} and {222} have been considered for the analysis.

The value of q, which helps assess the dislocation character for a particular *hkl* plane [149–151], was found to change with an initial value prior to deformation of 1.46 to 2.43 after rolling/sliding, indicating the dislocation character of bcc-ferrite changing from edge to screw dislocations [Fig. 6.10(a)]. The dislocation contrast

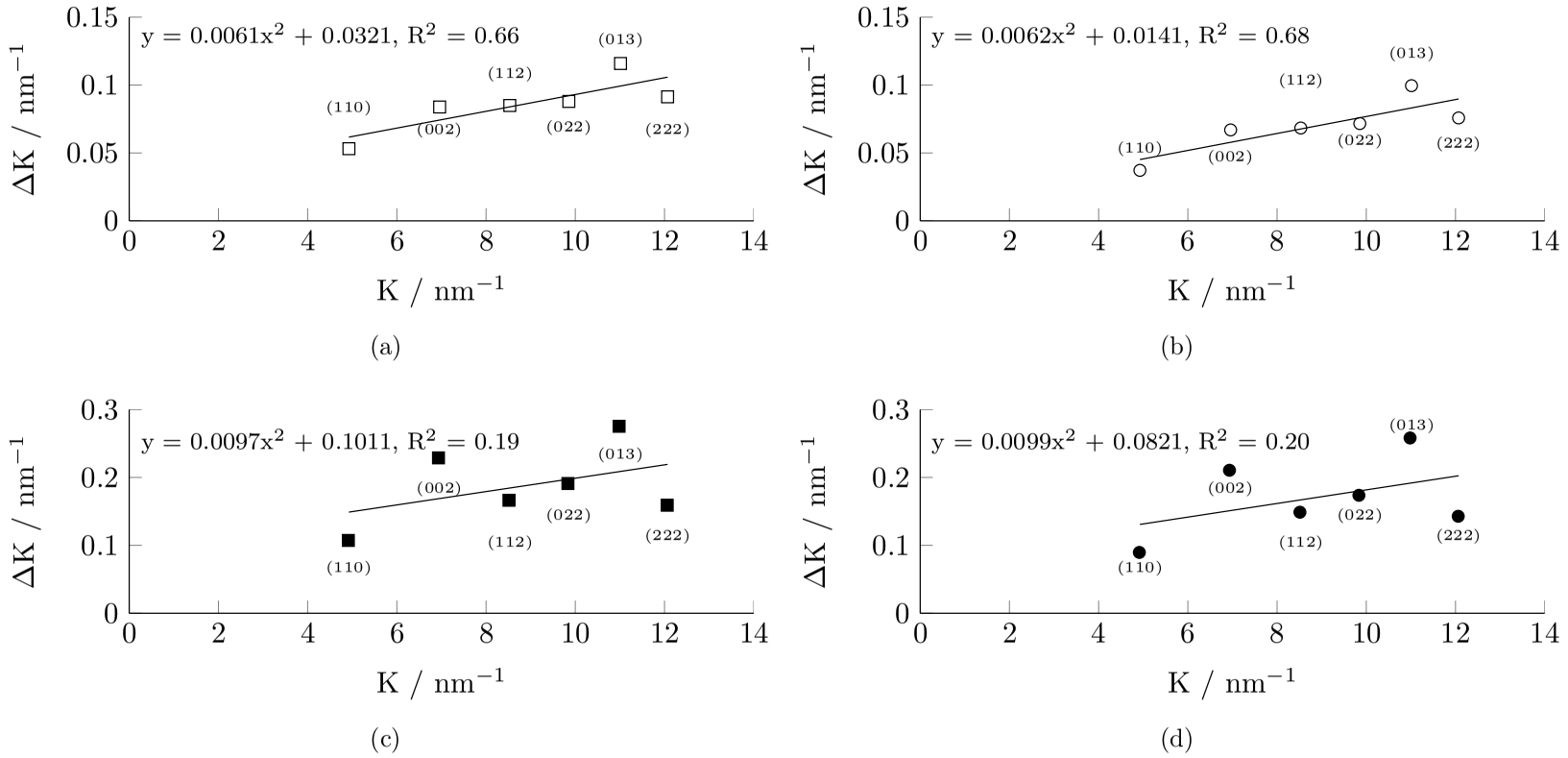

Figure 6.8: Williamson-Hall plot for ferrite (a) before rolling/sliding assuming Gaussian peak broadening, (b) before rolling/sliding assuming Lorentzian peak broadening, (c) after rolling/sliding assuming Gaussian peak broadening and (d) after rolling/sliding assuming Lorentzian peak broadening.

values were derived from q using the equation

$$\bar{C}_{\{hkl\}} = C_{\{h00\}}(1 - qH^2). \tag{6.1}$$

To use this equation $\bar{C}_{hkl}$ of $\{200\}$ is first obtained where $H^2 = 0$. Assuming the elastic constants, $c_{11} = 230.1\,\text{GPa}$, $c_{12} = 134.6\,\text{GPa}$ and $c_{44} = 116.6\,\text{GPa}$, $\bar{C}_{200}^{edge}$ for bcc-α Fe has been calculated as 0.2648 and that of $\bar{C}_{200}^{screw}$ is found to be equal to 0.3055 and subsequently $\bar{C}_{hkl}$ for other planes are listed in Table 6.4 [232].

Table 6.4: Average dislocation contrast factor of pure edge and pure screw dislocations for hkl planes in bcc-α Fe before rolling/sliding.

	$q = 1.46$		$q = 2.43$	
{hkl}	$\bar{C}_{hkl}^{edge}$	$\bar{C}_{hkl}^{screw}$	$\bar{C}_{hkl}^{edge}$	$\bar{C}_{hkl}^{screw}$
{110}	0.1681	0.1940	0.1040	0.1199
{002}	0.2648	0.3055	0.2648	0.3055
{112}	0.1681	0.1940	0.1040	0.1199
{022}	0.1681	0.1940	0.1040	0.1199
{013}	0.1681	0.1940	0.1040	0.1199
{222}	0.1359	0.1568	0.0503	0.0580

Fig. 6.8(c-d) can be replotted by introducing the average dislocation contrast factor, $\bar{C}_{\{hkl\}}$ in the term K for pure edge and pure screw dislocations, as shown in Fig. 6.9(a-d), where better correlation to the modified Williamson-Hall function is seen. The average sizes of the coherent domain of diffraction was calculated and presented in Table 6.5 for all possible combinations of dislocation type and peak shape. The coherent domain sizes are finer than the scale of the starting microstructure, and are reasonable given the finer scale of the deformed state. Since, the actual peak shape is a complex combination of Gaussian and Lorentzian profile, the actual domain size should lie in between 17-23 nm.

A gradual increase in the dislocation density from 4.0×10^{14} m^{-2} at a depth of 50 μm from the rolling/sliding surface to 7.49×10^{14} m^{-2} near surface has been

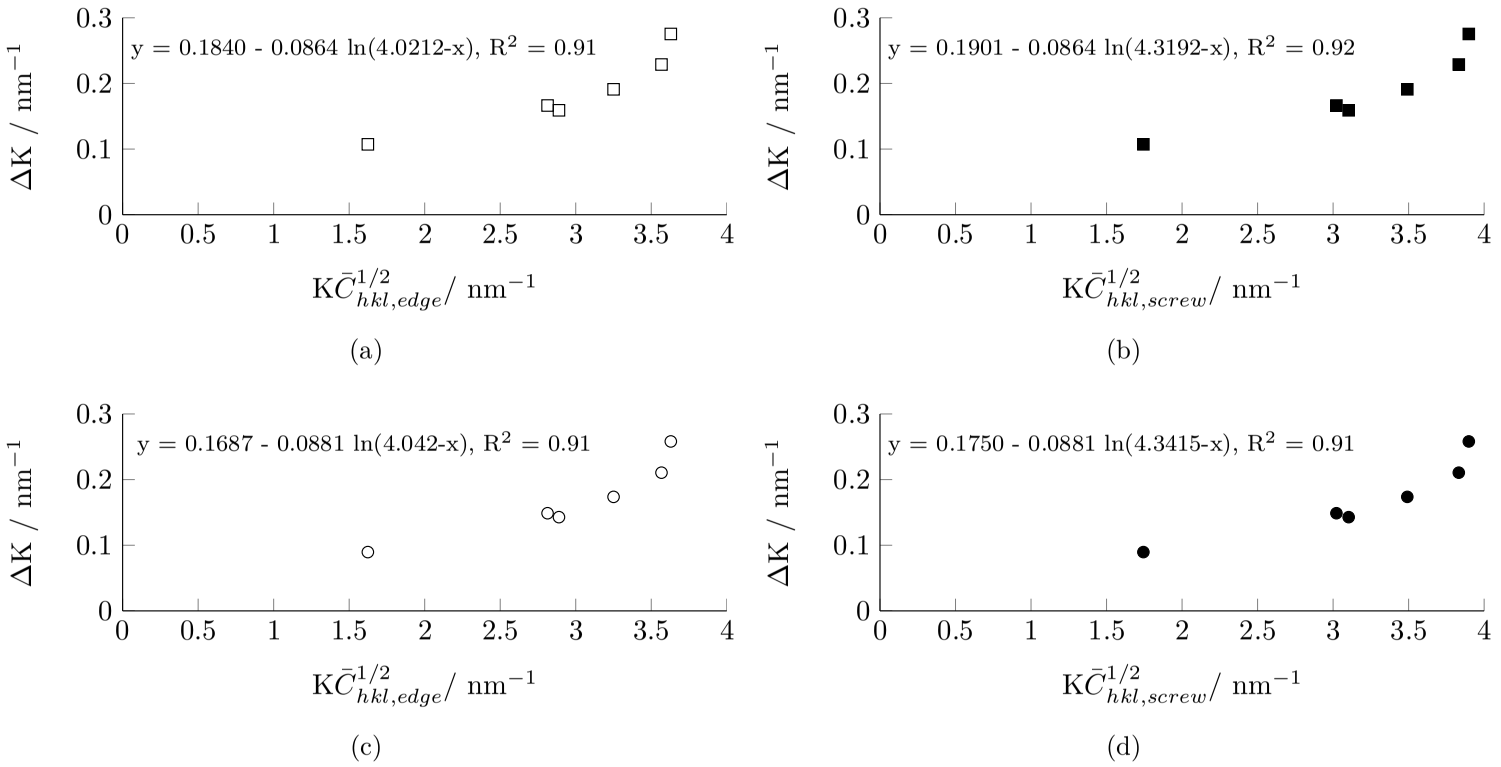

Figure 6.9: Modified Williamson-Hall plot for bcc-α considering (a) pure edge dislocation and Gaussian peak broadening, (b) pure screw dislocations and Gaussian peak broadening, (c) pure edge dislocation and Lorentzian peak broadening and (d) pure screw dislocations and Lorentzian peak broadening.

Table 6.5: Average size of the coherent domains of diffraction in bcc-α of pearlite after rolling/sliding, as a function of the diffraction peak shape.

Dislocation type	Coherent domain size / nm	
	Gaussian	Lorentzian
edge	17	23
screw	17	23

estimated from the slope of the $(\Delta K)^2$ vs. $K^2\bar{C}_{hkl}$ plot and its variation with depth is shown in Fig. 6.10(b). Plastic strain at the onset of deformation in ferrite results in rapid multiplication of dislocations. The low mean free path of dislocations in ferrite due to the intervention of cementite lamellae must contribute to the formation of dislocation forests within ferrite. While we do not have quality diffraction data from the cementite, it clearly does undergo plastic deformation, a phenomenon well known in the context of wire drawing [233].

The size of the coherent domain of diffraction can be calculated from the intercept of $(\Delta K)^2$ vs. $K^2\bar{C}_{hkl}$ plot for each depth and the calculated values are plotted against distance from rolling/sliding surface and is shown in Fig. 6.10(e). It is interesting that the domain size is comparable to that obtained during high pressure torsion tests on pearlite, where the shear strains are of the order of 60-200 [234], and indeed, the reported microhardness obtained for this range of shear strain is 4.5-8 GPa. Microhardness probably cannot be related directly to nanohardness, but the range recorded here is from 4-6 GPa, the higher value being below the surface of the sample [Fig. 6.6(a)]. The lattice parameter of bcc-α as calculated from the X-ray diffraction data obtained from various depths are shown in Fig. 6.10(c). A marginal increase in the lattice constant for the ferrite has been observed from which the carbon content in ferrite has been calculated following [235],

$$a_\alpha = a_0 + \frac{(a_0 - 0.279x_\mathrm{C})^2(a_0 + 2.496x_\mathrm{C}) - a_0^3}{3a_0^2} - 0.03x_\mathrm{Si} + 0.06x_\mathrm{Mn} + 0.07x_\mathrm{Ni} + 0.31x_\mathrm{Mo} + 0.05x_\mathrm{Cr} + 0.096x_\mathrm{V} \tag{6.2}$$

The calculated values of carbon in ferrite (wt%) is plotted against distance and was found to increase near the surface from that in the bulk [Fig. 6.10(d)]. It may be possible therefore that some of the cementite which undergoes shear close to

the wear surface is induced to dissolve into the surrounding ferrite [234]. However, the deduced concentration of carbon in ferrite is not large, and cementite clearly exists at the contact surface, so that the amount of cementite dissolution in the present case is small, consistent with reported atom probe data on wear of pearlite [214]. It should be emphasised that the shear strains involved in the torsion tests are very large, approaching $\gamma = 200$ [234], whereas the maximum measured here is $\gamma \approx 4$, Fig. 6.5. The fine domain size is therefore not simply a consequence of severe deformation but also due to the very fine starting structure with an interlamellar spacing that is about twice the final domain size.

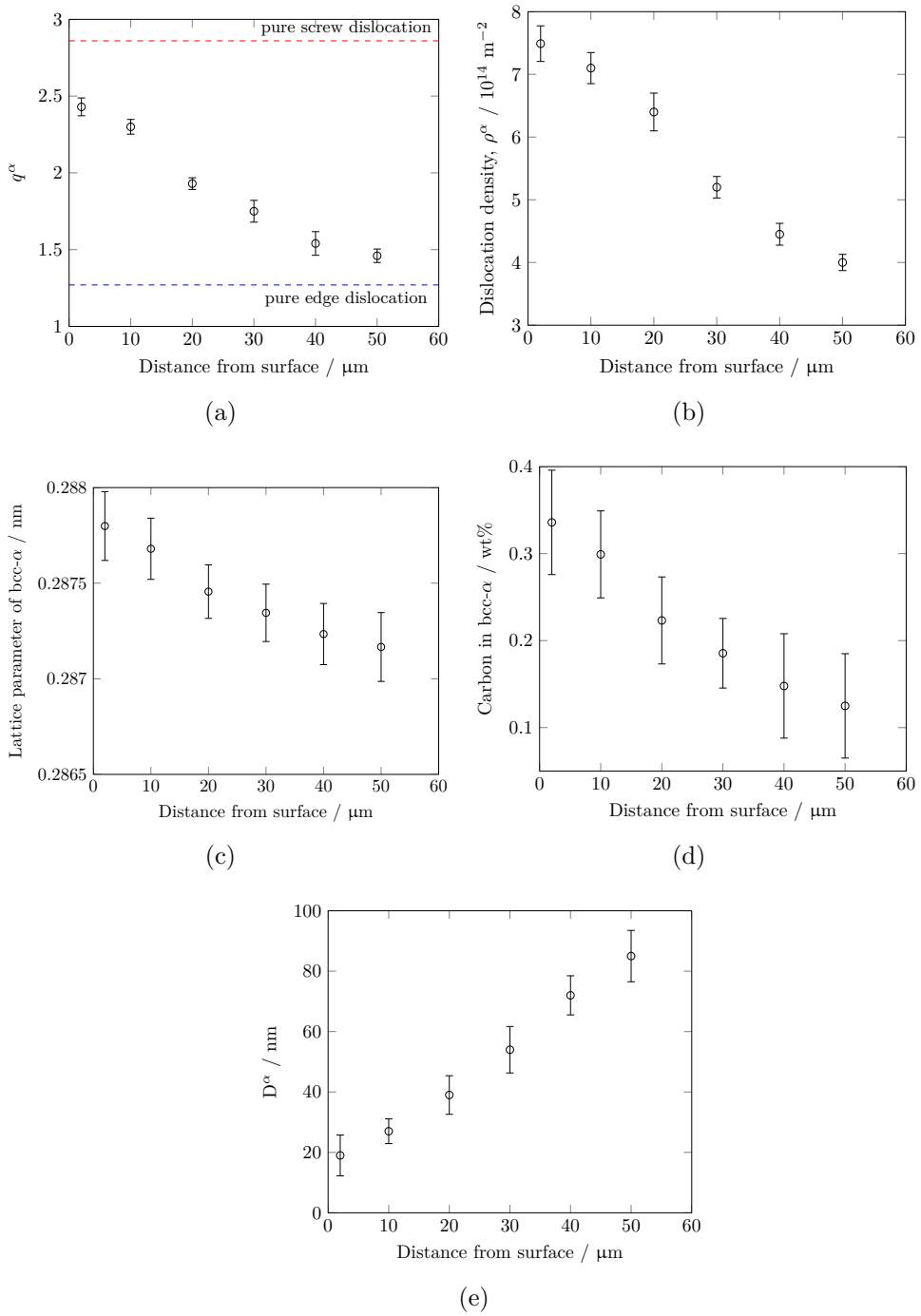

Figure 6.10: Change in the (a) q parameter, (b) dislocation density, ρ, (c) lattice parameter for ferrite and (d) carbon content in ferrite and (e) coherent domains of diffraction with decreasing distance from the core to the rolling/sliding surface.

6.4 Conclusions

1. It was found that pearlite with a very fine interlamellar spacing can outperform much harder bainitic steels in the context of rolling-sliding wear resistance. The wear causes substantial plastic deformation of the region in the vicinity of the contact surface, with both the ferrite and cementite exhibiting plasticity.

2. The coherent-domain size and hardness resulting from the plastic deformation caused by the wear process is comparable to that encountered in high pressure torsion tests on pearlite. The strains involved in the torsion tests are much larger. Therefore, the fine domain size observed is a consequence of the combined effect of the very small initial interlamellar spacing and the shear strains due to wear. There is evidence based on the lattice parameter of the deformed ferrite, that some of the cementite may have been forced into solution by the plastic strain.

3. The plastic deformation of the surface during the rolling-sliding test has been shown to introduce compressive stresses into the surface. This must help reduce the wear rate.

Chapter 7

Rolling/sliding wear of nanostructured bainite

7.1 Introduction

The wear behavior of bainitic steels subjected to rolling and sliding conditions has been studied for a variety of circumstances [5, 6, 100, 105, 109, 111, 122, 200, 236]. In many instances, the results have indicated that this microstructure does not in general outperform pearlite with similar hardness and loading conditions [200, 225, 237–239], the exception being a 0.04 wt%C bainitic steel that had a lower wear rate (rolling-sliding) than less-ductile pearlite of similar strength [109]. The greater wear resistance of pearlite is attributed to the ability of the microstructure to deform during rolling and sliding [239], the work-hardening of the ferritic component [225, 240] and the significant presence of hard cementite at the wear surface. In contrast, the interpretation of the response of bainite to similar loading tends to be complicated by the smaller fraction of cementite normally associated with bainitic microstructures, and the presence of residual phases such as martensite and retained austenite [200].

Some of these issues have been reviewed [241, pp. 382-389], but the purpose here is to consider a relatively new two-phase, carbide-free nanostructure consisting of exceptionally fine plates of bainitic ferrite embedded in carbon-enriched retained austenite [169, 242, 243]. There now exist many different alloy compositions that lead to similar nanostructures, and given hardness levels in excess of 600 HV,

and good combinations of strength, toughness and ductility. There has been considerable activity in exploring the wear resistance of the structure, under many different conditions, Table 7.1 [5, 6, 117, 159, 244]. While strict comparisons are difficult, there is a general impression from all this research that the nanostructure described above holds promise. Reasons offered for this include the fine scale of the nanostructure [5, 6, 116, 117, 244], and the role of the austenite in preventing crack propagation during sliding [117]. A general conclusion is that the finest structures generated by transformation at the lowest temperatures have the best resistance to dry sliding wear [244]. A recent set of three-body abrasion tests that compared the nanostructured bainite, pearlite and martensite in the same steel indicated quite different wear and surface-damage mechanisms for the three structures, with the bainite being the only one that leads to a hardening of the affected surface [Chapter 4].

The aim of the present work was to develop a deeper understanding of the dry rolling-sliding wear resistance of nanostructured bainite, using high-resolution characterisation methods combined with mathematical modelling.

7.2 Experimental Procedures

Similar to the previous experiment as detailed in Chapter 6, flat cylindrical discs were machined from the same alloy and heat treated to make nanostructured bainite. The rolling/sliding test was repeated with the same parameter so that a proper comparison can be made for the observed wear losses between different structures. The worn surface was characterised under optical, scanning electron microscope and X-ray diffraction to understand the damage mechanism of the nanostructured bainite.

7.3 Results

7.3.1 Microstructure

The structure following heat treatment is illustrated in Fig. 7.1, showing the expected mixture of slender platelets of bainitic ferrite and thin films of austenite,

Table 7.1: Wear data on the hardest, fine mixtures of bainitic ferrite and austenite reported, focusing on the lowest transformation temperatures used to generate the bainite. The Vickers hardness is also listed, and the chemical compositions are given in wt%.

C	Si	Mn	Cr	Mo	Ni	Al		Hardness	Test	Outcome	Ref.
0.89	1.43	0.19	0.47					697	dry sliding friction, cylindrical-end against disc	comparable wear to martensite of unspecified hardness	[116]
0.19	0.57	1.77	1.37	0.33	0.42	1.35	carburised	625	dry sliding friction, cylindrical-end against disc	comparable wear to martensite of similar hardness	[117]
0.61	1.72	0.75	0.35	0.04	0.12			627	rolling-sliding (5%) counter-rotating discs	specific wear rate 1.0 to 1.6 $\times$ $10^{-4}\,\mathrm{mm^3\,N^{-1}m^{-1}}$	[5]
0.83	1.56	1.37	0.81			1.44	0.87W	685	dry sliding friction, cylindrical-end against disc	much greater wear resistance than harder tempered-martensite	[244]
0.99	1.50	0.76	0.46					660	rolling-sliding (5%) counter-rotating discs	specific wear rate 1.1 $\times$ $10^{-4}\,\mathrm{mm^3\,N^{-1}m^{-1}}$	[6]
0.98	2.90	0.77	0.45					630	rolling-sliding (5%) counter-rotating discs	specific wear rate 0.9 $\times$ $10^{-4}\,\mathrm{mm^3\,N^{-1}m^{-1}}$	[6]
0.90	1.65	0.79	0.48					693	rolling-sliding (5%) counter-rotating discs	specific wear rate 0.4 $\times$ $10^{-4}\,\mathrm{mm^3\,N^{-1}m^{-1}}$	[6]
0.68	1.60	1.25	1.50					589	rolling-sliding (5%) counter-rotating discs	specific wear rate 1.0 $\times$ $10^{-4}\,\mathrm{mm^3\,N^{-1}m^{-1}}$	[6]

both containing a significant density of dislocations; carbides were not observed over five different locations studied. The mean lineal intercept ($\overline{L}$) was measured in the direction perpendicular to the trace of the habit plane of the bainitic ferrite plates from randomly selected locations of transmission micrographs, in order to estimate the true thickness (t) [135] and found to be equal to 35 ± 4 nm.

7.3.2 Surface topography

Fig. 7.2 shows the interferometry images from the surfaces of discs before and after the rolling/sliding tests. Parallel machining marks identified by steep ridges are evident on the circumference of the discs [Fig. 7.2(a,b)]. Clearly, the ridges would lead to non-conforming contact between two discs during rolling/sliding, possibly resulting in more of an asperity contact rather than that between two geometrically-smooth cylindrical surfaces in Hertzian contact. There will, therefore, be a running-in period before the contact area increases. This is indicated by the decrease in the overall roughness of the tracks after testing, Fig. 7.2b,d. The roughness parameters measured before and after wear are listed Table 8.1. Though the average roughness, R_a, was reduced by wear, the maximum height of the scanned profile, R_t, and average distance between the highest crest and lowest trough, R_z, nearly doubled. Pits marked as deep blue regions in Fig. 7.2d could also be the possible sites of material removal apart from the knocked off crests.

Table 7.2: Surface roughness parameters of discs before and after rolling/sliding.

	Disc	R_a/μm	R_z/μm	R_t/μm
Before	Disc 1	1.30	6.98	7.48
	Disc 2	1.27	7.04	7.17
After	Disc 1	1.08	13.91	15.23
	Disc 2	1.11	11.39	11.80

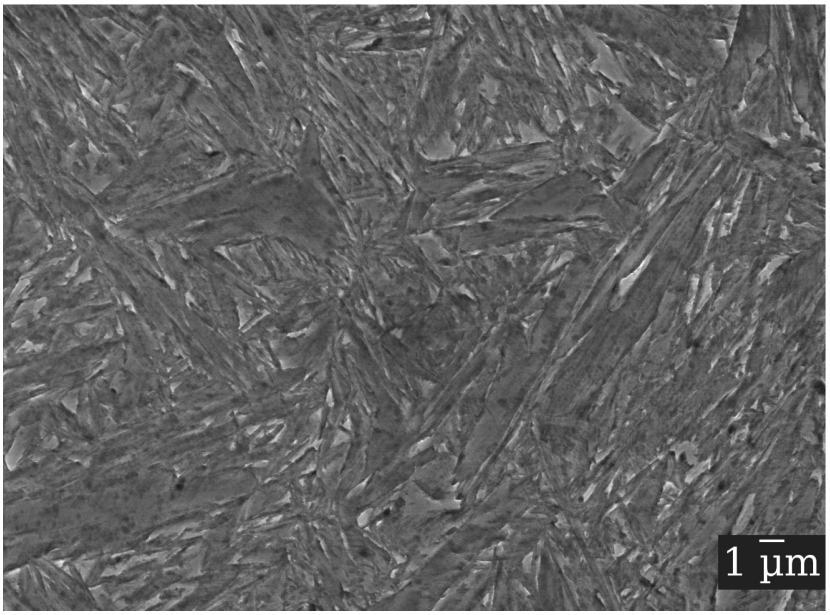

(a)

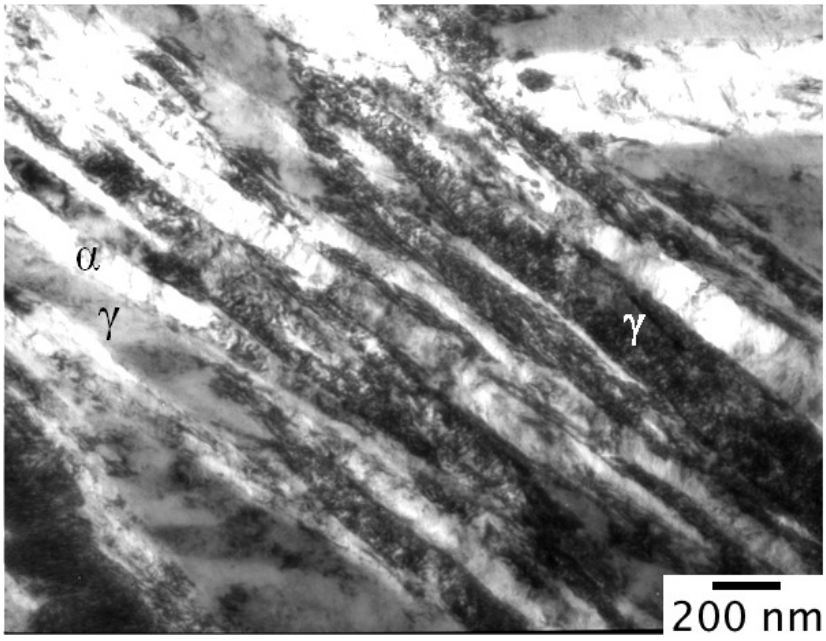

(b)

Figure 7.1: Structure following transformation at 200°C, (a) scanning electron micrograph, (b) bright-field transmission electron micrograph.

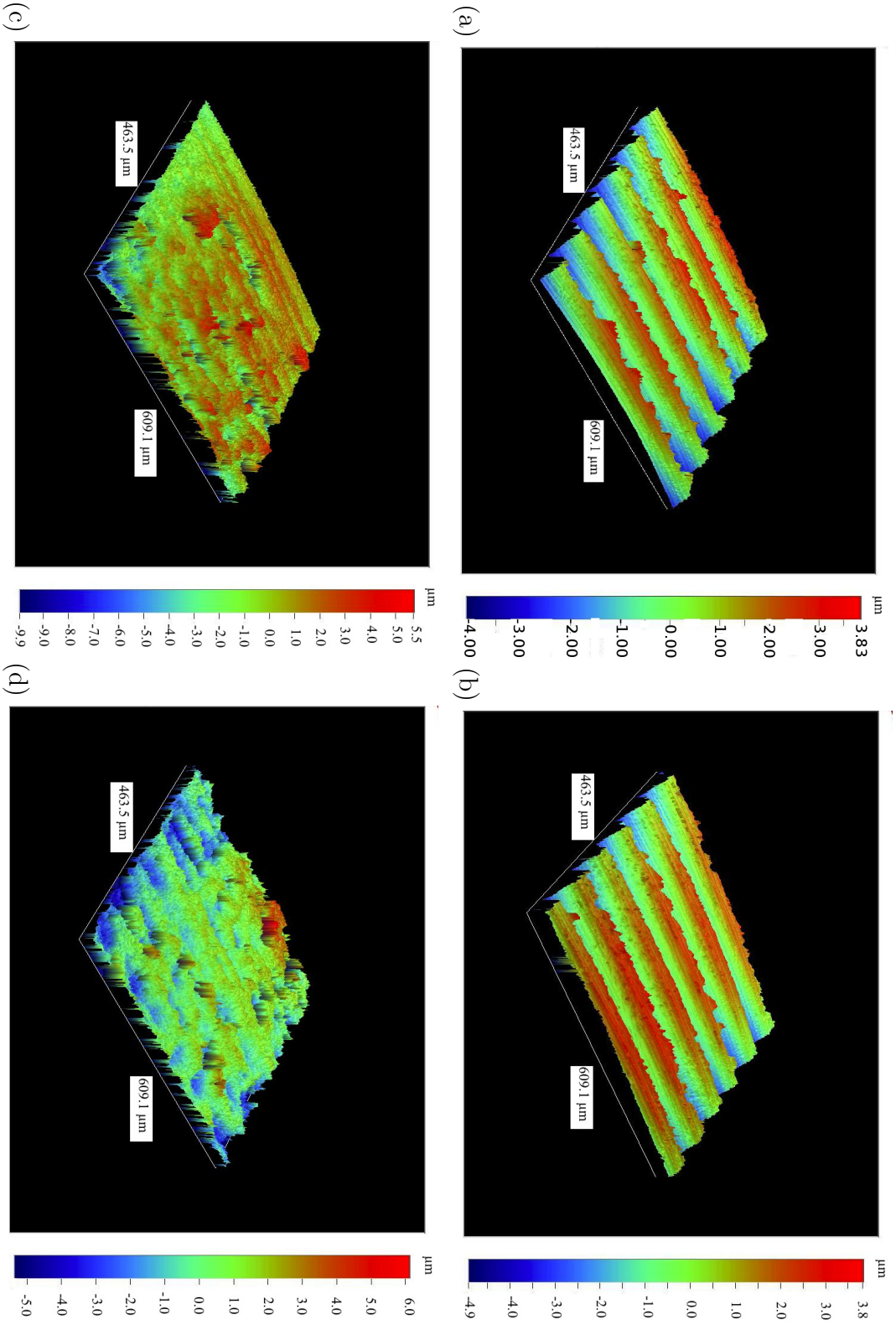

Figure 7.2: Light interferometry images of the surface of bainitic discs, (a,b) before rolling/sliding, (c,d) after rolling/sliding.

7.3.3 Wear data

A specific wear rate is the volume loss per unit load and distance traveled by a point on the perimeter over the duration of test. The rates recorded in the present work are compared against published data [5, 6] as a function of initial hardness, in Fig. 7.3. It is evident that in spite of the fact that the alloy studied here (Bainite200) does not have the maximum hardness, the specific wear rate is in fact the lowest ever recorded. That of the much harder alloy designated 09C220 is close to the present work; Bainite200 has more retained austenite (∼27 vol%) than 09C220 (∼22 vol%) with similar plate thickness of bainitic ferrite, whereas all the remaining alloys have been transformed at greater temperatures and hence have coarser structures.

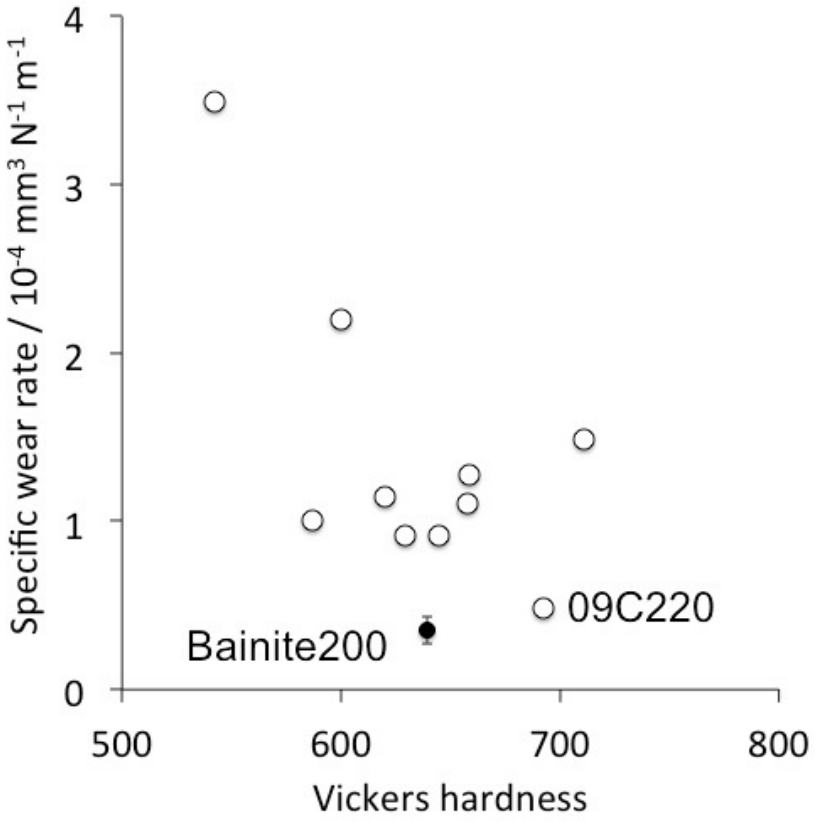

Figure 7.3: Specific wear rate recorded in the present work (filled dot with error bars, Bainite200), together with published data on other carbide-free bainitic steels [5, 6]. All the data are from tests with similar conditions of rolling/sliding.

7.3.4 Contact stress during rolling/sliding

7.3.4.1 Distribution of forces over the Hertzian contact width

The normal and shear stresses σ_z, σ_x and τ_{xz}, due to the combined effect of the distributed normal and tangential forces p_z and p_x, acting on the Hertzian contact width are then obtained by solving the set of equations described in Appendix A using the code listed in Appendix B. The necessary integrals were solved numerically, and some computations are presented in Fig. 7.4 for a variety of conditions. It is evident that sliding causes a major change and asymmetry in the distribution of stresses. The results illustrated will be used to interpret measured gradients in properties, later in the chapter.

7.3.5 Scanning electron microscopy

Fig. 7.5a shows the typical worn surface after rolling/sliding. Tracks of wear marks could be seen along with ledges protruding from the edge, indicating significant plasticity of the deformed material on the surface. The surface morphology is quite different from previous work [5, 6, 122], where extensive delamination, surface cracking and indentations were found. Almost no wear debris, in the form of metallic flakes was found to be attached on the surface. Therefore, 'type III' wear, which occurs due to mutual abrasion of wear debris generated during the initial running-in period was missing in this case [110]. Fig. 7.5b shows the cross section of the worn surface; there is a little damage to the nanostructure, with only a sparse distribution of what could be microscopic voids or sub-surface fatigue cracks, as observed in the case of other bainitic steels [5,6]. The extent of the deformed layer beneath the surface is also limited with a $\leqslant$5 µm non-etching layer that has formed, as shown in Fig. 7.5c. This layer indicates onset of wear, exactly matching with the location where maximum tractional stress σ_x is experienced. The layer is quite adherent to the underlying material, continuous and with very limited porosity. The temperature at the mating surfaces during rolling/sliding was close to room temperature and therefore possible reaustenitisation followed by martensitic transformation can be negated. Non-etching layers of the type observed here are a typical reflection of intense, repeated deformation, grain fragmentation and mechanical homogenisation [245].

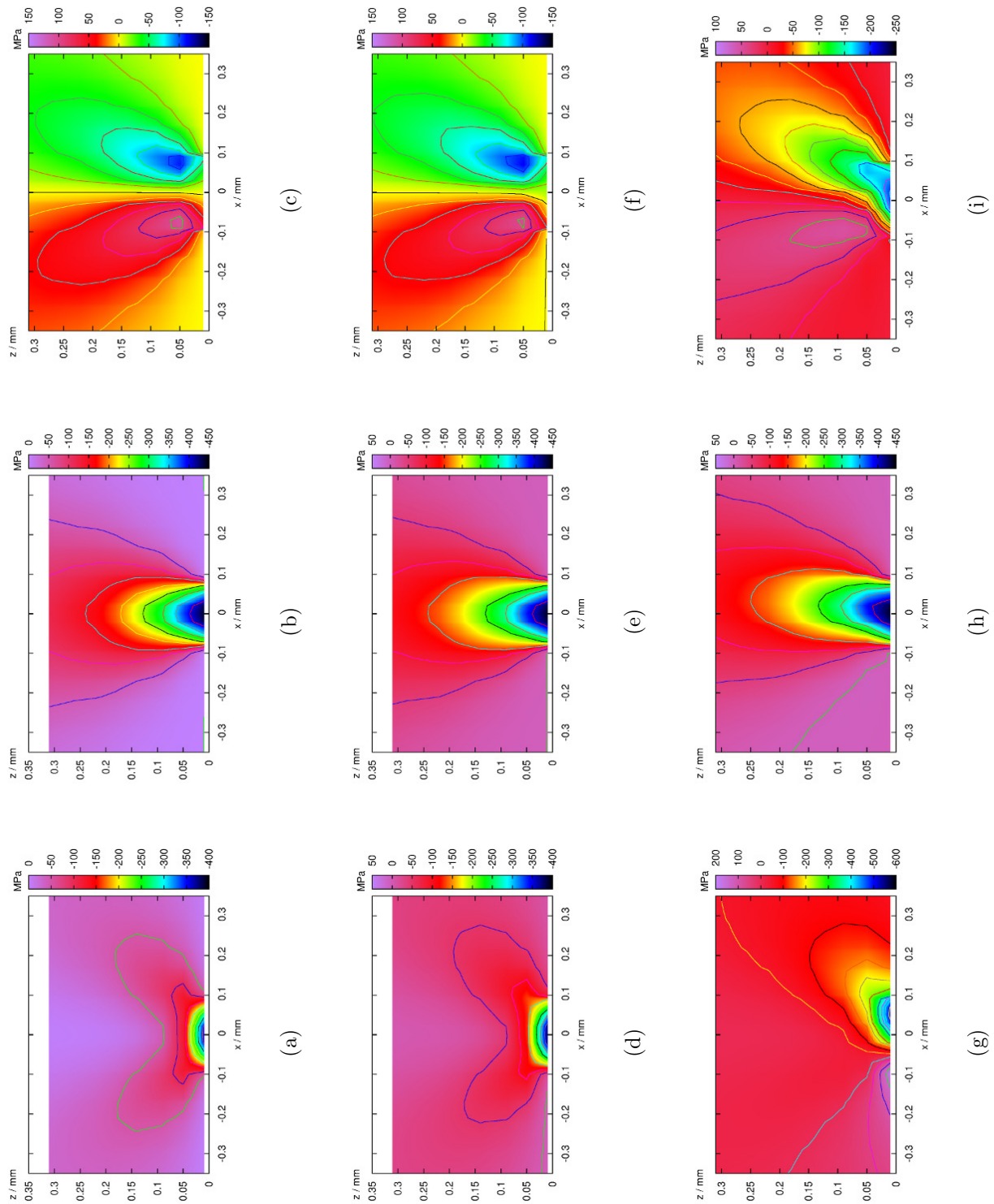

Figure 7.4: Calculation of tractional stress σ_x, normal stress σ_z and shear stress τ_{xz} for $l = 5\,\mathrm{mm}$. (a-c) Assuming perfect rolling, (d-f) roll-slide parameter $\xi = 0.95$, assuming marginal slip, and (g-i) assuming perfect sliding of rolling/sliding cylinders.

The intense deformation due to the traction of rolling/sliding remains limited within ∼5 μm of the surface and decreases sharply thereafter. This is a striking feature of this particular nanostructured bainite studied here compared to earlier work [5,6] where samples were tested under similar conditions. Leiro *et al.* found significant deformation of the microstructure, up to 20 μm from the wear surface, together with fatigue cracks and porosity in the microstructure [5, 6]; the results were explained by adhesion and subsequent elastic-plastic deformation of surface asperities augmenting a microscopic three-body abrasion effect. The observations are consistent with the fact that the wear rate recorded is the smallest of all the data presented in Fig. 7.3, in spite of the fact that the material is not the hardest available. It can only be speculated that the work-hardening capacity of the present material is large enough to limit the depth of deformation.

7.3.6 Nanoindentation tests

Nanohardness values measured on the polished cross-sectional specimen are plotted against the distance below the contact surface in Fig. 7.6. Significant hardening is detected under the surface, at a depth of some 40-50 μm. This is an important observation in the context of the calculations presented in Fig. 7.4, where the maximum shear stress under rolling-sliding conditions is predicted to be at approximately this depth. In contrast, if sliding plays a role in the process of wear, then the maximum shear stress is at the surface. This combination of results gives a clear interpretation that the mechanism of wear in the present case does not involve sliding, but rather, just rolling and sliding.

It is worth comparing the present data with previous work on carbide-free bainite. The earlier work [6] noted that adhesion contributed to the wear process, and that cracks were observed to initiate from the surface, with delamination contributing to the damage. In these circumstances, it is not surprising that the depth of the deformation zone was larger than in the present case. Although the steels studied [6] have a similar structure to the nanostructured bainite observed, there could be a number of explanations for the difference in behavior. In particular, Fig. 7.6 shows sub-surface hardening coincident with the depth at which the maximum shear stress occurs during rolling contact - the hardness has increased to some 750 HV, possibly due to the stress-induced transformation of retained

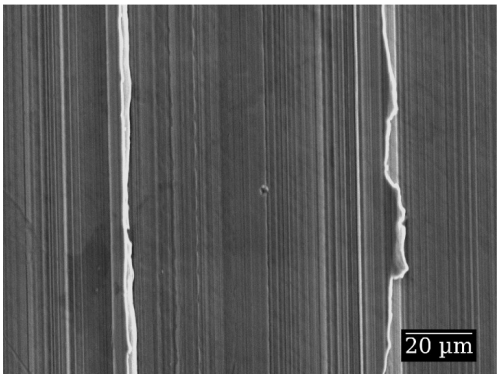

(a)

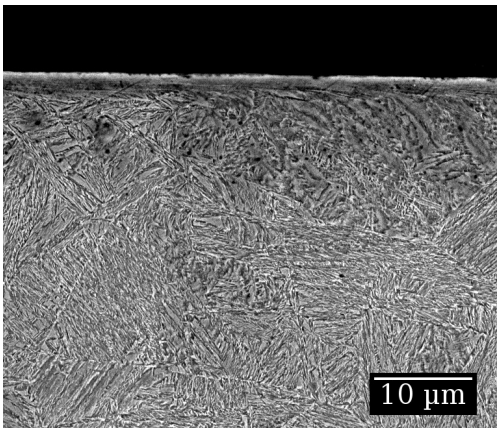

(b)

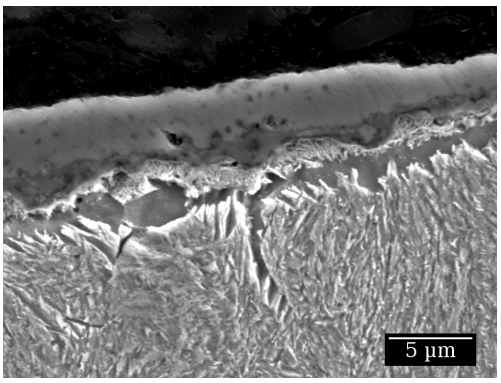

(c)

Figure 7.5: Structure after rolling-sliding (a) showing wear tracks on the surface with ledges indicating plastic deformation of the surface, (b) limited subsurface deformation of the microstructure in the direction of rolling/sliding and (c) a very thin non-etching layer on the surface.

austenite into hard martensite. This would make the material more resistant to rolling contact damage since the fine martensite that forms from the thin films of austenite in the present alloy would resist cracking [246]. Therefore, the mechanical stability and size-scale of the austenite could vary as a function of alloy content, and it is noteworthy that all the alloys reported in [6] were transformed at a higher temperature and for shorter times, leaving the possibility of blocky austenite or the presence of some martensite in the initial structure.

It will also be seen from the X-ray data on the present alloy, that while the austenite at the very surface of the sample undergoes some transformation, the majority of it remains stable, which would add to the ductility and toughness of the surface layer.

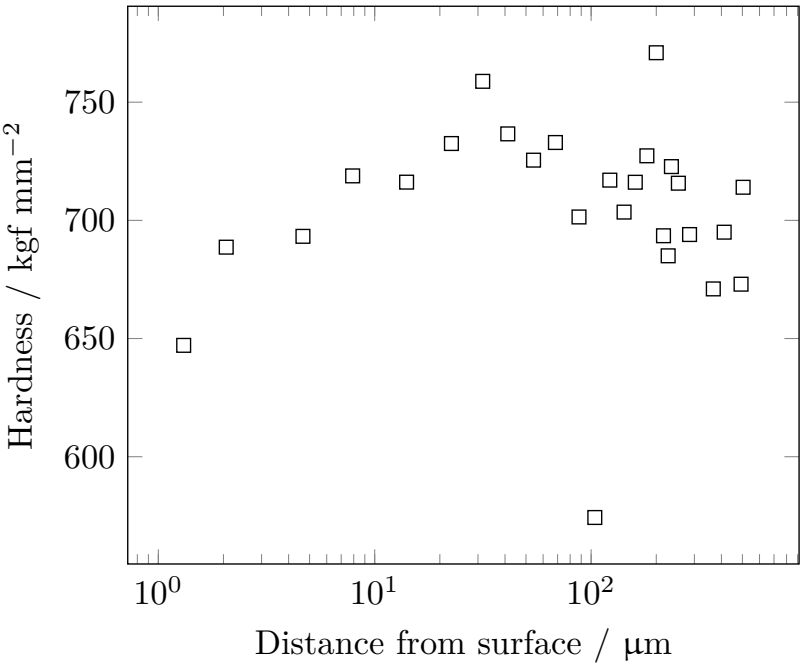

Figure 7.6: Distribution of nanohardness of the surface and subsurface layers after rolling/sliding as measured by nanoindentation.

7.3.7 X-ray diffraction

X-ray diffraction spectra taken before and after wear tests are illustrated in Fig. 7.7 and the quantitative phase analysis using full pattern Rietveld analysis using both X'Pert HighScore+ and MAUD [247] is listed in Table 7.3.

Individual reflections from the diffracting planes of fcc-austenite and bcc-ferrite are labeled in the Fig. 7.7. Bragg reflections from the $\{110\}_\alpha$, $\{200\}_\alpha$, $\{211\}_\alpha$, $\{220\}_\alpha$, $\{310\}_\alpha$ and $\{222\}_\alpha$ planes along with $\{200\}_\gamma$, $\{220\}_\gamma$ $\{311\}_\gamma$ reflections could be identified over the scanned 2θ range. Peaks of bcc-ferrite and bct-martensite had less than 0.1° separation and therefore could not be deconvoluted. As the temperature during rolling/sliding did not go beyond 29°C, the possibility of re-austenitisation of ferrite and subsequent transformation to martensite is neglected.

The relative intensity of the austenite peaks was diminished after wear testing, indicating stress-affected transformation into martensite. It is interesting, however, that the decrease in content was from 27.9 ± 0.4 vol% to 17.3 ± 0.3 vol%, meaning that the majority of the austenite remains stable under conditions where there is intense deformation at the surface. This is undoubtedly a consequence of a phenomenon known as mechanical stabilisation [248, 249], where the plastic deformation of austenite prevents martensitic transformation because the latter requires the existence of a glissile interface. It is likely that the effect is exaggerated by the fact that the austenite is present in a finely divided state - a reduction in the grain size of austenite reduces its martensite-start temperature [250, 251].

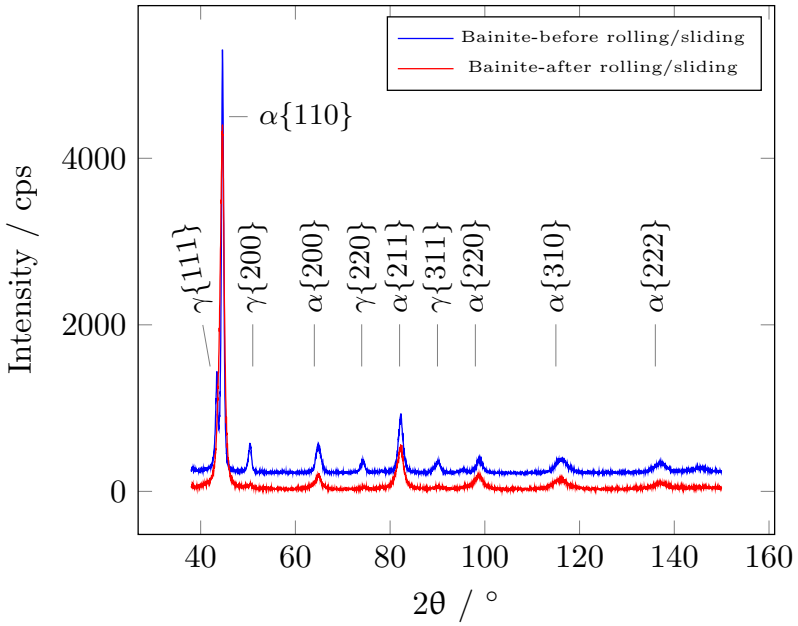

Figure 7.7: X-ray diffraction of bainite before and after rolling/sliding indicating strain induced transformation of retained austenite.

The broadening of diffraction peaks was studied to assess further the structural changes due to wear, associated with the retained austenite. The Williamson-Hall plots in Fig. 7.8 are able to separate the size of coherent domains from heterogeneous strains due to defects in the material [252]. The quantitative data obtained is listed in Table 7.3. It is interesting that they show that the extent of heterogeneous strain due to defects such as dislocations has not change sufficiently to mechanically stabilise austenite. Instead, the size of the austenite regions has been greatly refined, presumably by the formation of some martensite. The calculations [251] indicate that such a refinement would lead to a dramatic decrease in the martensite-start temperature. A calculation using the method described in [253] shows a drop in martensite start temperature from -54 °C to -70 °C as the coherent diffracting domain size of the austenite is reduced from 20 nm to 6 nm. It is concluded therefore that the stabilisation of the austenite must occur at the early stages of deformation, by plates of martensite sub-dividing the regions of austenite.

Table 7.3: Volume percent of austenite V_γ, crystallite size D and microstrain ε data, the latter presented for both the Gaussian and Lorentzian peak shapes. The 111, 002, 022, 113 and 222 reflections of austenite were included in the analysis.

		Gaussian		Lorentzian	
	V_γ	D	ε	D	ε
Before wear	27.9 ± 0.4	16.5	0.0014	20.0	0.0009
After wear	17.3 ± 0.3	6.0	0.0016	6.4	0.0011

7.4 Conclusions

The wear of a nanostructured mixture of bainitic ferrite and carbon-enriched retained austenite under rolling-sliding conditions has been studied, and the following general conclusions can be drawn from the combination of experimental work and theoretical analysis:

1. The fine structure produced by isothermal transformation at 200°C exhibits the lowest specific wear rate of any carbide-free bainite studied previously

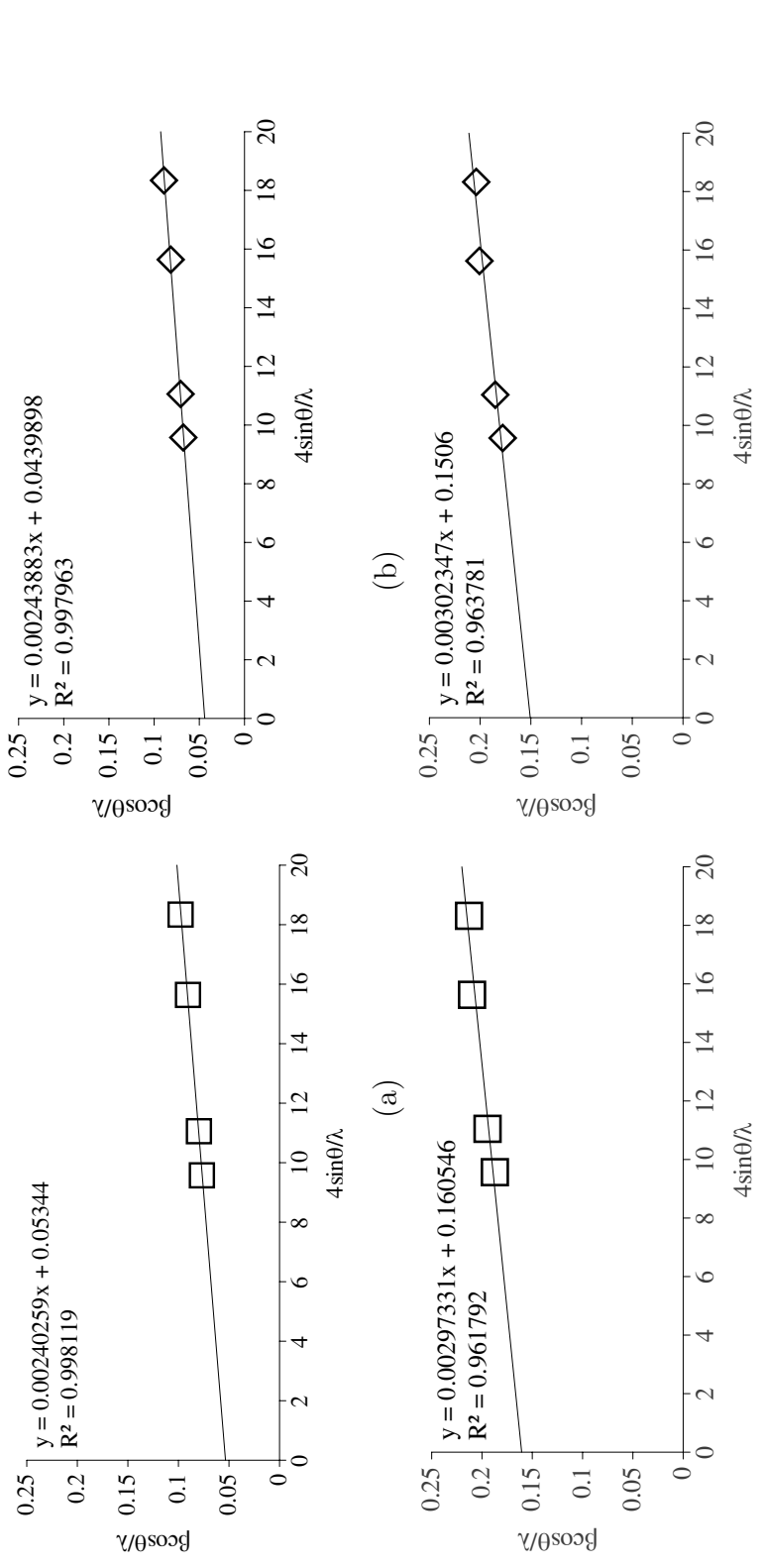

Figure 7.8: Williamson-Hall plot for austenite (a) before rolling/sliding assuming Gaussian peak broadening, (b) before rolling/sliding assuming Lorentzian peak broadening, (c) after rolling/sliding assuming Gaussian peak broadening and (d) after rolling/sliding assuming Lorentzian peak broadening.

under similar circumstances, even though the hardness is less than that attained in previous work. The significant difference here, apart from the 35 nm scale of the structure, is that the retained austenite content is about 27%. This provides a mechanism of work hardening that leads to an increase in hardness in the affected zone.

2. Rolling/sliding calculations suggest that in the absence of sliding, the maximum shear stresses should occur at a depth of about 50 μm below the contact surface, whereas pure sliding would lead to the maximum located at zero depth. Experimental results show that there is a significant peak in nanohardness developed, also at a depth of about 50 μm, indicating that sliding did not play a significant role in the mechanism of wear.

3. The absence of sliding under the conditions studied is consistent with the very low specific wear rate observed, and the topology of the wear surface following the tests.

4. The subsurface hardening mechanism will, as indicated by X-ray analysis, involve some transformation of the austenite into hard martensite, contributing to the change in hardness from about 650 to more than 750 kgf mm^{-2}. The sub-surface hardened regions did not reveal any evidence of damage, probably because any martensite that forms is itself very fine, and because the austenite that remains is mechanically stabilised against further transformation.

5. The work demonstrates a clear role of structure in the optimisation of wear by the mechanism believed to operate here. A general conclusion therefore, is that in addition to hardness, wear can be reduced by engineering the structure to contain some stable austenite, the stability of which is determined not just by a high carbon concentration, but also its fine scale. These results are relevant to the design of novel bearing steels based on nanostructured, carbide-free bainite, particularly because sliding has been avoided under dry conditions.

Chapter 8

Dry rolling/sliding wear of martensite

8.1 Introduction

Ferrous martensite is generally found to exhibit superior wear resistance compared to ferritic, pearlitic and bainitic structures owing to its high hardness and strength [254–257], although contradictory views exist [173, 258, 259]. The high hardness of untempered martensite resists indentation during impact and/or scoring by abrasives, whereas the strength of the structure keeps the deformation to the elastic regime as long as the contact stresses do not exceed the elastic limit. Moreover, the hardness of martensite prevents adhesion of meeting surfaces during wear and hence limits the wear mechanism to abrasion [260]. Because of these reasons, improvement in the rolling/sliding wear resistance by forming a thin layer of martensite on the surface of a rail or wheel by laser hardening is common [261–263], though the process of laser hardening results in additional benefits of solid solution strengthening, dislocation hardening, grain refinement and development of favourable residual stresses [264].

However, high-carbon plate martensite suffers from poor impact and fracture toughness which makes it susceptible to catastrophic failure initiated at local inhomogeneities. To mitigate this, the ductility may be enhanced by (a) tempering to precipitate excess carbon and (b) having a controlled amount of retained austenite in the hard martensitic matrix. Most of the commercial wear-resistant

martensitic steels are tempered to attain a mixed microstructure of tempered martensite and alloy carbides which offers an attractive combination of strength and toughness with some loss in bulk hardness [265]. These alloy carbides can be beneficial as long as wear resistance is controlled by hardness, but beyond that, they are small and dispersed so are easily extracted by hard abrasives. In those circumstances, they do not do not contribute towards this mode of wear resistance [197, 266].
A benefit of retained austenite is in enhancing the overall work-hardening rate and increasing the hardness during deformation-induced martensitic transformation. The fracture toughness may also be increased due to the same effect [266]. However, the volume fraction, stability and morphology of austenite plays a significant role in wear resistance. The volume fraction is important in context of the extent of transformation-induced plasticity that can be harvested. The mechanical stability of retained austenite is also a crucial parameter, as, very unstable austenite would transform completely at low plastic strains or an exceptionally stable austenite would not contribute sufficiently to strain hardening.
The experimental alloy has been air-cooled to 23 °C from its austenitising temperature $\sim$930 °C to produce hard plate martensite. The objective of the present work is to explain the observed wear behavior of the mixed microstructure by analysing the damage beneath the wear surface using appropriate characterisation techniques and mathematical modelling of the dry rolling/sliding process.

8.2 Experimental Procedure

Following rolling/sliding wear of bainite, fresh discs made from the same alloy, as mentioned in Chapter 6, Table 6.1, was austenitised and air-cooled to form martensite. Bulk hardness was measured after heat treatment and the rolling/sliding surfaces was polished to the required roughness before wear. Weight loss was measured after rolling/sliding and normalised against load and sliding distance to calculate the specific wear rate. This was compared with fine pearlite and nanostructured bainite to observe any change in SWR with increasing bulk hardness. The worn surface was characterised using metallography techniques and X-ray diffraction to understand the observed wear rate and damage.

8.3 Results

8.3.1 Microstructure

A secondary electron image of the heat treated sample showing coarse martensite plates along with blocks of austenite is shown in Fig. 8.1(a).

8.3.2 Surface roughness

The surface roughness parameters measured before and after wear are listed in Table 8.1. The average roughness, R_a, was found to decrease marginally after rolling/sliding, indicating mild abrasive wear. The interferometry images, Fig. 8.2(a-d), show smoothing of the surface and the absence of any flat plateau indicates that adhesive wear did not occur. Whereas the tractional stress, σ_x, demolishes the asperities, the compressive stress, σ_z, causes blunting leading to a reduction in R_a.

Table 8.1: Surface roughness parameters of discs before and after rolling/sliding. Data for nanostructured bainite (ref. Chapter 7) are presented for comparison.

	Disc 1		Disc 2	
	before test	after test	before test	after test
Untempered martensite, 780 kgf mm^{-2}				
Average roughness R_a/ µm	1.3	1.2	1.3	1.2
Distance between highest crest and lowest trough R_z/ µm	1.7	1.6	1.6	1.5
Maximum height of ridges R_t/ µm	11.5	12.5	9.4	13.8
Nanostructured bainite, 640 kgf mm^{-2}, (ref. Chapter 7)				
R_a/ µm	1.3	1.1	1.1	1.1
R_z/ µm	7.0	13.9	7.0	11.4
R_t/ µm	7.5	15.2	7.2	11.8

8.3.3 Wear data

Fig. 8.3 shows the specific wear rate (SWR) as a function of the bulk hardnesses for the microstructures tested under similar conditions [5, 6, 120, 127]. SWR decreases as the hardness increases, with saturation setting in at very high hardness, so that *Bainite* 200 performs similarly to martensite inspite of an increase in 1.5 GPa in hardness. An extremely fine scaled carbide-free bainite shows impres-

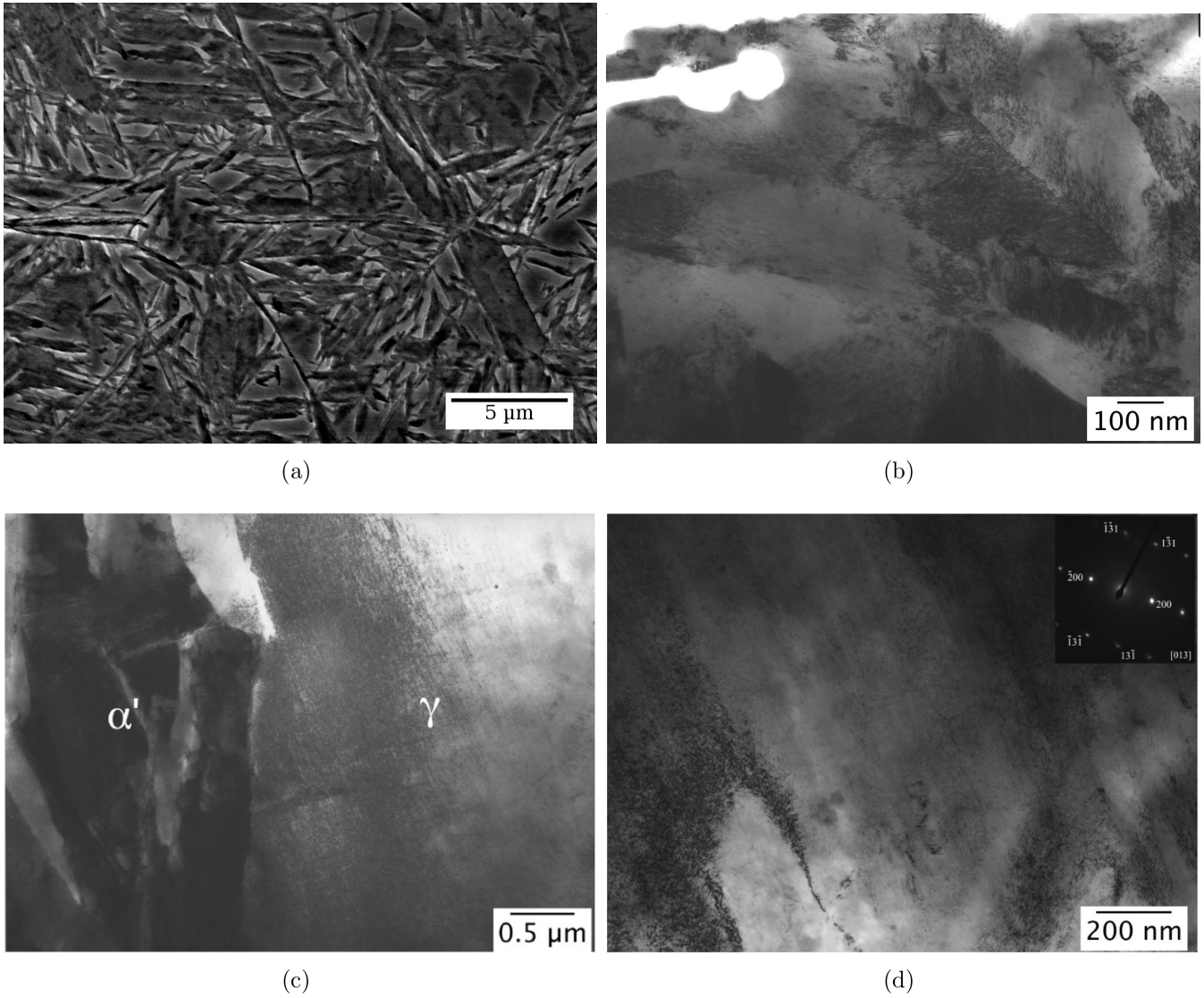

(a) (b)

(c) (d)

Figure 8.1: Scanning and transmission electron images of air-cooled martensite (a) secondary electron image showing plate martensite and blocky retained austenite, bright field TEM image of (b) martensite, (c) martensite-austenite boundary and (d) blocky retained austenite.

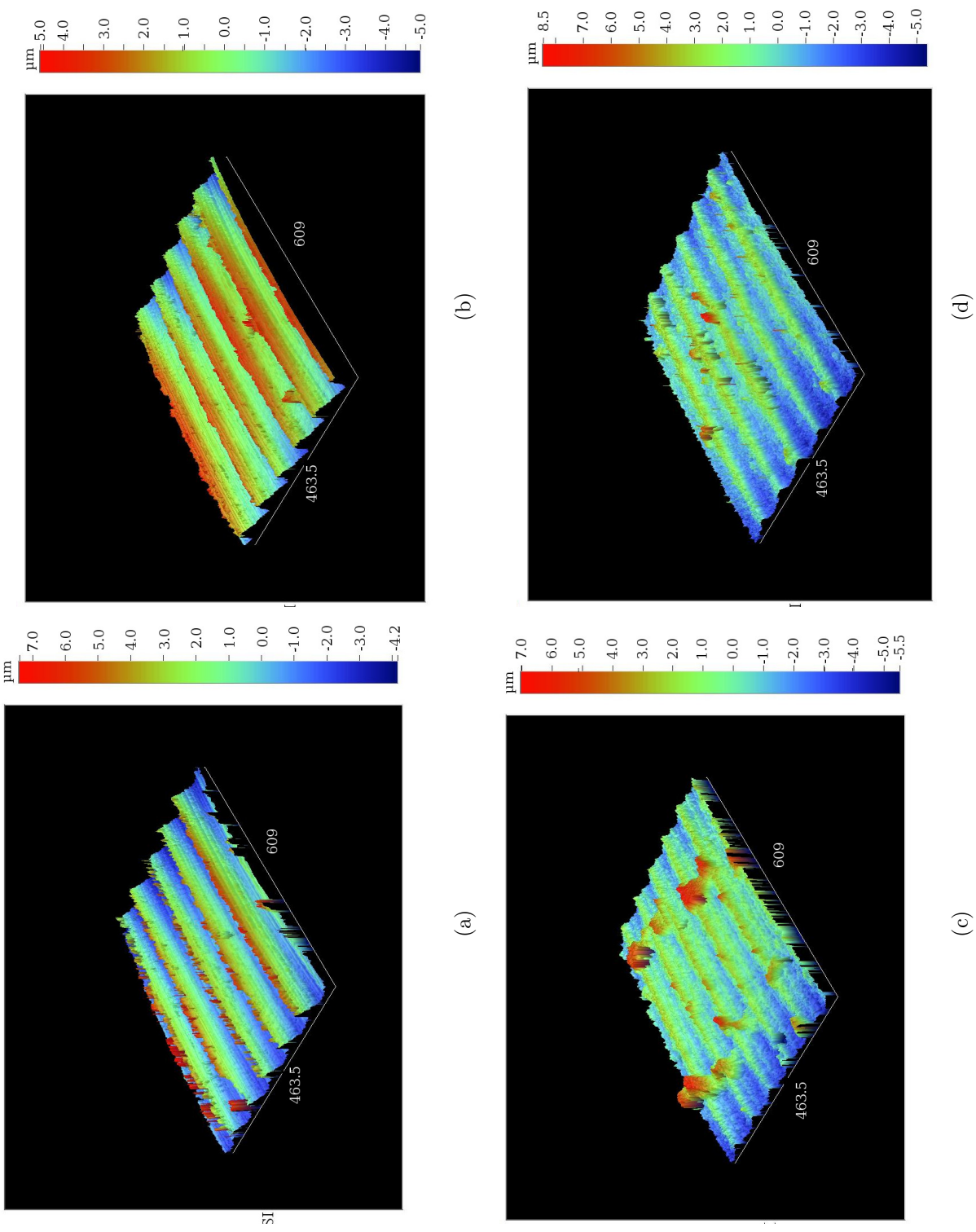

Figure 8.2: Surface topography observed using light interferometry, (a) before rolling/sliding, (b) after rolling/sliding.

sive wear resistance due to work-hardening and transformation plasticity [Chapter 7], whereas plates of hard untempered martensite resist deformation.

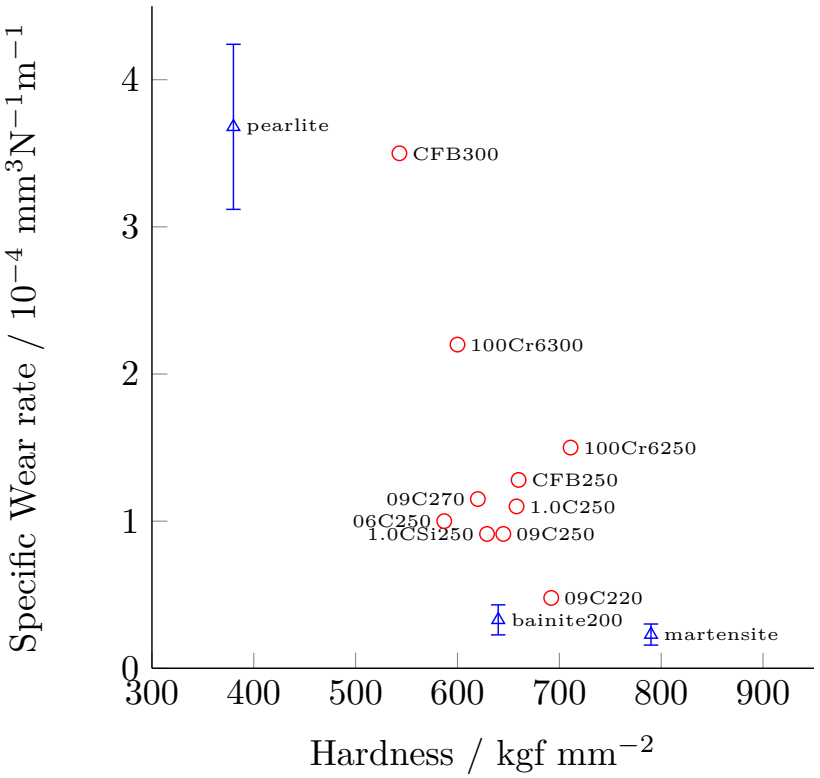

Figure 8.3: Specific wear rate of martensite after rolling/sliding compared against a few other commercial steels and experimental alloys with pearlitic [Chapter 6] and bainitic microstructures [Chapter 7].

8.3.3.1 Dynamic coefficient of friction

The magnitude and distribution of contact stresses at and below the rolling/sliding surface have been calculated based on Hertzian theory [95, 221].

Fig. 8.4(a) shows the dynamic coefficient of friction (COF) with the progress of wear. Once a steady-state is attained, the marginal increase in the coefficient indicates work-hardening of the martensite. Considering the maximum and the minimum values of the coefficient of friction, the change in σ_x, σ_z and τ_{xz} have been calculated and were found to be negligible, as shown in Fig. 8.5(a-d).

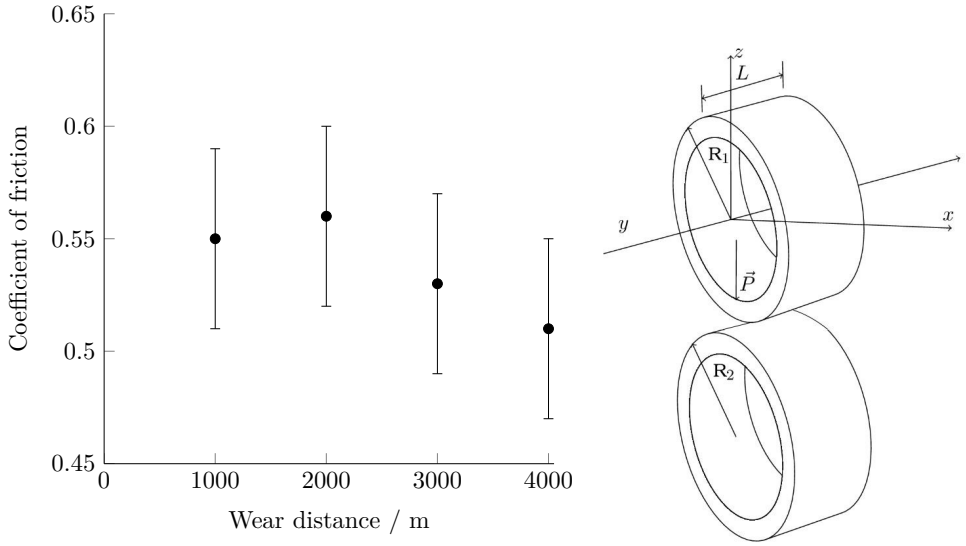

(a) (b)

Figure 8.4: (a) Measured dynamic coefficient of friction as a function of the wear distance, (b) Coordinate system with schematic of twin disc set up.

8.3.4 Contact stresses during rolling/sliding

The estimated magnitude and distribution of contact stresses around the line of contact in the xz plane are shown in Fig. 8.6. The assumption of 5% slip in the model keeps the maximum shear stress below the surface, at a depth ≈50 μm from the rolling/sliding surface. The calculations underestimate reality, as the model assumes geometrically smooth surfaces and elastic deformation. Roughness would exaggerate the contact stresses and induce local plastic deformation at asperities.

The effects described here are minor and probably incorrect in the context of damage given the assumptions. The main result is that the maximum shear stress occurs below the surface and that remains valid, and as seen later, backed by experimental data that show a sub-surface peak in hardness following rolling/sliding contact. The trailing zone from the line of contact increased with stronger distribution [*purple zone* in Fig. 8.7(b,d,f)], whereas, the maximum value of the negative shear stress drops. The effect of these changes on the magnitude and distribution of shear stress is most prominent below the surface and at a depth $\approx 0.78b$, where b is the Hertzian contact half width and gradually diminishes to zero at larger distance from the rolling/sliding surface. This oscillating nature of shear stress below the surface with high frequency causes the brittle martensite to

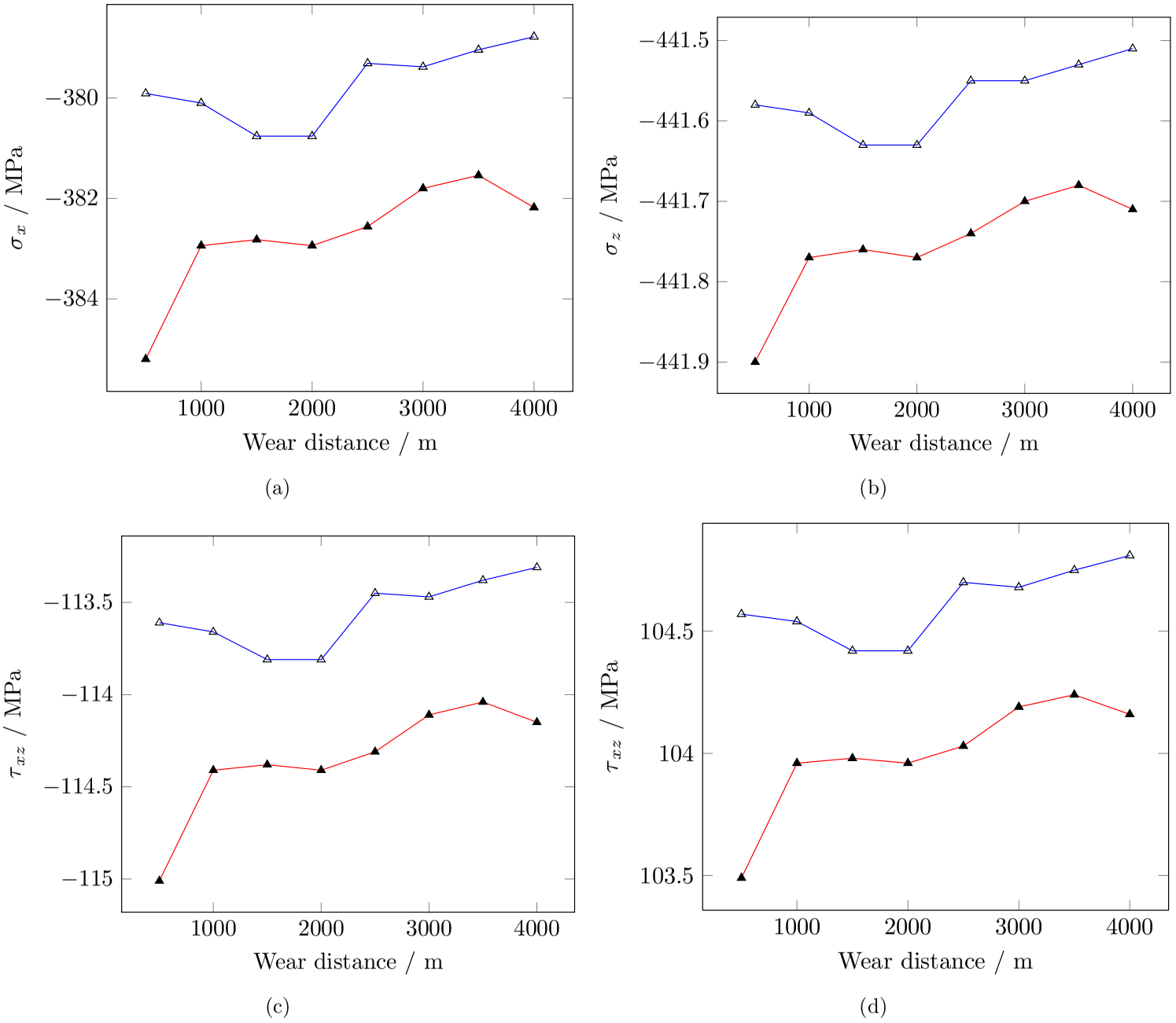

Figure 8.5: Change in (a) σ_x, (b) σ_z and (c-d) τ_{xz} for minimum (blue line) and maximum (red line) value of coefficient of friction at specified wear distance.

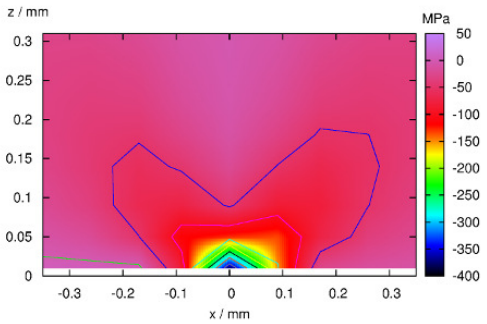

(a) σ_x

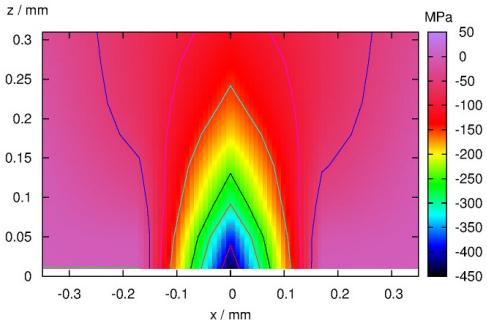

(b) σ_z

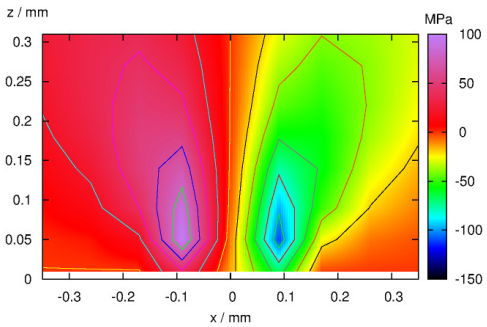

(c) τ_{xz}

Figure 8.6: Distribution of tractional, compressive and shear stresses calculated assuming $\mu = 0.63$ at $d = 1000\,\mathrm{m}$.

fatigue which is evidenced by the formation of numerous voids and micro-cracks below the surface, as shown in Fig. 8.8(c).

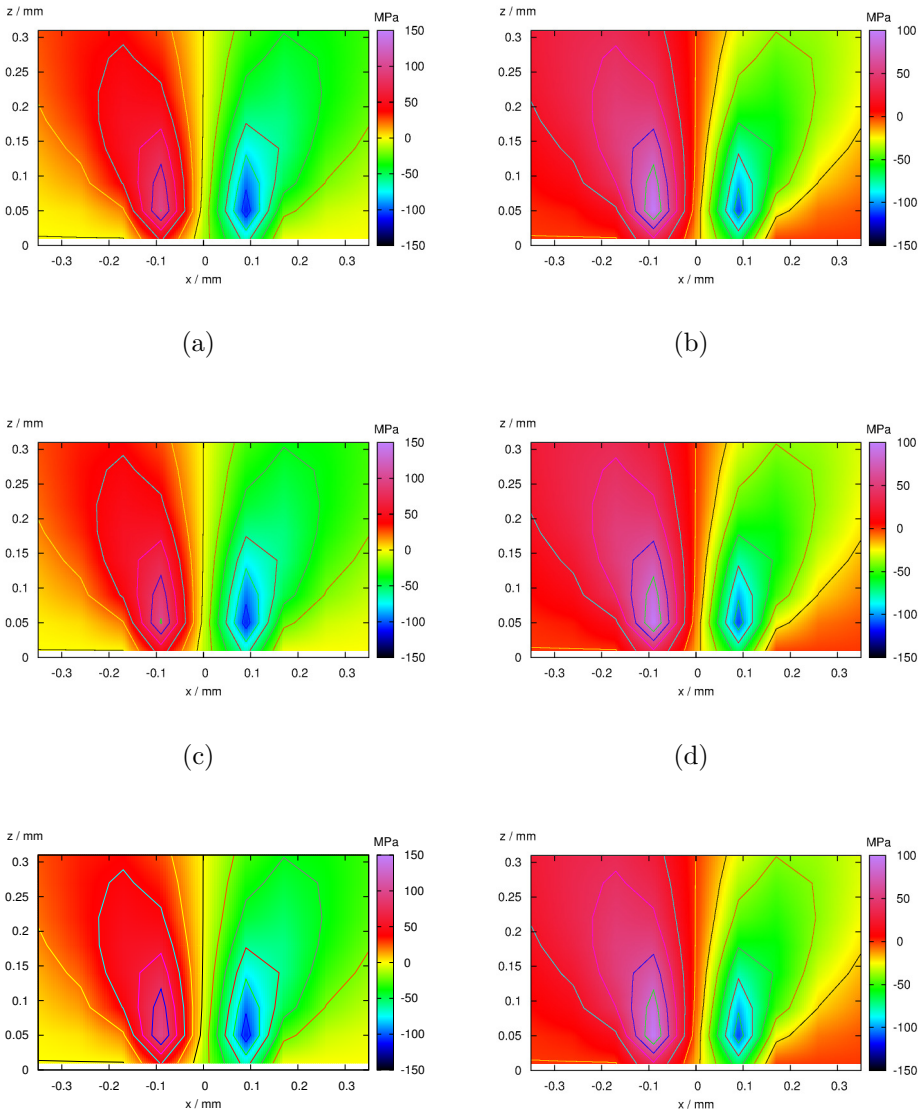

Figure 8.7: Variation in the shear stress with change in the dynamic coefficient of friction at $d = 1000$ (a-b), 2000(c-d) and 3000 m(e-f).

8.3.5 Scanning electron microscopy

The wear tracks shown in Fig. 8.8(a) are indicative of pure grooving, with almost no sign of adhesive wear. The absence of ledges around the wear tracks indicate negligible plastic deformation in the direction of sliding. This is unlike pearlite or other relatively ductile structures, which often form ledges around the wear tracks and forms adhesive joints between the contact surface, signifying damage due to σ_x and σ_z [Chapter 6]. However, the cross sectional images of the microstructure after rolling/sliding show significant damage under the wear surface. The microstructures in the direction of rolling/sliding, Fig. 8.8(b,c), reveal a large number of voids and small cracks beneath the surface. This is a reflection of the cyclic shear stress that peaks below the surface, causing damage to accumulate there. However, the large compressive component stress, σ_z, keeps these voids from coalescing and thus prevents early spalling. With increased number of cycles the number of voids and cracks would increase, leading to ultimate failure in the form of dramatically increased wear damage due to spalling.
The tractional and compressive stresses, within 0-5 μm of the surface, may assist the transformation of retained austenite into martensite, which is repeatedly deformed making the structure insensitive to chemical etching. This creates the *featureless zone* apparent in the micrographs, Fig. 8.8(c).

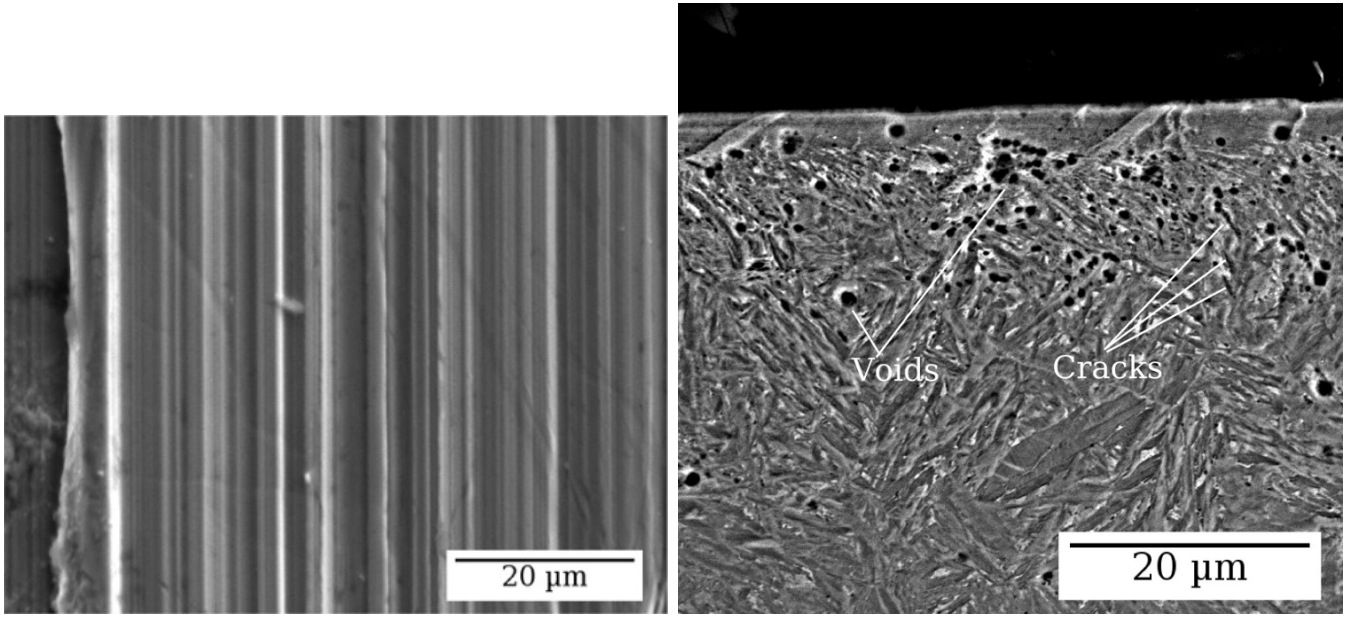

(a) (b)

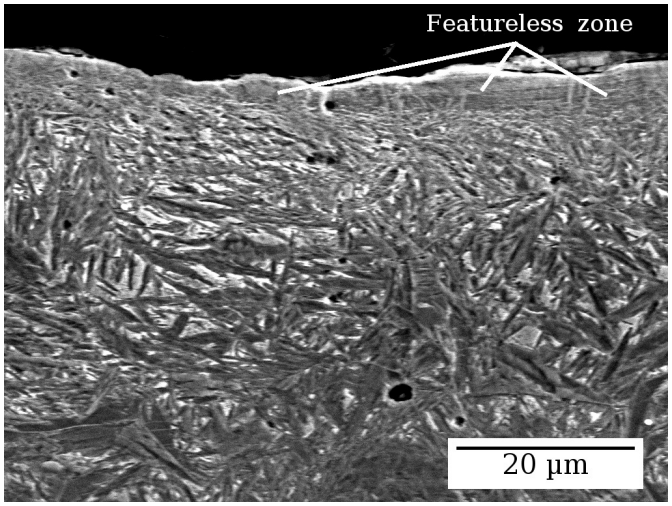

(c)

Figure 8.8: Secondary electron images of (a) wear tracks made after rolling/sliding, and damaged sub-surface structure (c) in the direction of and (d) transverse to the direction of rolling/sliding.

8.3.6 Nanoindentation results

8.3.6.1 Work-hardening

The hardness of martensite due to rolling/sliding has been measured from the slope of the unloading curve of nanoindentation tests and is shown in Fig. 8.9(a) [137]. There is an increase in the hardness compared to the undeformed material within ≈ 25 μm.

Fig. 8.9(b) shows the extent of elastic recovery, h_e, after removal of the indentation load. The deformed microstructure corresponding to the maximum hardness elastically recovers the most compared to unstrained regions, because of its high hardness.

8.3.6.2 Residual stress

Using the residual depth and residual cone angle after withdrawal of the nanoindentation load; the type, magnitude and distribution of residual stress has been calculated and plotted against depth using the theories described in literature [140, 141,143,228]. Fig. 8.9(c) shows the distribution of the compressive residual stress beneath the wear surface after rolling/sliding. The residual stress measured acts in the plane parallel to the wear surface and in the direction of rolling/sliding as other two components of the octahedral stresses are orthogonal and act out of the $x - z$ plane which would not have any effect on wear resistance [230]. The residual stress is compressive and peaks at the surface. This should be beneficial, although it falls off rapidly with depth as shown in Fig. 8.9(c). The maximum value of residual stress is higher than that of pearlite [Chapter 6] tested under similar conditions.

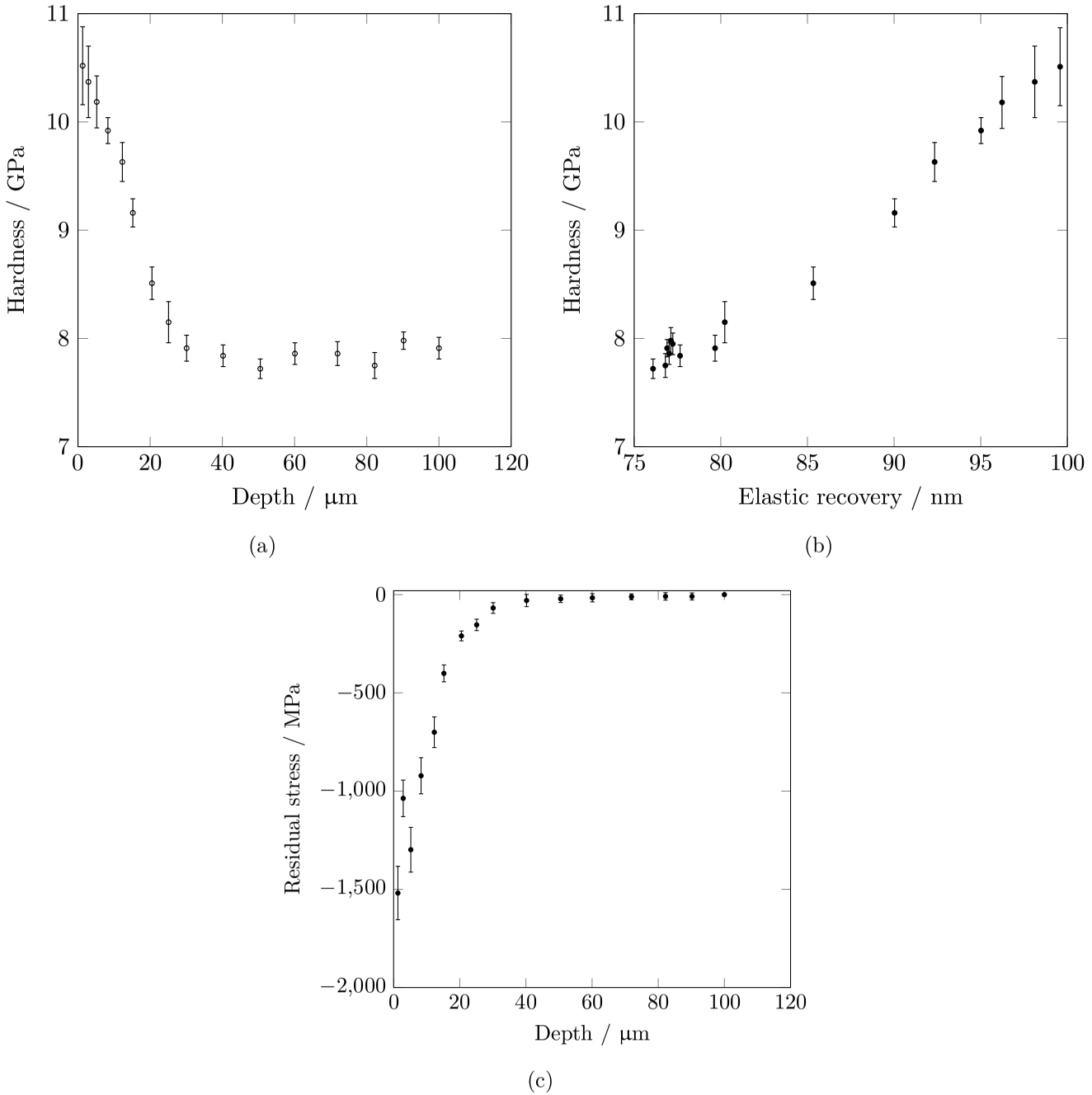

Figure 8.9: Nanoindentation test results; distribution of (a) hardness, (b) elastic recovery and (c) residual stress along the depth after rolling/sliding.

8.3.7 X-ray diffraction

The X-ray diffraction profiles [Fig. 8.10] indicate loss of austenite following wear. A full pattern Rietveld refinement of bct-martensite and fcc-austenite peaks using MAUD [247] was carried out and the results are listed in Table 8.2. An almost complete loss of retained austenite, compared with some 60% reduction in nanostructured bainite tested under similar conditions is noted [Chapter 7]. This is because of the lower carbon concentration of the coarser austenite associated with the martensite.

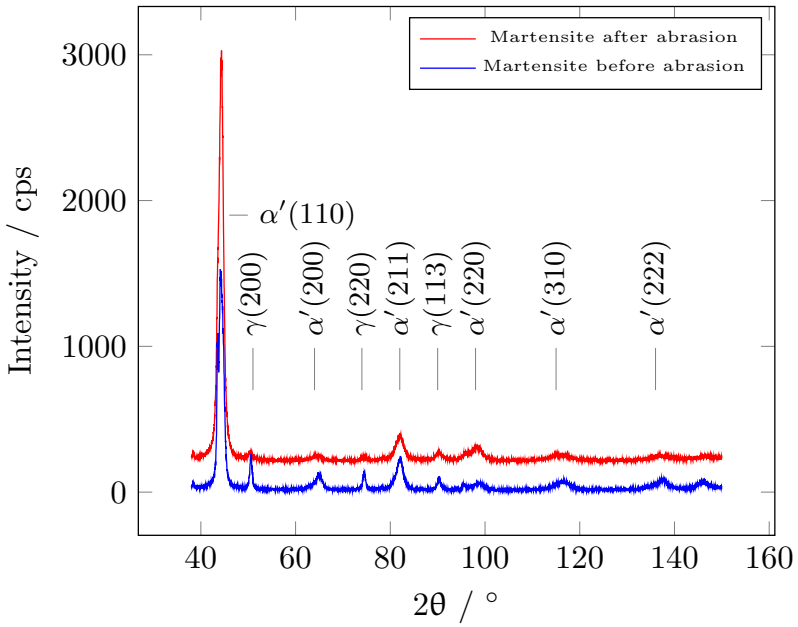

Figure 8.10: X-ray diffraction profiles from the surface of martensitic discs before and after rolling/sliding.

Table 8.2: Full pattern Rietveld analysis of the diffraction spectra before and after rolling/sliding.

	Austenite vol.%
Before rolling/sliding	15.2±3.1
After rolling/sliding	2.6±1.2

8.3.8 Williamson-Hall Plot

Conventional Williamson-Hall plots for diffraction from bct-martensite are shown in Fig. 8.11(a-d). The size of the coherent domain and the microstrain have been calculated using a modified Williamson-Hall approach. The increased non-linearity between ΔK against K after rolling/sliding [Fig. 8.11(c-d)] indicates asymmetric broadening of diffraction peaks compared to the unstrained sample [Fig. 8.11(a-b)]. Following the modified Williamson-Hall approach, the dislocation contrast factor, $\bar{C}_{hkl}$ for martensite was introduced to correct the non-linearity [147–149].

Fig. 8.12(a-b) plots the value of $[\Delta K^2 - \alpha]/K^2$ against H^2 from which the parameter q increases from 1.88 to 2.45 after rolling/sliding. Measurement of q at various depths beneath the wear surface [Fig. 8.14(a)] shows no significant change in dislocation character from edge to screw. Therefore, the lowest and the highest values, i.e., 1.88 and 2.45 are taken for calculating the average dislocation contrast factor, $\bar{C}_{hkl}$.

The C_{200} value has been calculated for the bct-martensite as a function of the elastic constants, c_{11} = 268.1 GPa, c_{22} = 268.4 GPa, c_{44} = 79.06 GPa and c_{12} = 111.2 GPa respectively [267] using eqn. 8.1 [148],

$$C_{h00} = a[1 - \exp(A_i/b)] + cA_i + d \tag{8.1}$$

where,

$$A_i = 2c_{44}/(c_{11} - c_{12}) \tag{8.2}$$

A_i for Fe-martensite is about unity and c_{12}/c_{44} is 1.40. Since, $\bar{C}_{h00}$ is insensitive to A_i for $1<c_{12}/c_{14}<2$, it is assumed that $\bar{C}_{200}^{edge} = 0.2648$ and $\bar{C}_{200}^{screw} = 0.3055$ [148]. Based on these values, $\bar{C}_{hkl}$ was calculated for other planes, as listed in Table 8.3.

ΔK was re-plotted against $K\bar{C}_{hkl}^{1/2}$ as are shown in Fig. 8.13(a-d) which yields a better correlation. However, if the extent of asymmetrical broadening in diffraction peaks can be expressed as $d\Delta K/d(K\bar{C}_{hkl}^{1/2})$, then, ferrite of pearlite shows

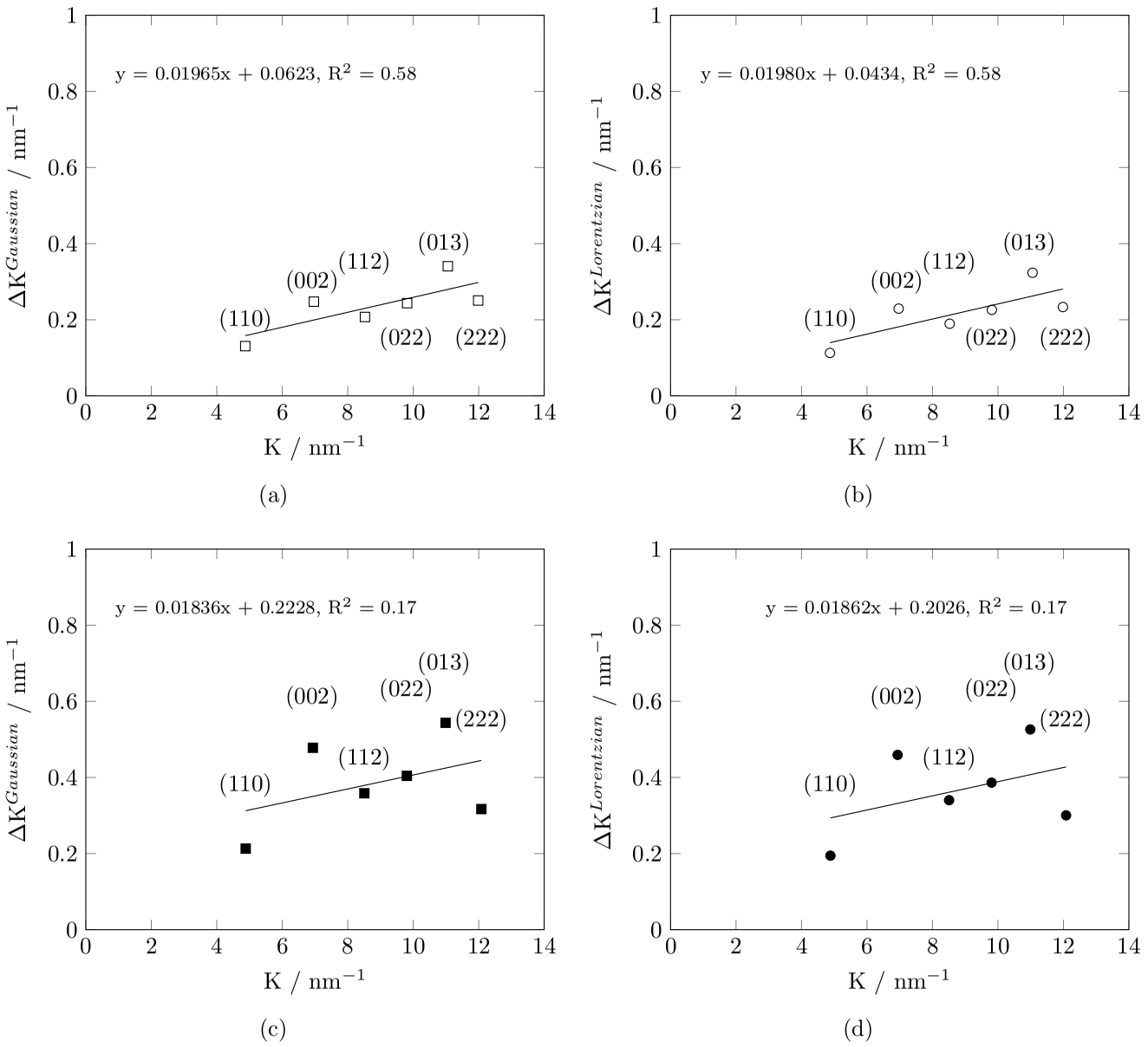

Figure 8.11: Conventional Williamson-Hall plot of bct-martensite peaks before rolling/sliding assuming (a) Gaussian, (b) Lorentzian peak broadening and after rolling/sliding assuming (c) Gaussian and (d) Lorentzian peak broadening.

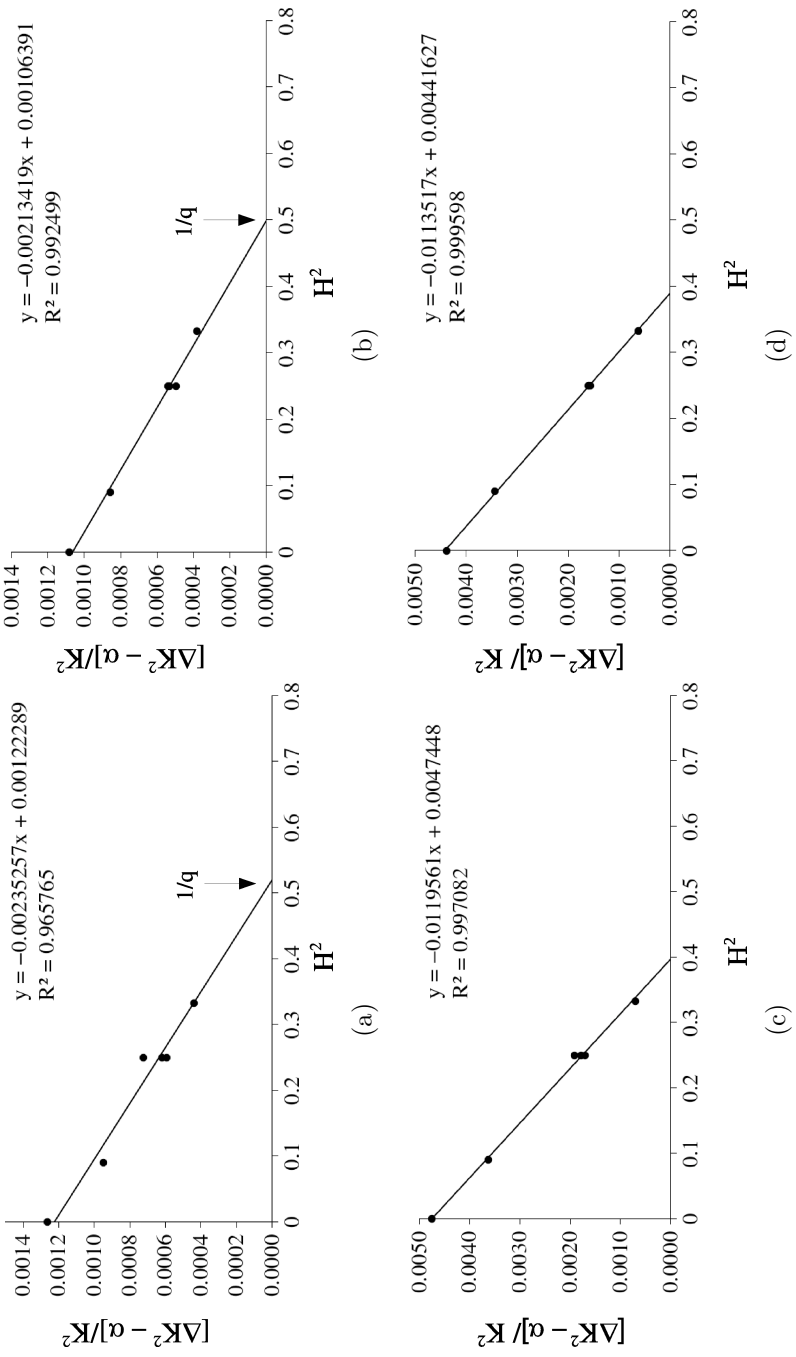

Figure 8.12: $[\Delta K^2 - \alpha]/K^2$ vs. H^2 plot for bct-martensite peaks (a,b) before rolling/sliding and (c,d) after rolling/sliding assuming Gaussian and Lorentzian peak broadening.

Table 8.3: Average dislocation contrast factor of pure edge and pure screw dislocations for *hkl* planes in bcc-α Fe before and after rolling/sliding.

	$q = 1.88$		$q = 2.45$	
{hkl}	$\bar{C}_{hkl}^{edge}$	$\bar{C}_{hkl}^{screw}$	$\bar{C}_{hkl}^{edge}$	$\bar{C}_{hkl}^{screw}$
{110}	0.10921	0.1260	0.1026	0.1183
{002}	0.2648	0.3055	0.2648	0.3055
{112}	0.1092	0.1260	0.1026	0.1183
{022}	0.1092	0.1260	0.1026	0.1183
{013}	0.2087	0.2408	0.2064	0.2381
{222}	0.0573	0.0661	0.0485	0.0560

Table 8.4: Average size of the coherent domains of diffraction in bct-martensite after rolling/sliding, as a function of the diffraction peak shape.

Dislocation type	Coherent domain size / nm	
	Gaussian	Lorentzian
edge	7	8
screw	7	8

more asymmetrical broadening [Chapter 6] of high order peaks compared to that of martensite.

The size of the coherent domains of diffraction before rolling/sliding calculated from the y-intercept of Fig. 8.11(a-d) which was found to decrease from 16-23 nm to 7-8 nm after rolling/sliding [Table 8.4] and its variation as a function of depth is plotted in Fig. 8.14(b).

8.3.9 Modified Warren-Averbach analysis

The modified Warren-Averbach analysis using Convolutional Multiple Whole Profile fitting [268] reveals a marginal increase in the dislocation density from 2.20×10^{16} m^{-2} at a depth equal to 50 μm to 2.55×10^{16} m^{-2} at the rolling/sliding surface [Fig. 8.14(c)]. The increase in dislocation density is less than that observed in ferrite of pearlite [Chapter 6] signifying limited plastic strain accommodated by brittle martensite and also limited to a smaller depth ($\approx$20 μm)

Figure 8.13: ΔK vs. $K\bar{C}^{1/2}_{hkl}$ plot for bct-martensite peaks after rolling/sliding assuming (a) Gaussian peak broadening with pure edge dislocations, (b) Gaussian peak broadening with pure screw dislocations, (c) Lorentzian peak broadening with pure edge dislocations, (d) Lorentzian peak broadening with pure screw dislocations.

owing to its high yield stress.

The change in the type of dislocation, as estimated from the weighted fraction of q-parameter according to eqn. 8.4, is listed in Table 8.5, which indicates possible cross-slip of dislocations to accommodate plastic strain.

$$f_{\alpha'(edge)} = \frac{2.8 - q_{\alpha'}}{2.8 - 1.2} \tag{8.3}$$

$$f_{\alpha'(screw)} = 1 - f_{\alpha'(edge)} \tag{8.4}$$

Table 8.5: Change in the type of dislocation in bct-martensite after rolling/sliding, as a function of the diffraction peak shape with depth from wear surface.

Depth	f_{edge}	f_{screw}
50	0.56	0.44
40	0.53	0.47
30	0.46	0.53
20	0.36	0.63
10	0.27	0.73
2	0.22	0.78

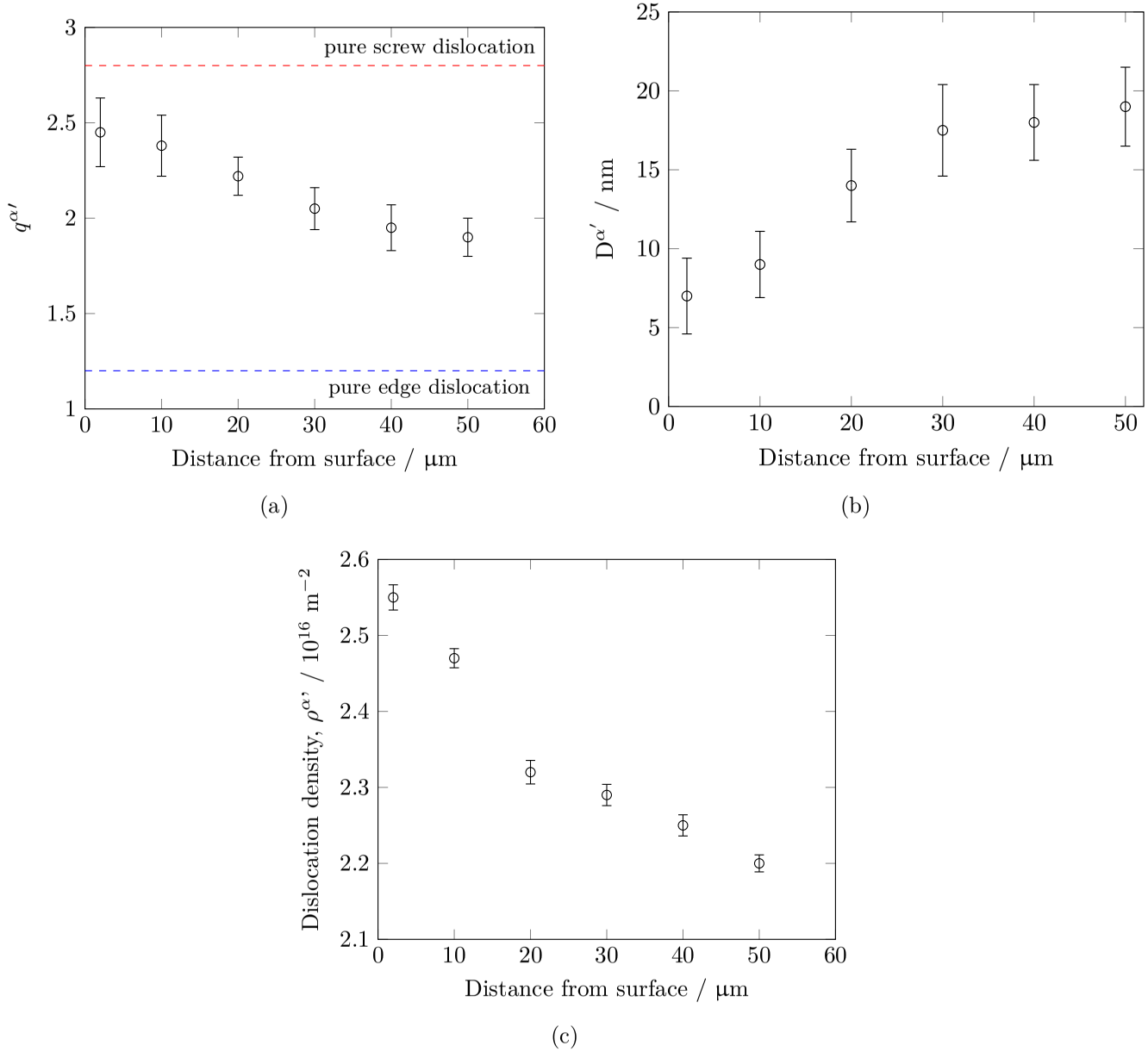

Figure 8.14: (a) Variation in q-parameter, (b) change in the size of the coherent domain of diffraction and (c) dislocation density with distance from the rolling/sliding surface.

8.4 Conclusions

The rolling/sliding wear of a mixed microstructure of martensite and retained austenite has been examined and following general conclusions can be drawn:

1. The high hardness of untempered martensite restricts the wear into type I mild abrasion. An increase in the mean value of the coefficient of friction indicates work hardening of martensite near the wear surface.

2. The dynamic coefficient of friction has a limited effect on the tractional and compressive components of the contact stress but influences the sub-surface shear stress. It is the sub-surface shear stress which causes the accumulation of damage.

3. It is probable that it is the combination of hardness and work-hardening capacity of the mixture of untempered martensite and retained austenite that helps resist wear. However, a sharp drop in compressive residual stress with in a small distance from rolling/sliding surface along with limited ductility of brittle martensite causes greater damage to accumulate underneath the wear surface, which may ultimately lead to spalling.

4. The relatively low carbon and coarse austenite in the microstructure readily undergoes deformation-induced transformation to untempered martensite at the rolling/sliding surface. This itself does not contribute significantly towards wear resistance, whereas, in nanostructured bainite, the more stable austenite significantly reduces wear by accommodating plastic strain.

5. The extent of asymmetric broadening in the crystallographic planes of martensite due to the strain of rolling/sliding is less compared to the ferrite of pearlite tested under similar conditions.

Chapter 9

General Conclusions and Future Work

This dissertation is an account of a set of investigations carried out around the abrasive wear behavior of three radically different structures in the same steel. The objective was to understand the role of individual phases and variation in hardness of the composite structures on wear resistance. An approach based on contact stress modelling and detailed characterisation of the worn surface assisted in understanding the response of fine scale pearlite, nanostructured bainitic ferrite, retained austenite and untempered martensite to a variety of conditions of loading during abrasion. It is possible that the work will lead to commercial products that are designed without, for example, placing excessive faith in the relationship between hardness and wear damage.

Three-body abrasive wear of extremely fine pearlite, nanostructured bainite and untempered martensite with radically different hardnesses has been investigated. It was found that although the abrasion rates and wear coefficients were not very different for the three states, the mechanisms of abrasion were quite different. A clear transition from the sliding of abrasives resulting in extensive micro-cutting of hard martensite, to stopping and pitting for pearlite has been revealed. The fine-scaled pearlite showed extensive deformation in the direction of abrasion with possible partial dissolution of cementite into the surrounding matrix of ferrite. The high ductility of the microstructure lead to building up of ploughed material around the troughs. Nanostructured bainite in this context showed a slightly

greater wear resistance and was the only structure to show hardening at the surface. This was attributed to reaustenitisation of the surface layer followed by martensitic transformation leading to the enhanced hardness. The brittleness of untempered high-carbon martensite resulted in extensive fragmentation of the wear surface, with limited accumulation of wear debris on the surface.

To further reveal the mechanism, tempered nanostructured-bainite with retained austenite eliminated, exhibited 50% more wear rate compared to the untempered structure at comparable hardness. A substantial change in the wear mechanism occured from ploughing to cutting after tempering. The structure showed a limited hardening at the surface due to plastic deformation, but no reaustenitisation as found in the case of the virgin nanostructured bainite. The fine scale of the carbides, that form due to the decomposition of austenite during tempering played a limited role in the abrasion process because the abrasive particles used are much coarser.

The dry rolling-sliding wear resistance of pearlite was found to be comparable to that of much harder bainitic steels. Microstructural observations indicate that there was substantial plastic deformation of both the ferrite and cementite components of the pearlite in the vicinity of the wear surface. The plasticity was expected to be a consequence of exaggerated stresses due to surface roughness. The material remained ductile to shear strains of the order of 4. Diffraction data indicated that the coherent domain size was reduced to about half the interlamellar spacing and that some of the cementite might have dissolved and contributed to the expansion of the lattice parameter of ferrite.

The rolling/sliding wear resistance of bainitic steel, transformed at 200°C, supersedes that of other carbide-free bainitic steels transformed at higher temperatures. The experimental results, in combination with a theoretical analysis of rolling/sliding indicated that under the conditions studied, the role of sliding was minimal, so that the maximum shear stresses during contact were generated below the contact surface. Thus, the hardness following testing was found to reach a maximum below the contact surface. The fine scale and associated strength of the structure combats wear during the running-in period, but the volume fraction, stability and morphology of retained austenite had been shown to play a significant role during wear, by work-hardening the surface through phase transformation into very hard martensite.

The untempered martensite showed comparable rolling/sliding wear resistance

to that of much softer bainitic steels. High work-hardening of the martensite along with large compressive residual stress near the surface has kept the abrasion to mild wear. However, a substantial damage comprising of micro-cracks and voids were observed near the sub-surface indicating shear instability of the structure, which is likely to fail catastrophically at larger wear distance. Low carbon, metastable and blocky retained austenite with low mechanical stability got readily transformed to martensite and therefore did not contribute much towards wear resistance.

There is a lot more to be gained from combining detailed characterisation, mathematical modelling and the insight from the present work. Some of the items which could be addressed in a foreseeable future are listed here,

1. All of the rolling/sliding experiments have been conducted with 5% slip. Increasing the amount of slip should have a marked effect on the rate of damage and possibly reveal spalling phenomena. The work so far has not subjected samples to sufficient sub-surface damage to induce gross failure mechanisms. A set of experiments on nanostructured bainitic and tempered bainitic structures with 25% slip is in progress at the Swinden Technology Centre, Tata Steel, UK. The outcomes will be fascinating for comparison against the behavior of commercial rail and wheel steels that are susceptible to rolling contact induced spalling.
   The characterisation of martensite after rolling/sliding revealed numerous voids and cracks just below the surface, the number densities of which have been found to increase with wear distance. Although a large compressive stress at the surface prevented these voids from coalescing, it would be interesting to conduct experiments with larger wear distance in order to increase the sub-surface damage to a point where gross mechanisms of failure set in. A set of experiments based on this idea has been planned to carry out at the Luleå University of Technology, Sweden.

2. The role of retained austenite in the wear of nanostructured bainite needs explicit proof. Therefore, dry rolling/sliding wear tests on tempered bainite with 5% slip have been conducted at the Luleå University of Technology, Sweden. The wear rate has been found to increase by 50% over the untem-

pered nanostructured bainite at similar hardness. The wear rate is nevertheless far lower than most commercially available materials for abrasion resistance. A detailed characterisation of the worn structure is in progress to explain the damage.

3. A high carbon (1.06 wt%) alloy has been intercritically annealed at 780°C for 30 mins and transformed at 200°C for 10 days to induce coarse proeutectoid carbides in a bainitic ferrite matrix. The size of the carbides are much larger than those observed after the tempering of bainite. The structure has similar hardness to that of nanostructured bainite and has been planned for both three-body and rolling/sliding wear tests.

4. The crystallographic orientation of grains at the surface and subsurface region changes with the progress of abrasion. Limited research has been carried out so far on the evolution of texture of the abraded surface and subsurface regions and consequences on abrasive wear. It would be interesting to find out the effect of texture on three-body abrasion and how grains fragment and re-orient during abrasion leading to a completely different structure. The effect of texture on abrasion may be useful.

5. Apart from these, the surface of the nanostructured bainite and fine pearlite could be shot-peened to deliberately make a work-hardened layer and introduce compressive residual stress, followed by three-body abrasion and rolling/sliding wear. It would be interesting to characterise the resultant worn structure and compare against the untreated surface.

Appendix A

Commercial wear resistant steel plates

Table A.1: Chemical composition of commercially available abrasion resistance hot rolled steel plates. The concentration stated are either in maximum allowable limit or range in wt%.

Steel	Manufacturer	C	Mn	Si	Al	P	S	Cr	Cu	Ni	Mo	V	Ti	Nb	W	B
Abrazo 400	Tata Steel (Europe)	0.20	1.60	0.50	-	0.025	0.010	1.00	0.40	1.50	0.70	0.10	-	0.06	-	0.004
Abrazo 450	Tata Steel (Europe)	0.25	1.50	0.50	-	0.025	0.010	1.50	-	1.50	0.70	-	-	-	-	0.005
Abrazo 500	Tata Steel (Europe)	0.30	1.50	0.50	-	0.025	0.010	1.50	-	1.50	0.70	-	-	-	-	0.005
Sumihard 400	Sumitomo (Japan)	0.21	1.60	0.70	-	0.025	0.010	-	-	-	-	-	-	-	-	0.003
Sumihard 500	Sumitomo (Japan)	0.35	1.60	0.70	-	0.008	0.003	0.90	-	-	-	-	-	-	-	0.003
Hardox 400	SSAB (Sweden)	0.14-0.32	1.60	0.70	-	0.025	0.010	0.3-1.40	-	0.25-1.50	0.25-0.60	-	-	-	-	0.004
Hardox 450	SSAB (Sweden)	0.21-0.26	1.60	0.70	-	0.025	0.010	0.25-1.40	-	0.25-1.00	0.25-0.60	-	-	-	-	0.004
Hardox 500	SSAB (Sweden)	0.27-0.30	1.60	0.70	-	0.025	0.010	1.00-1.40	-	0.25-1.50	0.25-0.60	-	-	-	-	0.004
JFE-EH360	JFE (Japan)	0.20	1.60	0.55	-	0.030	0.030	0.40	-	-	-	-	0.005-0.020	-	-	0.004
JFE-EH400	JFE (Japan)	0.25	1.60	0.55	-	0.030	0.030	0.80	-	-	-	-	0.005-0.020	-	-	0.004
JFE-EH500	JFE (Japan)	0.35	1.60	0.55	-	0.030	0.030	0.80	-	-	-	-	0.005-0.020	-	-	0.004
JFE-EH360A	JFE (Japan)	0.20	1.60	0.55	-	0.030	0.030	0.40-1.20	-	-	0.10-0.50	0.10	0.020	-	-	0.004
JFE-EH500A	JFE (Japan)	0.35	1.60	0.55	-	0.030	0.030	0.40-1.20	-	-	0.10-0.50	0.10	0.020	-	-	0.004
JFE-EH360LE	JFE (Japan)	0.17	1.60	0.55	-	0.020	0.010	0.40	-	-	0.35	-	0.020	-	-	0.004
JFE-EH400LE	JFE (Japan)	0.23	1.60	0.55	-	0.020	0.010	0.80	-	-	0.35	-	0.020	-	-	0.004
JFE-EH500LE	JFE (Japan)	0.29	1.60	0.55	-	0.020	0.010	0.40	-	-	0.35	-	0.020	-	-	0.004
Welhard400	NSC (Japan)	0.22	2.00	0.55	-	0.025	0.015	1.20	-	-	0.60	-	-	0.05	-	0.005
Welhard500	NSC (Japan)	0.35	2.00	0.55	-	0.015	0.010	1.20	-	-	0.60	-	-	0.05	-	0.005
WEL-TEN AR235E	NSC (Japan)	0.22	2.00	0.55	-	0.025	0.015	0.50	-	-	0.60	-	-	-	-	0.005
WEL-TEN AR285E	NSC (Japan)	0.22	2.00	0.55	-	0.025	0.015	0.50	-	-	0.60	-	-	-	-	0.005
WEL-TEN AR320E	NSC (Japan)	0.22	2.00	0.55	-	0.025	0.015	0.50	-	-	0.60	-	-	-	-	0.005
WEL-TEN AR360E	NSC (Japan)	0.22	2.00	0.55	-	0.025	0.015	0.50	-	-	0.60	-	-	-	-	0.005
Wel-TEN AR400E	NSC (Japan)	0.25	2.00	0.55	-	0.025	0.015	0.50	-	-	0.60	-	-	-	-	0.005
Wel-TEN AR500E	NSC (Japan)	0.35	2.00	0.55	-	0.015	0.010	0.50	-	-	0.60	-	-	-	-	0.005
Fora 400	Arcelor-Mittal (Belgium)	0.20	1.60	0.01	-	0.020	0.003	1.00	-	-	0.50	0.20	-	-	-	0.003
Fora 450	Arcelor-Mittal (Belgium)	0.20	1.5	-	-	0.02	0.003	1.0	-	0.70	0.20	-	-	-	-	0.003
Fora 500	Arcelor-Mittal (Belgium)	0.30	1.5	-	-	0.02	0.003	1.0	-	0.70	0.30	-	-	-	-	0.003
Creusabro-Superten	Arcelor-Mittal (Belgium)	0.16	1.6	0.6	-	0.015	0.005	1.0	-	2.5	0.7	0.07	-	-	-	
Creusabro-Dual	Arcelor-Mittal (Belgium)	0.40	1.30	-	-	-	0.002	0.70	-	0.45	0.34	-	0.60	-	-	
Creusabro-M	Arcelor-Mittal (Belgium)	1.13	13	0.40	-	0.02	0.003	-	-	-	-	-	-			
Creusabro-4800	Arcelor-Mittal (Belgium)	0.20	1.60	-	-	0.018	0.005	1.90	-	0.20	0.40	-	-	-	-	-
Creusabro-8000	Arcelor-Mittal (Belgium)	0.28	1.6	-	-	-	-	1.6	-	0.40	0.20	-	-	-	-	-
Raex 400	Rukki (Finland)	0.20	1.70	0.70	-	0.030	0.015	1.50	-	0.40	0.50	-	-	-	-	0.004
XAR400	Thyssenkrup (Germany)	0.28	1.50	0.80	-	0.025	0.01	1.00	-	0.50	0.50	-	-	-	-	0.005
Brinar400	Satzgitter (Germany)	0.18	1.50	0.30	0.015	0.015	0.005	1.55	-	1.20	0.60	-	-	-	-	0.005
Dillidur400	Dillinger (Germany)	0.20	1.80	0.50	-	0.025	0.01	1.50	-	0.80	0.50	0.08	-	0.05	-	0.005
Quard400	Duferco (Belgium)	0.16	1.60	0.70	-	0.025	0.01	0.50	-	0.25	0.25	-	-	-	-	0.005

Table A.2: Mechanical properties of commercially available abrasion resistant steel plates those listed in Table A.1.

Steel	Origin	Yield Strength (MPa)	Ultimate Tensile Strength (MPa)	%Elongation	Brinell Hardness	Toughness (J)	Microstrcuture	Ref
Abrazo 400	Tata Steel (Europe)	1100	1250	10(proportional)	360-400	KCVL(2 mm) : 27 J at -40°C	martensitic	[89]
Abrazo 450	Tata Steel (Europe)	1200	1450	10(proportional)	415-450	KCVL(2 mm) : 27 J at -40°C	martensitic	[89]
Abrazo 500	Tata Steel (Europe)	1400	1550	10(proportional)	460-500	KCVL(2 mm) : 27 J at -40°C	martensitic	[89]
Sumihard 400	Sumitomo (Japan)	1075	1322	10	360-440	KCVL(20 mm) : 73 J at 0°C	martensitic	[269]
Sumihard 500	Sumitomo (Japan)	1156	1325	10	360-440	KCVL(16 mm) : 43 J at 0 °C	martensitic	[269]
Hardox 400	SSAB (Sweden)	1000	1250	10	370-430	KCVL(20 mm) : 45 J at -40°C	martensitic	[90]
Hardox 450	SSAB (Sweden)	1200	1400	10	425-475	KCVL(20 mm) : 40 J at -40°C	martensitic	[91]
Hardox 500	SSAB (Sweden)	-	-	-	450-540	KCVL(20 mm) : 30 J at -40°C	martensitic	[92]
JFE-EH360	JFE (Japan)	1083	1246	20.8	>385	-	martensitic+Cr/Ti-C	[270]
JFE-EH400	JFE (Japan)	1163	1316	19.8	> 442	-	martensitic+Cr/Ti-C	[270]
JFE-EH500	JFE (Japan)	1297	1449	17.7	> 508	-	martensitic+Cr/Ti-C	[270]
JFE-EH360A	JFE (Japan)	1147	1203	23.9	> 388	KCVL : 156 J at 0°C	martensite+Cr/Mo/V/Ti-C	[270]
JFE-EH500A	JFE (Japan)	1321	1516	22.9	>542	KCVL : 65 J at 0°C	martensite+Cr/Mo/V/Ti-C	[270]
JFE- EH360LE	JFE (Japan)	1050	1308	23	411	KCVL : 61 J at -40°C	martensite + Cr/Mo/Ti-C	[270]
JFE- EH400LE	JFE (Japan)	1121	1442	19.6	450	KCVL : 45 J at -40°C	martensite + Cr/Mo/Ti-C	[270]
JFE- EH500LE	JFE (Japan)	1203	1681	17	502	KCVL : 42 J at -40°C	martensite + Cr/Mo/Ti-C	[270]
Welhard 400	NSC (Japan)	1070	1236	22	min.400	-	martensite	[271]
WEL-TEN AR320E	NSC (Japan)	1069	1177	25(longitudinal)	350-360	KCVL : 56 J at 0°C	tempered martensite	[271]
WEL-TEN AR360E	NSC (Japan)	1108	1216	23(longitudinal)	380-390	KCVL : 39 J at 0°C	tempered martensite	[271]
WEL-TEN AR400E	NSC (Japan)	1265	1393	20(longitudinal)	420-430	KCVL : 39 J at 0°C	tempered martensite	[271]
WEL-TEN AR500E	NSC (Japan)	1491	1667	16(longitudinal)	500-520	KCVL : 26 J at 0°C	tempered martensite	[271]
Fora 400	Arcelor Mittal (Belgium)	1100	1350	13	400	KCVL : 35 J at -20°C	martensitic	[272]
Fora 450	Arcelor Mittal (Belgium)	1200	1400	10	450	KCVL : 30 J at -20°C	martensitic	[273]
Fora 500	Arcelor Mittal (Belgium)	1200	1400	10	500	KCVL : 30 J at -40°C	martensitic	[274]
Creusabro-Superten	Arcelor Mittal (Belgium)	980	1080	15	340	KCVL : 48 J at -20 °C	tempered martensite	[275]
Creusabro-Dual	Arcelor Mittal (Belgium)	1200	1630	10	480	KCVL : 168 J at -20 °C	TRIP assisted + TiC	[276]
Creusabro-M	Arcelor Mittal (Belgium)	350	800	30	180-245	KCVL : 64 J at 20 °C	austenitic	[277]
Creusabro-4800	Arcelor Mittal (Belgium)	900	1200	12	370	KCVL : 36 J at -20 °C	TRIP assisted + TiC	[87]
Creusabro-8000	Arcelor Mittal (Belgium)	1250	1630	12	430-500	KCVL : 32 J at -20 °C	TRIP assisted + Ti/Mo/Cr-C	[88]
Raex 400	Rukki (Finland)	1000	1200	10	360-420	-	martensitic	[278]
Xar 400	Thyssenkrup (Germany)	1020	1250	12	360-440	-	martensitic	[279]
Brinar 400	Satzgitter (Germany)	1100	1300	12	360-440	-	martensitic	[280]
Dillidur 400	Dillinger (Germany)	1000	1200	12	370-430	-	martensitic	[281]
Quard 400	Duferco (Belgium)	1050	1250	10	370-430	KCVL : 35 J at -40°C	martensitic	[282]

proportional: uniform elongation; longitudinal : along the rolling direction.

Appendix B

Distribution of force over the Hertzian contact width

The pupose here is to illustrate the derivation of equations used in Chapter 6-8, based largely on the work of Johnson [95] and WenTao et al. [221]. The work has been implementd in a computer program, detailed in Appendix C, and also made freely available on:

http://www.msm.cam.ac.uk/map/steel/programs/contact.html

.

The assumptions involved in calculating contact stresses are :

1. The discs in contact are isotropic in terms of mechanical and physical properties.
2. The externally applied load is normal to the rolling/sliding surface.
3. The dimensions of the contact area between the two discs are small compared to the radii of the discs, and,
4. There are no significant distortions in the geometrical dimension of the discs.

Fig. B.1 shows the disc configuration with an initial straight line contact of length equal to the amount of overlap between the discs and the width of the

contact is given by [95] .

$$b = 2\sqrt{\frac{1-\nu^2}{\pi}\frac{P(\frac{1}{E_1}+\frac{1}{E_2})}{l(\frac{1}{R_1}+\frac{1}{R_2})}} \tag{B.1}$$

$\nu = 0.3$	Poisson's ratio of the materials in contact
$P = 300\,\mathrm{N}$	applied force on the cylinders
$E_1 = E_2 = 210\,\mathrm{GPa}$	Young's moduli of the materials in contact
$R_1 = R_2 = 22.5\,\mathrm{mm}$	disc radii
$l = 5\,\mathrm{mm}$	length of overlap of discs.

With above parameters, b calculates out to be equal to 86 µm, so that the full width of the contact strip is 172 µm. It is of course assumed that the surfaces in contact are geometrically smooth whereas in reality, there are asperities, initially from sample preparation and later from surface damage. There should be a gradual increase in contact area as the test progresses, with consequent decrease in the contact stress towards the calculated values, shown in Fig. B.2 for a steady-state overlap of 5 mm for various ξ[1].

The normal and tangential distributions of the forces per unit length, over the Hertzian contact zone, for the rolling-sliding condition are given by [95, p. 204], where the coordinate z is parallel to the normal load, and x to the direction of sliding:

$$p_z = \frac{2P}{\pi l b^2}\sqrt{b^2 - x^2}, \quad |x| \le b \tag{B.2}$$

which leads to a parabolic distribution of the normal force per unit length, over the Hertzian contact width as shown in Fig. B.2. The tangential components depend also on the roll-slide parameter and the size b_1 of the slide zone, [221]:

$$p_x = \begin{cases} \pm\frac{2\mu P}{\pi l b^2}\sqrt{b^2 - x^2}, & |x| \leqslant b, |x - b + b_1| > b_1, \\ \pm\frac{2\mu P}{\pi l b^2}[\sqrt{b^2 - x^2} - \sqrt{b_1^2 - (x - b - b_1)^2}], & |x| \leqslant b, |x - b + b_1| \leqslant b_1. \end{cases} \tag{B.3}$$

where the negative sign is for the shear along the sliding direction, μ is the dynamic coefficient of friction and b_1 is the half-width of the slide zone (Fig. B.1).

[1]The parameter is calculated from the difference of circumferential velocities of the two discs. Mathematically, it is 1-(% slip/100).

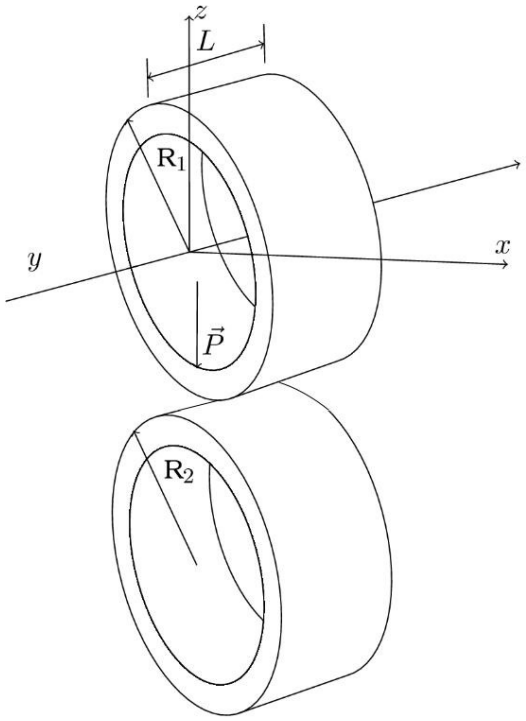

(a)

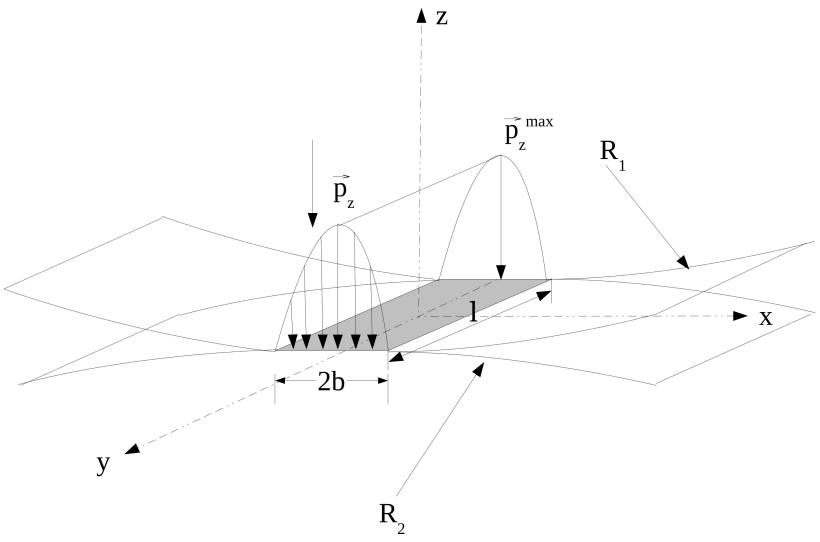

(b)

Figure B.1: Schematic of the (a) twin-disc set up, (b) stress distribution over the Hertzian contact.

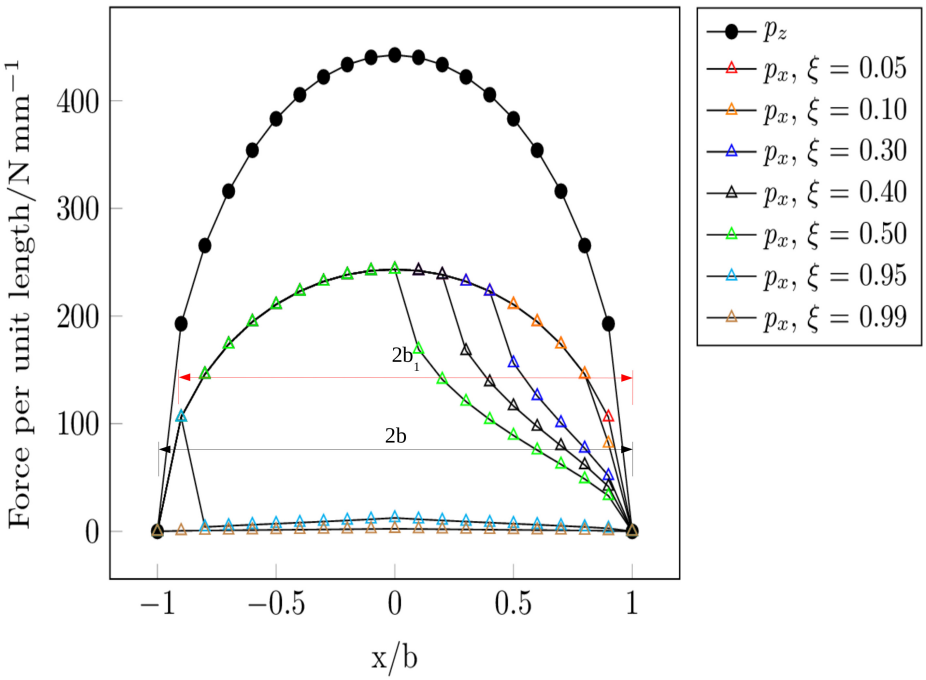

Figure B.2: Distribution of normal (p_z), and tangential force (p_x) over the Hertzian contact half-width for $\xi = 0.05$, 0.20, 0.40, 0.50, 0.95 and 0.99 during rolling-sliding assuming a contact length equal to 5 mm. Hertzian contact width ($2b$) and width of the slide zone ($2b_1$) for $\xi = 0.95$ are indicated respectively.

Integrating equation B.3 over the contact width $b, -b$ yields the size of the slide zone as:

$$\frac{b_1}{b} = \left(1 - \frac{p_t}{\mu p_n}\right)^{\frac{1}{2}} \qquad \text{with } p_t = \text{tangential load per unit length} \tag{B.4}$$

which on substitution into equation B.3 gives [221]:

$$p_x(x) = \begin{cases} \frac{2\mu p_n}{\pi b}\sqrt{1 - \left(\frac{x}{b}\right)^2}, & -b \leqslant x < b - 2b\xi, \\ -\frac{2\mu p_n}{\pi b}\left[\sqrt{1 - \left(\frac{x}{b}\right)^2} - \sqrt{\xi^2 - (\xi + \frac{x}{b} - 1)^2}\right], & b - 2b\xi \leqslant x \leqslant b. \end{cases} \tag{B.5}$$

p_n/b, can be taken as constant for a fixed load and length of overlap. In our experiment, the dynamic coefficient of friction was found to be $\mu = 0.55$ after reaching steady state conditions. The set of equations was solved numerically as a function of ξ, and the resulting distributions of p_x are plotted in Fig. B.2. This asymmetry of the tangential force results in a skewed distribution of normal, shear and von Mises stress near the surface and subsurface, as described in following section.

B.1 Calculation of stresses in the x-z plane

The normal and shear stresses due to the distributed normal and tangential force acting on the Hertzian contact width is expressed as [221];

$$\sigma_x(x,z) = -\frac{2z}{\pi}\int_{-b}^{b} \frac{p_z(s).(x-s)^2}{[(x-s)^2 + z^2]^2}\mathrm{ds} - \frac{2}{\pi}\int_{-b}^{b} \frac{p_x(s).(x-s)^3}{[(x-s)^2 + z^2]^2}\mathrm{ds} \tag{B.6}$$

$$\sigma_z(x,z) = -\frac{2z^3}{\pi}\int_{-b}^{b} \frac{p_z(s)}{[(x-s)^2 + z^2]^2}\mathrm{ds} - \frac{2z^2}{\pi}\int_{-b}^{b} \frac{p_x(s).(x-s)}{[(x-s)^2 + z^2]^2}\mathrm{ds} \tag{B.7}$$

$$\tau_{xz}(x,z) = -\frac{2z^2}{\pi}\int_{-b}^{b}\frac{p_z(s).(x-s)}{[(x-s)^2+z^2]^2}\mathrm{ds} - \frac{2z}{\pi}\int_{-b}^{b}\frac{p_x(s).(x-s)^2}{[(x-s)^2+z^2]^2}\mathrm{ds} \tag{B.8}$$

substituting $p_z(x)$, $p_x(x)$ and x/b = i, z/b = j and s/b = t;

$$\sigma_x(i,j) = -\frac{4p_n}{b\pi^2}\left[jI_{x1} + \mu I_{x2}(\xi) + \mu I_{x3}(\xi)\right] \tag{B.9}$$

$$\sigma_z(i,j) = -\frac{4p_n j^2}{b\pi^2}\left[jI_{z1} + \mu I_{z2}(\xi) + \mu I_{z3}(\xi)\right] \tag{B.10}$$

$$\tau_{xz}(i,j) = -\frac{4p_n j}{b\pi^2}\left[jI_{xz1} + \mu I_{xz2}(\xi) + \mu I_{xz3}(\xi)\right]. \tag{B.11}$$

where,

$$I_{x1} = \int_1^1 \frac{\sqrt{1-t^2}(i-t)^2}{[(i-t)^2+j^2]^2}\mathrm{dt}, \tag{B.12}$$

$$I_{x2}(\xi) = \int_{-1}^{1-2\xi} \frac{\sqrt{1-t^2}(i-t)^3}{[(i-t)^2+j^2]^2}\mathrm{dt}, \tag{B.13}$$

$$I_{x3}(\xi) = \int_{1-2\xi}^{1} \frac{[\sqrt{1-t^2} - \sqrt{\xi^2-(\xi+t-1)^2}](i-t)^3}{[(i-t)^2+j^2]^2}\mathrm{dt}, \tag{B.14}$$

$$I_{z1} = \int_{-1}^{1} \frac{\sqrt{1-t^2}}{[(i-t)^2+j^2]^2}\mathrm{dt}, \tag{B.15}$$

$$I_{z2}(\xi) = \int_{-1}^{1-2\xi} \frac{\sqrt{1-t^2}(i-t)}{[(i-t)^2+j^2]^2}\mathrm{dt}, \tag{B.16}$$

$$I_{z3}(\xi) = \int_{1-2\xi}^{1} \frac{[\sqrt{1-t^2} - \sqrt{\xi^2-(\xi+t-1)^2}](i-t)}{[(i-t)^2+j^2]^2}\mathrm{dt}, \tag{B.17}$$

$$I_{xz1} = \int_{-1}^{1} \frac{\sqrt{1-t^2}(i-t)}{[(i-t)^2+j^2]^2}\mathrm{dt}, \tag{B.18}$$

$$I_{xz2}(\xi) = \int_{-1}^{1-2\xi} \frac{\sqrt{1-t^2}(i-t)^2}{[(i-t)^2+j^2]^2}\mathrm{dt}, \tag{B.19}$$

$$I_{xz3}(\xi) = \int_{1-2\xi}^{1} \frac{[\sqrt{1-t^2}-\sqrt{\xi^2-(\xi+t-1)^2}](i-t)^2}{[(i-t)^2+j^2]^2}\mathrm{dt}, \tag{B.20}$$

These set of integrals are solved numerically by writing a program in "C"language. Having calculated σ_x, σ_z and τ_{xz}, the two principal stresses $\sigma_{1,xz}$ and $\sigma_{2,xz}$ are calculated as:

$$\sigma_{1,xz} = \frac{\sigma_x+\sigma_z}{2} + \sqrt{\left(\frac{\sigma_x-\sigma_z}{2}\right)^2 + \tau_{xz}^2} \tag{B.21}$$

$$\sigma_{2,xz} = \frac{\sigma_x+\sigma_z}{2} - \sqrt{\left(\frac{\sigma_x-\sigma_z}{2}\right)^2 + \tau_{xz}^2} \tag{B.22}$$

$$\tau_{45^\circ} = \frac{\sigma_1-\sigma_2}{2} \tag{B.23}$$

Shear stress plays an important role in deformation of the sub-surface microstructure. The value of τ_{xy} in the plane of symmetry ($x = 0$) will always be zero for pure rolling. which gradually gets skewed in the direction of rolling with increasing slip. The shear stress, τ_{45°, acts on a plane which makes and angle of 45° to the x-axis.

Under a plane stress condition, the von Mises stress can be expressed by two principle stresses;

$$\sigma_{VM} = \sqrt{{\sigma_1}^2 - \sigma_1\sigma_2 + {\sigma_2}^2} \tag{B.24}$$

The data files generated in the form of two dimensional matrix of stresses in the x-z plane are discussed below [283].

Testing of the code The accuracy of the code has been tested under perfect rolling condition with a constant coefficient of friction, $\mu = 0.30$. Under this condition, the maximum value of shear stress τ_{max} is equal to $0.30p_{max}$ and is observed at a depth of $0.78b$ [Fig. B.3(a)]. The plane shearing stress, τ_{xz} is found to be symmetrical around the z axis and vanishes at $x = 0$ [Fig. B.3(b)]. Under

pure sliding condition, the distribution of τ_{45° not only becomes asymmetrical but τ_{max} also migrates to the surface [Fig. B.3(c)]. Table B.1 lists the normalised σ_x, σ_z, τ_{xz} and τ_{45° for pure rolling conditions and $\mu = 0.30$, the results are found to corroborate published observations [221, 284].
The outcome of the calculations for various conditions are discussed in two different formats, the first one being the absolute values of stresses to explain the damage and the second form is in terms of normalised components of stresses to compare the change.

The calculations for pure rolling shows that the maximum tractional and compressive stress is achieved near the surface with tractional stress decaying at a faster rate compared to compressive stress as the depth is increased [Table B.1]. The distribution of tractional stress and compressive stress are symmetrical around the z-axis with maxima always lying over $x = 0$ for pure rolling. The shear stress over the $x - z$ plane is always equal to zero over the axis of symmetry ($x = 0$) with maxima attained on either sides of the z-axis at specific $x = ib$, where, $i = x/b$. τ_{45° is again symmetrical around the z-axis but the maxima attained at $(x, z : 0.0, 0.78b)$ and is equal to $0.30P_{max}$. However, at a smaller depth $z < 0.78b$, the maximum value of τ_{45° migrates away from $x = 0$ and is attained at specific $x = ib$.

Introduction of nominal slip equal to 5%, marginally increases the normalised tractional and compressive stress stress, though their distribution in terms of relative coordinates (i, j), remains unchanged [Table B.2]. Shear stress in $x - z$ plane undergoes major changes in terms of the magnitude and distribution with introduction of slip, as the magnitude of maximum negative shear stress increases and that of positive shear stress decreases which can be observed by comparing the data of $\tau_{xz}/P_{max}(i, j)$ in Table B.1 and Table B.2 respectively. The extent of the change is more pronounced near the surface. An increase in the dynamic coefficient of friction from 0.30 to 0.55 increases the absolute values of the contact stresses but has a marginal effect on the normalised tractional stress at the surface, where the normalised compressive, shear stress in $x-z$ plane and in the 45° plane remains unchanged [Table B.3].

Calculation of sub-surface stresses including the combinatorial effect of nominal slip (5%) and increased coefficient of friction ($\mu = 0.55$) is shown in Table B.4.

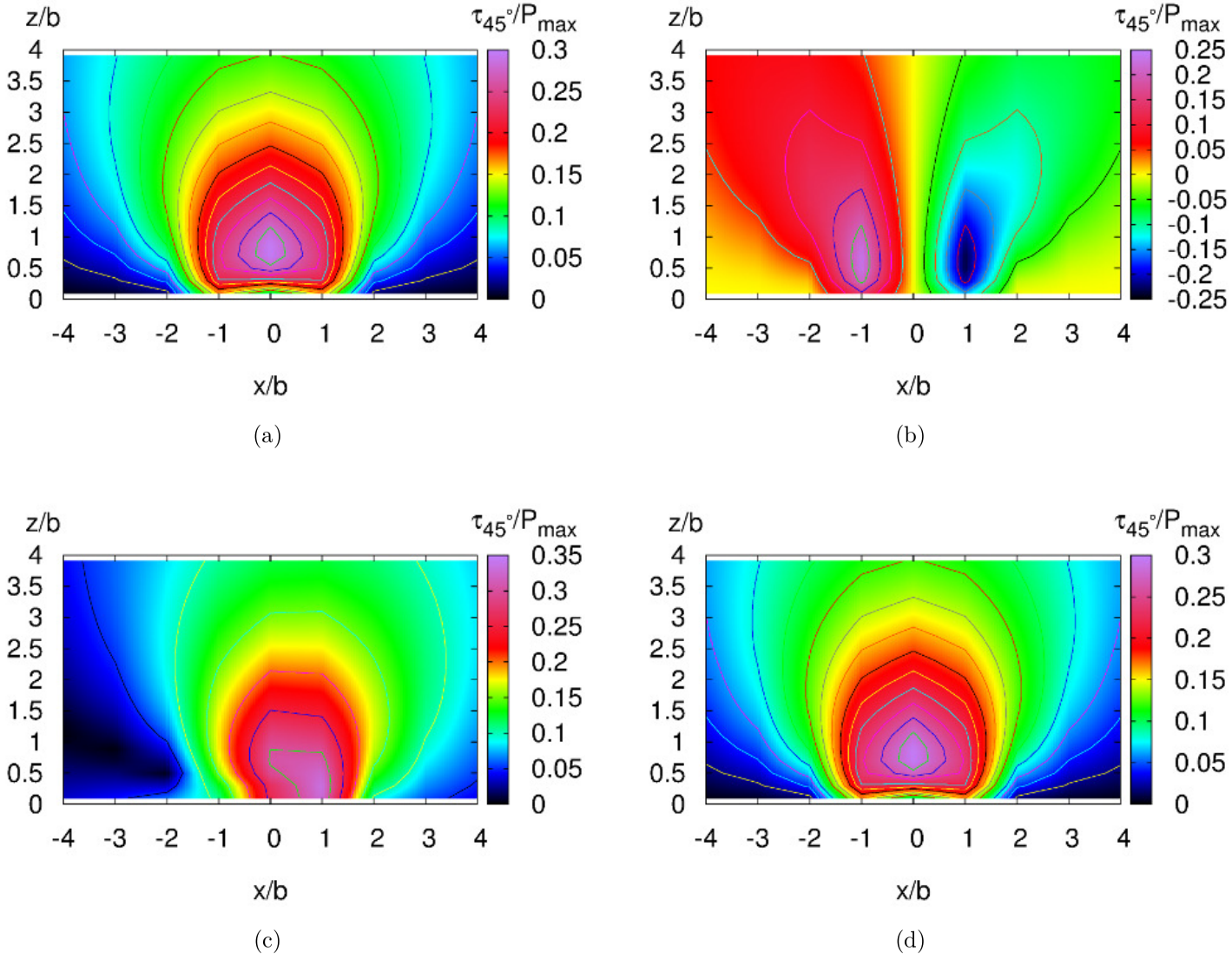

Figure B.3: Distribution of shear stress (a) τ_{45° for $P = 300\ N$, $\mu = 0.30$ for pure rolling, (b) τ_{xz} for $P = 300\ N$, $\mu = 0.30$ for pure rolling, (c) τ_{45° for $P = 300\ N$, $\mu = 0.30$ for pure sliding, (d) τ_{45° for $P = 300\ N$, $\mu = 0.55$ for pure rolling.

Table B.1: Maximum values of stresses and stresses at $x = 0$ in the contact zone normalised against P_{max} for pure rolling [$\xi = 1.0$], with $\mu = 0.30$, $R_1, R_2 = 22.5\,\text{mm}$ and $P = 300\,\text{N}$.

	Distance in z	$\sigma_x/\mathrm{P}_{max}(i,j)$	$\sigma_z/\mathrm{P}_{max}(i,j)$	$\tau_{xz}/\mathrm{P}_{max}(i,j)$	$\tau_{45°}/\mathrm{P}_{max}(i,j)$
Maximum stress	0.1b	-0.815(0.0,0.1)	-0.995(0.0,0.1)	±0.146(±1.0,0.1)	0.163(1.0,0.1)
	0.2b	-0.660(0.0,0.2)	-0.980(0.0,0.2)	±0.193(±0.8,0.2)	0.206(0.8,0.2)
	0.5b	-0.341(0.0,0.5)	-0.895(0.0,0.5)	±0.247(±0.8,0.5)	0.278(0.4,0.5)
	0.8b	-0.237(1.2,0.8)	-0.781(0.0,0.8)	±0.231(±0.8,0.8)	0.300(0.0,0.8)
	1.0b	-0.204(1.4,1.0)	-0.707(0.0,1.0)	±0.217(±1.0,1.0)	0.293(0.0,1.0)
Stress at $x = 0$	0.1b	-0.815(0.0,0.1)	-0.995(0.0,0.1)	±0.000(0.0,0.0)	0.090(0.0,0.1)
	0.2b	-0.660(0.0,0.2)	-0.980(0.0,0.2)	±0.000(0.0,0.0)	0.160(0.0,.0.2)
	0.5b	-0.341(0.0,0.5)	-0.895(0.0,0.5)	±0.000(0.0,0.0)	0.276(0.0,0.5)
	0.8b	-0.180(0.0,0.8)	-0.781(0.0,0.8)	±0.000(0.0,0.0)	0.300(0.0,0.8)
	1.0b	-0.121(0.0,1.0)	-0.707(0.0,1.0)	±0.000(0.0,0.0)	0.293(0.0,1.0)

Table B.2: Maximum values of stresses and stresses at $x = 0$ in the contact zone normalised against P_{max} for nominal slip [$\xi = 0.95$], with $\mu = 0.30$, $R_1, R_2 = 22.5\,\text{mm}$ and $P = 300\,\text{N}$.

	Distance in z	$\sigma_x/\text{P}_{max}(i,j)$	$\sigma_z/\text{P}_{max}(i,j)$	$\tau_{xz}/\text{P}_{max}(i,j)$	$\tau_{45°}/\text{P}_{max}(i,j)$
Maximum stress	0.1b	-0.840(0.0,0.1)	-0.997(0.0,0.1)	-0.149(1.0,0.1)/0.118(-1.0,0.1)	0.172(1.0,0.1)
	0.2b	-0.680(0.0,0.2)	-0.984(0.0,0.2)	-0.199(0.8,0.2)/0.174(-0.8,0.2)	0.208(0.8,0.2)
	0.5b	-0.352(0.0,0.5)	-0.900(0.0,0.5)	-0.254(0.8,0.5)/0.240(-0.8,0.5)	0.279(0.6,0.5)
	0.8b	-0.247(1.2,0.8)	-0.786(0.0,0.8)	-0.237(0.8,0.8)/0.227(0.8,0.8)	0.300(0.0,0.8)
	1.0b	-0.213(1.4,1.0)	-0.712(0.0,1.0)	-0.223(1.0,1.0)/0.213(-1.0,1.0)	0.294(0.0,1.0)
Stress at $x = 0$	0.1b	-0.840(0.0,0.1)	-0.997(0.0,0.1)	-0.015(0.0,0.0)	0.079(0.0,0.1)
	0.2b	-0.680(0.0,0.2)	-0.984(0.0,0.2)	-0.014(0.0,0.0)	0.152(0.0,0.2)
	0.5b	-0.352(0.0,0.5)	-0.900(0.0,0.5)	-0.010(0.0,0.0)	0.274(0.0,0.5)
	0.8b	-0.185(0.0,0.8)	-0.786(0.0,0.8)	-0.007(0.0,0.0)	0.300(0.0,0.8)
	1.0b	-0.124(0.0,1.0)	-0.712(0.0,1.0)	-0.005(0.0,0.0)	0.294(0.0,1.0)

Table B.3: Maximum values of stresses and stresses at $x = 0$ in the contact zone normalised against P_{max} for pure rolling [$\xi = 1.0$], with increased friction to $\mu = 0.55$, $R_1, R_2 = 22.5\,\text{mm}$ and $P = 300\,\text{N}$.

	Distance in z	$\sigma_x/\mathrm{P}_{max}(i,j)$	$\sigma_z/\mathrm{P}_{max}(i,j)$	$\tau_{xz}/\mathrm{P}_{max}(i,j)$	$\tau_{45^\circ}/\mathrm{P}_{max}(i,j)$
Maximum stress	0.1b	-0.816(0.0,0.1)	-0.995(0.0,0.1)	-0.146(1.0,0.1)/0.146(-1.0,0.1)	0.163(1.0,0.1)
	0.2b	-0.660(0.0,0.2)	-0.981(0.0,0.2)	-0.193(0.8,0.2)/0.193(-0.8,0.2)	0.206(0.8,0.2)
	0.5b	-0.342(0.0,0.5)	-0.895(0.0,0.5)	-0.247(0.8,0.5)/0.247(-0.8,0.5)	0.278(0.4,0.5)
	0.8b	-0.237(1.2,0.8)	-0.781(0.0,0.8)	-0.231(0.8,0.8)/0.231(0.8,0.8)	0.300(0.0,0.8)
	1.0b	-0.205(1.4,1.0)	-0.707(0.0,1.0)	-0.217(1.0,1.0)/0.217(-1.0,1.0)	0.293(0.0,1.0)
Stress at $x = 0$	0.1b	-0.816(0.0,0.1)	-0.995(0.0,0.1)	-0.0006(0.0,0.0)	0.089(0.0,0.1)
	0.2b	-0.660(0.0,0.2)	-0.981(0.0,0.2)	-0.0006(0.0,0.0)	0.160(0.0,0.2)
	0.5b	-0.342(0.0,0.5)	-0.895(0.0,0.5)	-0.0005(0.0,0.0)	0.276(0.0,0.5)
	0.8b	-0.180(0.0,0.8)	-0.781(0.0,0.8)	-0.0004(0.0,0.0)	0.300(0.0,0.8)
	1.0b	-0.121(0.0,1.0)	-0.707(0.0,1.0)	-0.0003(0.0,0.0)	0.293(0.0,1.0)

The normalised tractional stress at the surface increases to $0.862P_{max}$ compared to $0.840P_{max}$ for only nominal slip of 5% with low friction, μ =0.30 and $0.816P_{max}$ for increased friction ($\mu = 0.55$) in pure rolling. The ratio of σ_x/P_{max} shows that the presence of slip has a stronger effect on tractional stress compared to the coefficient of friction. The normalised compressive stress remains more of less unchanged with increased friction or %slip as the only change in the ratio is observed after 3rd place of the decimal. Increased friction alone does not have any effect on shear stress in $x - z$ plane or in τ_{45° [Table B.3], but introduction of slip changes the magnitude of shear stresses [Table B.2] which gets marginally augmented at higher coefficients of friction [Table B.4].

B.2 Effect of applied load

Increased in contact load from 100 N to 300 N enlarges the contact area, distributes the enhanced stresses over a larger volume, thus, providing a greater capacity for damage [Fig. B.4(a-h)]. Keeping the rest of the parameters same, an increase in load from 100 N to 300 N changes the Hertzian contact half width from 49 μm to 86 μm which causes the distribution of stress to spread over a larger depth below the contact area. The maximum shear stress, which are most prominently related to the sub-surface damage [245], almost double in magnitude. It is interesting that the normalised components of stresses remain unaltered as a function of load and normalised coordinate ($i = x/b$, $j = z/b$) as shown in Table B.5.

B.3 Effect of overlap width

It is expected that at constant load, the stresses developed must decrease as the overlap width increases Fig. B.5. At the begening of rolling/sliding, when asperities made the initial contact, the contact stress scales very high. In our

Table B.4: Maximum values of stresses and stresses at $x = 0$ in the contact zone normalised against P_{max} for nominal slip = 5% [$\xi = 0.95$], with increased friction to $\mu = 0.55$, $R_1, R_2 = 22.5\,\text{mm}$ and $P = 300\,\text{N}$.

	Distance in z	$\sigma_x/\mathrm{P}_{max}(i,j)$	$\sigma_z/\mathrm{P}_{max}(i,j)$	$\tau_{xz}/\mathrm{P}_{max}(i,j)$	$\tau_{45^\circ}/\mathrm{P}_{max}(i,j)$
Maximum stress	0.1b	-0.862(0.0,0.1)	-0.998(0.0,0.1)	-0.152(1.0,0.1)/0.095(-1.0,0.1)	0.179(1.0,0.1)
	0.2b	-0.697(0.0,0.2)	-0.986(0.0,0.2)	-0.204(0.8,0.2)/0.159(-0.8,0.2)	0.214(1.0,0.2)
	0.5b	-0.361(0.0,0.5)	-0.905(0.0,0.5)	-0.259(0.8,0.5)/0.235(-0.8,0.5)	0.281(0.6,0.5)
	0.8b	-0.256(1.2,0.8)	-0.791(0.0,0.8)	-0.243(0.8,0.8)/0.224(0.8,0.8)	0.301(0.2,0.8)
	1.0b	-0.220(1.4,1.0)	-0.716(0.0,1.0)	-0.227(1.0,1.0)/0.211(-1.0,1.0)	0.295(0.0,1.0)
Stress at x = 0	0.1b	-0.862(0.0,0.1)	-0.998(0.0,0.1)	-0.0278(0.0,0.0)	0.073(0.0,0.1)
	0.2b	-0.697(0.0,0.2)	-0.986(0.0,0.2)	-0.0266(0.0,0.0)	0.146(0.0,0.2)
	0.5b	-0.361(0.0,0.5)	-0.905(0.0,0.5)	-0.0197(0.0,0.0)	0.272(0.0,0.5)
	0.8b	-0.189(0.0,0.8)	-0.791(0.0,0.8)	-0.0128(0.0,0.0)	0.301(0.0,0.8)
	1.0b	-0.126(0.0,1.0)	-0.716(0.0,1.0)	-0.009(0.0,0.0)	0.295(0.0,1.0)

Table B.5: Maximum values of stresses in the contact zone normalised against P_{max} having $R_1, R_2 = 22.5$ mm, $\xi = 0.95$, $l = 5$ mm, $\mu = 0.55$ and $P = 100$ and 300 N respectively.

Load, N	Distance in z	$\sigma_x/\mathrm{P}_{max}$(x/b,z/b)	$\sigma_z/\mathrm{P}_{max}$(x/b,z/b)	$\tau_{xz}/\mathrm{P}_{max}$(x/b,z/b)	$\tau_{45^\circ}/\mathrm{P}_{max}$(x/b,z/b)
100	0.1b	-0.862(0.0,0.1)	-0.998(0.0,0.1)	-0.152(1.0,0.1)/0.095(-1.0,0.1)	0.179(1.0,0.1)
	0.2b	-0.697(0.0,0.2)	-0.986(0.0,0.2)	-0.204(0.8,0.2)/0.160(-0.8,0.2)	0.214(1.0,0.2)
	0.5b	-0.361(0.0,0.5)	-0.905(0.0,0.5)	-0.259(0.8,0.5)/0.235(-0.8,0.5)	0.281(0.6,0.5)
	0.8b	-0.256(1.2,0.8)	-0.791(0.0,0.8)	-0.243(0.8,0.8)/0.224(-0.8,0.8)	0.301(0.0,0.8)
	1.0b	-0.220(1.4,1.0)	-0.716(0.0,1.0)	-0.227(1.0,1.0)/0.211(-1.0,1.0)	0.295(0.0,1.0)
300	0.1b	-0.862(0.0,0.1)	-0.998(0.0,0.1)	-0.152(1.0,0.1)/0.095(-1.0,0.1)	0.179(1.0,0.1)
	0.2b	-0.697(0.0,0.2)	-0.986(0.0,0.2)	-0.204(0.8,0.2)/0.160(-0.8,0.2)	0.214(1.0,0.2)
	0.5b	-0.361(0.0,0.5)	-0.905(0.0,0.5)	-0.259(0.8,0.5)/0.235(-0.8,0.5)	0.281(0.6,0.5)
	0.8b	-0.256(1.2,0.8)	-0.791(0.0,0.8)	-0.243(0.8,0.8)/0.224(-0.8,0.8)	0.301(0.0,0.8)
	1.0b	-0.220(1.4,1.0)	-0.716(0.0,1.0)	-0.227(1.0,1.0)/0.211(-1.0,1.0)	0.295(0.0,1.0)

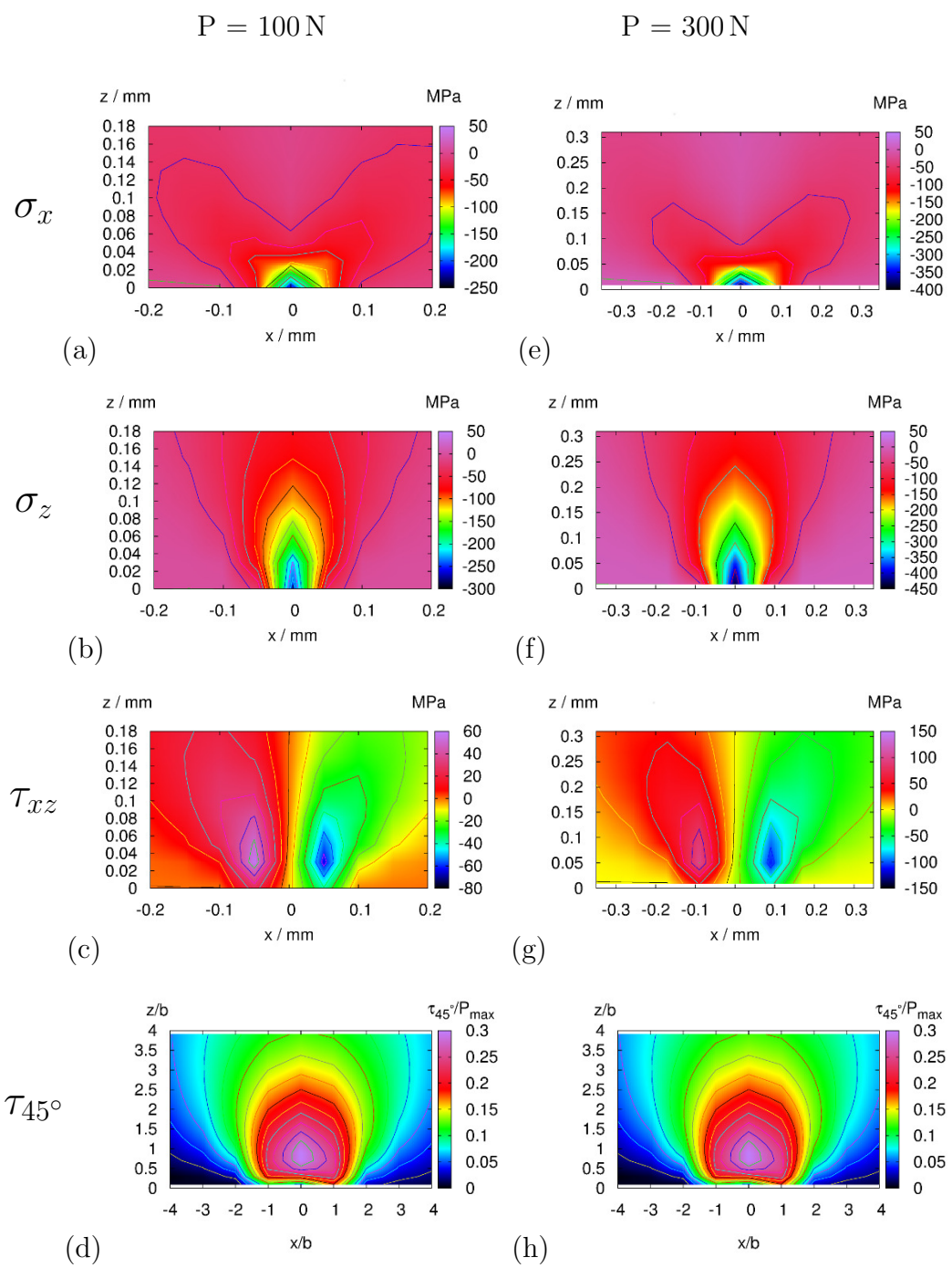

Figure B.4: Calculation of sub-surfaces stresses, σ_x, σ_z and τ_{xz}, and $\tau_{45°}$ under plane stress for a contact length (l) of 5 mm, $\mu = 0.55$, $\xi = 0.95$, for (a-d) $P =$ 100N, and (e-h) $P = 300$N.

set of experiments, the maximum contact stress in the range of 720-790 MPa has been registered, which gradually stabilises when more contact is made.

B.4 Effect of disc radii

The effects of geometry of the rolling/sliding discs on the magnitude and distribution of surface and sub-surface stresses are calculated and are shown in Fig. B.6. The effects are similar to overlap width, as the contact area increases with radius, which results in lower contact stresses under similar loading conditions.

B.5 Effect of Poisson's ratio, Young's moduli

The influence of the Poisson's ratio and Young's modulus on the magnitude and distribution of contact stresses are calculated and are shown in Fig. B.7(a-h). The Poisson's ratio and Young's modulii of Copper (E_1, E_2 = 110 GPa, ν = 0.34, $b \sim 117$ μm) and Tungsten (E_1, E_2 = 411 GPa, ν = 0.28, $b \sim 62$ μm) are taken for calculation of stresses. A higher Young's modulus results in smaller Hertzian contact half width. This results in an increase in the magnitude in all three components of stresses. The distribution of stresses at the surface narrows down progressively from copper to tungsten, with magnitude and distribution spreading deeper towards the core, signifying more concentrated stress over smaller length scale with increase in Young's modulus. The distance at which maximum shear stress is experienced from the rolling/sliding surface reduces with increasing Young's modulus, which could result in maximum shear damage of the microstructure within a smaller distance from the rolling/sliding surface.

B.6 Effect of dynamic coefficient of friction

The effect of changes in the dynamic coefficient of friction on the magnitude and distribution of contact stresses are shown in Fig .B.8(a-h). Greater coefficients of friction cause the normalised tractional and shear stress at the surface to increase [Table B.9]. Moreover, with increased friction, the distribution of

Table B.6: Maximum values of stresses in the contact zone normalised against P_{max} having $P = 300N$, $\xi = 0.95$, $\mu = 0.55$ and for $l = 1$ mm and 10 mm respectively.

lap (l),mm	Distance in z	$\sigma_x/\mathrm{P}_{max}$(x/b,z/b)	$\sigma_z/\mathrm{P}_{max}$(x/b,z/b)	$\tau_{xz}/\mathrm{P}_{max}$(x/b,z/b)	$\tau_{45^\circ}/\mathrm{P}_{max}$(x/b,z/b)
1.0	0.1b	-0.862(0.0,0.1)	-0.998(0.0,0.1)	-0.152(1.0,0.1)/0.095(-1.0,0.1)	0.179(1.0,0.1)
	0.2b	-0.697(0.0,0.2)	-0.986(0.0,0.2)	-0.204(0.8,0.2)/0.160(-1.0,0.2)	0.214(1.0,0.2)
	0.5b	-0.361(0.0,0.5)	-0.905(0.0,0.5)	-0.259(0.8,0.5)/0.235(-0.8,0.5)	0.281(0.6,0.5)
	0.8b	-0.256(1.2,0.8)	-0.791(0.0,0.8)	-0.243(0.8,0.8)/0.226(-0.8,0.8)	0.301(0.0,0.8)
	1.0b	-0.220(1.4,1.0)	-0.716(0.0,1.0)	-0.227(1.0,1.0)/0.211(-1.0,1.0)	0.295(0.0,1.0)
10.0	0.1b	-0.862(0.0,0.1)	-0.998(0.0,0.1)	-0.152(1.0,0.1)/0.095(-1.0,0.1)	0.179(1.0,0.1)
	0.2b	-0.697(0.0,0.2)	-0.986(0.0,0.2)	-0.204(0.8,0.2)/0.160(-1.0,0.2)	0.214(1.0,0.2)
	0.5b	-0.361(0.0,0.5)	-0.905(0.0,0.5)	-0.259(0.8,0.5)/0.235(-0.8,0.5)	0.281(0.6,0.5)
	0.8b	-0.256(1.2,0.8)	-0.791(0.0,0.8)	-0.243(0.8,0.8)/0.226(-0.8,0.8)	0.301(0.0,0.8)
	1.0b	-0.220(1.4,1.0)	-0.716(0.0,1.0)	-0.227(1.0,1.0)/0.211(-1.0,1.0)	0.295(0.0,1.0)

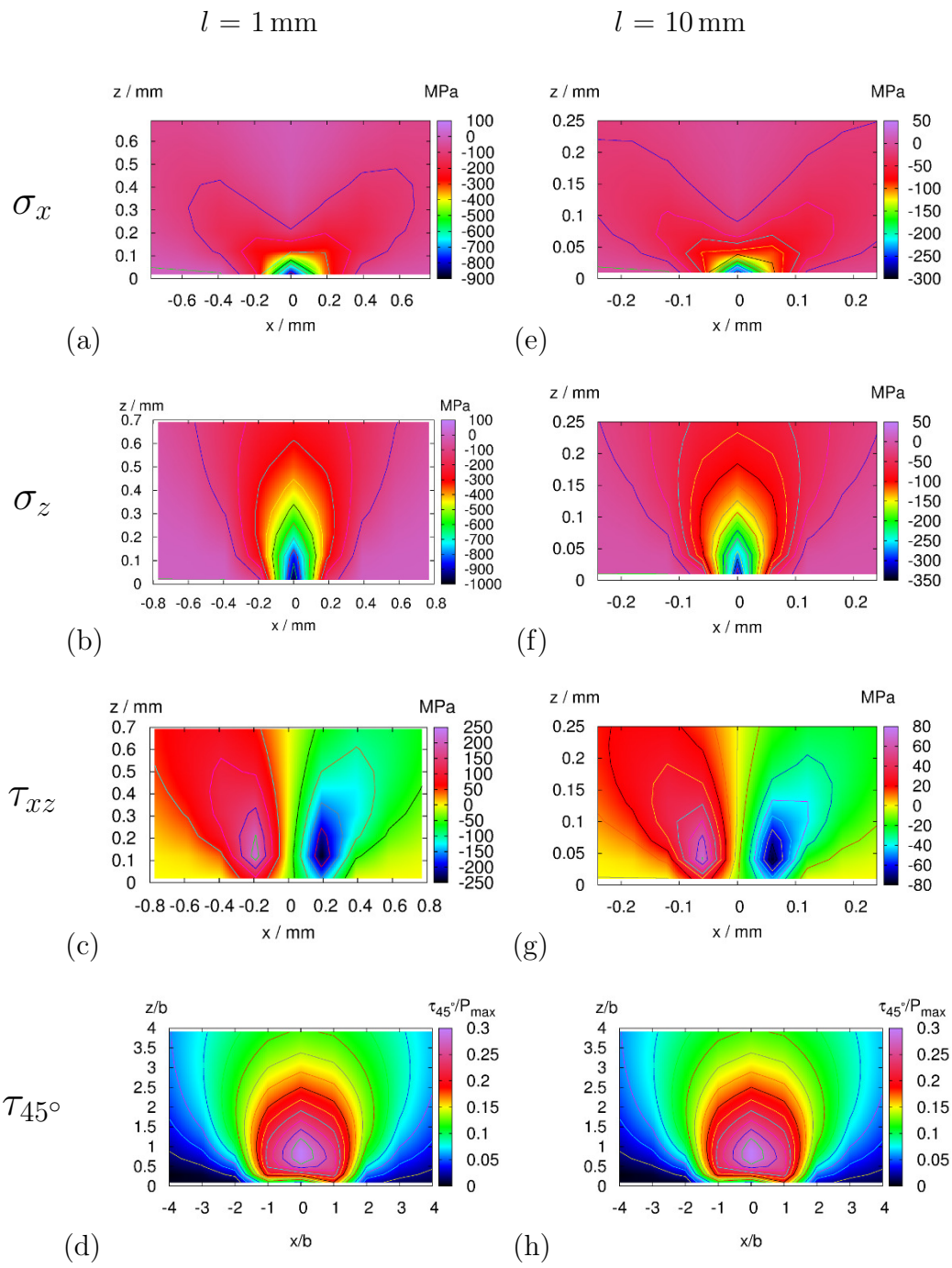

Figure B.5: Calculation of sub-surfaces stresses, σ_x, σ_z and τ_{xz} and $\tau_{45°}$ under plane stress for $\mu = 0.55$, $\xi = 0.95$, for (a-d) $l = 1$ mm and (e-h) $l = 10$ mm.

Table B.7: Maximum values of stresses in the contact zone normalised against P_{max} having $P = 300N$, $\xi = 0.95$, $\mu = 0.55$, $l = 5$ mm and $R_1, R_2 = 10$ mm and 30 mm respectively.

Radius (R_1,R_2) / mm	Distance in z	σ_x/P$_{max}$(x/b,z/b)	σ_z/P$_{max}$(x/b,z/b)	τ_{xz}/P$_{max}$(x/b,z/b)	τ_{45°/P$_{max}$(x/b,z/b)
10.0	0.1b	-0.862(0.0,0.1)	-0.998(0.0,0.1)	-0.152(1.0,0.1)/0.095(-1.0,0.1)	0.179(1.0,0.1)
	0.2b	-0.697(0.0,0.2)	-0.986(0.0,0.2)	-0.204(0.8,0.2)/0.160(-1.0,0.2)	0.214(1.0,0.2)
	0.5b	-0.361(0.0,0.5)	-0.905(0.0,0.5)	-0.259(0.8,0.5)/0.235(-0.8,0.5)	0.281(0.6,0.5)
	0.8b	-0.256(1.2,0.8)	-0.791(0.0,0.8)	-0.243(0.8,0.8)/0.226(-0.8,0.8)	.301(0.0,0.8)
	1.0b	-0.220(1.4,1.0)	-0.716(0.0,1.0)	-0.227(1.0,1.0)/0.211(-1.0,1.0)	0.295(0.0,1.0)
30.0	0.1b	-0.862(0.0,0.1)	-0.998(0.0,0.1)	-0.152(1.0,0.1)/0.095(-1.0,0.1)	0.179(1.0,0.1)
	0.2b	-0.697(0.0,0.2)	-0.986(0.0,0.2)	-0.204(0.8,0.2)/0.160(-1.0,0.2)	0.214(1.0,0.2)
	0.5b	-0.361(0.0,0.5)	-0.905(0.0,0.5)	-0.259(0.8,0.5)/0.235(-0.8,0.5)	0.281(0.6,0.5)
	0.8b	-0.256(1.2,0.8)	-0.791(0.0,0.8)	-0.243(0.8,0.8)/0.226(-0.8,0.8)	0.301(0.0,0.8)
	1.0b	-0.220(1.4,1.0)	-0.716(0.0,1.0)	-0.227(1.0,1.0)/0.211(-1.0,1.0)	0.295(0.0,1.0)

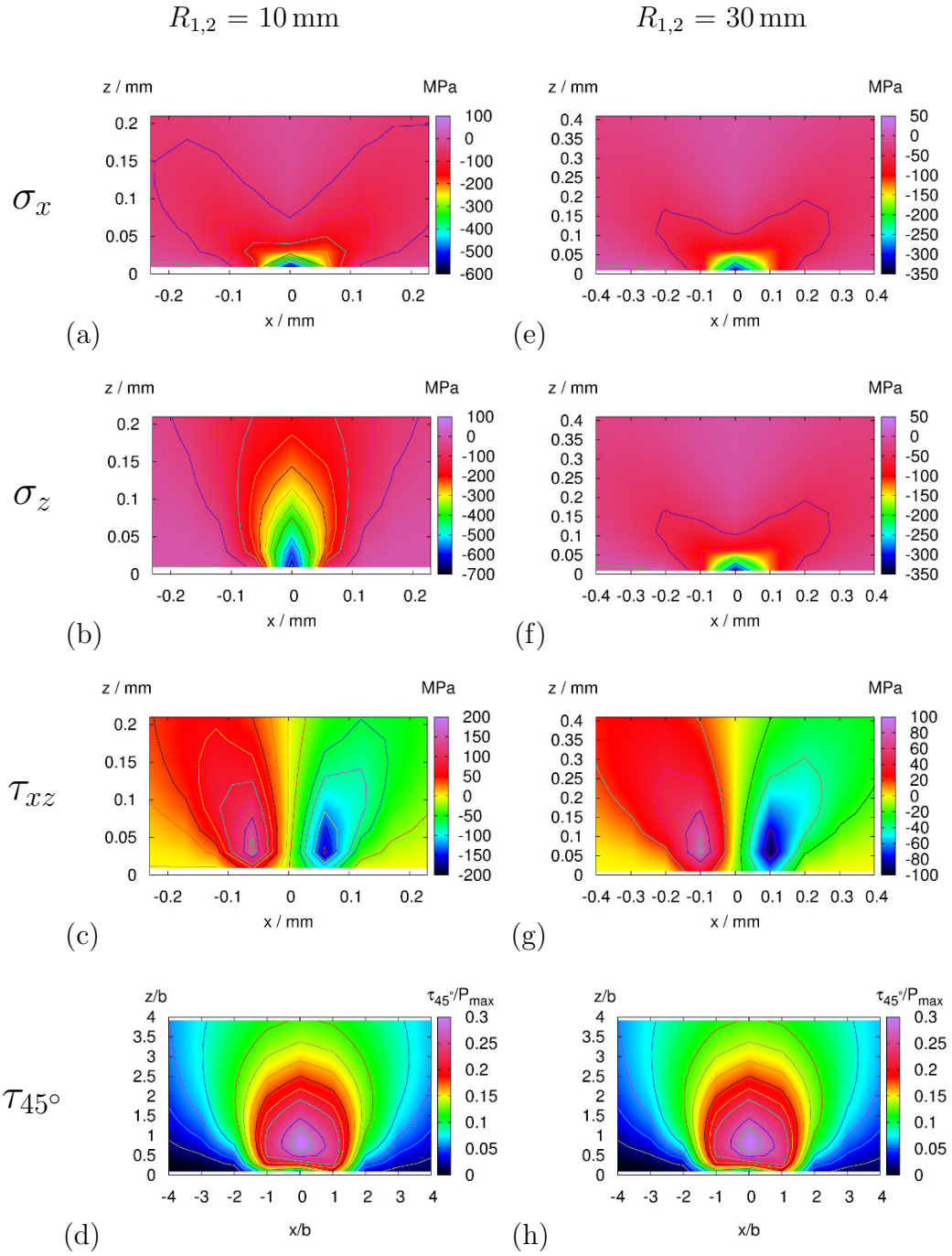

Figure B.6: Calculation of sub-surfaces stresses, σ_x, σ_z and τ_{xz} and $\tau_{45°}$ under plane stress for $\mu = 0.55$, $\xi = 0.95$, $P = 300$ N, $l = 5$ mm for (a-d) R_1, $R_2 = 10$ mm and (e-h) R_1, $R_2 = 30$ mm.

Table B.8: Maximum values of stresses in the contact zone normalised against P_{max} having $R_1, R_2 = 22.5\ mm$, $\xi = 0.95$, $l = 5\ mm$, $\mu = 0.55$ and $P = 300\ N$, for Copper ($\nu = 0.34$, E = 110 GPa) and Tungsten ($\nu = 0.28$ and E = 411 GPa) respectively.

Element	Distance in z	$\sigma_x/\mathrm{P}_{max}$(x/b,z/b)	$\sigma_z/\mathrm{P}_{max}$(x/b,z/b)	$\tau_{xz}/\mathrm{P}_{max}$(x/b,z/b)	$\tau_{45^\circ}/\mathrm{P}_{max}$(x/b,z/b)
Copper	0.1b	-0.874(0.0,0.1)	-1.00(0.0,0.1)	-0.155(1.0,0.1)/0.096(-1.0,0.1)	0.181(1.0,0.1)
	0.2b	-0.708(0.0,0.2)	-0.998(0.0,0.2)	-0.207(0.8,0.2)/0.162(-0.8,0.2)	0.217(1.0,0.2)
	0.5b	-0.366(0.0,0.5)	-0.918(0.0,0.5)	-0.263(0.8,0.5)/0.238(-0.8,0.5)	0.285(0.6,0.5)
	0.8b	-0.260(1.2,0.8)	-0.803(0.0,0.8)	-0.246(0.8,0.8)/0.228(-0.8,0.8)	0.305(0.0,0.8)
	1.0b	-0.224(1.4,1.0)	-0.727(0.0,1.0)	-0.231(1.0,1.0)/0.214(-1.0,1.0)	0.299(0.0,1.0)
Tungsten	0.1b	-0.856(0.0,0.1)	-0.992(0.0,0.1)	-0.151(1.0,0.1)/0.094(-1.0,0.1)	0.178(1.0,0.1)
	0.2b	-0.693(0.0,0.2)	-0.980(0.0,0.2)	-0.203(0.8,0.2)/0.159(-0.8,0.2)	0.213(1.0,0.2)
	0.5b	-0.358(0.0,0.5)	-0.899(0.0,0.5)	-0.258(0.8,0.5)/0.234(-0.8,0.5)	0.280(0.6,0.5)
	0.8b	-0.254(1.2,0.8)	-0.786(0.0,0.8)	-0.242(0.8,0.8)/0.223(-0.8,0.8)	0.299(0.0,0.8)
	1.0b	-0.219(1.4,1.0)	-0.712(0.0,1.0)	-0.226(1.0,1.0)/0.209(-1.0,1.0)	0.293(0.0,1.0)

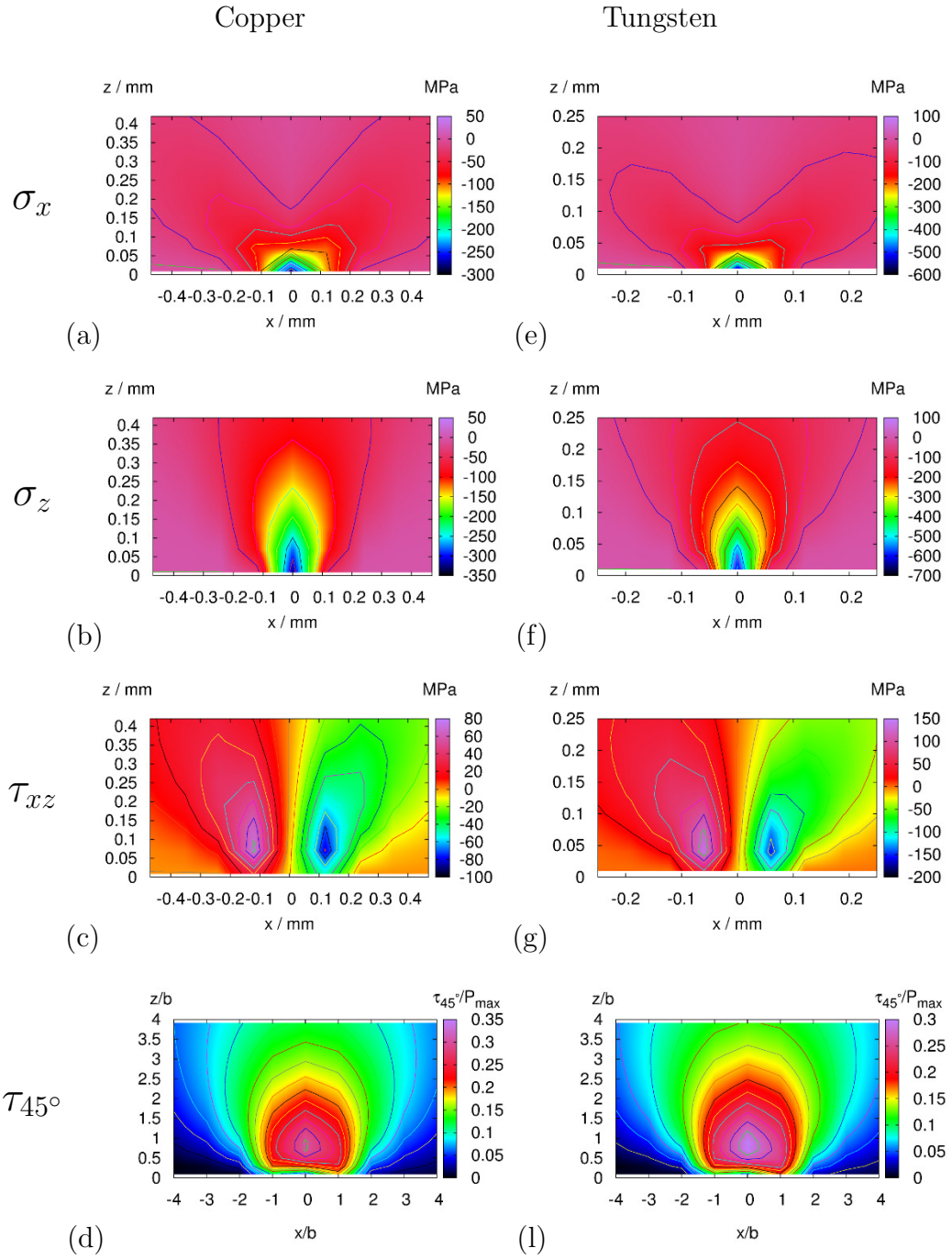

Figure B.7: Calculation of sub-surfaces stresses, σ_x, σ_z and τ_{xz} and $\tau_{45°}$ under plane stress for $\mu = 0.55$, $\xi = 0.95$, $P = 300$ N, $l = 5$ mm for (a-d) Copper and (e-h) Tungsten discs.

stress-fields gets narrower, causing more localised damage due to increased stress concentration.

B.7 Effect of slip ratio

Introduction of slip during rolling/sliding has different effects on the tractional, normal and shear stress components, as shown in Fig. B.9(a-h). With introduction of nominal slip, the tractional stress, σ_x, marginally increases and gets slightly biased towards towards positive x-direction compared to the completely symmetrical distribution in perfect rolling [Fig. B.9(e)]. In the case of pure sliding, as shown in [Fig. B.9(a)], the distribution gets heavily skewed in the direction of sliding. However, the influence of slip on compressive stress, σ_z, is nominal compared to other components of stresses [Fig. B.9(b,f)]. Perfect sliding causes the maximum shear stress to migrate on to the surface [Fig. B.9(c)], which otherwise under the condition of perfect rolling is normally achieved below the surface, at a depth of 0.78b [Fig. B.9(c)]. With a greater amount of slip, the damage of the structure caused by shear stress is therefore more likely to happen near the surface.

During the running-in period and as it reaches the steady-state, where the maximum contact length equal to 5 mm was gradually being achieved, the value of the von Mises stress drops further below the yield stress of the nanostructured bainite [Fig. B.9(e-h)]. Not only the magnitude of the stress drops, but also the spatial distribution of stress becomes progressively smaller with increased contact length. This would mean that the severity of damage caused by the stress would also diminish.

Table B.9: Maximum values of stresses in the contact zone normalised against P_{max} having $P = 300N$, $\xi = 0.95$, $l = 5$ mm and for $\mu = 0.40$ and 0.80 respectively.

μ	Distance in z	$\sigma_x/\mathrm{P}_{max}$(x/b,z/b)	$\sigma_z/\mathrm{P}_{max}$(x/b,z/b)	$\tau_{xz}/\mathrm{P}_{max}$(x/b,z/b)	$\tau_{45^\circ}/\mathrm{P}_{max}$(x/b,z/b)
0.40	0.1b	-0.849(0.0,0.1)	-0.997(0.0,0.1)	-0.151(1.0,0.1)/0.109(-1.0,0.1)	0.174(1.0,0.1)
	0.2b	-0.687(0.0,0.2)	-0.985(0.0,0.2)	-0.201(0.8,0.2)/0.169(-0.8,0.2)	0.210(1.0,0.2)
	0.5b	-0.355(0.0,0.5)	-0.902(0.0,0.5)	-0.256(0.8,0.5)/0.238(-0.8,0.5)	0.280(0.6,0.5)
	0.8b	-0.251(1.2,0.8)	-0.788(0.0,0.8)	-0.240(0.8,0.8)/0.226(-0.8,0.8)	0.300(0.0,0.8)
	1.0b	-0.216(1.4,1.0)	-0.714(0.0,1.0)	-0.224(1.0,1.0)/0.212(-1.0,1.0)	0.294(0.0,1.0)
0.80	0.1b	-0.883(0.0,0.1)	-0.999(0.0,0.1)	-0.155(1.0,0.1)/0.072(-1.0,0.1)	0.186(1.0,0.1)
	0.2b	-0.715(0.0,0.2)	-0.989(0.0,0.2)	-0.209(0.8,0.2)/0.146(-0.8,0.2)	0.221(1.0,0.2)
	0.5b	-0.371(0.2,0.5)	-0.909(0.0,0.5)	-0.265(0.8,0.5)/0.230(-0.8,0.5)	0.284(0.6,0.5)
	0.8b	-0.265(1.2,0.8)	-0.796(0.0,0.8)	-0.247(0.8,0.8)/0.221(-0.8,0.8)	0.302(0.2,0.8)
	1.0b	-0.228(1.4,1.0)	-0.721(0.0,1.0)	-0.232(1.0,1.0)/0.208(-1.0,1.0)	0.296(0.0,1.0)

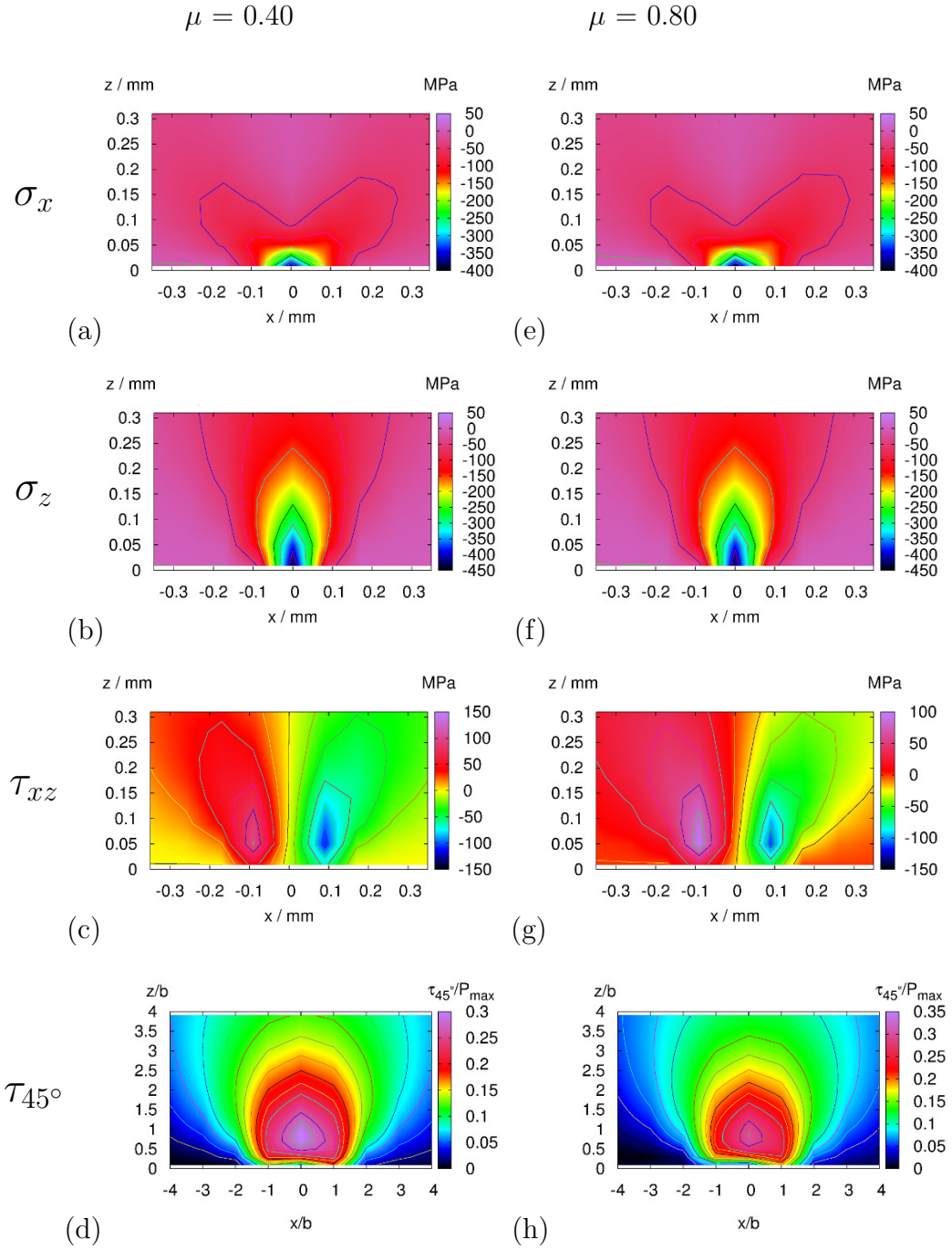

Figure B.8: Calculation of sub-surfaces stresses, σ_x, σ_z and τ_{xz} and $\tau_{45°}$ under plane stress for $\xi = 0.95$, $P = 300$ N, R_1, $R_2 = 22.5$ mm, $l = 5$ mm for (a-d) $\mu = 0.40$ and (e-h) $\mu = 0.80$.

Table B.10: Maximum values of stresses in the contact zone normalised against P_{max} having $R_1, R_2 = 22.5\ mm$, $l = 5$ mm, $\mu = 0.55$ and $P = 300$ N, for pure rolling,pure sliding, $\xi = 0.95$ (5% slip) and 0.05 (95% slip) respectively.

Rolling/Sliding	Distance in z	σ_x/P$_{max}$(x/b,z/b)	σ_z/P$_{max}$(x/b,z/b)	τ_{xz}/P$_{max}$(x/b,z/b)	τ_{45°/P$_{max}$(x/b,z/b)
Pure rolling	0.1b	-0.816(0.0,0.1)	-0.995(0.0,0.1)	-0.146(1.0,0.1)/0.146(-1.0,0.1)	0.163(1.0,0.1)
	0.2b	-0.660(0.0,0.2)	-0.981(0.0,0.2)	-0.193(0.8,0.2)/0.193(-0.8,0.2)	0.206(0.8,0.2)
	0.5b	-0.342(0.0,0.5)	-0.895(0.0,0.5)	-0.247(0.8,0.5)/0.247(-0.8,0.5)	0.278(0.4,0.5)
	0.8b	-0.237(1.2,0.8)	-0.781(0.0,0.8)	-0.231(0.8,0.8)/0.231(-0.8,0.8)	0.300(0.0,0.8)
	1.0b	-0.205(1.4,1.0)	-0.707(0.0,1.0)	-0.217(1.0,1.0)/0.217(-1.0,1.0)	0.293(0.0,1.0)
Pure sliding	0.1b	-1.169(0.6,0.1)	-0.995(0.0,0.1)	-0.457(0.2,0.1)	0.457(0.2,0.1)
	0.2b	-0.938(0.6,0.2)	-0.981(0.0,0.2)	-0.413(0.8,0.2)/0.011(-1.0,0.2)	0.460(1.0,0.2)
	0.5b	-0.580(1.0,0.5)	-0.911(0.2,0.5)	-0.411(0.8,0.5)/0.082(-0.8,0.5)	0.413(0.8,0.5)
	0.8b	-0.425(1.4,0.8)	-0.802(0.2,0.8)	-0.359(1.0,0.8)/0.112(-0.8,0.8)	.371(0.8,0.8)
	1.0b	-0.357(1.6,1.0)	-0.728(0.2,1.0)	-0.323(1.0,1.0)/0.116(-0.8,1.0)	0.343(0.6,1.0)
$\xi = 0.95$	0.1b	-0.862(0.0,0.1)	-0.998(0.0,0.1)	-0.152(1.0,0.1)/0.095(-1.0,0.1)	0.179(1.0,0.1)
	0.2b	-0.697(0.0,0.2)	-0.986(0.0,0.2)	-0.204(0.8,0.2)/0.160(-0.8,0.2)	0.214(1.0,0.2)
	0.5b	-0.361(0.0,0.5)	-0.905(0.0,0.5)	-0.259(0.8,0.5)/0.235(-0.8,0.5)	0.281(0.6,0.5)
	0.8b	-0.256(1.2,0.8)	-0.791(0.0,0.8)	-0.243(0.8,0.8)/0.224(-0.8,0.8)	0.301(0.0,0.8)
	1.0b	-0.221(1.4,1.0)	-0.716(0.0,1.0)	-0.227(1.0,1.0)/0.211(-1.0,1.0)	0.295(0.0,1.0)
$\xi = 0.05$	0.1b	-1.174(0.6,0.1)	-0.995(0.0,0.1)	-0.457(0.2,0.1)/-0.0034(-4.0,0.1)	0.457(0.2,0.1)
	0.2b	-0.941(0.6,0.2)	-0.981(0.0,0.2)	-0.412(0.8,0.2)/0.011(-1.0,0.2)	0.460(1.0,0.2)
	0.5b	-0.580(1.0,0.5)	-0.911(0.2,0.5)	-0.411(0.8,0.5)/0.083(-0.8,0.5)	0.413(0.8,0.5)
	0.8b	-0.424(1.4,0.8)	-0.802(0.2,0.8)	-0.359(1.0,0.8)/0.112(-0.8,0.8)	.371(0.8,0.8)
	1.0b	-0.357(1.6,1.0)	-0.728(0.2,1.0)	-0.323(1.0,1.0)/0.116(-0.8,1.0)	0.343(0.6,1.0)

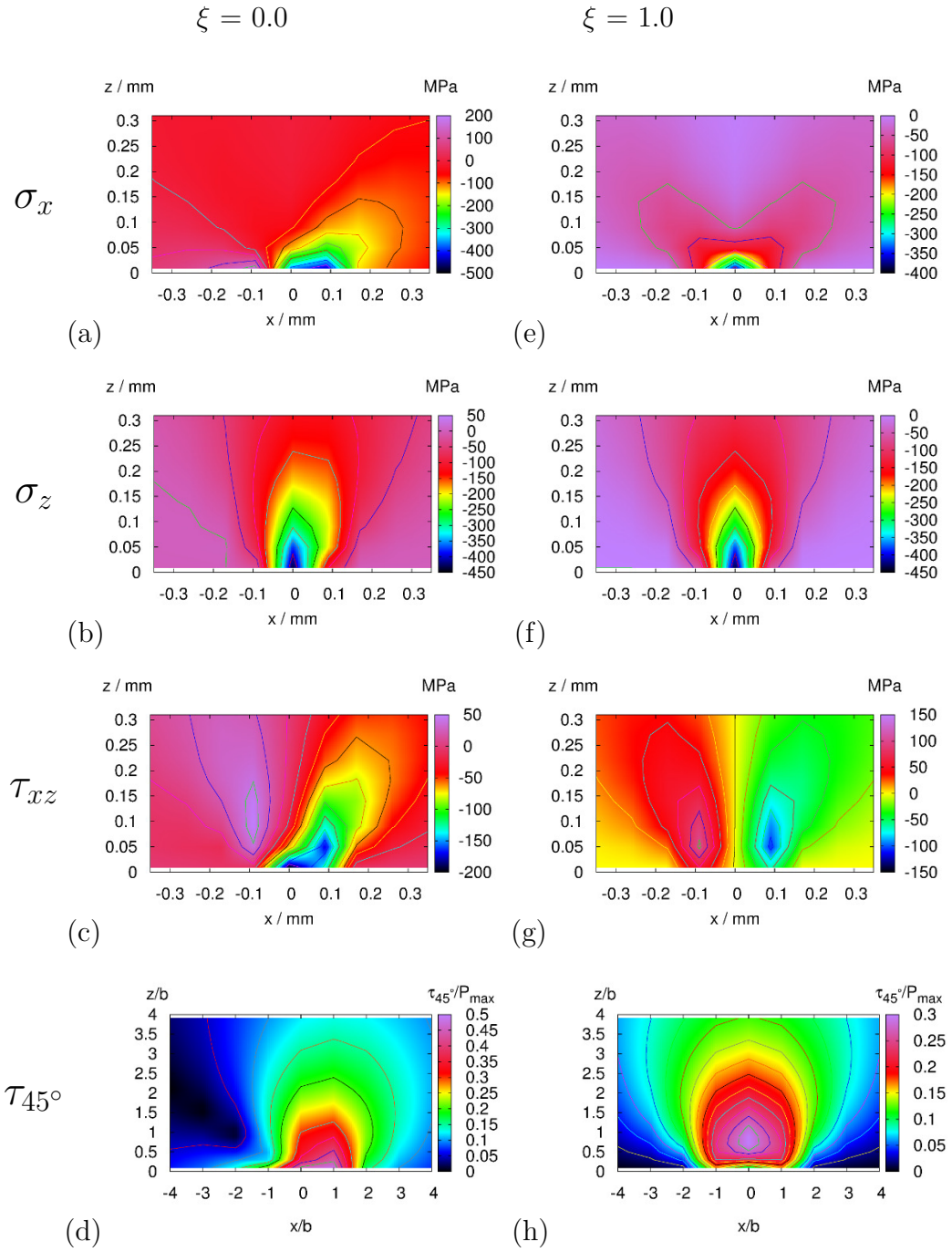

Figure B.9: Calculation of sub-surfaces stresses, σ_x, σ_z and τ_{xz} and τ_{45° under plane stress for $\mu = 0.55$, $P = 300$ N, R_1, $R_2 = 22.5$ mm, $l = 5$ mm for (a-d) $\xi = 0.0$ and (e-h) $\xi = 1.0$.

B.8 Conclusions

1. Greater loads lead to larger contact stresses, but the normalised components remain unchanged both in terms of their ratios and coordinates with respect to the maximum load and Hertzian contact half width. Similarly, a change in overlap width and disc radii changes the absolute values and coordinates of contact stresses, but the normalised components of the stress remain unchanged.

2. Greater Young's moduli increase the absolute value of the contact stresses below the surface, but their respective normalised components against maximum load decrease. This signifies less damage to the stiffer material under similar conditions of loading and geometrical configuration during rolling/sliding.

3. Increase in friction during rolling/sliding causes normalised shear and tractional stresses to increase, without increasing the compressive component of the stress. This could lead to more subsurface damage together with a higher rate of material removal from the surface.

4. Introduction of slip in rolling/sliding brings a nominal increase in the magnitude and distribution of the normalised compressive stress, whereas the tractional and shear stress components undergo significant change, especially at depths $z < 0.78b$.

Appendix C

Code for rolling/sliding of two rigid, axial and parallel cylinders with slip

---

C.1 Statement of Purpose of the code

The code is written to calculate the distribution of forces and stresses during rolling contact of two rigid, parallel and flat cylinders assuming Hertzian contact between the mating surfaces under various conditions of slip. It aims to estimate the magnitude and distribution of normal and tangential forces acting over the Hertzian contact half-width and subsequently calculates the tangential, normal and shear stresses under plane stress condition. A range of stress distribution from perfect rolling to perfect sliding between mating cylinders can be calculated.

C.2 Input and output parameters

A list of input parameters to be called from an **input_data.txt** file are listed below in Table C.1. The list of the output parameters, generated in an output

file is listed in Table C.2.

Table C.1: List of input parameters for the code.

Parameter, unit	variable type
Poisson's ratio	double
Load, N	double
Overlap length, mm	double
Young's modulus, disc 1, GPa	double
Young's modulus, disc 2, GPa	double
Radius, disc 1, mm	double
Radius, disc 2, mm	double
Coefficient of friction	double
1-(%Slip/100)	double

Table C.2: List of output parameters for the code.

Parameter, unit	variable type
Distance in x-direction, mm	double
Distance in z-direction, mm	double
Tractionals stress, σ_x, MPa	double
Tractional force/Nornal load, σ_x.b/P$_{normal}$	double
Normal stress, σ_z, MPa	double
Normal force/Nornal load, σ_z.b/P$_{normal}$	double
Shear stress, τ_{xz}, MPa	double
Shear force/Nornal load, τ_{xz}.b/P$_{normal}$	double

C.3 Accuracy limits

The stress values are accurate to the errors equivalent to that of the input values.

```
1
2
3  /*** Declare the standard library ***/
4 #include<stdio.h>
5 #include<math.h>
6 #include<stdlib.h>
7 #define N 100
8 void read_input();
9 void initialise();
10 void normal_force_rolling_sliding();
11 void tangential_force_rolling_sliding();
12 void I_integral();
13 void write_test();
14 /*void stress_rolling_sliding();*/
15 void write_force();
16 void write_stress();
17 void append_write_force();
18 void append_write_stress();
19 /*** Global variables declaration ***/
20 int imax,jmax;
21 double nu,l,P,E1,E2,R1,R2,x,absx,z,i,j,t,mu, sigma1, sigma2;
22 double b,B,P_normal,pzx,pxx,xi,r1,f0,f1,f2, sigma_x,sigma_x1,
    sigma_x_ratio,sigma_z, sigma_z_ratio, tau_xz,tau_xz_ratio,
    tau_max,sigma_vm;
23 /*** variable declaration for I_integral() subroutine ***/
24 /*** variable declaration for I1() integral ***/
25 double m,r,l1, u1,t, xi, Ix1,Ix1sum,Iz1, Iz1sum, Ixz1, Ixz1sum,
    Ix1sum1, Iz1sum1, Ixz1sum1;
26 /*** variable declaration for I2() integral ***/
27 double l2, u2, Ix2xi,Ix2xisum, Iz2xi, Iz2xisum, Ixz2xi, Ixz2xisum,
    Ix2xisum1, Iz2xisum1, Ixz2xisum1;
28 /*** variable declaration for I3() integral ***/
29 double n,g,h,k,l3,u3, Ix3xi, Ix3xisum, Iz3xi, Iz3xisum, Ixz3xi,
    Ixz3xisum,Ix3xisum1, Iz3xisum1,Ixz3xisum1;
30 /** r defined as counter in void I_integral() subroutine **/
31 FILE *fp;
32 FILE *fp1;
33 /*FILE *gnuplot = open("gnuplot", "w");*/
34
35 void main()
36 {
37 read_input();
```

```
b = 2*sqrt(((1-nu*nu)*P*(1/(E1*1000)+1/(E2*1000)))/(3.1415*l*(1/R1
    +1/R2)));
scanf("%lf",&b);
printf("The valueof b is : %lf", b);
getchar();
/*initialise();*/
/*write_force();*/
/*write_stress();*/
/*for(i=-1;i=1;i=i+0.1)*/
for(z=0.1*b;z<=4.1*b;z=z + 0.5*b)
/*for(x=-4*b;x<=4.1*b;x=x+0.1*b)*/
  {

    /*normal_force_rolling_sliding();*/
    /*tangential_force_rolling_sliding();*/
    /*append_write_force();*/
    /*for(j=0.1;j<=1;j=j+0.1)*/
    /*for(z=0.1*b;z<=1.1*b;z=z + 0.1*b)*/
    /*if(z=0.1*b)*/
    for(x=-4*b;x<=4.1*b;x=x+0.2*b)
    {

        /*x=i*b;
        scanf("%lf",&x);
        z = j*b;
        scanf("%lf",&z);*/
        i=x/b;
        scanf("%lf",&i);
        j=z/b;
        scanf("%lf",&j);

        I_integral();

        append_write_stress();
        /*return;*/
        initialise();

    }
                /*initialise();*/


  }
```

```
79 /*write_test();*/
80 }
81 /******* End Main *******/
82
83 /**** Start of read_input *************/
84 void read_input()
85 {
86 FILE *fp;
87 fp = fopen("input_data_stress.txt","r+");
88 fscanf(fp,"\n%lf\n%lf\n%lf\n%lf\n%lf\n%lf\n%lf\n%lf\n%lf",&nu,&P,&l
       ,&E1,&E2,&R1,&R2,&mu,&xi);
89 fclose(fp);
90 }
91 /*************** End of read_input **************/
92 /*************** Start of I_integral ************/
93 void I_integral()
94 {
95 /****** I_integrals for limit (-1, +1) *******/
96 P_normal = P/(l);
97 scanf("%lf",&P_normal);
98 l1= -1.0;
99 u1=1.0;
100 scanf("%lf%lf",&l1,&u1);
101 if (l1 > u1) {
102   t = l1;
103   l1 = u1;
104   u1 = t;
105  }
106   for(t=l1; t<=u1; t= t+(u1-l1)/N)
107     {
108       m = sqrt(1-(t*t));
109       scanf("%lf", &m);
110       /*printf("for x=%lfb, z=%lfb, m is: %lf\n", i,j,m);*/
111       Ix1 = m*(i-t)*(i-t)/(((i-t)*(i-t) + j*j)*((i-t)*(i-t) + j*j));
112       scanf("%lf",&Ix1);
113       /*printf("Ix1 = %lf\n", Ix1);*/
114       Ix1sum += Ix1*(u1-l1)/N;
115       /*printf("Ix1sum = %lf\n", Ix1sum);*/
116       /*scanf("%lf",&Ix1sum);*/
117
118       Iz1 = m/(((i-t)*(i-t) + j*j)*((i-t)*(i-t) + j*j));
119       Iz1sum += Iz1*(u1-l1)/N;
```

```
120
121       Ixz1 =   m*(i-t)/(((i-t)*(i-t) + j*j)*((i-t)*(i-t) + j*j));
122       Ixz1sum += Ixz1*(u1-l1)/N;
123
124       /*return;*/
125     }
126       scanf("%lf",&Ix1sum);
127       Ix1sum1 =Ix1sum ;
128       scanf("%lf", &Ix1sum1);
129       /*return Ix1sum1;*/
130       Iz1sum1 = Iz1sum;
131       scanf("%lf", &Iz1sum1);
132       /*return Iz1sum1;*/
133       Ixz1sum1 = Ixz1sum;
134       scanf("%lf", &Ixz1sum1);
135       /*return Ixz1sum1;*/
136       /*printf("\n for x=%lfb, z=%lfb, Ix1sum is : %.2lf, Iz1sum is
    : %.2lf, Ixz1sum is : %2lf\n",i,j,Ix1sum,Iz1sum, Ixz1sum);*/
137             /*getchar();*/
138       /*return;*/
139 /******* I_integrals for limit (-1, 1-2*xi) *******/
140 l2= -1;
141 u2= 1-(2*xi);
142 if (l2 > u2)
143   {
144     t = l2;
145     l2 = u2;
146     u2 = t;
147
148    }
149 for(t=l2; t<=u2; t= t+(u2-l2)/N)
150     {
151       m = sqrt(1-(t*t));
152       scanf("%lf", &m);
153       Ix2xi = m*(i-t)*(i-t)*(i-t)/(((i-t)*(i-t) + j*j)*((i-t)*(i-t)
    + j*j));
154       scanf("%lf",&Ix2xi);
155       Ix2xisum += Ix2xi*(u2-l2)/N;
156       /*scanf("%lf",&Ix2xisum);*/
157       Iz2xi = m*(i-t)/(((i-t)*(i-t) + j*j)*((i-t)*(i-t) + j*j));
158       Iz2xisum += Iz2xi*(u2-l2)/N;
```

```
159       Ixz2xi = m*(i-t)*(i-t)/(((i-t)*(i-t) + j*j)*((i-t)*(i-t) + j*j
    ));
160       Ixz2xisum += Ixz2xi*(u2-l2)/N;
161       /*return;*/
162
163     }
164       scanf("%lf",&Ix2xisum);
165       Ix2xisum1 = Ix2xisum;
166       scanf("%lf", &Ix2xisum1);
167       /*return Ix2xisum1;*/
168       Iz2xisum1 = Iz2xisum;
169       scanf("%lf", &Iz2xisum1);
170       /*return Iz2xisum1;*/
171       Ixz2xisum1 = Ixz2xisum;
172       scanf("%lf", &Ixz2xisum1);
173       /*return Ixz2xisum1;*/
174     /*printf("\n for x=%lfb, z=%lfb,Ix2xisum is: %.4lf, Iz2xisum is:
     %.4lf, Ixz2xisum is: %.4lf\n",i,j,Ix2xisum,Iz2xisum,Ixz2xisum );
    */
175
176 /******* I_integrals for limit (1-2*xi, 1) *******/
177 l3= 1-(2*xi);
178 u3= 1;
179 if (l3 > u3)
180   {
181     t = l3;
182     l3 = u3;
183     u3 = t;
184
185    }
186 for(t=l3; t<u3; t= t+(u3-l3)/N)
187     {
188       m = sqrt(1-(t*t));
189       scanf("%lf", &m);
190       g=xi+t-1;
191       h = xi*xi;
192       scanf("%lf%lf",&g,&h);
193       /*printf("g = %lf, h = %lf\n", g,h);*/
194       /*getchar();*/
195       k = (h-(g*g));
196       scanf("%lf", &k);
197       /*printf("k = %lf", k);*/
```

```
198       if (k == 0)
199       {
200         n == k;
201         scanf("%lf", &n);
202       }
203       else if (k>0)
204       {
205       n = sqrt(k);
206       scanf("%lf", &n);
207       }
208       /*printf("n = %lf\n",n);*/
209       /*printf("for x = %lfb, z = %lfb, m is : %lf, n is : %lf\n",i,
      j, m,n);*/
210       /*getchar();*/
211       Ix3xi = ((m-n)*(i-t)*(i-t)*(i-t))/(((i-t)*(i-t) + j*j)*((i-t)
      *(i-t) + j*j));
212       scanf("%lf",&Ix3xi);
213       Ix3xisum += Ix3xi*(u3-l3)/N;
214       /*scanf("%lf",&Ix3xisum);*/
215       Iz3xi = ((m-n)*(i-t))/(((i-t)*(i-t) + j*j)*((i-t)*(i-t) + j*j)
      );
216       Iz3xisum += Iz3xi*(u3-l3)/N;
217       Ixz3xi = ((m-n)*(i-t)*(i-t))/(((i-t)*(i-t) + j*j)*((i-t)*(i-t)
       + j*j));
218       Ixz3xisum += Ixz3xi*(u3-l3)/N;
219
220
221     }
222       /*getchar();*/
223       scanf("%lf",&Ix3xisum);
224       Ix3xisum1 = Ix3xisum;
225       scanf("%lf", &Ix3xisum1);
226       /*return Ix3xisum1;*/
227       Iz3xisum1 = Iz3xisum;
228       scanf("%lf", &Iz3xisum1);
229       /*return Iz3xisum1;*/
230       Ixz3xisum1 = Ixz3xisum;
231       scanf("%lf", &Ixz3xisum1);
232       /*return Ixz3xisum1;*/
233
234 /*printf("\n for x=%lfb, z=%lfb,Ix3xisum is: %.4lf, Iz3xisum is: %.4
      lf, Ixz3xisum is: %0.4lf\n",i,j,Ix3xisum, Iz3xisum, Ixz3xisum);*/
```

```
235 /*sigma_x = -(4*P_normal)*(j*Ix1sum + mu*Ix2xisum + mu*Ix3xisum)/(b
        *3.1415*3.1415);*/
236 sigma_x = -(4*P_normal)*(j*Ix1sum1 + mu*Ix2xisum1 + mu*Ix3xisum1)/(b
        *3.1415*3.1415);
237 scanf("%lf", &sigma_x);
238 sigma_x_ratio = sigma_x*b/P_normal;
239 /*scanf("%lf", &sigma_x_ratio);*/
240 printf("\n for x=%lfb, z=%lfb, Ix1sum1 = %lf, Ix2xisum1 = %lf,
        Ix3xisum1=%lf, sigma_x is: %lf, sigma_x_ratio is: %lf ", i,j,
        Ix1sum1,Ix2xisum1, Ix3xisum1,sigma_x, sigma_x_ratio);
241
242 /*sigma_z = -((4*P_normal*j*j)*(j*Iz1sum + mu*Iz2xisum + mu*Iz3xisum
        ))/(b*3.1415*3.1415);*/
243 sigma_z = -((4*P_normal*j*j)*(j*Iz1sum1 + mu*Iz2xisum1 + mu*
        Iz3xisum1))/(b*3.1415*3.1415);
244 scanf("%lf", &sigma_z);
245 sigma_z_ratio = sigma_z*b/P_normal;
246 printf("\n for x=%lfb, z=%lfb, Iz1sum1 = %lf, Iz2xisum1 = %lf,
        Iz3xisum1 = %lf, sigma_z is: %lf, sigma_z_ratio is: %lf", i,j,
        Iz1sum1,Iz2xisum1,Iz3xisum1,sigma_z, sigma_z_ratio);
247 /*tau_xz = -((4*P_normal*j)*(j*Ixz1sum + mu*Ixz2xisum + mu*Ixz3xisum
        ))/(b*3.1415*3.1415);*/
248 tau_xz = -((4*P_normal*j)*(j*Ixz1sum1 + mu*Ixz2xisum1 + mu*
        Ixz3xisum1))/(b*3.1415*3.1415);
249 scanf("%lf", &tau_xz);
250 tau_xz_ratio = tau_xz*b/P_normal;
251 printf("\n for x=%lfb, z=%lfb, Ixz1sum1 = %lf,Ixz2xisum1 = %lf,
        Ixz3xisum1 = %lf, tau_xz is: %lf, tau_xz_ratio is: %lf\n", i,j,
        Ixz1sum1,Ixz2xisum1,Ixz3xisum1,tau_xz, tau_xz_ratio);
252
253 sigma1 = (sigma_x + sigma_z)/2 + sqrt(((sigma_x - sigma_z)/2)*(
        sigma_x - sigma_z)/2 + tau_xz*tau_xz );
254 sigma2 = (sigma_x + sigma_z)/2 - sqrt(((sigma_x - sigma_z)/2)*(
        sigma_x - sigma_z)/2 + tau_xz*tau_xz );
255 scanf("%lf%lf",&sigma1,&sigma2);
256 printf("\n for x=%lfb, z=%lfb, sigma1 = %lf, sigma2 = %lf", i,j,
        sigma1, sigma2);
257 tau_max = 0.5*(sigma1 - sigma2);
258 scanf("%lf", &tau_max);
259 printf("tau_max = %lf", tau_max);
260 sigma_vm = sqrt(sigma1*sigma1 -sigma1*sigma2 + sigma2*sigma2 + 3*
        tau_xz*tau_xz);
```

```
scanf("%lf", &sigma_vm);
printf("sigma_vm = %lf", sigma_vm);
/*void initialise();*/
/*getchar();*/
}

/*************** Start initialise() ***************/
void initialise()
{

        Ix1=0;
        Ix1sum=0;
        Iz1=0;
        Iz1sum=0;
        Ixz1=0;
        Ixz1sum=0;
        Ix1sum1=0;
        Iz1sum1=0;
        Ixz1sum1=0;

        Ix2xi=0;
        Ix2xisum=0;
        Iz2xi=0;
        Iz2xisum=0;
        Ixz2xi=0;
        Ixz2xisum=0;
        Ix2xisum1=0;
        Iz2xisum1=0;
        Ixz2xisum1=0;

        Ix3xi=0;
        Ix3xisum=0;
        Iz3xi=0;
        Iz3xisum=0;
        Ixz3xi=0;
        Ixz3xisum=0;
        Ix3xisum1=0;
        Iz3xisum1=0;
        Ixz3xisum1=0;


printf("\n initialise complete\n");
```

```
303 }
304 /************** end initialise() ****************/
305 /***************** start of write_test() ************************/
306 void write_test()
307 {
308 Ix1sum1 =Ix1sum ;
309 scanf("%lf", &Ix1sum1);
310 sigma_x1=sigma_x;
311 scanf("%lf", &sigma_x1);
312 sigma_x_ratio = sigma_x1*b/P_normal;
313 printf("\n for x=%lfb, z=%lfb, sigma_x1 is: %lf, sigma_x_ratio is: %
    lf ", i,j,sigma_x1, sigma_x_ratio);
314 }
315 /***************** End of I_integral ****************************
    */
316 /************* Start of write_stress() ***************************
    */
317 void write_stress()
318 {
319 FILE *fp1;
320 fp1 = fopen("load.csv","a");
321 fprintf(fp1,"xi\ti\tj\tx\tz\tIx1sum\tIz1sum\tIxz1sum\tIx2xisum\
    tIz2xisum\tIxz2xisum\tIx3xisum\tIz3xisum\tIxz3xisum\tsigma_x\
    tsigma_x_ratio\tsigma_z\tsigma_z_ratio\ttau_xz\ttau_xz_ratio\
    tsigma1\tsigma2\ttau_max\n");
322 fclose(fp1);
323 }
324 /************* Start of write_stress() ***************************
    */
325 /********** Start append_write_stress () **************/
326 void append_write_stress()
327 {
328 FILE *fp1;
329 fp1 = fopen("Tungstentauxz300N.txt","a");
330 /*fprintf(fp1,"\t\t\t\t
    ***********************************************************************\
    n");
331 fprintf(fp1,"\t\t\t\tThe program calculates contact stresses during
    rolling of two cylinders\n");
332 fprintf(fp1,"\t\t\t\t
    ***********************************************************************
    t\t
```

```
    **********************************************************************\
    n");
fprintf(fp1,"\n\n");
fprintf(fp1,"The value of Poisson's ratio is %lf\n", nu);
fprintf(fp1,"The value of External load is %lf MPa\n",P);
fprintf(fp1,"The value of overlapping length ratio is %lf mm\n",l);
fprintf(fp1,"The value of Young's Modulus for disc 1 is %lf GPa\n",
    E1);
fprintf(fp1,"The value of Young's Modulus for disc 2 is %lf GPa\n",
    E2);
fprintf(fp1,"The value of the radius for disc 1 is %lf mm\n",R1);
fprintf(fp1,"The value of the radius for disc 1 is %lf mm\n",R2);*/
fprintf(fp1,"%0.2lf %0.2lf %0.2lf\n",/*xi,i,j,*/x,z,/*Ix1sum,Iz1sum,
    Ixz1sum,Ix2xisum,Iz2xisum,Ixz2xisum,Ix3xisum,Iz3xisum,Ixz3xisum,
    sigma_x/*, sigma_x_ratio/*,sigma_z/*,sigma_z_ratio,*/tau_xz/*,
    tau_xz_ratio/*,sigma2/*,sigma2,*tau_max,sigma_vm*/);
/*fprintf(fp1,"%lfb\t%lfb\t%lf\t%lf\t%lf\n",i,j,sig_zt,sig_zn,sig_z)
    ;*/
}
/************* End of append_write **********************/
```

Bibliography

[1] Y. C. Tasan. *Measurement of deformation in rolling and sliding contacts*. PhD thesis, University of Twente, the Netherlands, 2005.

[2] A. C. Fischer-Cripps. *Nanoindentation, Mechanical Engineering Series 1*. Springer Science and Business Media, LLC, 2011.

[3] K. M. Wu and H. K. D. H. Bhadeshia. Extremely fine pearlite by continuous cooling transformation. *Scripta Materialia*, 67:53–56, 2012.

[4] T. Sourmail, F. G. Caballero, C. Garcia-Mateo, V. Smanio, C. Ziegler, M. Kuntz, R. Elvira, A. Leiro, E. Vuorinen, and T. Teeri. Evaluation of potential of high Si high C steel nanostructured bainite for wear and fatigue applications. *Materials Science and Technology*, 29:1166–1173, 2013.

[5] A. Leiro, A. Kankanala, E. Vuorinen, and B. Prakash. Tribological behaviour of carbide-free bainitic steel under dry rolling/sliding conditions. *Wear*, 273:2, 2011.

[6] A. Leiro, E. Vuorinen, K. G. Sundin, B. Prakash, T. Sourmail, V. Smanio, F. G. Caballero, C. Gracia-Mateo, and R. Elvira. Wear of nano-structured carbide-free bainitic steels under dry rolling-sliding conditions. *Wear*, 298–299:42–47, 2013.

[7] J. T. Burwell. Survey of possible wear mechanism. *Wear*, 1:119–141, 1958.

[8] J. D. Gates. Two-body and three-body abrasion: a critical discussion. *Wear*, 214:139–146, 1998.

[9] D. A. Rigney. Sliding wear of metals. *Annual review of materials science*, 18:141, 1988.

[10] M. Godet. The third-body approach: A mechanical view of wear. *Wear*, 100:437, 1984.

[11] M. Oki, T. Sasada, and N. Emori. The effect of abrasive grain size on the transition between abrasive and abrasion wear. *Wear*, 97:291, 1984.

[12] E. Rabinowicz, L. A. Dunn, and P. G. Russel. A study of abrasive wear under three-body conditions. *Wear*, 4:345–355, 1961.

[13] Y. L. Wang and Z. X. Wang. An analysis of the influence of plastic indentation on three body abrasive wear of metals. In *Proceedings of the International Conference on Wear of Materials*, pages 619–626, New York, 1987. ASME.

[14] K. H. Zum Gahr. The number of particle contacts in two-body abrasive wear of metals by coated abrasive papers. *Wear*, 129:120–121, 1989.

[15] C. Spero, D. J. Hargreaves, R. K. Kirkcaldie, and H. J. Flitt. Review of test methods for abrasive wear in ore grinding. *Wear*, 146:389–408, 1991.

[16] A. Misra and I. Finnie. A classification of three-body abrasive wear. *Wear*, 60:111–117, 1980.

[17] T. S. Eyre. The mechanism of wear. *Tribology International*, pages 91–96, April 1978.

[18] E. Rabinowicz. Tribology ii, video course mannual. Center for Advanced Engineering Study, Cambridge, MA, 1983. 1.2-1.3.

[19] Y. C. Lin, S. W. Wang, and T. M. Chen. A study on the wear behavior of hardened medium carbon steel. *Journal of Materials Processing Technology*, 120:126–132, 2002.

[20] M. A. Moore. *Fundamentals of friction and wear of materials.* ASM international,OH, Metals Park, OH, 1981.

[21] K. H. Zum-Gahr. *Microstructure and wear of materials.* Elsevier, 1981.

[22] H. S. Avery. *Work hardening in relation to abrasion resistance.* Climax molybdenum company, Greenwich, Conn, USA, 1974.

[23] O.Vingsbo and S. Hogmark. *Fundamentals of friction and weat of materials.* American Society for Metals, Metals Park, OH, 1981.

[24] N. Prasad and S. D. Kulkarni. Relations between microstrcuture and abrasive wear of plain carbon steel. *Wear*, 63:329–338, 1980.

[25] M.A.Moore. The relationship between the abrasive wear resistance, hardness and microstrcuture of ferritic materials. *Wear*, 28:59–68, 1974.

[26] J. Larsen-Badse and K. G. Mathew. Influence of structure on the abrasion resistance of a 1040 steel. *Wear*, 14:199–206, 1969.

[27] N. N. Serpik and M. M. Kantor. Effect of heat treatment on abrasive resistance of steels for earth moving eqipments. *Metalloved. Obrab. Met.*, 7:46–50, 1958.

[28] T. Chandrasekaran, K. A. Natarajan, and Kishore. Influence of microstructure on the wear of grinding media. *Wear*, 147:267–274, 1991.

[29] Y. Wang, L. Pan, and T. C. Lei. Sliding wear behavior of pearlitic structures in eutectoid steels. *Wear*, 143:57–69, 1991.

[30] Y. Wang and T.Lei. Wear behavior of steel 1080 with different microstructures during dry sliding. *Wear*, 194:44–53, 1996.

[31] P. L. Hurricks. Overcoming industrial wear. *Industrial lubrication and tribology*, pages 345–356, October 1971.

[32] O. P. Modi, D. P. Mondal, B. K. Prasad, M. Singh, and H. K. Khaira. Abrasive wear behaviour of a high carbon steel : effects of microstructure and experimental parameters and correlation with mechanical properties. *Materials Science & Engineering, A*, 343:235–242, 2003.

[33] G. W. Stachowiak and A. W. Batchelor. *Engineering Tribology.* Elsevier, 3rd edition, 2005.

[34] G. B. Stachowiak, G. W. Stachowiak, and J. M. Brandt. Ball-cratering abrasion tests with large abrasive particles. *Tribology International*, 30:1–11, 2006.

[35] R. C. D. Richardson. The wear of metals by hard abrasives. *Wear*, 10:291–309, 1967.

[36] L. Xu and N. F. Kennon. A study of the abrasive wear of carbon steels. *Wear*, 148:101–112, 1991.

[37] O. Scheffier and C. Allen. The abrasive wear of steels in South African soils. *Tribology International*, 21(3):127–135, 1988.

[38] Z. L. Liu, Y. X. Zhou, Q. C. Rao, and Z. H. Jin. An investigation of the abrasive wear behavior of ductile cast iron. *Journal of Materials Processing technology*, 116:176–181, 2001.

[39] C. C. Viafara, M. I. Castro, J. M. Velez, and A. Toro. Unlubricated sliding wear of pearlitic and bainitic steels. *Wear*, 259:405–411, 2005.

[40] K. M. Lee and A. A. Polycarpou. Wear of conventional pearlitic and improved bainitic rail steel. *Wear*, 259:391–399, 2005.

[41] K. C. Barker. *The development of abrasive-corrosive wear resistance of steels by microstructural control.* PhD thesis, University of Cape Town, 1988.

[42] D. E. Diesburg and F. Borik. Optimizing abrasion resistance and toughness in steel and irons for the mining industry. In *Materials for the Mining Industry*, pages 14–41, Ann Arbor, MI, 1974.

[43] J. Suchanek and V. Kuklik. Influence of heat and thermochemical treatment on abrasion resistance of structural and tool steels. *Wear*, 267:2100–2108, 2009.

[44] O. P. Modi, B. K . Prasad, A. K . Jha, R. Dasgupta, and A. H. Yagneswaran. Low-stress abrasive wear behaviour of a 0.2% C steel : influence of microstructure and test parameters. *Tribology Letters*, 15:249–255, 2003.

[45] S. Kumar, A. Bhattacharyya, D. K. Mondal, K. Biswas, and J. Maity. Dry sliding wear behaviour of medium carbon steel against an alumina disk. *Wear*, 270:413–423, 2011.

[46] A. Gocke, I. Schmidt, and M. Wilhelm. Gouging and sliding abrsion of austenitic manganese steels reinforced by hard phases. *Wear*, 119:313–327, 1987.

[47] W. Huaming, Z. Qing, and S. Hesheng. Behaviors of austenite under impact abrasion. *Acta Metallurgica Sinica(English Edition)*, 4(1):37–42, January 1991.

[48] G. L. Dunlop and R. Gang. Development of microstructure during heat treatment of high speed steels. In *Proc First Int HSS Conf*, pages 33–40, Leoben,Wiez:Klampfer GmbH, 1990.

[49] Q. A. Shaikh, D. S. Coleman, J. Bates, P. D. Nurthen, and P. R. Brewin. Wear and microstructural studies of alloy sintered steels. *Materials Science and Technology*, 7:728–738, 1991.

[50] E. Badisch and C. Mitterer. Abrasive wear of high speed steels: Influence of abrasive particles and primary carbides on wear resistance. *Tribology International*, 36:765–770, 2003.

[51] G. J. Gore and J. D. Gates. Effect of hardness on three very different forms of wear. *Wear*, 203-204:544–563, 1997.

[52] M. M. Khruschov. In *Conference on Lubrication and Wear*, page 655, 1957.

[53] M. M. Khrushchov and M. A. Babichev. Friction and wear in machinery. *Translated from the Russian, American Society of Mechanical Engineers,*, (12):5, 1960.

[54] M. M. Khruschov. Principles of abrasive wear. *Wear*, 28:69–88, 1974.

[55] M. M. Khruschov and M. A. Babichev. *Investigations into the wear of metals*. USSR Academy of Sciences (in Russian), 1960.

[56] J. Goddard, H. J. Harker, and H. Wilman. A theory of the abrasion of solids such as metals. *Nature*, 184:333–335, 1959.

[57] S. M. Nahvi, P. H. Shipway, and D. G. McCartney. Particle motion and modes of wear in the dry sand-rubber wheel abrasion test. *Wear*, 267:2083–2091, 2009.

[58] J. G. Chacon-Nava, A. Martinez-Villafane, F. Almeraya-Calderon, J. A. Cabral-Miramontes, and M. M. Stack. Some remarks on particle size effects on the abrasion of a range of Fe based alloys. *Tribology International*, 43:1307–1317, 2010.

[59] B. W. E. Avient, J. Goddard, and H. Wilman. An experimental study of friction and wear during abrsion. *Proceedings of the Royal Society London A*, 258:159, 1960.

[60] J. Larsen-Badse. The abrasion resistance of some hardened and tempered carbon steels. *Transactions of the Metallurgical Society AIME*, 236:1461, 1966.

[61] P. J. Mutton and J. D. Watson. Some effects of microstrcuture on the abrasion resistance of metals. *Wear*, 48:385–398, 1978.

[62] A. Sundstrom, J. Rendon, and M. Olsson. Wear behaviour of some low alloyed steels under combined impact/abrasion contact conditions. *Wear*, 250:744–754, 2001.

[63] M. A. Moore. A preliminary investigation of frictional heating during wear. *Wear*, 17:51–58, 1971.

[64] N. Wing. The transformation of soft-abrasive wear into hard-abrasive wear under the effect of heat. *Tribology Transactions*, 32:85–90, 1989.

[65] M. Pellizzari, A. Molinari, and G. Straffelini. Tribological behaviour of hot rolling rolls. *Wear*, 259:1281–1289, 2005.

[66] T. O. Mulhearn and L. E. Samuels. The abrasion of metals : A model of the process. *Wear*, 3:478–498, 1962.

[67] I. I. Garbar. Abrasion resistance as a fuction of substructural changes in steel. *Wear*, 258:275–280, 2005.

[68] E. Rabinowicz. *Friction and wear of materials.* John Wiley & Sons, 1995.

[69] D. V. De Pellegrin, A. A. Torrance, and E. Haran. Wear mechanisms and scale effects in two-body abrasion. *Wear*, 266:13–20, 2009.

[70] M. A. Moore. Laboratory simulation testing for service abrasive wear testing. In K. C. Ludema, editor, *Wear of Materials*, pages 558–556, New York, 1987. ASME.

[71] P. A. Swanson. Comparison of laboratory abrasion tests and filed tests of materials used in the tillage equipment. In A. W. Ruff and R. G. Bayers, editors, *Tribology, Wear tests Selection for Design and Application*, pages 80–99, Philadelphia, 1993. ASTM.

[72] P. A. Swanson and R. W. Klann. Abrasive wear studies using the wet sand and dry rubber wheel tests. In S. K. Rhee, A. W. Ruff, and K. C. Ludema, editors, *Wear of Materials*, pages 379–389, New York, 1981. ASME, ASME.

[73] S. Wirojanupatump and P. H. Shipway. A direct comparison of wet and dry abrasion behaviour of mild steel. *Wear*, 233-235:655–665, 1999.

[74] S. Wirojanupatump and P. H. Shipway. *Wear*, 239:91–101, 2000.

[75] J. Larsen-Basse and S. S. Sokoloski. Influence of atmospheric humidity on abrsive wear - ii. 2-body abrasion. *Wear*, 32:9–14, 1975.

[76] A. P. Mercer and I. M. Hutchings. The influence of atmospheric humidity on the abrasive wear of metals. *Wear*, 103:205–215, 1985.

[77] F. Katsuki, K. Watari, H. Tahira, and M. Umino. Abrasive wear behavior of a pearlitic 0.4% C steel microalloyed with vanadium. *Wear*, 264:331–336, 2008.

[78] M. V. Swain. Microscopic observation of abrasive wear in polycrystaline alumina. *Wear*, 35:185–189, 1975.

[79] T. Kayaba. The latest investigations of wear by the microscopic observations. *JSLE Transactions*, 29:9–14, 1984.

[80] S. C. Lim and J. H. Brunton. A dynamic wear rig for the scanning electron microscope. *Wear*, 101:81–91, 1985.

[81] K. Philips. *Study of the free abrasive grinding of glass and fused silica*. PhD thesis, University of Sussex, 1975.

[82] W. A. Glaeser. Wear experiments in the scanning electron microscope. *Wear*, 73:371–386, 1981.

[83] M. A. Moore and F. S. King. In *Wear of Materials*, page 275. American Society of Mechanical Engineers, 1979.

[84] H. Sin, N. Saka, and N. P. Suh. Abrasive wear mechanisms and the grit size effect. *Wear*, 55:163–190, 1979.

[85] A. Misra and I. Finnie. On the size effect in abrasive and erosive wear. *Wear*, 65:359–373, 1981.

[86] P. Hosseini and P. Radziszewski. Combined study of wear and abrasive fragmentation using steel wheel abrasion test. *Wear*, 271:689–696, 2011.

[87] Arcelor-Mittal. Technical specification - creusabro 4800, 2009.

[88] Arcelor-Mittal. Technical specification - creusabro 8000, 2009.

[89] Tata Steel. Abrazo pack. Technical report, Tata Steel, 2009. Personal collection.

[90] SSAB. Hardox400 technical datasheet. Technical report, SSAB, 2011. Personal collection.

[91] SSAB. Hardox450 technical datasheet. Technical report, SSAB, 2011. Personal collection.

[92] SSAB. Hardox500 technical datasheet. Technical report, SSAB, 2011. Personal collection.

[93] H. K. D. H. Bhadeshia. Bulk nanocrystalline steel. *Ironmaking and Steelmaking*, 32:405–410, 2005.

[94] H. Hertz. Über die berübrung fester elastiscber Körper (on the contact of elastic solids). *Journal Reine und Angewandte Mathematik*, 92:156–171, 1882.

[95] K. L. Johnson. *Contact Mechanics*. Cambridge University Press, Cambridge, U. K., 1985.

[96] L. WenTao, Y. Zhang, F. ZhiJing, and Z. JingShan. Effects of stick-slip on stress intensity factors for subsurface short cracks in rolling contact. *Science China Technological Sciences*, 56(10):2413–2421, 2013.

[97] A. Kapoor, K. L. Johnson, and J. A. Williams. A model for the mild rachetting wear of metals. *Wear*, 200:38–44, 1996.

[98] H. Ichinose, J. Takehara, and M. Ueda. High strength rails produced by two stage flame heating and slack quenching. In *2nd International Conference on Heavy Haul Railways, Colorado Springs, USA*, pages 178–186, Colorado Springs, CO, 1982.

[99] J. Kalousek, D. M. Fegredo, and E. E. Laufer. The wear resistance and worn metallography of pearlite, bainite and tempered martensite rail steel microstructures of high hardness. *Wear*, 105(3):199 – 222, 1985.

[100] P. J. Mutton. The influence of microstructure of the wear behavior of rail and wheel materials. M.App.Sc. thesis, University of Melbourne, 1985.

[101] J. E. Garnham and J. H. Beynon. Dry rolling-sliding wear of bainitic and pearlitic steels. *Wear*, 157:81–109, 1992.

[102] P. Clayton, R. Devanathan, N. Jin, and R. K. Steele. *A review of bainitic steels for wheel/rail contact, Rail Quality and Maintenance for Modern Railway Operation*. Kluwer Academic Publishers, Dordrecht, 1993.

[103] D. Danks and P. Clayton. Comparison of the wear process for eutectoid rail steels: Field and laboratory tests. *Wear*, 120:233 – 250, 1987.

[104] P. Clayton and D. Danks. Effect of interlamellar spacing on the wear resistatnce of eutectoid steels under rolling–sliding conditions. *Wear*, 135:369–389, 1990.

[105] N. Jin and P. Clayton. Effect of microstructure on rolling/sliding wear of low carbon bainitic steels. *Wear*, 202:202–207, 1997.

[106] P. Clayton. The relations between wear behaviour and basic material properties for pearlitic steels. *Wear*, 60:75–93, 1980.

[107] P. J. Bolton and P. Clayton. Rollingsliding wear damage in rail and tyre steels. *Wear*, 93(2):145 – 165, 1984.

[108] P. Clayton, K. J. Sawley, P. J. Bolton, and G. M. Pell. Wear behaviour of rail steel. *Wear*, 120:199–220, 1987.

[109] R. Devanathan and P. Clayton. Rolling-sliding wear of three bainitic steels. *Wear*, 151:255–267, 1991.

[110] P. Clayton and R. Devanathan. Rolling/sliding wear behavior of a chromium-molybdenum rail steel in pearlitic and bainitic conditions. *Wear*, 156:121 – 131, 1992.

[111] P. Clayton and N. Jin. Unlubricated sliding and rolling/sliding wear behavior of continuously cooled low/medium carbon bainitic steels. *Wear*, 200:74–82, 1996.

[112] N. Jin and P. Clayton. Effect of microstructure on rolling/sliding wear of low carbon bainitic steels. *Wear*, 202:202–207, 1997.

[113] P. H. Shipway, S. J. Wood, and A. H. Dent. The hardness and sliding wear behaviour of a bainitic steel. *Wear*, 203-204:196–205, 1997.

[114] P. Clayton and N. Jin. Unlubricated sliding and rolling/sliding wear behavior of continuously cooled low/medium carbon bainitic steels. *Wear*, 200:74–82, 1996.

[115] H. K. D. H. Bhadeshia and D. V. Edmonds. Bainite in silicon steels: a new composition property approach i. *Metal Science*, 17:411–419, 1983.

[116] T. S. Wang, J. Yang, C. J. Shang, X. Y. Li, B. Lv, M. Zhang, and F. C. Zhang. Sliding frction surface microstructure and wear resistance of 9SiCr steel with low–temperature austempering treatment. *Surface & Coatings Technology*, 202:4036–4040, 2008.

[117] P. Zhang, F. C. Zhang, Z. G. Yan, T. S. Wang, and L. H. Qian. Wear property of low-temperature bainite in the surface layer of a carburized low carbon steel. *Wear*, 271:697–704, 2011.

[118] J. Yang, T. S. Wang, B. Zhang, and F. C. Zhang. Sliding wear resistance and worn surface microstructure of nanostructured bainitic steel. *Wear*, 282–283:81–84, 2012.

[119] E. Vuorinen, D. Pino, J. Lundmark, and B. Prakash. Wear characteristic of surface hardenend ausferritic si-steel. *Journal of Iron and Steel Research Institute*, 14:245–248, 2007.

[120] S. Das Bakshi, A. Leiro, B. Prakash, and H. K. D. H. Bhadeshia. Dry rolling/slidinng wear of nanostructured bainite. *Wear*, 316:72–78, 2014.

[121] R. Rementeria, I. Garcia, M. M. Aranda, and F. G. Caballero. Reciprocating-sliding wear behavior of nanostructured and ultra-fine high-silicon bainitic steels. *Wear*, 338-339:202–209, 2015.

[122] L. C. Chang. The rolling/sliding wear performance of high silicon carbide-free bainitic steels. *Wear*, 258:730–743, 2005.

[123] H. K. D. H. Bhadeshia and A. L. Greer. *Introduction to Materials Modelling*, chapter 5. Maney, London, 2005.

[124] ASTM G65-04, Standard test method for measuring abrasion using the dry rubber wheel apparatus, Annual Book of Standards, ASTM international, No 03.02, West Conshohocken, Pennsylvania, USA.

[125] S. Das Bakshi, P. H. Shipway, and H. K. D. H. Bhadeshia. Three-body abrasive wear of fine pearlite, nanostructured bainite and martensite. *Wear*, 308:46–53, 2013.

[126] S. M. Nahvi, P. H. Shipway, and D. G. McCartney. Particle motion and modes of wear in the dry sand-rubber wheel abrasion test. *Wear*, 267:2083–2091, 2009.

[127] T. Sourmail, F. G. Caballero, C. Garcia-Mateo, V. Smanio, C. Ziegler, M. Kuntz, R. Elvira, A. Leiro, E. Vuorinen, and T. Teeri. Evaluation of potential of high Si high C steel nanostructured bainite for wear and fatigue applications. *Materials Science and Technology*, 29(10):1166–1173, 2013.

[128] F. Sadeghi, B. Jalahmadi, T. S. Slack, N. Raje, and N. K. Arakere. A review of rolling contact fatigue. *Journal of Tribology*, 131:041403, 2009.

[129] F. Sadeghi and P. C. Sui. Subsurface stresses in rolling/sliding machine components. *International Compressor Engineering Conference*, pages 629–638, 1988.

[130] T. M. Ahn, P. J. Blau, K. L. Hsu, and D. A. Rigney. Metallographic techniques for wear tests. *Wear*, 56:409–413, 1979.

[131] A. A. Torrance. The metallography of worn surfaces and some theories of wear. *Wear*, 50:169–182, 1978.

[132] W. S. Rasband. ImageJ, 1997-2014.

[133] E. E. Underwood. *Quantitative Stereology*. Addison–Wesley Publication Company, 1970.

[134] S. A. Saltykov. *Stereometric Metallography*. Metallurgizat, Moscow, 2nd edition, 1958.

[135] L. C. Chang and H. K. D. H. Bhadeshia. Austenite films in bainitic microstructures. *Materials Science and Technology*, pages 874–881, 1995.

[136] *Techical Manual : Vecco WYCO NT1100*.

[137] W. C. Oliver and G. M. Pharr. Measurement of hardness and elastic modulus by instrumented indentation: Advances in understanding and refinements to methodology. *Journal of Materials Research*, 19(1):3–20, 2004.

[138] M. Multigner E. Frutos and J.L. Gonzalez-Carrasco. Novel approaches to determining residual stresses by ultramicroindentation techniques: Application to sandblasted austenitic stainless steel. *Acta materialia*, 58:4191–4198, 2010.

[139] J. Woirgard and J-C. Dargenton. An alternative method for penetration depth determination in nanoindentation measurements. *Journal of Materials Research*, 12(9):2455–2458, 1997.

[140] Q. Wang, K. Ozaki, H. Ishikawa, S. Nakano, and H. Ogiso. Indentation method to measure the residual stress induced by ion implantation. *Nuclear Instruments and Methods in Physics Research Section B: Beam Interactions*

with Materials and Atoms, 242(12):88 – 92, 2006. Proceedings of the 14th International Conference on Ion Beam Modification of Materials.

[141] Y. Bao, L. Liu, and Y. Zhou. Assessing the elastic parameters and energy-dissipation capacity of solid materials: A residual indent may tell all. *Acta Materialia*, 53(18):4857 – 4862, 2005.

[142] M. Sakai and Y. Nakano. Elastoplastic load–depth hysteresis in pyramidal indentation. *Journal of Materials Research*, 17(8):2161–2173, 2002.

[143] J. Woirgard and J-C. Dargenton. An alternative method for penetration depth determination in nanoindentation measurements. *Journal of Materials Research*, 12(9):2455–2458, 1997.

[144] G. Caglioti, A. Paoletti, and F. P. Ricci. Choice of coillimators for a crystal spectrometer for neutron diffraction. *Nuclear Instruments*, 3:223–228, 1958.

[145] G. Ribarik. *Modeling of diffraction patterns based on microstructural properties*. PhD thesis, Department of Materials Physics, Eotvos Lorand University, Hungary, 2008.

[146] V. D. Mote, Y. Purushotham, and B. N. Dole. Williamson-Hall analysis in estimation of lattice strain in nanometer size ZnO particles. *Journal of Theoritical and Applied Physics*, 6:2–8, 2012.

[147] T. Ungar, S. Ott, P. G. Sanders, A. Brobely, and J. R. Weertman. Dislocations, grain size and planar faults in nanostructured copper determined by high resolution X-ray diffraction and a new procedure of peak profile analysis. *Acta Materialia*, 46:3693–3699, 1998.

[148] T. Ungar, I. Dragmoir, A. Revesz, and A. Borbely. The contrast factors of dislocations in cubic crystals: the dislocation model of strain anisotropy in practice. *Journal of Applied Crystallography*, 32:992, 1999.

[149] T. Ungar. Dislocation densities, arrangements and character from X-ray diffraction experiments. *Materials Science & Engineering, A*, 309–310:14–22, 2001.

[150] E. Schafler, M. Zehetbauer, and T. Ungar. Measurement of screw and edge dislocation density by means of X-ray Bragg profile analysis. *Materials Science and Engineering A*, 319-321:220–223, 2001.

[151] T. Shintani and Y. Murata. Evaluation of the dislcoation density and dislocation character in cold rolled type 304 steel determined by profile analysis of X-ray diffraction. *Acta Materialia*, 59:4314–4322, 2011.

[152] J. F. Nye. *Physical properties of crystals : their representation by tensors and matrices*. Clarendon Press, Oxford, 1957.

[153] T. Ungar and A. Borbely. The effect of dislocation contrast on Xray line broadening: A new approach to line profile analysis. *Journal of Applied Physics*, 69:3173, 1996.

[154] B. E. Warren. X-ray studies of the deformed metals. *Progress in Metal Physics*, 8:147–202, 1959.

[155] T. Ungar and G. Tichy. The effect of dislocation contrast on Xray line profiles in untextured polycrystals. *Physica Status Solidi A*, 171(2):425–434, 1999.

[156] T. Ungar. Dislocation densities, arrangements and character from X-ray diffraction experiments. *Materials Science and Engineering A*, 309–310:14 – 22, 2001.

[157] H. K. D. H. Bhadeshia. Design of ferritic creep-resistant steels. *ISIJ International*, 41:621–640, 2001.

[158] H. K. D. H. Bhadeshia. *Science and Technlogy of Advanced Materials*, 2013. In Press.

[159] T. S. Wang, J. Yang, C. J. Shang, X. Y. Li, B. Lv, M. Zhang, and F. C. Zhang. Sliding friction surface microstructure and wear resistance of 9SiCr steel with low-temperature austempering treatment. *Surface and Coating Technology*, 202:4036–4040, 2008.

[160] P. Zhang, F. C. Zhang, Z. G. Tan abd T. S. Wang, and L. H. Qian. Wear property of low-temperature bainite in the surface layer of a carburized low carbon steel. *Wear*, 271:697–704, 2011.

[161] J. Yang, T. S. Wang, B. Zhang, and F. C. Zhang. *Wear*, 282-283:81–84, 2012.

[162] H. K. D. H. Bhadeshia. Nanostructured bainite. *Proceedings of the Royal Society of London A*, 466:3–18, 2010.

[163] C. G. Mateo and F. G. Caballero. Ultra-high-strength bainitic steels. *ISIJ International*, 45:1736–1740, 2005.

[164] H. K. D. H. Bhadeshia. Large chunks of very strong steel. *Materials Science and Technology*, 21:1293–1302, 2005.

[165] H. K. D. H. Bhadeshia and D. V. Edmonds. Bainite in silicon steels : New composition property approach, part 2. *Metal Science*, 17:420–425, 1983.

[166] R. A. Jaramillo, S. S. Babu, G. M. Ludtka, R. A. Kisner, J. B. Wilgen, G. Mackiewicz-Ludtka, D. M. Nicholson, M. Murugananth, and H. K. D. H. Bhadeshia. *Scripta Materialia*, 52:461–466, 2004.

[167] K. M. Wu and H. K. D. H. Bhadeshia. Extremly fine pearlite by continuous cooling trasnformation. *Scripta Materialia*, 67:53–56, 2012.

[168] S. A. Saltykov. *Stereometric Metallography*. Metallurgizat, Moscow, 2nd edition, 1958.

[169] F. G. Caballero and H. K. D. H. Bhadeshia. Very strong bainite. *Current Opinion in Solid State and Materials Science*, 8:251–257, 2004.

[170] H. K. D. H. Bhadeshia. Archive of micrographs, http://www.msm.cam.ac.uk/phase-trans/2005/bulk.html, 2005.

[171] L. C. Chang and H. K. D. H. Bhadeshia. Austenite films in bainitic microstructures. *Materials Science and Technology*, 11:874–881, 1995.

[172] P. Koshy, R. C. Dewes, and D. K. Aspinwall. High speed end milling of hardened AISI D2 tool steel (58 HRC). *Journal of Materials Processing Technology*, 127:266–273, 2002.

[173] P. L. Hurricks. Some metallurgical factors controlling the adhesive and abrasive wear resistance of steels: a review. *Wear*, 26:285–304, 1973.

[174] J. Larsen-Badse and K. G. Mathew. Influence of structure on the abrasion resistance of a 1040 steel. *Wear*, 14:199–206, 1969.

[175] A. Misra and I. Finnie. An experimental study on three-body abrasive wear. *Wear*, 85:57–68, 1983.

[176] O.Vingsbo and S. Hogmark. *Fundamentals of friction and wear of materials*. American Society for Metals, Metals Park, OH, 1981.

[177] B. K. Prasad and S. V. Prasad. Abrasion-induced microstructural changes during low stress abrasion of a plain carbon (0.5% c) steel. *Wear*, 151:1–12, 1991.

[178] S. Kondapally. Personal communication. Welding Alloys UK, 2011.

[179] J. A. Hawk, R. D. Wilson, J. H. Tylczak, and O. N. Dogan. Laboratory abrasive wear tests: investigation of test methods and alloy correlation. *Wear*, 225-229:1031–1042, 1999.

[180] S. M. Nahvi, P. H. Shipway, and D. G. McCartney. Particle motion and modes of wear in the dry sand-rubber wheel abrasion test. *Wear*, 267:2083–2091, 2009.

[181] L. Xu, S. Clough, P. Howard, and D. StJohn. Laboratory assesment of the effect of white layers on wear resistance for digger teeth. *Wear*, 181-183:112–117, 1995.

[182] K. M. Mashloosh and T. S. Eyre. Abrasive wear and its application to digger teeth. *Tribology International*, 18:259, 1985.

[183] A. L. Wingrove. A note on the structure of adiabatic shear bands in steel. *J. of Aust. Int. Met.*, 16(1):67–70, 1971.

[184] J. R. Yang and H. K. D. H. Bhadeshia. Continuous heating transformation of bainite to austenite. *Materials Science & Engineering A*, 131:99–113, 1991.

[185] J. W. Stead. *Journal of West Scotland Iron Steel Institure*, 19:169, 1911-1912.

[186] E. M. Trent. The formation and properties of martensite on the surface of rope wire. *Journal of Iron and Steel Institute*, 143:401, 1941.

[187] F. P. Bowden and D. Tabor. *The friction and lubrication of solids*. Oxford University Press, 1950.

[188] T. S. Eyre and A. Baxter. The formation of white layers at rubbing surfaces. *Tribology*, pages 256–261, December 1972.

[189] S. L. Rice, H. Nowotny, and S. F. Wayne. Characteristics of metallic subsurafce zones in sliding and impact wear. *Wear*, 74:131–142, 1981-1982.

[190] T. F. J. Quinn. Role of oxidation in the mild wear of steel. *British Journal of Applied Physics*, 13:33–37, 1962.

[191] Y. L. Wang and Z. S. Wang. An analysis of the influence of plastic indentation on three-body abrasive wear of metals. *Wear*, 122:123–133, 1988.

[192] L. Fang, Q. D. Zhou, and J. J. Li. An explanation of the relation between wear and material hardness in 3-body abrasion. *Wear*, 151:313–321, 1991.

[193] S. Das, B. K. Prasad, A. K. Jha, O. P . Modi, and A. H. Yegneswaran. Three-body abrasive wear of 0.98% carbon steel. *Wear*, 162-164:802–810, 1993.

[194] C. Garcia-Mateo, M. Peet, F. G. Caballero, and H. K. D. H. Bhadeshia. Tempering of a hard mixture of bainitic ferrite and austenite. *Materials Science and Technology*, 20:814–818, 2004.

[195] R. Colaco and R. Vilar. On the influence of retained austenite in the abrasive wear behaviour of a laser surface melted tool steel. *Wear*, 258:225–231, 2005.

[196] Z. Fucheng and L. Tingquan. A study of friction-induced martensitic transformation for austenitic manganese steel. *Wear*, 212:195–198, 1997.

[197] G. W. Stachowiak and A. W. Batchelor. *Engineering Tribology*. Elsevier, 3rd edition, 2005.

[198] D. M. Fegredo and C. Pritchard. A metallographic examination of rollers subjected to wear under rolling-sliding conditions. *Wear*, 49:67 – 78, 1978.

[199] T. Yamada. Rolling wear characteristics of annealed carbon steels under dry contact conditions. *Wear*, 51:279 – 288, 1978.

[200] J. E. Garnham and J. H. Beynon. Dry rolling-sliding wear of bainitic and pearlitic steels. *Wear*, 157:81–109, 1992.

[201] A. Ramalho, M. Esteves, and P. Marta. Friction and wear behaviour of rolling–sliding steel contacts. *Wear*, 302:1468–1480, 2013.

[202] T. M. Beagley. Severe wear of rolling/sliding contacts. *Wear*, 36(3):317 – 335, 1976.

[203] M. Sato, P. M. Anderson, and D. A. Rigney. Rolling-sliding behavior of rail steels. *Wear*, 162164, Part A(0):159 – 172, 1993. Wear of Materials: Proceedings of the 9th International Conference.

[204] F. Katsuki and M. Yonemura. Subsurface characteristics of an abraded Fe-0.4 wt%C pearlitic steel: A nanoindentation study. *Wear*, 263:1575–1578, 2007.

[205] A. J. Perez-Unzueta and J. H. Beynon. Microstructure and wear resistance of pearlitic rail steels. *Wear*, 162-163:173–182, 1993.

[206] F. T. Barwell. The effect of lubrication and nature of superficial layer after prolonged periods of running. In *Symposium on Properties of Metallic Surfaces, Institute of Metals Monograph and Report No. 13*, pages 101–122, London, U.K., 1953. Insitute of Metals.

[207] F. T. Barwell. Wear of metals. *Wear*, 1(4):317 – 332, 1958.

[208] D. M. Fegredo, J. Kalousek, and M. T. Shehata. The effect of progressive minor spheroidization on the dry-wear rates of a standard carbon and a Cr-Mo alloy rail steel. *Wear*, 161:29 – 40, 1993.

[209] T. Takahashi and M. Nagumo. Flow stress and work-hardening of pearlitic steel. *Transactions of the Japan Institute of Metals*, 11:113–119, 1970.

[210] J. D. Grozier and J. H. Bucher. Correlation of fatigue limit with microstructure and composition of ferrite-pearlite steels. *Journal of Matererials*, 2:393 – 407, 1967.

[211] G. M. da Fonseca Gomes, L. H. de Almeida, L. C. F. C. Gomes, and I. L. May. Effects of microstructural parameters on the mechanical properties of eutectoid rail steels. *Materials Characterization*, 39:1 – 14, 1997.

[212] J. Larsen-Badse and K. G. Mathew. Influence of structure on the abrasion resistance of a 1040 steel. *Wear*, 14:199–206, 1969.

[213] D. A. Rigney. Viewpoint set on materials aspects of wear - Introduction. *Scripta Materialia*, 24:799 – 803, 1990.

[214] J. Takahashi, Y. Kobayashi, M. Ueda, T. Miyazaki, and K. Kawakami. Nanoscale characterisation of rolling contact wear surface of pearlitic steel. *Materials Science and Technology*, 29:1212–1218, 2013.

[215] J. E. Garnham and C. L. Davis. The role of deformed rail microstructure on rolling contact fatigue initiation. *Wear*, 265:1363 – 1372, 2008.

[216] K. K. Ray and D. Mondal. Effect of interlamellar spacing on strength of pearlite in annealed eutectoid and hypoeutectoid plain carbon steels. *Acta Metallurgica and Materialia*, 39:2201–2208, 1991.

[217] B. E. Q'Donnelly, R. L. Reuben, and T. N. Baker. Quantitative assessment of strengthening parameters in ferrite-pearlite steels from microstructural measurements. *Metals Technology*, 11:45–51, 1984.

[218] E. M. Taleff, J. J. Lewandowski, and B. Pouladian. Microstructure-property relationships in pearlitic eutectoid and hypereutectoid carbon steels. *Journal of Metals*, 54:25–30, 2002.

[219] A. Kapoor, F. J. Franklin, S. K. Wong, and M. Ishida. Surface roughness and plastic flow in rail wheel contact. *Wear*, 253:257–264, 2002.

[220] A. Basak, D. C. Reddy, and D. V. K. Kanth. Computer modelling of wear resistance for plain carbon steels. *Materials Science and Technology*, 14:776–782, 1998.

[221] L. WenTao, Y. Zhang, F. ZhiJing, and Z. JingShan. Effects of stick-slip on stress intensity factors for subsurface short cracks in rolling contact. *Science China Technological Sciences*, 56:2413–2421, 2013.

[222] H. C. Eden, J. E. Garnham, and C. L. Davis. Influential microstructural changes on rolling contact fatigue crack initiation in pearlitic rail steels. *Materials Science and Technology*, 21:623–629, 2005.

[223] J. Gil-Sevillano. Room temperature plastic deformation of pearlitic cementite. *Materials Science & Engineering*, 21:221–225, 1975.

[224] G. Langford. Deformation of pearlite. *Metallurgical Transactions A*, 8:861 – 875, 1977.

[225] J. Kalousek, D. M. Fegredo, and E. E. Laufer. The wear resistance and worn metallography of pearlite, bainite and tempered martensite rail steel microstructure of high hardness. In K. C. Ludema, editor, *Proceedings of the 6th International Conference on Wear of Material,*, pages 212–231, New York, USA, 1987. American Society of Mechanical Engineers.

[226] W. R. Tyfour, J. H. Beynon, and A. Kapoor. The steady state wear behaviour of pearlitic rail steel under dry rolling-sliding contact conditions. *Wear*, 180:79 – 89, 1995.

[227] J. H. Beynon, J. E. Garnham, and K. J. Sawley. Rolling contact fatigue of three pearlitic rail steels. *Wear*, 192(12):94 – 111, 1996.

[228] M. Sakai and Y. Nakano. Elastoplastic load–depth hysteresis in pyramidal indentation. *Journal of Materials Research*, 17:2161–2173, 2002.

[229] S. Jahanmir and N. P. Suh. Mechanics of subsurface void nucleation in delamination wear. *Wear*, 44:17 – 38, 1977.

[230] J. W. Ho, C. Noyan, and J. B. Cohen. Residual stress and sliding wear. *Wear*, 84:183–202, 1983.

[231] P. J. Withers and H. K. D. H. Bhadeshia. Residual stress part 2 - nature and origins. *Materials Science and Technology*, 17:366–375, 2001.

[232] N. Armstrong and P. Lynch. *Determination of the dislocation contrast factor for X-ray line profile analysis in : Diffraction Analysis of the Microstructure of Materials*. Springer, 2004.

[233] X. D. Zhang, A. Godfrey, W. Liu, and Q. Liu. Study on dislocation slips in ferrite and deformation of cementite in cold drawn pearlitic steel wires from medium to high strain. *Materials Science and Technology*, 27:562–567, 2011.

[234] Y. Ivanisenko, W. Lojkowski, R. Z. Valiev, and H. J. Fecht. The mechanism of formation of nanostructure and dissolution of cementite in a pearlitic steel during high pressure torsion. *Acta Materialia*, 51:5555–5570, 2003.

[235] D. J. Dyson and B. Holmes. Effect of alloying additions on the lattice parameter austenite. *Journal of the Iron and Steel Institute*, 208:469–474, 1970.

[236] K. M. Lee and A. A. Polycarpou. Wear of conventional pearlitic and improved bainitic rail steel. *Wear*, 259:391–399, 2005.

[237] H. Masumoto, K. Sugino, and H. Hayashida. Development of wear resistant and anti-shelling high strength rails in Japan. In *Heavy Haul Railway Conference*, Perth,Australia, September 1978. lnstitute of Engineers.

[238] W. Heller and R. Schweitzer. Hardness, microstructure and wear behaviour of rail steels. In *Proceedings of the 2nd International Heavy Haul Railway Conference, Colorado Springs*, pages 282–286, 1982.

[239] H. Ichinose, J. Takehara, and M. Ueda. High strength rails produced by two-stage flame heating and slack–quenching. In *2nd International Conference on Heavy Haul Railways, Colorado Springs, USA*, pages 178–182, 1982.

[240] J. Kalousek, D. M. Fegredo, and E. E. Laufer. *The wear resistance and worn metallography of pearlite, bainite, and tempered martensite rail steel microstructure of high hardness*, pages 212–231. American Society of Mechanical Engineers, New York, editor K. C. Ludema, 1985.

[241] H. K. D. H. Bhadeshia. *Bainite in Steels, 2nd edition*. Institute of Materials, London, U.K., 2001.

[242] F. G. Caballero, H. K. D. H. Bhadeshia, K. J. A. Mawella, D. G. Jones, and P. Brown. Very strong, low–temperature bainite. *Materials Science and Technology*, 18:279–284, 2002.

[243] H. K. D. H. Bhadeshia. The first bulk nanostructured metal. *Science and Technology of Advanced Materials*, 14:014202, 2013.

[244] J. Yang, T. S. Wang, B. Zhang, and F. C. Zhang. Sliding wear resistance and worn surface microstructure of nanostructured bainitic steel. *Wear*, 282–283:81–84, 2012.

[245] H. K. D. H. Bhadeshia. Steels for bearings. *Progress in Materials Science*, 57:268–435, 2012.

[246] S. Chatterjee and H. K. D. H. Bhadeshia. TRIP–assisted steels: cracking of high carbon martensite. *Materials Science and Technology*, 22:645–649, 2006.

[247] L. Lutterotti. Total pattern fitting for the combined size-strain-stress-texture determination in thin film diffraction. *Nuclear Institute and Methods in Physics Research B*, 268:334–340, 2010.

[248] M. J. Carr J. R. Strife and G. S. Ansell. Effect of austenite prestrain above the M_d temperature on the M_s temperature in Fe-Ni-Cr-C alloys. *Metallurgical Transactions A*, 8A:1471–1484, 1977.

[249] S. Chatterjee, H. S. Wang, J. R. Yang, and H. K. D. H. Bhadeshia. Mechanical stabilisation of austenite. *Materials Science and Technology*, 22:641–644, 2006.

[250] P. J. Brofman and G. S. Ansell. On the effect of fine grain size on the martensite–start temperaure in Fe-27Ni-0.025C alloys. *Metallurgical Transactions A*, 14A:1929–1931, 1983.

[251] H. S. Yang and H. K. D. H. Bhadeshia. Austenite grain size and the martensite-start temperature. *Scripta Materialia*, 60:493–495, 2009.

[252] G. K. Williamson and W. H. Hall. X-ray line broadening from filed aluminium and wolfram. *Acta Metallurgica*, 1:22–31, 1953.

[253] H. S. Yang, D. W. Suh, and H. K. D. H. Bhadeshia. More complete theory for the calculation of the martensite-start temperature in steels. *ISIJ International*, 52:162–164, 2012.

[254] D. E. Diesburg and F. Borik. Optimizing abrasion resistance and toughness in steel and irons for the mining industry. In *Materials for the Mining Industry*, pages 14–41, Michigan, USA, 1974. ASM International.

[255] K. C. Barker. *The development of abrasive-corrosive wear resistance of steels by microstructural control*. PhD thesis, University of Cape Town, 1988.

[256] J. Suchanek and V. Kuklik. Influence of heat and thermochemical treatment on abrasion resistance of structural and tool steels. *Wear*, 267:2100–2108, 2009.

[257] S. M. Shariff, T. K. Pal, G. Padmanabhan, and S. V. Joshi. Sliding wear behavior of laser surface modified pearlitic rail steel. *Surface Engineering*, 26(3):199–208, 2010.

[258] R. C. D. Richardson. The wear of metals by hard abrasives. *Wear*, 10:291–309, 1967.

[259] P. L. Hurricks. Overcoming industrial wear. *Industrial lubrication and tribology*, pages 345–356, 1971.

[260] M. Pellizzari and M.G. De Flora. Influence of laser hardening on the tribological properties of forged steel for hot rolls. *Wear*, 271(910):2402 – 2411, 2011. 18th International Conference on Wear of Materials.

[261] R. J. DiMelfi, P. G. Sanders, and B. Hunter. Mitigation of subsurface crack propagation in railroad rails by laser surface modification. *Journal of the Surface Coating and Technology*, 106(1):30–43, 1998.

[262] P. Corengia, F. Walther, G. Ybarra, S. Sommadossi, R. Corbari, and E. Broitman. Friction and rollingsliding wear of DC-pulsed plasma nitrided AISI 410 martensitic stainless steel. *Wear*, 260(45):479 – 485, 2006.

[263] J. Li and L. Wei. Effects of high magnetic field on isothermal pearlite transformation and microstructure in a hypereutectoid steel. *Journal of Magnetism and Magnetic Materials*, 362:159–164, 2014.

[264] R. Vilar, R. Colaco, and A. Almeida. Laser surface treament of tool steels. *Optical and Quantum Electronics*, 27:1273–1289, 1995.

[265] S. Das Bakshi. *Abrasive wear of steels*. CPGS thesis, University of Cambridge, UK, June 2012.

[266] R. Colaco, C. Pina, and R. Vilar. Influence of the processing conditions on the abrasive wear behavior of a laser surface melted tool steel. *Scripta Materialia*, 41(7):715–721, 1999.

[267] S. A. Kim and W. L. Johnson. Elastic constants and internal friction of martensitic steel, ferritic-pearlitic steel, and -iron. *Materials Science and Engineering: A*, 452453(0):633 – 639, 2007.

[268] G. Ribarik, T. Ungar, and J. Gubicza. MWP-fit: a program for multiple whole profile fitting of diffraction peak profiles by ab-initio theoretical functions. *Journal of Applied Crystallography*, 34:669–676, 2001.

[269] Sumitomo Metals. Sumihard technical datasheet. Technical report, Sumitomo metals, 2011. Personal Collection.

[270] JFE Steel Corporation. Everhard series technical report. Technical report, JFE Steel Corporation, 2011. Personal Collection.

[271] Nippon Steel Corporation. NSC catalouge AC304, 2010.

[272] Arcellor-Mittal. Fora 400 technical datasheet. Technical report, Arcellor-Mittal, 2011. Personal Collection.

[273] Arcellor-Mittal. Fora 450 technical datasheet. Technical report, Arcellor-Mittal, 2011. Personal collection.

[274] Arcellor-Mittal. Fora 500 technical report. Technical report, Arcellor-Mittal, 2011. Personal collection.

[275] Arcelor-Mittal. Creusabro superten technical report. Technical report, Arcellor-Mittal, 2009. personal collection.

[276] Arcelor-Mittal. Cruesabro dual technical report. Technical report, Arcelor-Mittal, 2009. personal collection.

[277] Arcellor-Mittal. Cruesabro-m. Technical report, Arcellor-Mittal, 2009. Personal Collection.

[278] Rukki Steel. Raex technical report. Technical report, Rukki Steel, 2012. Personal Collection.

[279] Thyssen Krupp. Xar 400 technical report. Technical report, Thyssen Krupp Steel AG, 2003. Personal Collection.

[280] Salzgitter. Brinar 400 technical report. Technical report, Salzgitter, 2005. personal collection.

[281] AG der Dillinger. Dillidur 400 technical report. Technical report, Dillinger, 2007. personal collection.

[282] Duferco. Quard 400 technical report. Technical report, Duferco Steel, 2011. Personal Collection.

[283] T. Williams and C. Kelley. GNUplot 4.5: an interactive plotting program., 2011.

[284] E. I. Radzimovsky. Stress distribution and strength condition of two rolling cylinders pressed together. University of Illinois Bulletin 44, University of Illinois Engineering Experiment Station, Illinois, Urbana, February 1953.